

Generation of Peptidomimetic Fluorophores via Amenable Chemistry with Multicomponent Reaction (ACMR) Scaffolds

A thesis submitted to the
University of Calicut in partial fulfillment of
the requirements for the degree of

DOCTOR OF PHILOSOPHY IN CHEMISTRY

By

SHYAM SHANKAR E. P.



**DEPARTMENT OF CHEMISTRY
UNIVERSITY OF CALICUT
KERALA**

AUGUST 2019

DEPARTMENT OF CHEMISTRY

University of Calicut

Dr. D. Bahulayan

Professor

CERTIFICATE

This is to certify that the thesis titled **“Generation of Peptidomimetic Fluorophores via Amenable Chemistry with Multicomponent Reaction (ACMR) Scaffolds”** submitted by Shyam Shankar E. P. to the University of Calicut for the award of the degree of Doctor of Philosophy in Chemistry, is the result of the bonafide research work carried out at the Department of Chemistry, University of Calicut under my guidance and supervision. The contents of the thesis have been checked for plagiarism using the software ‘Urkund’ and the similarity index falls under permissible limit. I further certify that the topic discussed in this thesis has not been previously formed the basis of the award of any degree, diploma or associateship of any other University or Institute.

August 2019

D. Bahulayan

DEPARTMENT OF CHEMISTRY
University of Calicut


Dr. D. Bahulayan
Professor

Calicut University campus,
Malappuram, Kerala,
Tel. (o) 0494 2401144*414
E-mail: bahulayan@yahoo.com

CERTIFICATE

This is to certify that the corrections/suggestions from the adjudicators have been addressed and are incorporated in the appropriate sections of the revised thesis entitled **“Generation of Peptidomimetic Fluorophores via Amenable Chemistry with Multicomponent Reaction (ACMR) Scaffolds”** submitted by Shyam Shankar E. P. to the University of Calicut for the award of the degree of Doctor of Philosophy in Chemistry.

July 2020


D. Bahulayan

DECLARATION

I, Shyam Shankar E. P. hereby declare that the thesis titled **“Generation of Peptidomimetic Fluorophores via Amenable Chemistry with Multicomponent Reaction (ACMR) Scaffolds”** is the report of the original research work carried out by me under the supervision of Dr. D. Bahulayan, Professor, Department of Chemistry, University of Calicut for the award of the degree of Doctor of Philosophy in Chemistry of the University of Calicut and further that this thesis contains no material previously submitted for a degree, diploma, associateship, fellowship or other similar titles of any other University or Society.

University of Calicut
August 2019

Shyam Shankar E. P.

ACKNOWLEDGMENT

First and foremost, I thank “Almighty” for being kind to me throughout this journey and also for enabling me to finish this research work successfully.

This thesis could not have been completed without the generous support that I have received from so many people over these years, and I express my gratitude to all of them.

It's a genuine pleasure to express my deep sense of gratitude to my mentor and research supervisor Dr. D. Bahulayan, Professor, Department of chemistry, University of Calicut, for his inspiring guidance, encouragement, support and patience throughout my course.

I wish to express my sincere gratitude to the former Head of the department Prof. K. Muraleedharan, Prof. P Raveendran and the present Head of the Department Dr. Yahya Ismail for providing me the necessary facilities for the successful completion of this research work.

I extend my sincere gratitude to all of my beloved teachers and other faculty members in the Chemistry department.

I also extend my thanks to all the non-teaching staffs, Chemistry department, for their assistance and support.

I would also like to express my sincere thanks to my friends from other institutions such as Ms. Dijo Prasannan, Ms. Jiji A. C., for their valuable support during the course of my research work.

I am also grateful to STIC Cochin University, IIT Madras and NIIST Trivandrum for Mass and NMR analysis and Nanyang Technical University, Singapore for recording the AFM.

I am grateful to Dr. Vimala K, Women Scientist, Division of Cancer nanomedicine, Periyar University for helping me to do the biochemical analysis.

I thank the research scholars Mrs. Shameera and Mrs. Sumaiyya for their valuable support for the DFT studies and the Central Instrumentation Facility (CIF) for providing me the computer facilities.

I deeply acknowledge my dear and respected senior research scholars Dr. Jithin Raj P, Dr. Soumya T. V., Dr. Jency Mohan T., Dr. Rajeena Pathoor and Dr. Thasnim T. from my research group for their genuine support during my research work.

I deeply extend my heartfelt gratitude to my dear friend Mrs. Shamsiya A. for her care and support throughout this journey, and also for understanding me and supporting me in all possible ways at all stages of the work.

It is also a pleasure to acknowledge the enthusiastic support given to me by all research scholars from our department and other departments.

Above all, I am grateful to my dear parents for their love, kindness, and support throughout. And also I am grateful to my dear wife and beloved daughter Shivanya for the love and constant support.

I also extend my sincere gratitude to the other members of my family for their support and love. Without the encouragement and prayers of all of them, I could not have completed this thesis.

Finally, I acknowledge the financial assistance provided by the University of Calicut for carrying out my research.

Shyam Shankar E. P.

*This thesis is dedicated to the memories of my beloved Grandmother
Mrs. Savithri Antherjanam*

CONTENTS

	Page No.
Chapter 1	1-36
An overview of the Benzopyran based Small Molecule Fluorophores and Fluorescent probes	
1.1 Coumarin	3
1.1.1 Coumarin scaffolds in light emission	4
1.1.2 Fluorescence bioimaging applications of coumarin derivatives	6
1.1.3 Coumarin derivatives as the promising scaffolds for developing therapeutics	9
1.2 Chromene	12
1.2.1 Material applications of Chromene derivatives	14
1.2.2 Chromene derivatives as the promising lead scaffolds for therapeutics	15
1.3 Property oriented synthesis of functional scaffolds: MCR-Click strategy	18
1.3.1 Multicomponent Reactions (MCRs)	18
1.3.1.1 Ugi four component reaction (Ugi-4CR)	20
1.3.1.2 Na ₂ CO ₃ -catalyzed one-pot solventless synthesis of 2-amino-4H-chromenes	25
1.3.2 Click-reaction	25
1.4 Conclusion	28
References	30
Chapter 2	37-72
Multicomponent-Reaction- (MCR-) Assisted Synthesis of a Coumarin-Based Deep Blue Fluorescent Emitter	
2.1 Introduction	37
2.2 Results and Discussion	39

2.2.1 Synthesis and Fluorescence Study	39
2.2.2 The Structural and Photo-physical Characterization	43
2.2.2.1 Effect of pH on the fluorescence of Ugi EML BLUE	48
2.2.2.2 Quantum Yield of Ugi EML BLUE	49
2.2.3 The DFT Studies on Light emission mechanism	49
2.3 Conclusions	54
2.4 Structural Characterization of Ugi EML BLUE	54
2.5 Experimental Section	56
2.5.1 Materials and Methods	56
2.5.2 Synthetic Procedures	57
2.5.2.1 Synthesis of Ugi EML BLUE	57
2.5.2.2 Synthesis of Ugi Chloride	58
2.5.2.3 Conversion of Ugi Chloride to Ugi Azide	59
2.5.3 Measurements of Fluorescence in various pH	59
2.5.4 Thin film of Ugi EML BLUE for measuring the solid state UV-Vis _{abs} & PL _{ems}	60
2.5.5 Fluorescence Quantum Yields	60
References	62
Supporting Information	67
Chapter 3	73-104
Studies on the applications of Ugi EML BLUE for the CDK2 Targeted Bioimaging and Cytotoxic Activities on HeLa Cells	
3.1 Introduction	73
3.2 Results and Discussion	76
3.2.1 Evaluation of the CDK2 targeted imaging potential of Ugi EML BLUE	76
3.2.2 Evaluation of the cytotoxicity of Ugi EML BLUE targeted against CDK2 present in human cervical cancer (HeLa) cells.	80

3.2.2.1 <i>In vitro</i> cytotoxic effect of the Ugi EML BLUE against the HeLa cells and primary H8 cells	80
3.2.2.2 Morphology study	82
3.2.2.3 Mitochondrial membrane potential analysis	83
3.2.2.4 Cell cycle analysis	84
3.2.2.5 Western Blot analysis and mechanis	85
3.3 Conclusions	89
3.4 Experimental Section	89
3.4.1 Materials and Methods	89
3.4.1.1 Cell culture	90
3.4.1.2 Evaluation of cytotoxicity against cervical cancer (HeLa) cells	90
3.4.1.3 Evaluation of cytotoxicity against primary cervical (H8) cells	91
3.4.1.4 Cell cycle analysis	92
3.4.1.5 Rhodamine 123 Staining	92
3.4.1.6 Western Blot Analysis	93
3.4.1.7 Bioimaging	93
3.4.1.8 Docking Analysis	94
References	95
Supporting Information	101
Chapter 4	105-178
Chemistry, Chemical Biology and Photophysics of Certain New Chromene-Triazole-Coumarin Triads as Fluorescent Inhibitors of CDK2 and CDK4 Induced Cancers	
4.1 Introduction	105
4.2 Results and Discussions	107
4.2.1 Evaluation of Fluorescence Properties	109
4.2.2 Fluorescence properties of the Chromene-Triazole-Coumarin triads in solid state	112
4.2.3 DFT Studies and Fluorescence Mechanisms	113

4.2.4 Docking Studies of Chromene-Triazole-Coumarin Triads against CDKs	117
4.2.5 Evaluation of <i>in vitro</i> cytotoxic activities of T2 and T5 against Human Cervical Cancer Cell line (HeLa)	119
4.2.6 Morphology Study	120
4.2.7 Western Blot Analysis	121
4.2.8 Cell cycle Analysis	122
4.3 Comparison between Chromene-Triazole-Coumarin Triads T1 , T2 , T5 and Ugi EML BLUE	124
4.4 Conclusions	127
4.5 Structural Characterizations	128
4.5.1. Structural characterization of Ch4 (alkyne)	128
4.5.2. Structural Characterization of Coumarin-azide	130
4.5.3. Structural Characterization of Chromene-Triazole-Coumarin Triad 4 (T4)	131
4.6 Experimental Section	132
4.6.1 Materials and Methods	132
4.6.2. Synthetic Procedures	133
4.6.3 Biochemical Procedures	143
4.6.3.1 Cell culture	143
4.6.3.2 Evaluation of cytotoxicity [MTT Assay]	143
4.6.3.3 Morphological study	144
4.6.3.4 Cell cycle analysis	144
4.6.3.5 Western Blot Analysis	145
References	146
Supporting Information	151
Chapter 5	179-186
Conclusions and Future Perspectives	
Research Publications	

PREFACE

Fluorescent peptides are an important class of compounds since such moieties have a plethora of applications in medicinal chemistry, drug discovery, diagnosis and therapy. The peptide fluorophores are used in visualizing intracellular processes and have vast applications as fluorescent inhibitors and drug carriers. However, the preparation of such probes requires multistep synthetic protocols, large resources, manpower and expensive machinery leading to the escalation of manufacturing costs. Hence the search for new cost-effective alternatives in terms of the utility of potential new synthetic methodologies is highly demanding. Multicomponent reactions (MCR) and Click-Chemistry are examples of such potential synthetic protocols useful for the step economic and cost-effective synthesis of functional scaffolds. Inspired with these thoughts, two widely accepted bioactive heterocycles such as coumarin and chromene were selected and decorated with suitable functionalities using MCR-Click protocols to obtain peptidomimetic fluorophores. The discussion on the synthesis and the evaluation of the photophysical and biological properties of these new fluorescent inhibitors are the subject matter of this thesis.

The thesis has been divided into five chapters. The first chapter presents an overview of the significance of simple and properly functionalized fluorescent probes for material applications, cellular level bioimaging, and medicinal applications, with a special focus to coumarin and chromene derivatives. Various features and applications of the derivatives of these two moieties have been summarized in this chapter. Moreover, brief descriptions of a few potential synthetic

strategies which can be used for the proper functionalization of the aforesaid molecules are also included in this chapter.

Chapter 2 presents a multicomponent reaction (MCR) assisted step economic protocol for the synthesis of coumarin based deep blue-emitting fluorescent molecule named as “Ugi EML BLUE” suitable for various light emission based applications. The solution state and solid-state fluorescence, pH sensitivity and significant physical properties were evaluated, interpreted and documented. A plausible mechanism for the origin of light emission from this molecule is also presented based on experimental and computational methods.

Chapter 3 is the continuation of chapter 2 and in this chapter, the biological applications of the Intramolecular Charge Transfer (ICT) based blue emitting fluorescent probe Ugi EML BLUE is presented. The binding properties of the Ugi EML BLUE against human CDK2 protein were studied via docking methods. The docking studies showed that Ugi EML BLUE can effectively interact with the ATP binding sites of CDK2. The positive results obtained from the docking studies were extended to the bioimaging as well as antineoplastic applications on HeLa cells. The *in vitro* biological activity studies revealed the remarkable potential of Ugi EML BLUE as a dual functional molecule that can be used not only as a CDK2 targeted fluorescent probe for bioimaging but also as a CDK2 targeted inhibitor for HeLa cells.

Chapter 4 presents a new series of Chromene-Triazole-Coumarin Triads synthesized through the employment of a solvent free mechanochemical multicomponent reaction followed by copper catalyzed (3+2) azide-alkyne cycloaddition (click chemistry). The

molecules were investigated for their fluorescence and CDKs induced anticancer properties. Half numbers of the molecules showed the fluorescence in the solution state through ICT based electronic transitions whereas, the other half showed solid state fluorescence through aggregation induction. Computational studies on binding affinity revealed that all the molecules are in general selective towards CDK2 and CDK4. The studies on *in vitro* biological activity showed that the selected molecules are promising lead structures for undertaking further studies to develop fluorescent inhibitors of CDK2/CDK4 induced tumors. They showed appreciable IC₅₀ values against the human cervical cancer cell line (HeLa).

Chapter 5 presents the conclusions and future aspects of the work presented in this thesis. As discussed in chapters 2 to 4, this study has demonstrated the facile synthetic routes to the efficient fluorescent inhibitors decorated with the appropriate functionalities and their applications in various fields such as light emission devices, bioimaging, and anticancer agents, etc. We hope that further in-depth studies based on this work will make an impact on the development of cost effective cancer therapeutics and efficient fluorescent probes for a broad spectrum of applications.

AN OVERVIEW OF THE BENZOPYRAN BASED SMALL MOLECULE FLUOROPHORES AND FLUORESCENT PROBES

The fluorophores or fluorescent probes are the class of molecules which are capable to re-emit light upon excitation via absorbing the radiation from the appropriate region of electromagnetic spectra. In general, the fluorescent probes constitute the combined aromatic moieties or cyclic or planar molecules with long π -conjugations. Normally, the fluorophores re-emit light at longer wavelengths after absorbing the spectral energy of a specific wavelength in the electromagnetic spectra. The nature of fluorescence and other photophysical properties are depending on the structure and chemical environment of the fluorophore, which implies the properties of the fluorophores can be tuned according to the various requirements. In the recent decade, fluorescent probes become an integral part of various smart applications such as Light Emitting Diodes (LEDs), sensors, bioimaging, spectroscopy, microscopy, forensics, engineering, signage, etc.^[1] Fluorescence-based bioimaging techniques are capable to provide high resolution images of cellular entities useful for accurate medical diagnosis. Fluorescence based lighting techniques are also very significant since they provide a cost-effective alternative to energy efficient lighting systems. The small molecule fluorescent probes have received considerable importance in recent years due to their structural simplicity, high efficiency, metal-free and bio-friendly nature, appreciable cell permeability, etc. Hence, these probes are

highly focused by fields like organic electronics, bioimaging, drug designing, environmental analysis, chemosensor, etc. Typical examples of such potential small molecule fluorescent probes are presented in Figure 1. A recent attraction in this field is the development of “fluorescent inhibitors”.

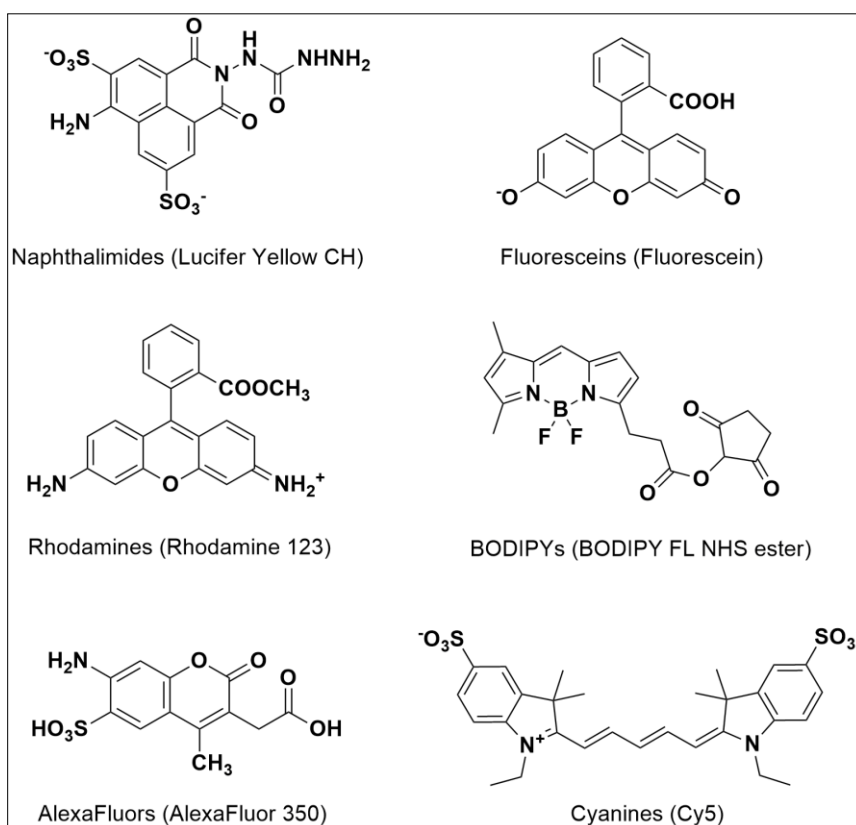


Figure 1. Representative examples for potential small molecule fluorescent probes

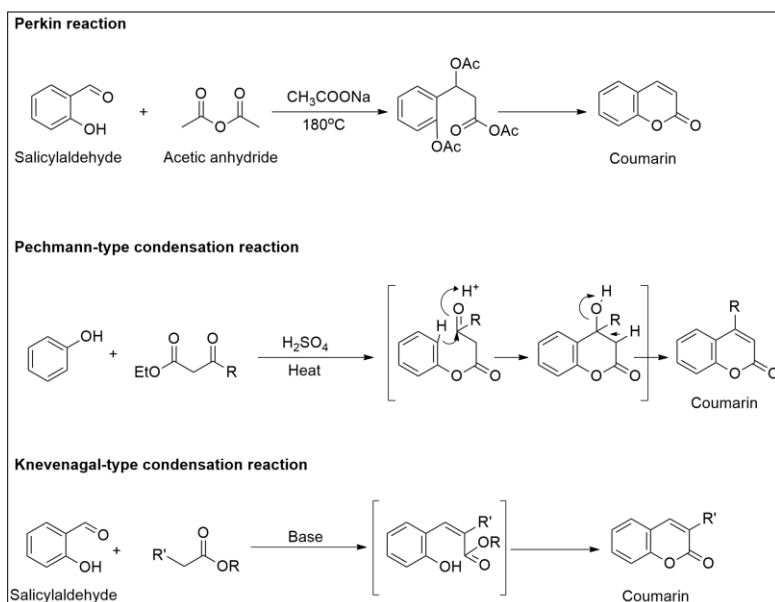
The fluorescent inhibitors are dual-functional probes capable of inhibiting and characterizing intracellular substrates simultaneously, where the inhibition of such target substrate leads to curing.^[2] However, the synthesis of these kinds of probes involves multistep processes which are

resource-intensive even though they are small molecule based. This will lead to the escalation of manufacturing costs. Moreover, the integration of the aforementioned dual properties in the development of such dual-functional fluorescent inhibitor probes may be complicated. Hence the search for new cost-effective and property oriented alternatives in terms of the utility of potential new synthetic methodologies is highly desirable. The multicomponent reactions (MCR) and Click Chemistry, which is a facile route to synthesize the peptidomimetics, can be utilized as a perfect solution for the step-economic, cost-effective and property oriented synthesis. In this manner, the dual-functional peptidomimetic fluorophores can be afforded by introducing the appropriate fluorophores as scaffolds in the MCR-Click protocols. The best two examples for such fluorophores are the coumarin and chromene, which are well known for their fluorescence as well as the biological activities. Several derivatives of coumarin and chromene have been reported for their applications as light emitting material and Donor/Acceptor part in many fluorescent dyes etc.^[3] Moreover, plenty of natural as well as synthetic derivatives of the coumarin and chromene has been reported as potential therapeutic agents against various diseases including cancers.^[4]

1.1 Coumarin

The coumarin or *2H-chromene-2-one* is an aromatic compound belongs to the class of benzopyrones. Coumarin was primarily isolated in 1820 from Tonka beans by A. Vogel and the same was primarily synthesized in 1868 by the chemist W. H. Perkin. Coumarin can be synthesized by different types of reactions like Pechmann or Knevenagel type condensation reactions and also by the Perkin reaction between

salicylaldehyde and acetic anhydride which is a popular method (Scheme 1).^[5] Large numbers of coumarin derivatives are available for the use as lighting materials, fluorescence imaging dyes, and therapeutic agents.



Scheme 1. Different types of coumarin synthesis

1.1.1 Coumarin scaffolds in light emission

The fluorescence ability makes coumarin a potential core scaffold for the development of cost-effective and high efficiency lighting systems.^[6] Organic Light Emitting Diodes (OLEDs) are the best examples for such lighting technologies based on the fluorescence. Most of the trendy researches in these fields have targeted on the small molecule organic fluorescent materials or fluorophores since they are easy to synthesize, highly efficient, simple and cost-effective.^[7,8] The properly functionalized derivatives of coumarin have a significant role in these

kinds of material researches. The derivatives of coumarin are widely accepted for the various fluorescence related applications due to their promising high fluorescence intensity and quantum yields.^[9-12] Such materials have been majorly used as the emitting materials for the Emissive Layers (EML) in OLEDs.^[13,14] For example, coumarin 540 (3-(2-benzothiazole)-7-diethylaminocoumarin) is a coumarin based efficient emitting material reported by Tang's group in 1989.^[15] As a consequence, the derivatives of coumarin have been widely studied as the fluorescent emitters in OLEDs. Three coumarin derivative with relatively high quantum yields were reported as emitting materials for OLEDs by Chen et al. in 2003.^[16] In 2013, J. X. Chen et al. reported a coumarin derivative as the blue emitter for the hybrid white OLEDs.^[17] In 2016, Patil's group reported a coumarin derivative (7-(9H-carbazol-9-yl)-4-methylcoumarin) with high quantum yield in a doped matrix which is suitable for the deep blue OLEDs.^[18]

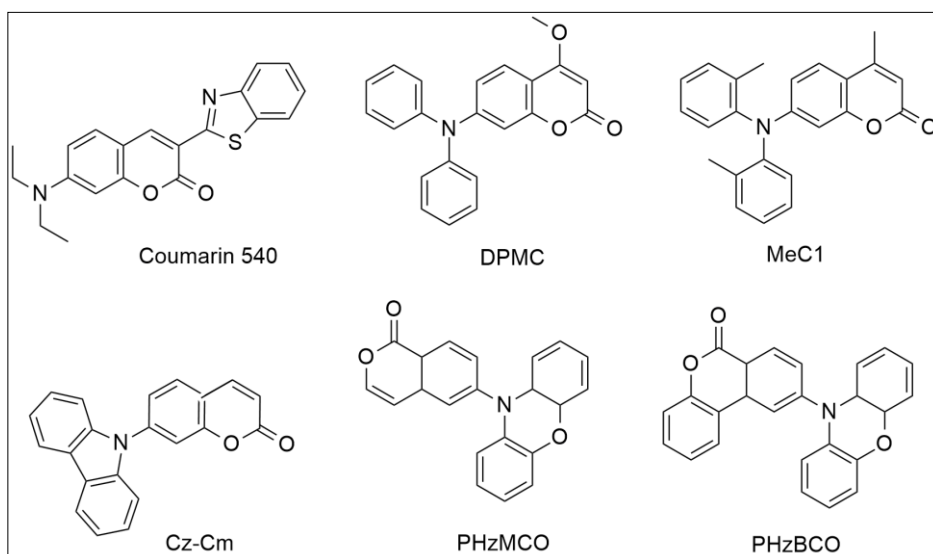


Figure 2. Selected coumarin derivatives as emitters for OLEDs

Again, J. X. Chen et al. reported two derivatives of coumarin, 3-methyl-6-(10H-phenoxazin-10-yl)-1H-isochromen-1-one (PHzMCO) and 9-(10H-phenoxazin-10-yl)-6H-benzo[c]-chromen-6-one (PHzBCO), as the thermally activated delayed fluorescence (TADF) emitters.^[19] These kinds of extensive reports have proved the significance of coumarin derivatives as the materials in lighting related applications. Few selected coumarin derivatives from the aforesaid research outputs are presented in Figure 2.

1.1.2 Fluorescence bioimaging applications of coumarin derivatives

As discussed early, the coumarin derivatives possess relatively high fluorescence and quantum yields. Hence, many of them have widely accepted as imaging probes. The fluorescence based microscopic techniques and bioimaging techniques are useful for cellular level imaging diagnosis methods.^[20,21] The fluorescence based bioimaging techniques have a high impact on medical diagnosis since it allows the cellular level imaging, where the other classic imaging techniques provides only morphological imaging. The majority of the trendy researches in these fields have targeted on the ICT/FRET based small molecule organic fluorescent materials or fluorophores since they are metal free, bio-friendly, easy to synthesize, highly efficient, simple and cost-effective.^[22,23] Coumarin derivatives are the perfect examples for this kind of small molecule fluorescent probes. Plenty of researches have been conducting with these coumarin derivatives for various bioimaging applications. Few interesting examples are discussed here. In 2011, L. Yuan et al. reported a coumarin based fluorescent hypochlorite probe for

cellular imaging based on the OCl^- promoted de-diaminomaleonitrile reaction (Figure 3).^[24] The OCl^-/HOCl is a significant reactive Oxygen Specious (ROS) and which plays a crucial role in different biological processes. X. Cheng's group reported a coumarin based fluorescent and colorimetric probes, Coum-1 and Coum-2 for the Cyanide sensing and bioimaging applications (Figure 4).^[25] Similarly, in 2015, C. Zhang et al. reported a few probes sensitive to the H_2S and suitable for bioimaging (Figure 5).^[26] The H_2S is an endogenous signaling molecule and the concentration of which is correlated with various diseases like Alzheimer's disease, diabetes, liver cirrhosis, etc.

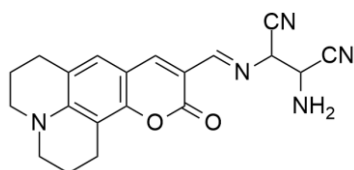


Figure 3. Coumarin based fluorescent hypochlorite probe for cellular imaging

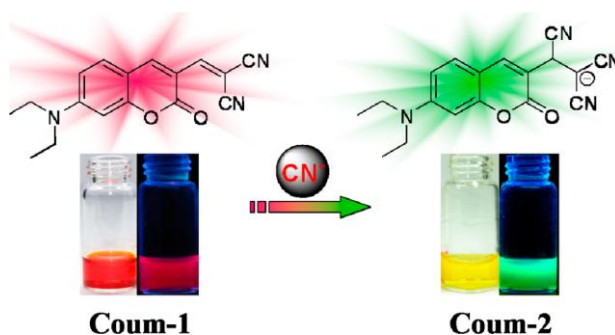


Figure 4. Coumarin based cyanide sensing bioimaging probes

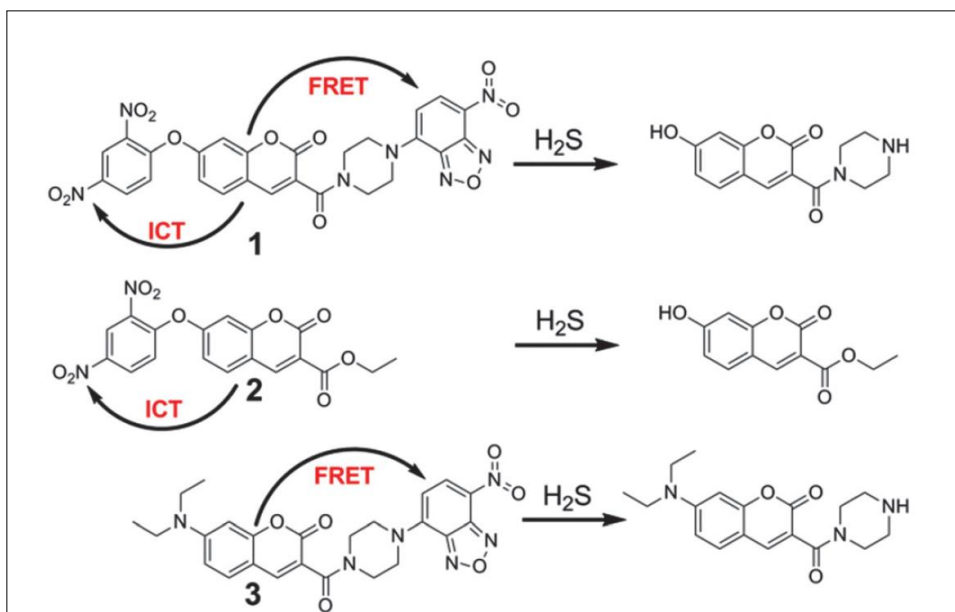


Figure 5. Coumarin based H₂S sensing bioimaging probes and their reactions with H₂S

In 2017, B. X. Zhao's group developed an ICT/FRET platform based on coumarin-hemicyanine dyad which is highly sensitive to the endogenous sulphite in a living cell and is suitable for the bioimaging (Figure 6).^[22] Overall, these kinds of ongoing research works imply that the coumarin derivatives are suitable candidates for developing the dyes/probes for the fluorescence bioimaging.

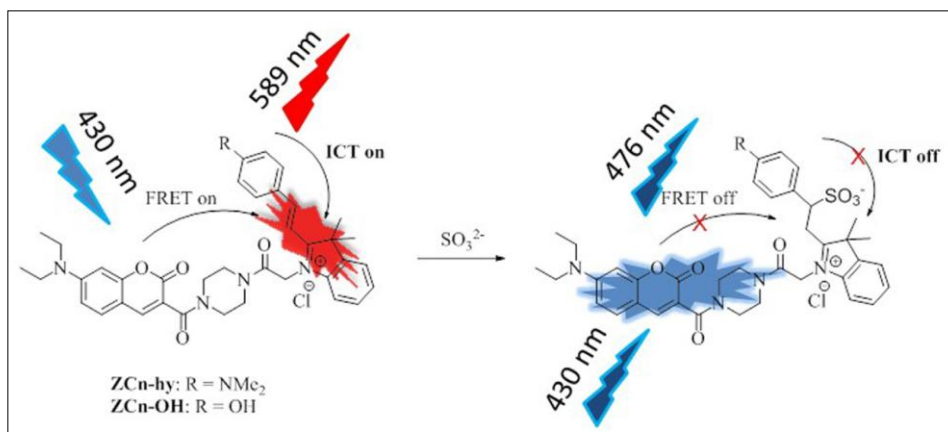


Figure 6. Coumarin-Hemicyanine based Sulphite sensing bioimaging probes and their reactions with sulphite

1.1.3 Coumarin derivatives as the promising scaffolds for developing therapeutics

Coumarin and coumarin derivatives are part of flavonoid groups and have a plethora of therapeutic applications like anti-inflammatory, antioxidant, anti-nociceptive, hepatoprotective, antithrombotic, antiviral, antimicrobial, anti-tuberculosis, anticarcinogenic, antidepressant, antihyperlipidemic and anticholinesterase activities.^[27] Selected examples of the clinically proven therapeutic agents containing natural/synthetic coumarin moieties are presented in Figures 7 and 8. Among them, hymecromone (4-methylumbelliferone) has been used as a choleric and antispasmodic drug. Scopoletin has properties such as antioxidant, hepatoprotective, anti-inflammatory and antifungal. Carbochromen was suitable for the treatment of coronary disease. 4-Hydroxycoumarin derivatives acenocoumarol, phenprocoumon, warfarin, difenacoum, and brodifacoum are anticoagulant agents that can act as vitamin K

antagonists. Armillarisin A and novobiocin are antibiotics. The geiparvarin is an antiproliferative agent,

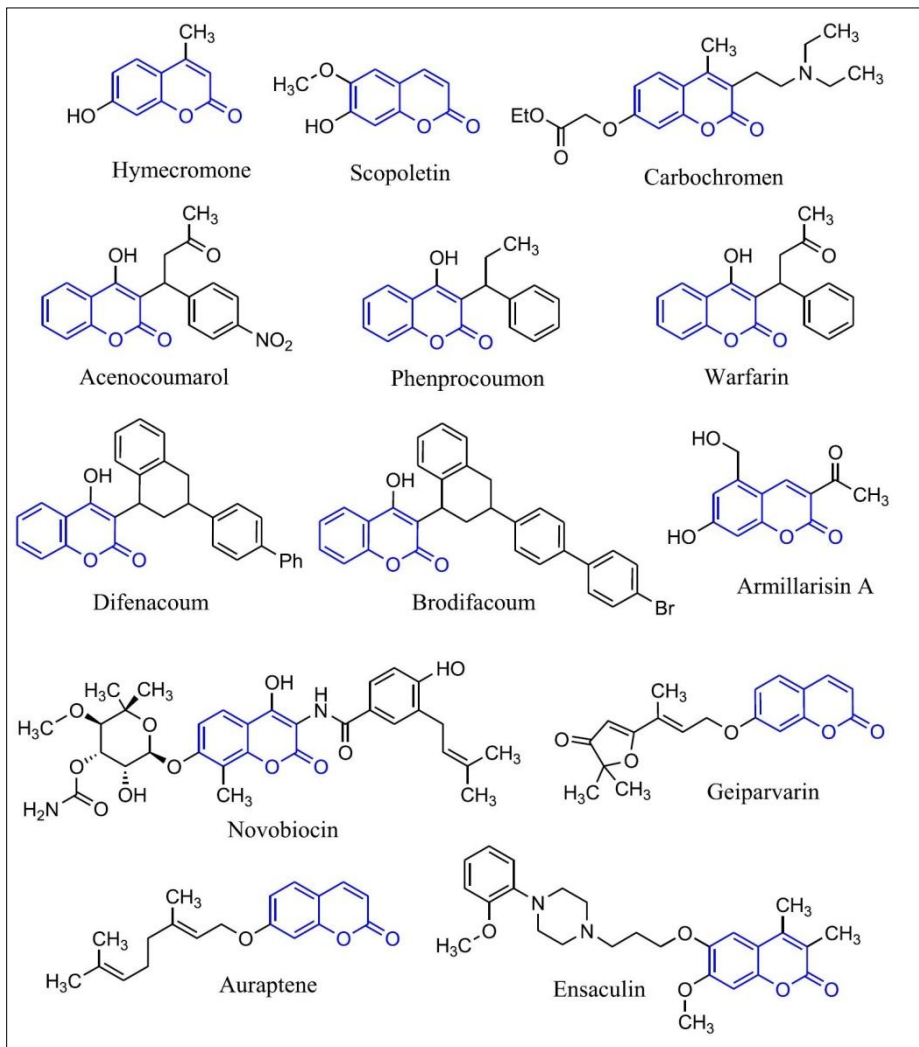


Figure 7. Selected examples of coumarin containing natural/synthetic therapeutic agents

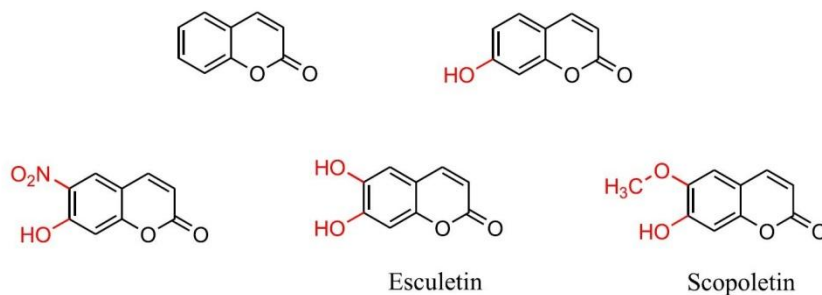


Figure 8. Selected examples of simple coumarins with cytotoxic activities

auraptene is a chemoprotective agent and ensaculin used in treatment for dementia and which are medicinally potential agents that have been studied and extensively used in therapeutics. The coumarin and 7-hydroxycoumarin are potent cytotoxic agents against renal cancer. Similarly, 6-nitro-7-hydroxycoumarin, scopoletin (6-methoxy-7-hydroxycoumarin) and esculetin (6,7-dihydroxycoumarin) are anti-proliferative agents induces the apoptosis through Cyclin Dependent Kinase (CDK) inhibition and other mechanisms. In summary, a major part of coumarin derivatives has the capability to show the anticancer activity against different cancers through different mechanisms like kinase inhibition, apoptotic cell induction, cell cycle blocking, etc. Therefore, extensive researches have been ongoing in this field for developing coumarin based anticancer molecules with improved selectivity and efficiency. Few selected studies are discussed here. The tricyclic coumarin sulfamate (STX64)(Figure 9), ($IC_{50} = 8 \text{ nM}$) a non-steroid based irreversible aromatase-steroid sulfatase (STS) inhibitor provides remarkable activity against the prostate cancer, and its clinical trials have been accomplished in 2011.^[28-30] Similarly, 3,8-dibromo-7-hydroxy-4-methyl coumarin (DBC) ($IC_{50} = 100 \text{ nM}$) is a potent CDK2 inhibitor to

suppress neoplastic growth.^[31,32] In 2014, Narayanachar's group reported few iodinated-4-aryloxymethylcoumarins which has the anticancer activity against human adenocarcinoma mammary gland (MDAMB) and human lung carcinoma (A-549).^[33] In 2016, Malic's group reported 4-substituted 1,2,3-triazole core in designed coumarin hybrids with cytotoxic activity against hepatocellular carcinoma HepG2 cells.^[34] Furthermore, T. Abdizadeh et al. reported few coumarin based benzamides as potent histone deacetylase inhibitors and anticancer agents in 2017.^[35] These results and ongoing research works showing the potential of the coumarin derivatives in therapeutics.

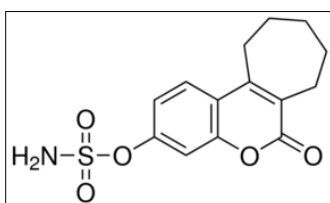


Figure 9. Potential example for the coumarin based anticancer drug under clinical trials

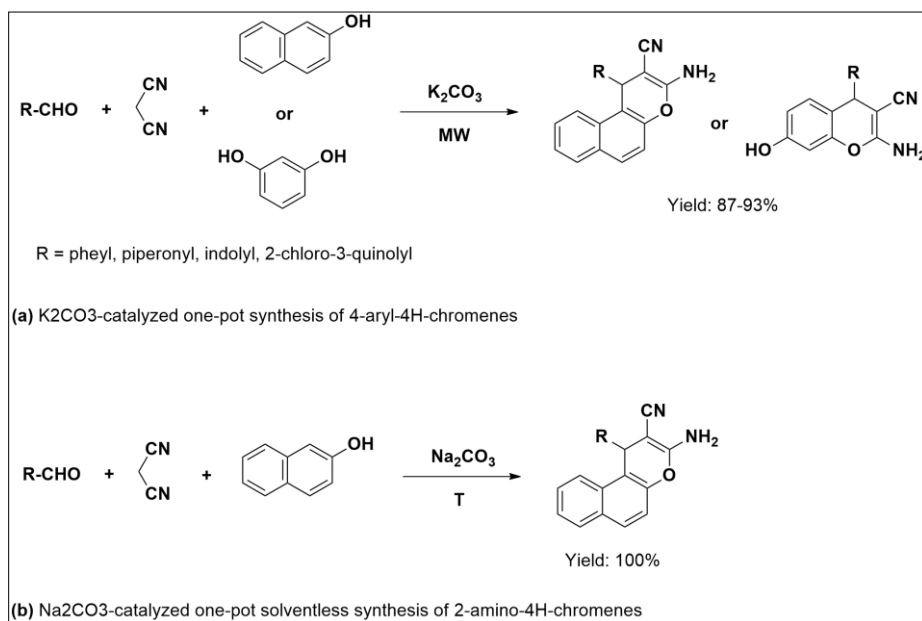
1.2 Chromene

Chromene or benzopyran is a bicyclic molecule in which benzene is fused to a pyran ring. Chromenes are divided into different classes like 2H-chromene or 2H-1-benzopyran and 4H-chromene or 4H-1-benzopyranas based on the position of the double bond in the pyran ring (Figure 10).



Figure 10. General structures of 2H-chromene and 4H-chromene

Chromene constitutes several naturally occurring alkaloids, flavonoids, anthocyanins and tocopherols.^[36] There are plenty of chromene derivatives where, the chromenes like furochromenes, bezofurochromenes, pyranochromenes, benzochromenes, naphthochromenes, etc. are isolated from various plants and which have potent drug properties.^[37] Similarly, chromene derivatives are also synthesized in laboratories as per the structural requirements. There are multiple synthetic routes available to synthesize the chromene derivatives and among them, the two efficient examples are K_2CO_3 -catalyzed one-pot synthesis of 4-aryl-4H-chromenes and Na_2CO_3 -catalyzed one-pot solventless synthesis of 2-amino-4H-chromenes (Scheme 2).^[38]



Scheme 2. (a) K_2CO_3 -catalyzed one-pot synthesis of 4-aryl-4H-chromenes (b) Na_2CO_3 -catalyzed one-pot solventless synthesis of 2-amino-4H-chromenes

1.2.1 Material applications of Chromene derivatives

Several chromene derivatives have a significant role in the fields of light emitting devices, optical brighteners, dyes and imaging probes since they possess excellent chromophoric and fluorescent properties. Yoon et al. reported two series of di-*tert*-butyl chromene containing red fluorescent materials suitable for the emissive layers of OLEDs (Figure 11).^[39]

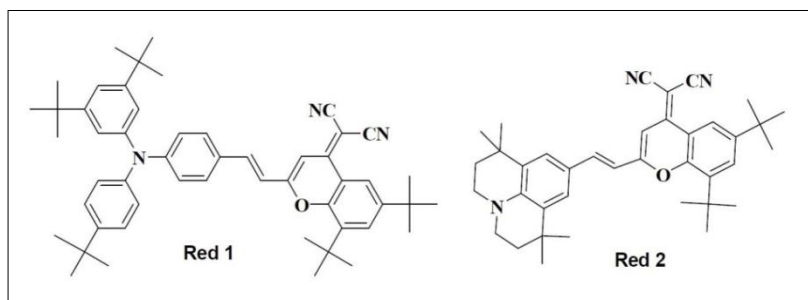


Figure 11. Examples for the chromene based red-emitting materials for OLEDs

Similarly, Feng et al. reported a conjugated dicyanomethylenebenzopyran molecule near IR (NIR) fluorescent probe for the detection of thiophenols in living cells.^[40] The compound 2,4-dinitrobenzene-1-sulfonamide used as the reaction site for the turn-on fluorescence detection of thiols is shown in Figure 12.

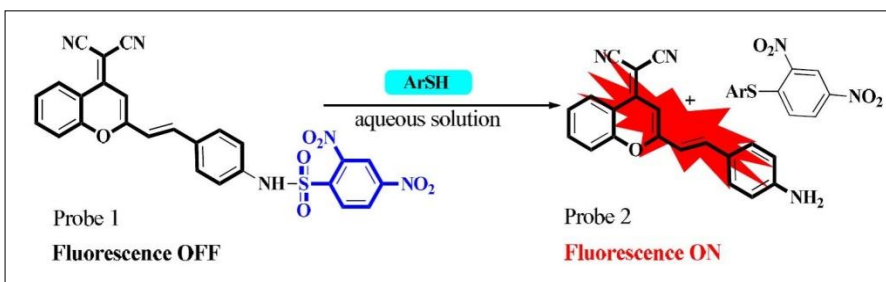
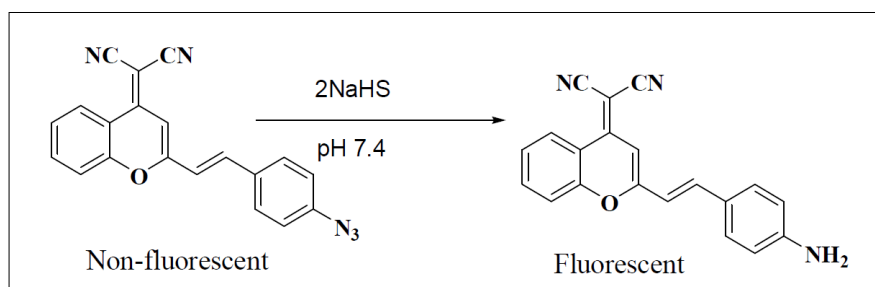


Figure 12. Examples for the chromene based thiol sensing probe suitable for bioimaging

Furthermore, Y. Zheng et al. reported a dicyanomethylene-4H chromene derivative which is sensitive to hydrogen sulphide based on the reduction reaction of azide to an amine by H_2S (Scheme 3).^[41]



Scheme 3. Example for the chromene based H_2S sensing probe

1.2.2 Chromene derivatives as the promising lead scaffolds for therapeutics

The chromene derivatives are part of flavonoid groups and have vast applications in medicinal chemistry. Many natural or synthetic chromene derivatives show antibacterial, antimicrobial, antioxidant, anti-HIV, anti-vascular, antiviral and antiproliferative activities.^[42]

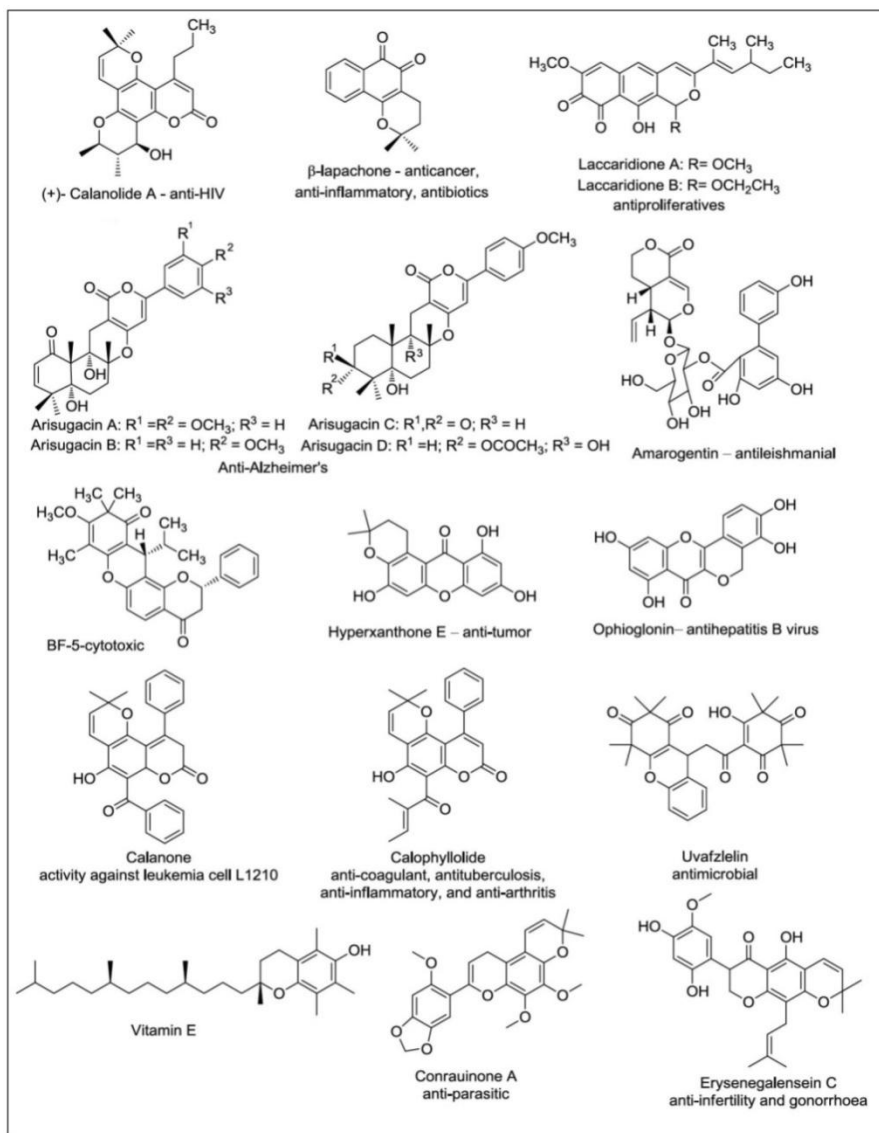


Figure 13. Chromene based naturally occurring biologically active molecules

The key feature of the benzopyran derivatives is their lipophilic nature which helps them to cross the cell membrane easily.^[43] As a consequence, chemists have been taking great efforts to utilize the potential bioactivities of chromene derivatives to develop new drug candidates. For example,

calanolide A is chromene based potential therapeutic agent for the treatment of HIV.

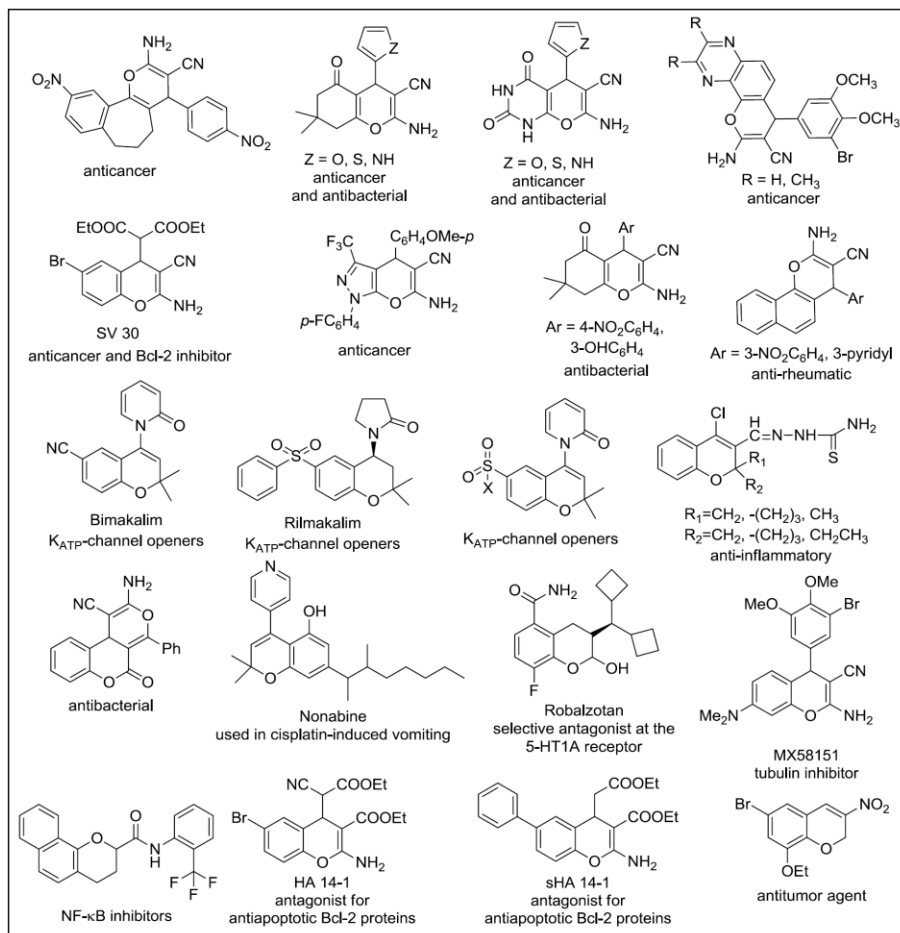


Figure 14. Potential examples for the synthetic chromene derivatives possessing different biological activities

Similarly, the β -Lapachones are potent agents against malignant gliomas cells. Selected examples of naturally occurring chromene derivatives with potential therapeutic applications are presented in Figure 13.^[43,44-58] Furthermore, plenty of synthetic chromene scaffolds are also available for drug discovery purpose. For example, bimakalim and rilmakalim are the

potential openers of KATP channels. Nonabine is an effective antidote for cisplatin induced vomiting. Robalzotan is a selective antagonist at the serotonin 1A (5-HT1A) receptor. HA141 and MX58151 are small molecule antagonists for anti-apoptotic Bcl-2 proteins which are now developed as anticancer agents. A collection of synthetic chromene derivatives possessing different biological activities are presented in Figure 14.^[43,59-80] In summary, the naturally occurring and synthetic derivatives of chromene scaffolds have a plethora of medicinal applications with major focus as anticancer agents. From the above discussions, structure optimized chromene derivatives are promising scaffolds for developing the therapeutic agents against various diseases including cancers.

1.3 Property oriented synthesis of functional scaffolds: MCR-Click strategy

1.3.1 Multicomponent Reactions (MCRs)

Reactions are the tool kits of organic chemists for the assembly of novel molecules having essential properties. In former times, chemists put much efforts to discover and new reactions, whereas today's chemist's efforts have shifted more towards other questions (e.g. improvements of stereoselectivity, catalysis and total synthesis of complex natural products, improvements in the percentage of yields, etc.). Almost no new reactions are discovered anymore in the chemistry of two-component reactions. In the field of MCRs, this seems to be different: one notices a growing number of publications on novel MCRs than ever before.

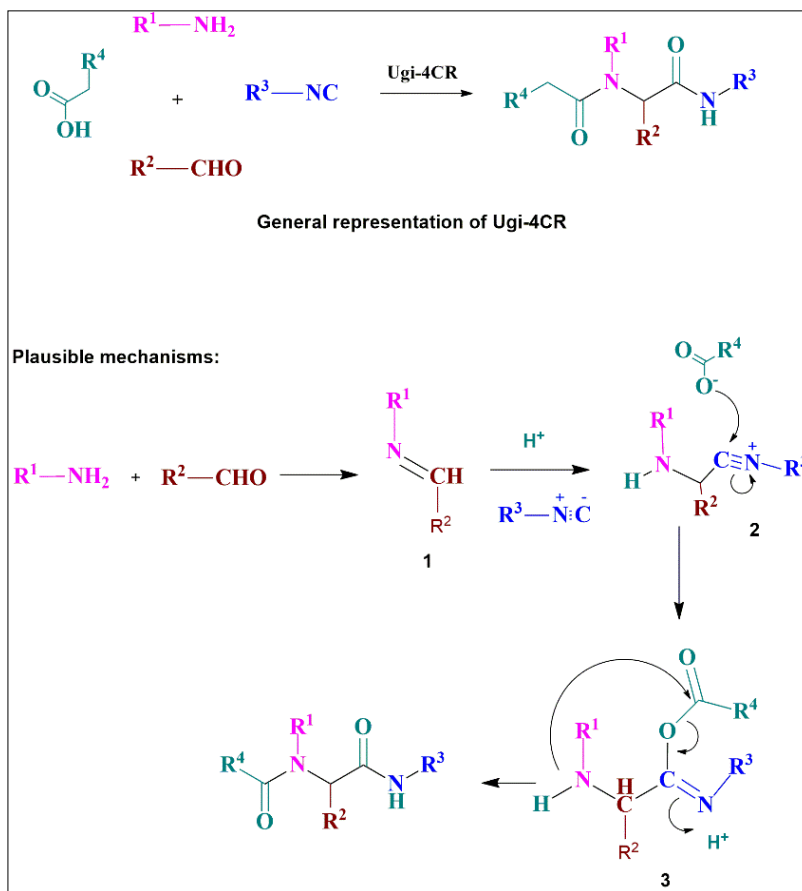
Multicomponent reactions (MCRs) are special types of synthetically useful organic reactions in which three or more starting materials react to give a product. Essential parts of the starting materials must be part of the product. In the last two decades, multicomponent reactions have demonstrated themselves to be very powerful in the synthesis of natural products, as well as in combinatorial chemistry. The combination of three or more different series of reagents allows the straightforward construction of large libraries while accepting a broad variety of chemical functionality. Most applications of MCRs described are in the area of drug discovery where it is often crucial to access rapidly and efficiently a large diversity of structures. Indeed, the ease of performance, the time saving aspect, versatility, the diversity of obtained scaffolds and the very large chemical space explored have makes the MCRs very significant in molecular designing.^[81-85] The history of the MCR begins with the Strecker synthesis of α -amino acids in 1850.^[86] The first important application of MCRs in natural product synthesis was Robinson's tropinone synthesis from succinic dialdehyde, methylamine, and dimethyl acetone dicarboxylate. Subsequently, many MCRs were reported for the synthesis of heterocyclic or non-heterocyclic scaffolds. For example, Hantzsch synthesis of dihydropyrimidine as well as pyrroles,^[87] The Biginelli reaction for the synthesis of 3,4-dihydropyrimidin-2(1H)-ones,^[88] Debus - Radziszewski synthesis of imidazoles,^[89] Mannich reaction for β -amino carbonyl compounds,^[90] K_2CO_3 -catalyzed one-pot synthesis of 4-aryl-4H-chromenes,^[38] Na_2CO_3 -catalyzed one-pot solventless synthesis of 2-amino-4H-chromenes (Scheme 2) etc.^[38] are few of the perfect examples of MCR synthesis of privileged scaffolds. Furthermore, the Isocyanide base Multicomponent

reaction (IMCRs) such as Ugi reaction for the synthesis of α -N-acylamino amides,^[85] Passerini reaction for the synthesis of α -acyloxy amides,^[91] Van Leusen reaction,^[92] Bucherer-Bergs for the synthesis of hydantoins and α -amino acids, etc.^[93] were emerged as classical examples of multicomponent synthesis of medicinally active scaffolds. The molecules presented in the coming chapters are synthesized with aforesaid Isocyanide based Ugi four-component reaction and Na₂CO₃-catalyzed one-pot solventless synthesis of 2-amino-4H-chromenes.

1.3.1.1 Ugi four-component reaction (Ugi-4CR)

In 1959, Ugi *et al.* reported the most important variants of the four-component condensation to represent a powerful one-pot method to assemble α -acylamino carboxamides from a primary amine, a carbonyl compound, a carboxylic acid, and an isocyanide. The general representation and the plausible mechanism for the Ugi four-component reaction are presented in Scheme 4.^[85] Depending upon the R groups and the replacement/removal of starting materials, post-Ugi reactions have been reported.

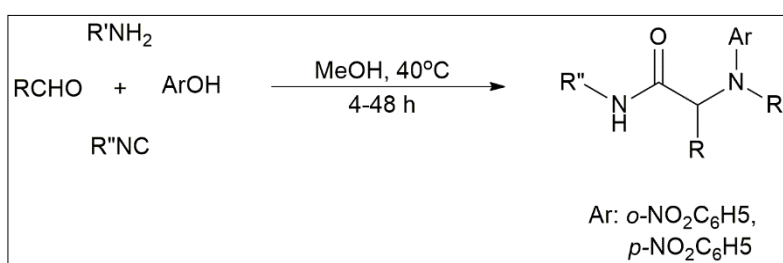
The amine (R¹NH₂) and aldehyde (R²CHO) form the imine **1** with loss of one equivalent of water. The proton exchange with carboxylic acid (R⁴COOH) activates the iminium ion **2** for nucleophilic addition of the isocyanide (R³N⁺C⁻) with its terminal carbon atom to form the nitrilium ion. A second nucleophilic addition takes place at this intermediate with the carboxylic acid anion to **3**. The final step is a rearrangement with the transfer of the R⁴ acyl group from oxygen to nitrogen.



Scheme 4. General representation of Ugi four-component reaction (Ugi-4CR) and plausible mechanisms

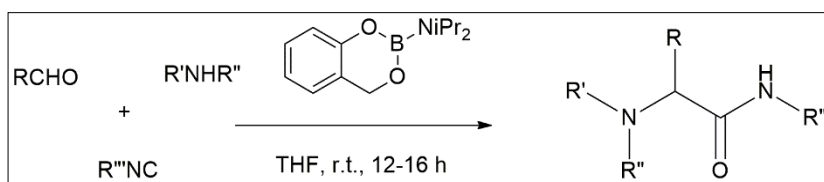
The high diversity of Ugi reaction products originate from the four substitutable diversity points present in it. Since there are large numbers of diversely substituted aldehydes, amines, carboxylic acids and isocyanides are available, it is facile to develop a large collection of carboxamides, where the carboxamide derivatives are well known for their biological activities. Hence, the research works have been ongoing in the field of Ugi reaction. Typical examples are discussed here.

In 2005, Kaim et al. reported the phenol Ugi-Smiles systems strategies for the N-arylation of the primary amines.^[94] In Ugi reaction, they replaced the carboxylic acid by *o*-nitrophenol, *p*-nitrophenol, or salicylate (Scheme 5). The final step is then a smiles rearrangement, in Ugi reaction which is a Mumm type rearrangement.



Scheme 5. General representation of phenol Ugi-Smiles strategy

In 2007, Tanaka et al. developed an aminoborane mediated Ugi type reaction in which the aminoborane act as an iminium ion generator which facilitates the effective usage of the various secondary amines in Ugi reaction (Scheme 6).^[95]



Scheme 6. General representation of aminoborane mediated Ugi reaction

In 2008, Ross and co-workers proved that multicomponent reaction can be used to prepare already marketed therapeutic compounds quite simply.^[96] They showed two examples of this concept by preparing clopidogrel (Plavix) and bicalutamide (Casodex) using MCR chemistry

(Ugi, Passerini, Petasis), where the Plavix is an antiplatelet agent used to inhibit the formation of blood clots in coronary artery disease (Figure 15).

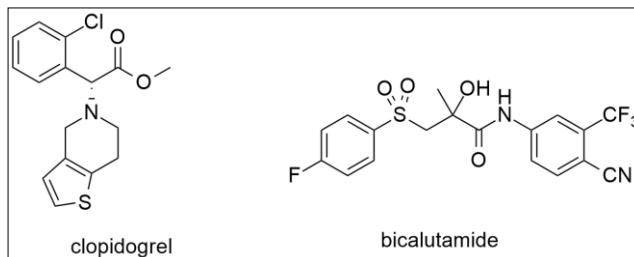
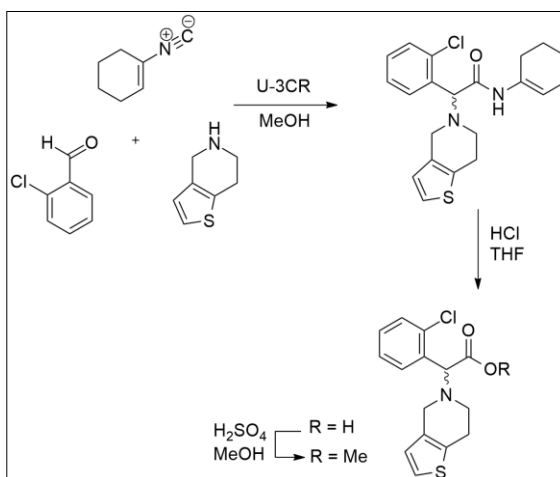


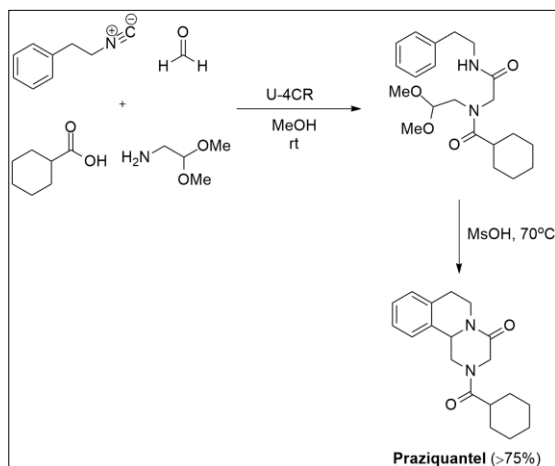
Figure 15. Structures of clopidogrel (Plavix) and bicalutamide (Casodex).

They presented the preparation of racemic clopidogrel in 3 steps from commercially available starting materials employing U-3CR as the key step (Scheme 7). After acidic hydrolysis of the enamide and subsequent methyl ester formation, rac-clopidogrel is obtained in 73% yield. This is a very efficient synthetic route in which the product is obtained as a racemate, where the drug is administered as the (R)-enantiomer.



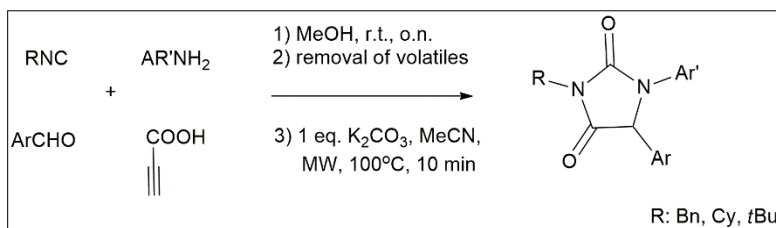
Scheme 7. Synthesis of rac-clopidogrel.

In 2012, Domling et al. reported a very short multicomponent synthesis of praziquantel employing an Ugi four-component reaction followed by Pictet–Spengler cyclization (Scheme 8) to give the Praziquantel in 75% overall yield.^[97]



Scheme 8. Synthesis of Praziquantel through a U-4CR followed by a Pictet-Spengler cyclization.

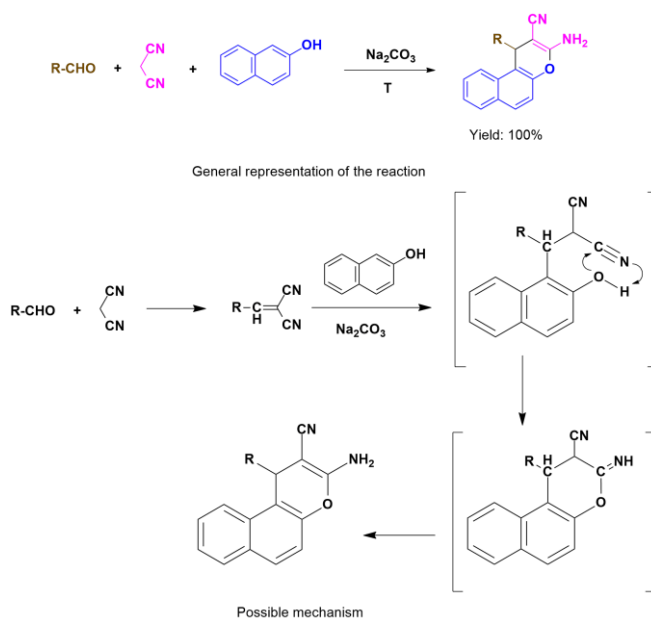
In 2018, Xu et al. reported the synthesis of Hydantoin scaffolds through a Post-Ugi Cascade reaction (Scheme 9).^[98] They showed a microwave assisted efficient two-step Ugi/cyclization reaction sequence for preparing the hydantoin which are drug like molecules.



Scheme 9. Genel representation of Post-Ugi Cascade reaction

1.3.1.2 Na₂CO₃-catalyzed one-pot solventless synthesis of 2-amino-4H-chromenes

In 2010, Jamal et al. reported a Solvent-free one-pot three-component reaction for the synthesis of 2-amino-4H-chromene scaffold using sodium carbonate as a catalyst with excellent yields, which is efficient, simple and environment-friendly.^[38] The general representation of the reaction and the possible mechanisms are presented in Scheme 10.



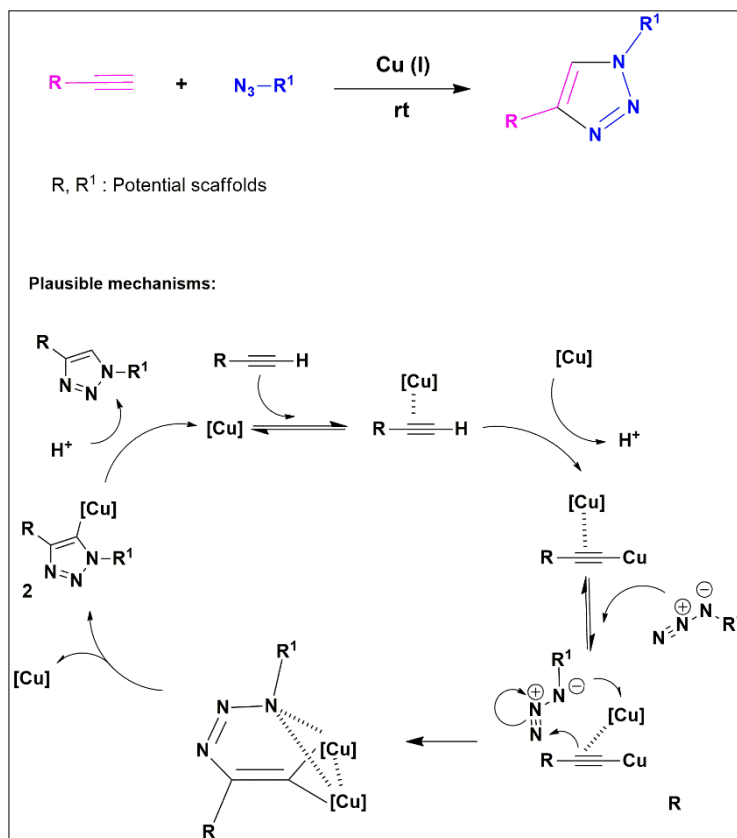
Scheme 10. The general representation of the Na₂CO₃-catalyzed one-pot solventless synthesis of 2-amino-4H-chromenes and the possible mechanisms

1.3.2 Click-reaction

In 2001, K. B. Sharpless et al. introduced the click-chemistry which represents an ideal set of near perfect reactions.^[99] The major characteristics of the click-reactions are: they are wide in scope, producing high yields, only non-chromatographic methods (such as

crystallization or distillation) are required for purification since it produces only inoffensive by-products, simple reaction conditions, readily available starting materials and reagents, the use of no solvent or a solvent that is benign (such as water) or easily removed, etc. In recent years, click chemistry has emerged as a fast and powerful approach for the synthesis of novel compounds with desired properties.

There are various types of click reactions such as cycloaddition reaction, nucleophilic substitution reaction, addition reaction, thiol-ene click reaction, etc. Among the various click reactions, the copper catalyzed [3+2] azide and alkyne cycloaddition (CuAAC) resulting in the formation of 1,2,3-triazoles has drawn considerable attention as an archetypical example of click chemistry. In fact, the CuAAC is the modified Huisgen 1,3-dipolar cycloaddition of an alkyne and an azide. The active Cu (I) catalyst can be generated from Cu (I) or Cu (II) salt by the in situ reduction using sodium ascorbate as a reducing agent. The addition of a slight excess of sodium ascorbate prevents the formation of oxidative homo-coupling products. This Cu (I) catalyzed cycloaddition results a regioselective 1,4-disubstituted 1,2,3-triazole derivative as the product. General representation of the CuAAC reaction and plausible mechanisms are depicted in Scheme 11.



Scheme 11. General representation and plausible mechanisms of CuAAC

The same alkyne molecule forms σ -bond and π -bond with two copper atoms. In the next step, the alkyne bearing the σ and π bonded copper atoms coordinates the azide. Then, an unusual six-membered copper metallacycle is formed. The second copper atom acts as a stabilizing donor ligand for the moiety. Finally, the ring contraction to a triazolyl-copper derivative is followed by protonolysis that affords the triazole product and closes the catalytic cycle.^[100]

The CuAAC is particularly useful for the synthesis of a variety of molecules ranging from enzyme inhibitors to molecular materials. 1,2,3-

Triazoles are an important class of target molecules due to their interesting biological properties such as anti-allergic, antibacterial and anti-HIV activity.^[101] Additionally, due to the resemblance in physiochemical properties such as planarity, dipole moment, C α distance and H-bond acceptor properties (of the lone pairs in nitrogen atoms), 1,2,3-triazoles are considered as peptide bond isosteres.^[102] In addition to this, the 1,2,3-triazole ring is chemically stable under hydrolytic as well as reductive and oxidative conditions. Consequently, amide-to-triazole substitutions are now common in the synthesis of drug-like molecules whose amide bonds are known to be crucial for biological activity. Selected examples for triazole based biologically active molecules are presented in Figure 16.

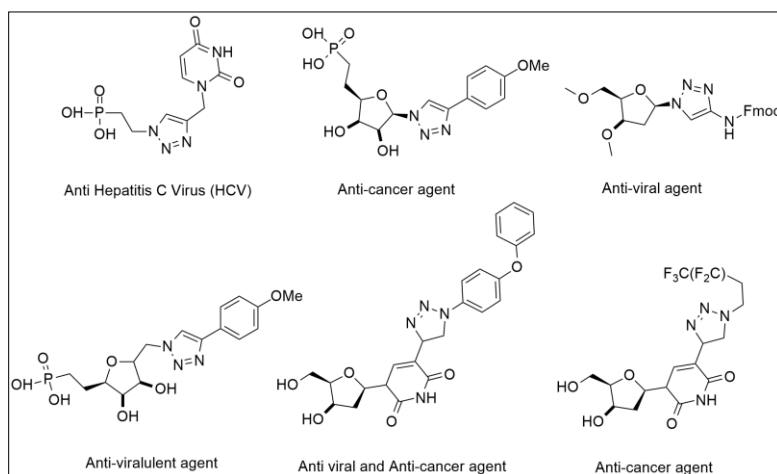


Figure 16. Representative examples for the triazole based biologically active molecules

1.4 Conclusion

The coumarin and chromene moieties have a plethora of applications in various fields like lighting, materials, imaging,

therapeutics, etc. The literature survey revealed the multifaceted applications and significance of the coumarin and chromene scaffolds. Furthermore, the perspective to the MCR-Click synthetic strategies has given clear ideas about the facile synthetic routes to the designing of molecules capable to show good photophysical as well as biological applications. Hence, we decided to develop new molecules with dual applications as fluorescent inhibitors. MCR/MCR-Click assisted the synthesis of a collection of new molecules, their detailed photophysical and biological studies are discussed in the coming chapters. The work presented in this thesis is summarised in Figure 17.

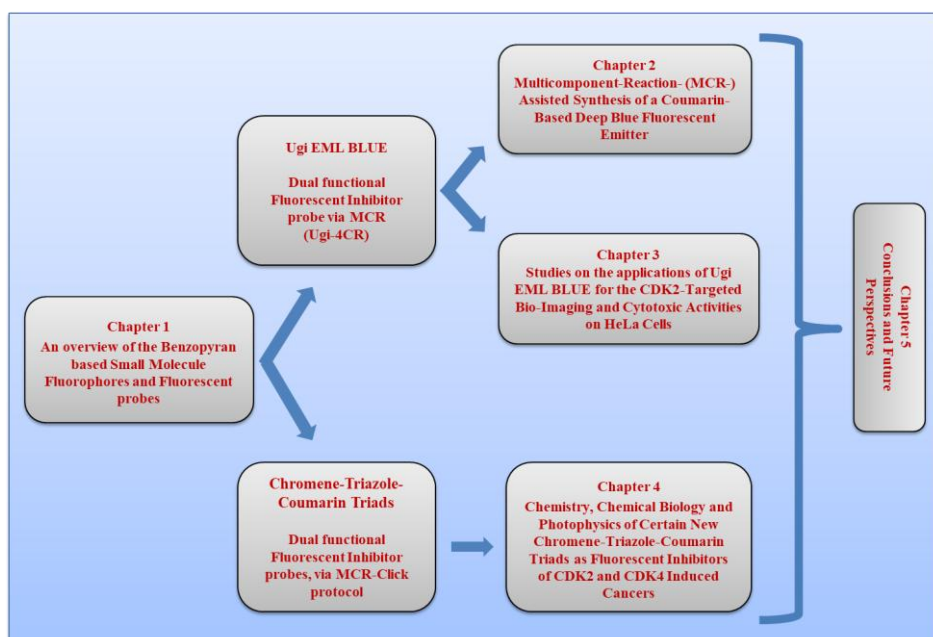


Figure 17. Summary of the work

References

- [1] (a) Zhu, M.; Yang, C. *Chem. Soc. Rev.*, **2013**, *42*, 4963-4976; (b) Silva, A. P. D.; Eilers, J.; Zlokarnik, G. *Proc. Natl. Acad. Sci. USA* **1999**, *96*, 8336 – 8337; (c) Rye, H. S.; Dabora, J. M.; Quesada, M. A.; Mathies, R. A.; Glazer, A. N. *Anal. Biochem.* **1993**, *208*, 144–150; (d) Yuan, L.; Lin, W.; Zheng, K.; Zhu, S. *Acc. Chem. Res.* **2013**, *46*, 1462-1473; (e) Lakowicz, J. R. *Principles of Fluorescence Spectroscopy*, 2nd edition, Plenum Press, New York, **1999**; (f) Leung, B. O.; Chou, K. C. *Appl. Spectrosc.* **2011**, *65*, 967-980; (g) Basavaraj, R. B.; Nagabhushana, H.; Darshan, G. P.; Prasad, B. D.; Rahul, M.; Sharma, S. C.; Sudaramani, R.; Archana, K. V. *Dyes. Pigm.* **2017**, *147*, 364-377; (h) Grabchev, I.; Moneva, I. *J. Appl. Polym. Sci.* **1999**, *74*, 151-157; (i) Hawkins, H. G.; Carlson, P. J.; Elmquist, M. (**2000**) "Evaluation of fluorescent orange signs", Texas Transportation Institute Report 2962-S.
- [2] Humpolickova, J.; Mejdrová, I.; Matousova, M.; Nencka, R.; Boura, E. *J. Med. Chem.* 2017, **60**, 119–127.
- [3] (a) Xia, S.; Wang, J.; Bi, J.; Wang, X.; Fang, M.; Phillips, T.; May, A.; Conner, N.; Tanasova, M.; Luo, F. T.; Liu, H. *Sens. Actuators, B*, **2018**, *265*, 699-708; (b) Xiaohong, C.; Runli, T.; Huizhen, J.; Jun, F.; Jingui, Q.; Zhen, Li. *Appl. Mater. Interfaces* **2012**, *4*, 4387–4392; (c) Eun, J. N.; Lee, K. H.; Han, H.; Kim, Y. K.; Yoon, S. S. *J. Nanosci. Nanotechnol.* **2013**, *554–557*; (d) Yu, D.; Huang, F.; Ding, S. H.; Feng, G. *Anal. Chem.* **2014**, *86*, 8835–8841.
- [4] (a) Thakur, A.; Singla, R.; Jaitak, V. *Eur. J. Med. Chem.* **2015**, *101*, 476-495; (b) Ahn, Y. M.; Vogeti, L.; Liu, C. J.; Santhapuram, H. K. R.; White, J. M.; Vasandani, V.; Mitscher, L. A.; Lushington, G. H.; Hanson, P. R.; Powell, D. R.; Himes, R. H.; Roby, K. F.; Ye, Q.; Georg, G. I. *Bioorg. Med. Chem.*, 2007, **15**, 702–713.
- [5] Borges1, F.; Roleira, F.; Milhazes N.; Santana L.; Uriarte, E. *Curr. Med. Chem.* **2005**, *12*, 887-916.
- [6] Fleetham, T.; Li, G.; Wen, L.; Li, J. *Adv. Mater.* **2014**, *26*, 7116-7121.
- [7] Sasabe, H.; Kido, J. *J. Mater. Chem. C* **2013**, *1*, 1699-1707.
- [8] Im, Y.; Byun, S. Y.; Kim, J. H.; Lee, D. R.; Oh, C. S.; Yook, K. S.; Lee, J. Y. *Adv. Funct. Mate.* **2017**, *27*, 1603007.

- [9] Schiedel, M.-S.; Briehn, C. A.; Bäuerle, P. *Angew. Chem., Int. Ed.* **2001**, *40*, 4677–4680.
- [10] Haque, M. M.; Sun, H.; Liu, S.; Wang, Y.; Peng, X. *Angew. Chem., Int. Ed.* **2014**, *53*, 7001–7005.
- [11] Chan, J.; Dodani, S. C.; Chang, C. J. *Nat. Chem.* **2012**, *4*, 973–984.
- [12] Jiang, X.-J.; Ng, D. K. P. *Angew. Chem., Int. Ed.* **2014**, *53*, 10481–10484.
- [13] Swanson, S. A.; Wallraff, G. M.; Chen, J. P.; Zhang, W.; Bozano, L. D.; Carter, K. R.; Salem, J. R.; Villa, R.; Scott, J. C. *Chem. Mater.* **2003**, *15*, 2305–2312.
- [14] Jurow, M. J.; Mayr, C.; Schmidt, T. D.; Lampe, T.; Djurovich, P. I.; Brutting, W.; Thompson, M. E. *Nat. Mater.* **2015**, *15*, 85–91.
- [15] Tang, C. W.; VanSlyke, S. A.; Chen, C. H. *J. Appl. Phys.* **1989**, *65*, 3610–3616.
- [16] Chen, C.-T.; Chiang, C.-L.; Lin, Y.-C.; Chan, L.-H.; Huang, Tsai, Z.-W.; Chen, C.-T. *Org. Lett.* **2003**, *5*, 1261–1264.
- [17] Zheng, C.-J.; Wang, J.; Ye, J.; Lo, M.-F.; Liu, X.-K.; Fung, M.-K.; Zhang, X.-H.; Lee, C.-S. *Adv. Mater.* **2013**, *25*, 2205–2211.
- [18] Kumar, S.; Puttaraju, B.; Patil, S. *ChemPlusChem* **2016**, *81*, 384–390.
- [19] Chen, J. X.; Liu, W.; Zheng, C. J.; Wang, K.; Liang, K.; Shi, Y. J.; Ou, X. M.; Zhang, X. H. *ACS Appl. Mater. Interfaces* **2017**, *9*, 8848–8854.
- [20] Weissleder, R.; Pittet, M. J. *Nature* **2008**, *452*, 580–589.
- [21] Fernández-Suárez, M.; Ting, A. Y. *Nat. Rev. Mol. Cell Biol.* **2008**, *9*, 929–943.
- [22] Zhang, L. J.; Wang, Z. Y.; Liu, J. T.; Miao, J. Y.; Zhao, B. X. *Sens. Actuators B* **2017**, *253*, 19–26.
- [23] Chan, J.; Dodani, S. C.; Chang, C. J. *Nat. Chem.* **2012**, *4*, 973–984.
- [24] Yuan, L.; Lin, W.; Song, J.; Yang, Y. *Chem. Commun.* **2011**, *47*, 12691–12693.

- [25] Cheng, X.; Tang, R.; Jia, H.; Feng, J.; Qin, J.; Li, Z. *Appl. Mater. Interfaces* **2012**, *4*, 4387–4392.
- [26] Zhang, C.; Wei, L.; Wei, C.; Zhang, J.; Wang, R.; Xi, Z.; Yi, L. *Chem. Commun.* **2015**, *51*, 7505-7508.
- [27] Emami, S.; Dadashpour, S. *Eur. J. Med. Chem.* **2015**, *102*, 611-630.
- [28] Woo, L. W. L.; Purohit, A.; Malini, B.; Reed, M. J.; Potter, B. V. L. *Chem. Biol.* **2000**, *7*, 773-791.
- [29] Malini, B.; Purohit, A.; Ganeshapillai, D.; Woo, L. W. L.; Potter, B. V. L.; Reed, M. J. *J. Steroid Biochem. Mol. Biol.* **2000**, *75*, 253-258.
- [30] Purohit, A.; Woo, L. W. L.; Potter, B. V. L.; Reed, M. J. *Cancer Res.* **2000**, *60*, 3394-3396.
- [31] Meggio, F.; Pagano, M. A.; Moro, S.; Zagotto, G.; Ruzzene, M.; Sarno, S.; Cozza, G.; Bain, J.; Elliott, M.; Deana, A. D.; Brunati, A. M.; Pinna, L. A. *Biochemistry* **2004**, *43*, 12931-12936.
- [32] Chilin, A.; Battistutta, R.; Bortolato, A.; Cozza, G.; Zanatta, S.; Poletto, G.; Mazzorana, M.; Zagotto, G.; Uriarte, E.; Guiotto, A.; Pinna, L. A.; Meggio, F.; Moro, S. *J. Med. Chem.* **2008**, *51*, 752-759.
- [33] Basanagouda, M.; Jambagi, V. B.; Barigheid, N. N.; Laxmeshwar, S. S.; Devaru, V.; Narayanachar, *Eur. J. Med. Chem.* **2014**, *74*, 225-233.
- [34] Kraljevic, T. G.; Harej, A.; Sedic, M.; Pavelic, S. K.; Stepanic, V.; Drenjancevic, D.; Talapko, J.; Raic-Malic, S. *Eur. J. Med. Chem.* **2016**, *124*, 794-808.
- [35] Abdizadeh, T.; Kalani, M. R.; Abnous, K.; Tayarani-Najaran, Z.; Khashyarmansh, B. Z.; Abdizadeh, R.; Ghodsi, R.; Hadizadeh, F. *Eur. J. Med. Chem.* **2017**, *132*, 42-62.
- [36] Thomas, N.; Zachariah, S. M. *Asian J. Pharm. Clin. Res.* **2013**, *6*, 11-15.
- [37] Pratap, R.; Ram, V. J. *Chem Rev.* **2014**, *114*, 10476-10526
- [38] Kidwai, M.; Saxena, S.; Khan, M. K. R.; Thukral, S. S. *Bioorg. Med. Chem. Lett.* **2005**, *15*, 4295–4298; Naimi-Jamal, M. R.; Mashkouri, S.; Sharifi, A. *Mol. Divers.* **2010**, *14*, 473–477.
- [39] Eun, J. N.; Lee, K. H.; Han, H.; Kim, Y. K.; Yoon, S. S. *J. Nanosci. Nanotechnol.* **2013**, *554*–557.

- [40] Yu, D.; Huang, F.; Ding, S. H.; Feng, G. *Anal. Chem.* **2014**, *86*, 8835–8841.
- [41] Zheng, Y.; Zhao, M.; Qiao, Q.; Liu, H.; Lang, H.; Zhaochao Xu, *Dyes. Pigm.* **2013**, *98*, 367-371.
- [42] Costantino, L.; Barlocob, D. *Curr. Med. Chem.* **2006**, *13*, 65-85.
- [43] Laskar, S.; Brahmachari, G. *Org. Biomol. Chem.* **2014**, *2*, 1-50.
- [44] Xu, Z. Q.; Hollingshead, M. G.; Borgel, S.; Elder, C.; Khilevich, A.; Flavin, M. T. *Bioorg. Med. Chem. Lett.* **1999**, *9*, 133-138.
- [45] Almeida, E. R. *Open Nat. Prod. J.* **2009**, *2*, 42-47.
- [46] Berg, A.; Reiber, K.; Dorfelt, H.; Walther, G.; Schlegel, B.; Grafe, U. J. *Antibiot.* **2000**, *53*, 1313-1316.
- [47] Otaguro, K.; Shiomi, K.; Yamaguchi, Y.; Arai, N.; Sunazuka, T.; Masuma, R.; Iwai, Y.; Omura, S. *J. Antibiot.* **2000**, *53*, 50-57.
- [48] Ray, S.; Majumder, H. K.; Chakraborty, A. K.; Mukhopadhyay, S. *J. Nat. Prod.* **1996**, *59*, 27-29.
- [49] Makino, M.; Fujimoto, Y. *Phytochemistry* **1999**, *50*, 273–277.
- [50] Schmidt, W.; Beerhues, L. *FEBS Lett.* **1997**, *420*, 143-146.
- [51] Lin, Y. L.; Shen, C. C.; Huang, Y. J.; Chang, Y. Y. *J. Nat. Prod.* **2005**, *68*, 381–384.
- [52] Brahmachari, G.; Jash, S. K. *Rec. Pat. Biotechnol.* **2014**, *8*, 3-16.
- [53] Ito, C.; Itoigawa, M.; Mishina, Y.; Filho, V. C.; Enjo, F.; Tokuda, H.; Nishino, H.; Furukawa, H. *J. Nat. Prod.* **2003**, *66*, 368–371.
- [54] Hufford, C. D.; Oguntimein, B. O.; Engen, D. V.; Muthard, D.; Clardy, J. *J. Am. Chem. Soc.* **1980**, *102*, 7365–7367.
- [55] Herrera, E.; Barbas, C. *J. Physiol. Biochem.* **2001**, *57*, 43–56.
- [56] Fuendjiep, V.; Nkengfack, A. E.; Fomum, Z. T.; Sondengam, B. L.; Bodo, B. *J. Nat. Prod.* **1998**, *61*, 380–383.
- [57] Wandji, J.; Fomum, Z. T.; Tillequin, F.; Libot, F.; Koch, M. *J. Nat. Prod.* **1995**, *58*, 105–108.

- [58] Thomas, N.; Zachariah, S. M. *Asian J. Pharm. Clin. Res.* **2013**, *6*, 11-15.
- [59] Amr, A. G. E.; Mohamed, A. M.; Mohamed, S. F.; Abdel-Hafez, N. A.; Hammam, A. E. F. G. *Bioorg. Med. Chem.* **2006**, *14*, 5481-5488.
- [60] Paliwal, P. K.; Jetti, S. R.; Jain, S. *Med. Chem. Res.* **2013**, *22*, 2984-2990.
- [61] Bhavanarushi, S.; Kanakaiah, V.; Yakaiah, E.; Saddanapu, V.; Adlagatta, A.; Rani, V. J. *Med. Chem. Res.* **2013**, *22*, 2446-2454.
- [62] Erichsen, M. N.; Huynh, T. H. V.; Abrahamsen, B.; Bastlund, J. F.; Bundgaard, C.; Monrad, O.; Jensen, A. B.; Nielsen, C. W.; Frydenvang, K.; Jensen, A. A.; Bunch, L. *J. Med. Chem.* **2010**, *53*, 7180-7191.
- [63] Kemnitzer, W.; Drewe, J.; Jiang, S.; Zhang, H.; Grundy, C. C.; Labreque, D.; Bubenick, M.; Attardo, G.; Denis, R.; Lamothe, S.; Gourdeau, H.; Tseng, B.; Kasibhatla, S.; Cai, S. X. *J. Med. Chem.* **2008**, *51*, 417-423.
- [64] Mahmoodi, M.; Aliabadi, A.; Emami, S.; Safavi, M.; Rajabalian, S.; Mohagheghi, A. M.; Khoshzaban, A.; Kermani, A. S.; Lamei, N.; Shafiee A.; Foroumadi, A. *Arch. Pharm. Chem. Life Sci.* **2010**, *343*, 411-416.
- [65] Abdelrazeka, F. M.; Metza, P.; Farrag, E. K. *Arch. Pharm. Pharm. Med. Chem.* **2004**, *337*, 482-485.
- [66] Paliwal, P. K.; Jetti, S. R.; Jain, S. *Med. Chem. Res.* **2013**, *22*, 2984-2990.
- [67] Kumar, D.; Reddy, V. B.; Sharad, S.; Dube, U.; Kapur, S. *Eur. J. Med. Chem.* **2009**, *44*, 3805-3809.
- [68] Selvam, N. P.; Babu, T. H.; Perumal, P. T. *Tetrahedron* **2009**, *65*, 8524-8530.
- [69] Bedair, A. H.; Emam, H. A.; El-Hady, N. A.; Ahmed, K. A. R.; El-Agrody A. M. *Farmaco* **2001**, *56*, 965-973.
- [70] Khafagy, M. M.; El-Wahab, A. H. F. A.; Eid, F. A.; El-Agrody, A. M. *Farmaco* **2002**, *57*, 715-722.
- [71] Eid, F. A.; El-Wahab, A. H. F. A.; Gameel, A. M. E. H. A.; Khafagy, M. A. M. *Acta. Pharm.* **2004**, *54*, 13-26.

- [72] Smith, C. W.; Bailey, J. M.; Billingham, M. E. J.; Chandrasekhar, S.; Dell, C. P.; Harvey, A. K.; Hicks, C. A.; Kingston, A. E.; Wishart, G. N. *Bioorg. Med. Chem.* **1995**, *5*, 2783-2788.
- [73] Salamon, E.; Mannhold, R.; Weber, H.; Lemoine, H.; Frank, W. *J. Med. Chem.* **2002**, *45*, 1086-1097.
- [74] Hegab, M. I.; Yousef, N. M.; Nour, H. F.; Ellithey, M.; Arbid, M. S. *Acta. pharm.* **2008**, *58*, 15–27.
- [75] El-Saghier, A. M. M.; Naili, M. B.; Rammash, B. K.; Saleh, N. A.; Kredan, K. M. *ARKIVOC* **2007**, 83-91.
- [76] Staquet, M.; Bron, D.; Rozenzweig, M.; Kenis, Y. *J. Clin. Pharmacol.* **1981**, *21*, 60S-63S.
- [77] Jerning, E.; Svantesson, G. T.; Mohell, N. *Eur. J. Pharmacol.* **1998**, *360*, 219-25.
- [78] Doshi, J. M.; Tian, D.; Xing, C. *J. Med. Chem.* **2006**, *49*, 7731-7739.
- [79] Choi, M.; Hwang, Y. S.; Kumar, A. S.; Jo, H.; Jeong, Y.; Oh, Y.; Lee, J.; Yun, J.; Kim, Y.; Han, S. b.; Jung, J. K.; Cho, J.; Lee, H. *Bioorg. Med. Chem. Lett.* **2014**, *24*, 2404-2407.
- [80] Yin, S. Q.; Shi, M.; Kong, T. T.; Zhang, C. M.; Han, K.; Cao, B.; Zhang, Z.; Du, X.; Tang, L. Q.; Mao, X.; Liu, Z. P. *Bioorg. Med. Chem. Lett.* **2013**, *23*, 3314-3319.
- [81] Jiang, H.; Yang, J.; Tang, X.; Li, J.; Wu, W. *J Org Chem.* **2015**, *80*, 8763.
- [82] Zarganes-Tzitzikas, T.; Chandgude, A.L, Dömling, A. *Chem Rec.* **2015**, *15*, 981.
- [83] Zhu, J.; Bienaymé, H. *Multicomponent Reactions*; Wiley-VCH: Weinheim, Germany, **2005**.
- [84] Dömling, A.; Ugi, I. *Angew. Chem., Int. Ed.* **2000**, *39*, 3168-3210.
- [85] Dömling, A. *Chem. Rev.* **2006**, *106*, 17-89; Dömling, A.; Wang, W.; Wang, K. *Chem. Rev.* **2012**, *112*, 3083-3135.
- [86] Strecker, A.; Liebig, J. *Ann. Chem.* **1850**, *75*, 27-45.
- [87] Hantzsch, A.; *Ber. Dtsch. Chem. Ges.* **1890**, *23*, 1474-1476.

- [88] (a) Biginelli, P.; *Ber. Dtsch. Chem. Ges.* **1891**, *24*, 1317-1319. (b) P. Biginelli, *Ber. Dtsch. Chem. Ges.* **1891**, *24*, 2962-2967.
- [89] Domling, A. *Chem. Rev.* **2006**, *106*, 17-89.
- [90] Mannich, C. *J. Chem. Soc. Abstracts*, **1917**, *112*, 634-635; Mannich, C. *Arch. Pharm.* **1917**, *255*, 261-276.
- [91] Passerini, M. *Gazz. Chim. Ital.* 1921, *51*, 126-129.
- [92] Leusen, D.V.; Leusen, A.M.V. **Organic Reactions, 2004** -Wiley Online Library
- [93] (a) H. Bergs, Ger. Pat. **1929**, DE566094; Bucherer, H. T.; Steiner, W. *J. Prakt. Chem.* **1934**, *140*, 291-316; (b) Bucherer, H. T.; Lieb, V. A. *J. Prakt. Chem.* **1934**, *141*, 5-43.
- [94] Kaim, L. El.; Grimaud, L.; Oble, J. *Angew. Chem. Int. Ed.* **2005**, *44*, 7961-7964.
- [95] Tanaka, Y.; Hasui, T.; Suginome, M. *Org. Lett.* **2007**, *9*, 4407-4410.
- [96] Kalinski, C.; Lemoine, Schmidt, J.; Burdack, C.; Kolb, J.; Umkehrer, M.; Ross, G. *Synthesis* **2008**, *24*, 4007-4011.
- [97] Liu, H.; William, S.; Herdtweck, E.; Botros, S.; Dömling, A. *Chem. Biol. Drug Des.* **2012**, *79*, 470-477.
- [98] Xu, Z. G.; Ding, Y.; Meng, J. P.; Tang, D. Y.; Li, Y.; Lei, J.; Xu, C.; Chen, Z. *Z. Synlett.* **2018**, *29*, 2199-2202.
- [99] Kolb, H.C.; Finn, M.G.; Sharpless, K.B. *Angew Chem Int Ed.* **2001**, *40*, 2004-2021.
- [100] Worell, B. T.; Malik, J. a.; Fokin, V. V. *Science* **2013**, *340*, 457-460.
- [101] (a) Dehaen, W.; Bakulev, V.A. *Chemistry of 1,2,3-triazoles*, Springer, **2014**; (b) Agalave, S. G.; Maujan, S. R.; Pore, V. S. *Chem. Asian J.* **2011**, *6*, 2696 - 2718.
- [102] Kolb, H. C.; Sharpless, K. B. *Drug Discov. Today* **2003**, *8*, 1128.

MULTICOMPONENT-REACTION- (MCR-) ASSISTED SYNTHESIS OF A COUMARIN-BASED DEEP BLUE FLUORESCENT EMITTER

2.1 Introduction

The fluorescence is the phenomenon of light emission after absorbing the radiation from the appropriate region of electromagnetic spectra. During these decades, the fluorescent lamps and fluorescent LEDs (Light Emitting Diodes) have replaced the other conventional lighting methods and Displays. Among the different LEDs, the Organic Light Emitting Diodes (OLEDs) have potential applications in the area of ultra-thin full-color displays as well as solid state lighting.^[1,2] Hence there is an ongoing interest in developing suitable fluorescent-materials for light emission and related applications. In general, an OLED consists of three organic layers sandwiched between the electrodes. The organic layers adjacent to cathode and anode are the Electron Transport Layer (ETL) and Hole Transport Layer (HTL) respectively. The electrons and holes are injected from the opposite poles to these organic layers and are collected at the Emissive Layer (EML). The electron-hole recombination at the emissive layer leads to the formation of singlet excitons that decay radiatively.^[3,4] The emissive layer usually consists of light emitting dyes or such small organic molecules which plays a crucial role in the external quantum efficiency (EQE) of the LED or OLED. The full color display is generally achieved by mixing equal intensity and equal stability red, yellow, green and deep blue emitters together. In this combination, the

blue emitter helps to reduce the power consumption of the device as well to generate other colors. Highly conjugated fluorescent or phosphorescent molecular systems are currently used as deep blue emitters in OLEDs.^[5–10] However, an inherent problem with these blue emitters is their wide bandgap causing poor charge injection, exciton instability, and consequent poor device performance. Molecules based on pyrene, anthracene, fluorene, di(styryl)arylene, etc. are the most studied systems in this category showing excellent fluorescent quantum yield in solutions. However, these molecules suffer fluorescence quenching in the solid state due to aggregation.

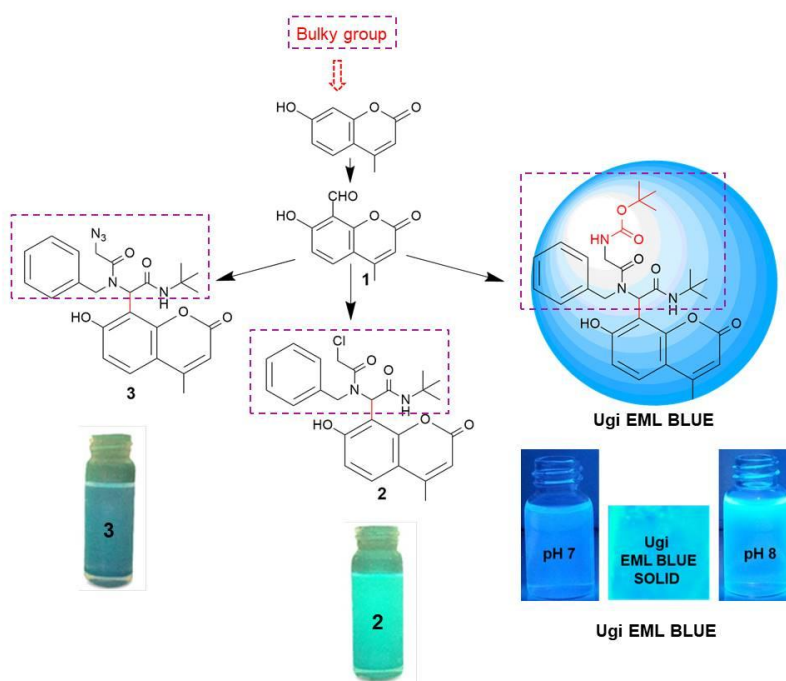


Figure 1. Structure of coumarin derivatives and their Photoluminescence under UV light

One of the methods to overcome the fluorescence quenching at the solid state is the introduction of bulky substituents to the emission core to attain

non-coplanar structures of the emitters with restricted rotation.^[11,12] Such rational strategies have been employed to attain non-coplanar structures of anthracene, pyrene and coumarin derivatives by integrating bulky substituents such as tetraphenylsilane, triphenylbenzene, spirobifluorene or various carboxamide derivatives to them.^[13,14] However, the synthesis of such molecules involves multistep protocols leading to the escalation of manufacturing cost. As an attempt to address these challenges, we decided to integrate various bulky carboxamide groups to the 8-position of 4-methyl-7-hydroxy coumarin core as shown in Figure 1.

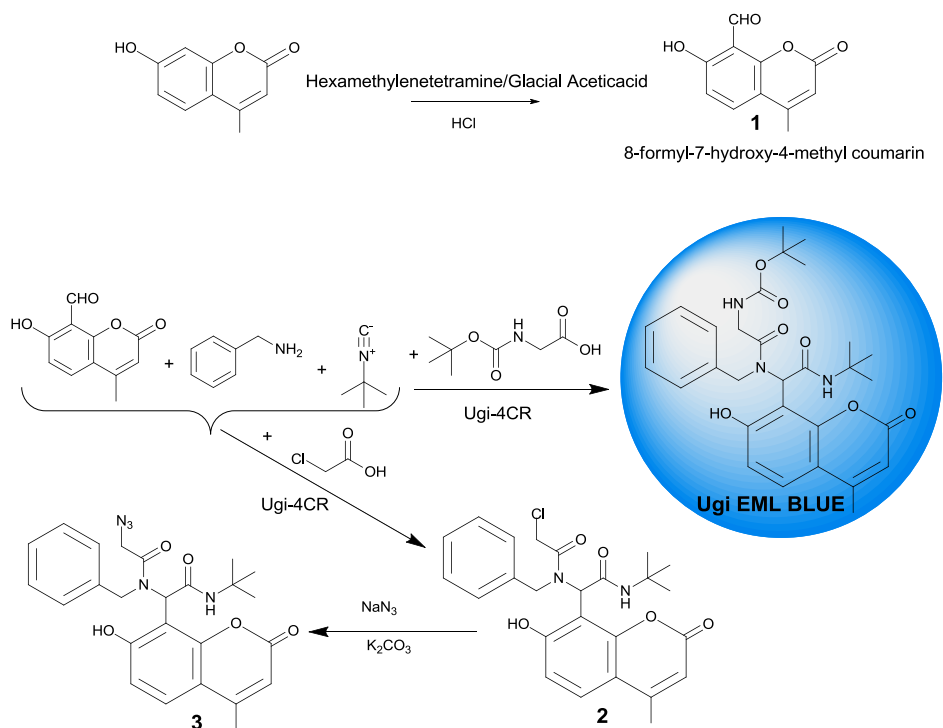
Three new compounds such as **2**, **3** and Ugi EML BLUE (we coined this name to this new molecule since its synthesis involved the classical Ugi reaction) were synthesized of which Ugi EML BLUE showed strong fluorescence in solution as well as in the solid state. The synthetic methodology was based on an Ugi four-component condensation (Ugi-4CC) which is a unique multicomponent reaction (MCR) for the diversity oriented synthesis of N-acylaminocarboxamides.^[15-18] Weak emission was observed for **2** and **3** with carboxamide groups at the 8 position of the coumarin. However, a significant enhancement in the blue emission was observed with Ugi EML BLUE which is obtained by substituting chlorine or the azide in **2** and **3** with a *tert*-butyl carbamate group.

2.2 Results and Discussion

2.2.1 Synthesis and Fluorescence Study

The studies were started with the introduction of a carboxamide moiety at the 8 position of the coumarin core. For this, we decided to use

Ugi-4CR as our synthetic tool. Since Ugi reaction needs an aldehyde component, we decided to introduce an aldehyde group to the 8 position of the coumarin. This reaction was carried out as shown in Scheme 1 and the coumarin aldehyde **1** was obtained in high purity.



Scheme 1. Synthesis of 1, 2, 3 and Ugi EML BLUE

The coumarin aldehyde **1** was then reacted with chloroacetic acid, benzylamine (electron rich), *tert*-butyl isocyanide (contains an electron pushing *tert*-butyl group and ‘–NC’ bond which makes the molecule electron dense) to form the carboxamide chloride **2** as shown in Scheme 1. **2** showed a weak fluorescence under UV light (Figure 2E) and no fluorescence in the solid state under UV irradiation. Subsequently, chlorine in **2** was substituted with an azide moiety to obtain **3** by reacting

2 with sodium azide as shown in Scheme 1. This compound also showed a very weak fluorescence in the solution state (Figure 2F) and no fluorescence in the solid state.

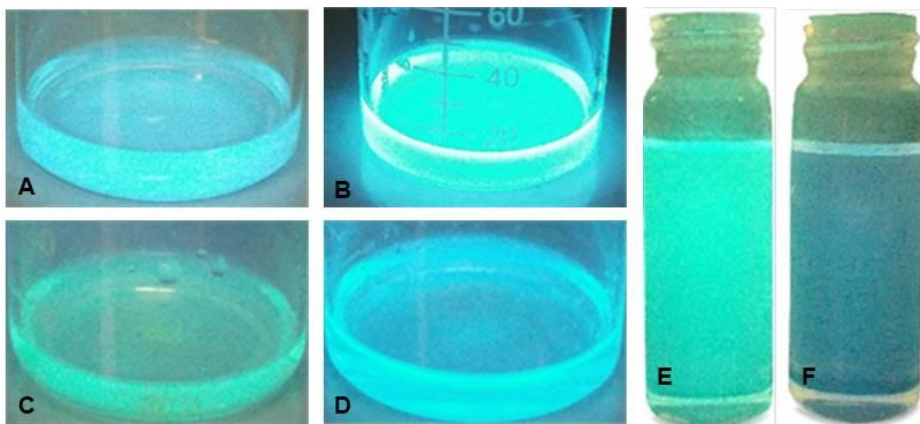


Figure 2. Fluorescence of 7-hydroxy-4-methyl coumarin at pH 7 (A) and pH 8 (B), Fluorescence of **1** at pH 7 (C) and pH 8 (D), Fluorescence of **2** (E) and **3** (F).

The weak fluorescence observed for the starting 7-hydroxy-4-methyl coumarin and its aldehyde derivative **1** in neutral and alkaline pH are shown in Figures 2A-D. Since all the three compounds showed only weak fluorescence, we decided to introduce a more bulky group to the 8 position of the coumarin. For this, we used Boc-glycine as our carboxylic acid component in the Ugi-4CR, as shown in Scheme 1. The Ugi EML BLUE thus obtained showed significant enhancement in fluorescence in the solution state as shown in Figure 3.



Figure 3. Fluorescence of Ugi EML BLUE in G) pH 2.3, H) pH 3.6, I) pH 7.2, J) pH 8.2, K) pH 8.4, L) pH 8.5, M) pH 8.7, N) pH 9.3

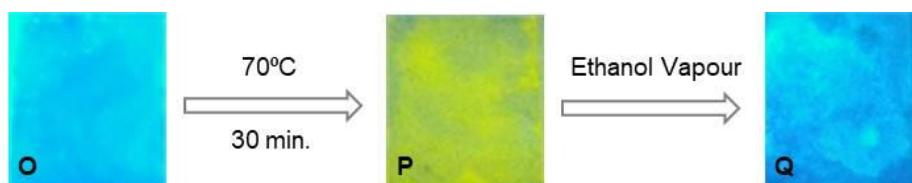


Figure 4. Solid state Fluorescence of Ugi EML BLUE: O) an air dried film made by drop-casting an ethanol solution of Ugi EML BLUE on a glass substrate. P) Yellowish green fluorescence showed by film O when subjected to thermal annealing at 70°C for 15 minutes. Q) Reinstating the bluish fluorescence by ethanol vapor etching.

A thin film of this material was prepared by drop-casting an ethanol solution of this material on top of a glass substrate. This thin film also showed strong fluorescence as shown in Figure 4. The film was then kept in ambient and its fluorescence was monitored in various time intervals. The film did not show any significant decrease in fluorescence even after one day. However, the same film when subjected to heat treatment at 70°C for 15 minutes showed a yellowish-green fluorescence as shown in Figure 4P.

2.2.2 The Structural and Photo-physical Characterization

The structural and photo-physical characterization of Ugi EML BLUE was carried out using XRD, NMR, AFM, TGA, UV-Vis and Fluorescence measurements. Figure 5 shows the X-Ray Diffraction pattern of the Ugi EML BLUE and from the graph it is clear that the molecule is crystalline in nature. The Full Width at Half Maxima (FWHM) of the prominent peak observed at 2θ 18.92° is 0.600° , the interplanar distance (d) is 4.686 \AA and the approximate particle size is 14.0 nm .^[19,20] The ultrafine particle size of the material allows the preparation of ultrafine thin layers while constructing the OLED devices.^[21-26,1-10]

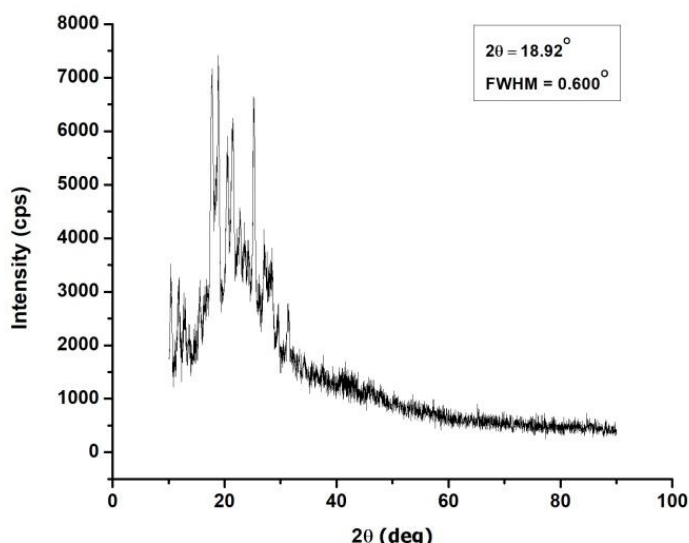


Figure 5. X-Ray Diffraction Pattern of Ugi EML BLUE

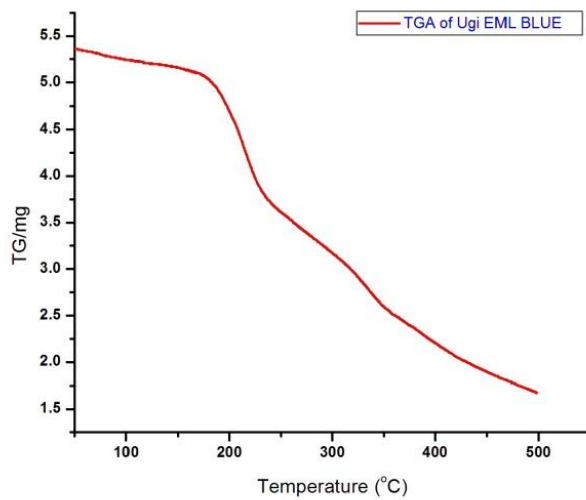


Figure 6. Thermogravimetric data of Ugi EML BLUE

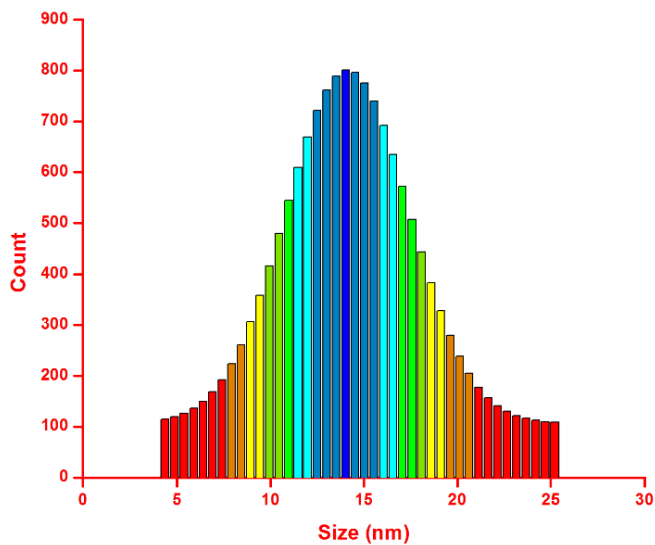


Figure 7. AFM Histogram: Size distribution of Ugi EML BLUE particles

In addition to this, the molecule possesses a sharp melting point (178°C) and which is in good agreement with the same obtained from the thermogravimetric analysis (Figure 6). The sharp melting at relatively high temperature also ensures good physicochemical properties towards light emission applications.

Figure 7 shows the AFM histogram of the particle size distribution and Figure 8 shows the AFM images of Ugi EML BLUE. The AFM study of Ugi EML BLUE showed uniformly dispersed particles with an average size of 14-15 nm, which is in good agreement with the approximate particle size obtained from X-Ray diffraction analysis.

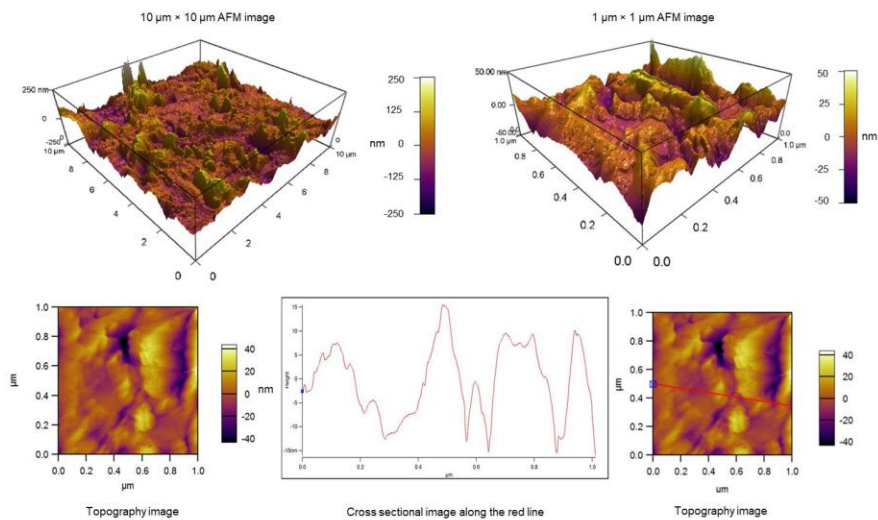


Figure 8. AFM images of Ugi EML BLUE

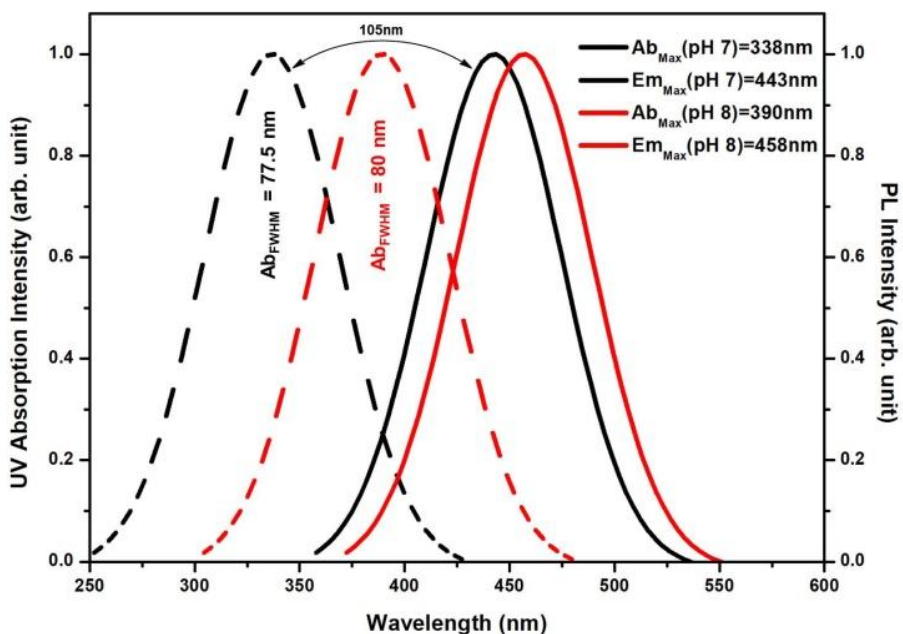


Figure 9. UV-Vis absorption (dashed lines) and fluorescence spectra (solid lines) for Ugi EML BLUE at pH 7 and pH 8

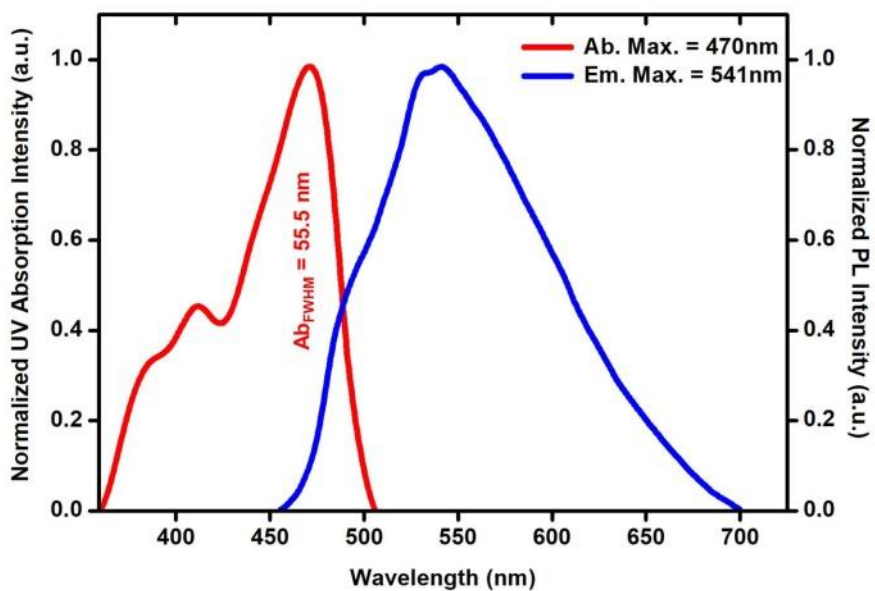


Figure 10. Solid state absorption and emission spectra of Ugi EMLBLUE

The UV-Vis and fluorescence spectra of the Ugi EML BLUE (50 ppm solution in DMSO) are shown in Figure 9 (pH 7). The solution state UV-Vis absorption maxima and fluorescence emission maxima are observed at 338 nm and 443 nm respectively with a large Stokes shift of 105 nm. Ugi EML BLUE showed strong fluorescence in the solid state also. The solid state UV-Vis absorption maxima and fluorescence emission maxima of Ugi EML BLUE are observed at 470 nm and 541 nm respectively (Figure 10). The solid state fluorescence observed for the molecule is attributed to the unconventional phenomenon of Aggregation Induced Emission (AIE). The observed redshifts in the solid state absorption and emission are due to the restriction of intramolecular rotation (RIR) due to aggregation which intern helps to create a pool of electrons conjugated within the system leading to the redshifts in the absorption and emission spectra. The solid state and solution state fluorescence emission peaks at longer wavelengths (541 nm and 443 nm) reveal the presence of a transition like a donor (coumarin core) to acceptor (introduced bulky groups) intramolecular charge transfer (ICT) transition in the system.^[27,28]

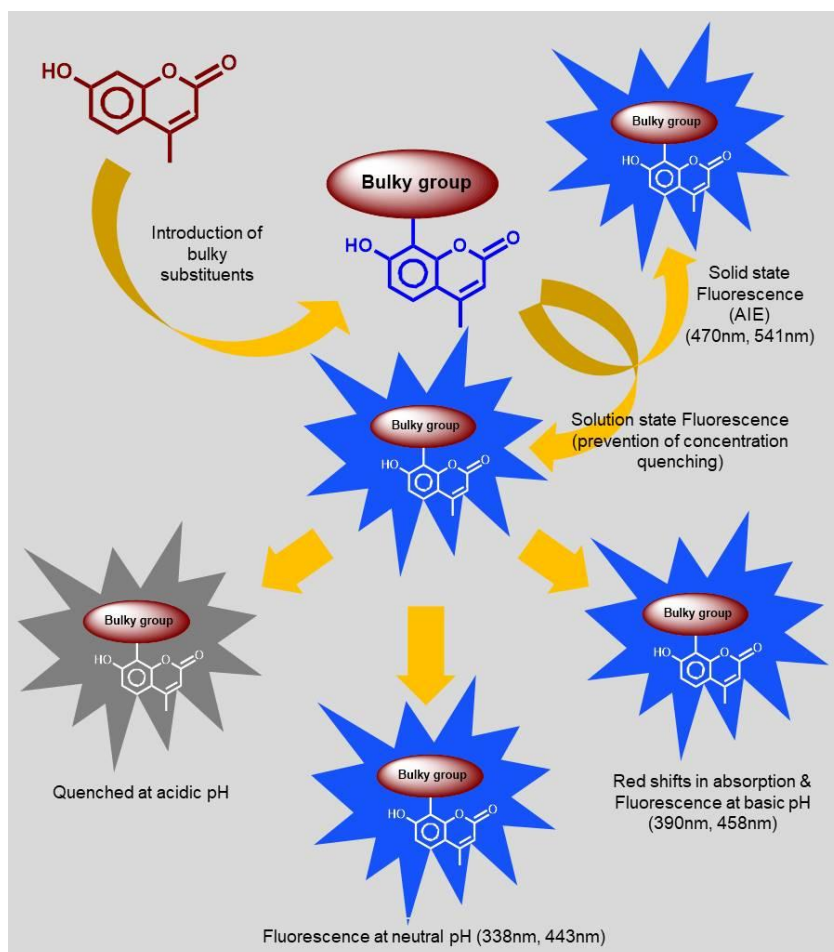


Figure. 11 Summarized fluorescent properties of Ugi EML BLUE

2.2.2.1 Effect of pH on the fluorescence of Ugi EML BLUE

Interestingly, the solution state fluorescence of Ugi EML BLUE is sensitive to the changes in pH. The UV-Vis absorption and fluorescence spectra of the Ugi EML BLUE (50 ppm solution in DMSO) at neutral pH (pH 7) and higher pH (pH 8) are shown in Figure 9. At pH 8 the UV-Vis absorption maxima and emission maxima are red-shifted to 390 nm and

458 nm respectively, whereas at acidic pH the fluorescence was found to be quenched.

In Ugi EML BLUE, the intramolecular charge transfer (ICT) type electronic transitions between the coumarin core and the bulky substituent at the 8 position are responsible for the characteristic absorption and emission properties observed at various pH. At neutral pH, the electronic transitions occur normally on excitation and show the absorption and emission peaks at 338 nm and 443 nm respectively. However, in basic conditions, the hydroxyl proton of coumarin core are in the deprotonate which is susceptible to resonance transformations. Due to this resonance, the overall electron density in the coumarin core increases and which in turn reduces the energy required for the ICT type electronic transitions within the system. This causes the redshift of the absorption and emission peaks to 390 nm and 458 nm respectively. Similarly, at acidic pH, the abstraction of transitive electrons by the hydrons will hinder the electronic transitions from the coumarin core leading to the quenching of the fluorescence.^[29,30] These observations are summarized in Figure 11.

2.2.2.2 Quantum Yield of Ugi EML BLUE

The fluorescence quantum yields of the material Ugi EML BLUE at pH 7 and 8 were measured in DMSO, using anthracene as the standard ($\phi = 0.27$) and were found to be 0.12 and 0.21 respectively.

2.2.3 The DFT Studies on Light emission mechanism

The ground state geometry, HOMO/LUMO energies and the theoretical absorption wavelength of the Ugi EML BLUE in the gas phase were obtained by means of density functional theory (DFT) and TD-DFT

using the GAUSSIAN 09 software with the basis set B3LYP/6-31G*.^[31] The B3LYP/6-31G* chosen for the DFT calculations was on the basis of the structural features of the molecule as well as on the basis of previous reports on its use in small organic molecules.^[32-36]

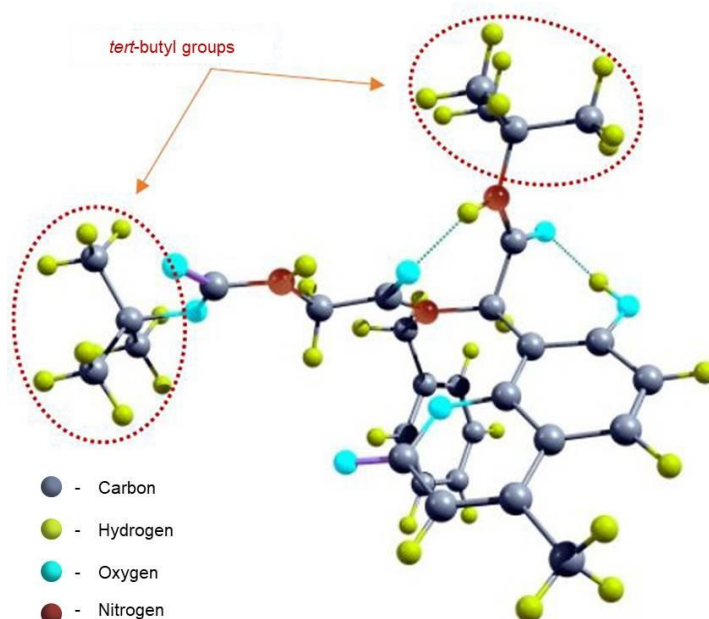


Figure 12. The optimized ground state geometry of Ugi EML BLUE

In the present study with B3LYP/6-31G* basis set showed stable ‘ground state absorption energy’ and which is very close to the experimental values. Figure 12 shows the optimized ground state geometry of Ugi EML BLUE and Figure 13 shows the images of HOMO and LUMO obtained by DFT method from which we can understand the extending of electron delocalization through the bulkier substituents introduced to the coumarin core.

Figure 13(A_H-A_L) reveals that the molecular conformation with two upper terminal *tert*-butyl group ensures the prevention of concentration quenching and enhances the fluorescence.^[21-26] The amide groups adjacent to the *tert*-butyl groups at each terminal pull the electrons while the *tert*-butyl groups push the electrons and the electron rich phenyl group shuttles the electron through the bonds inside and outside the ring. This push-pull mechanism enhances easier electronic movements. The optimized ground state geometry for Ugi EML BLUE supports the above mechanism perfectly.

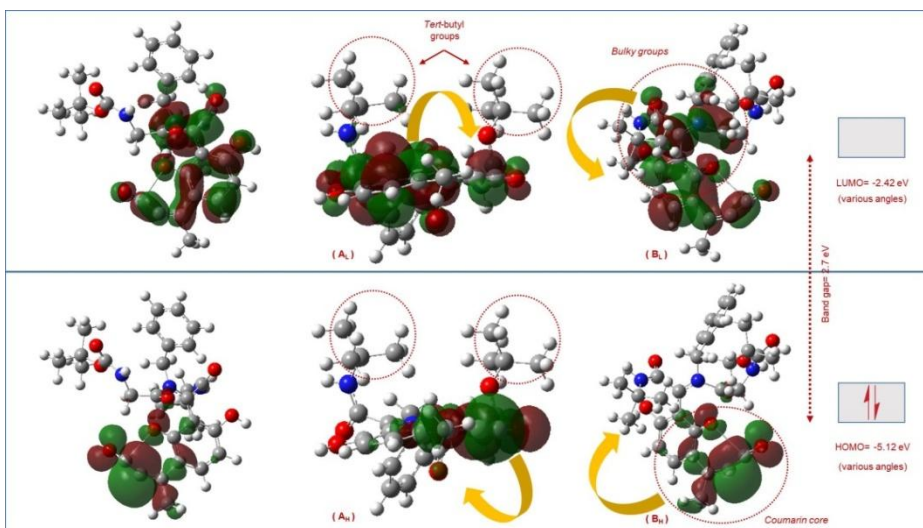


Figure 13. The images of HOMO and LUMO computed by DFT/B3LYP/6-31G* method.

The DFT study also accounts for the ICT type transition within the Ugi EML BLUE molecule which we already understood from its observed longer emission peaks. The HOMO consist the electron dense orbitals of coumarin core alone while the LUMO consists the orbitals of

coumarin core and the bulky groups (Figure 13 (B_H-B_L), which implies the transfer of electrons from the coumarin core (donor) to the bulky groups (acceptor) on excitation. This extended electronic delocalization observed in between the coumarin core and bulky groups to facilitate the ICT type transitions in the molecule. From the TD-DFT calculations, the absorption wavelength and the bandgap at the gas phase (theoretical) are 482 nm and 2.6 eV. The HOMO/LUMO energy levels of the Ugi EML BLUE are -5.12 eV/-2.42 eV respectively and the bandgap is 2.7 eV which are responsible for the intense blue radiative decay of the excitons.^[1-4]

The TD-DFT computations were also carried out in a solvent (DMSO) environment using the solvent model IEFPCM.^[35,37,38] The solvent phase TD-DFT showed an absorption maxima at 346 nm and a bandgap of 2.8 eV for the material. The solvent phase calculations are also in good agreement with the experimental data obtained.

CIE coordinates	Ugi EML BLUE pH7	Ugi EML BLUE pH8	NTSC standard	EBU Standard	IEC Standard (sRGB)
CIE (x)	0.16	0.14	0.14	0.15	0.15
CIE (y)	0.01	0.03	0.08	0.06	0.06

Table 1. Comparison of CIE chromaticity coordinates

Appearance	Melting Point(°C)	UVabs Max (nm)	PLems Max (nm)	Color	C.I.E. (x, y) (pH7)	C.I.E. (x, y) (pH8)	HOMO (eV)	LUMO (eV)	Number of Synthetic Steps
Yellowish-brown solid	178	338 (pH 7), 390 (pH 8)	443 (pH 7), 458 (pH 8)	Deep Blue	0.16, 0.01	0.14, 0.03	-5.12	-2.42	2

Table 2. Properties of Ugi EML BLUE.

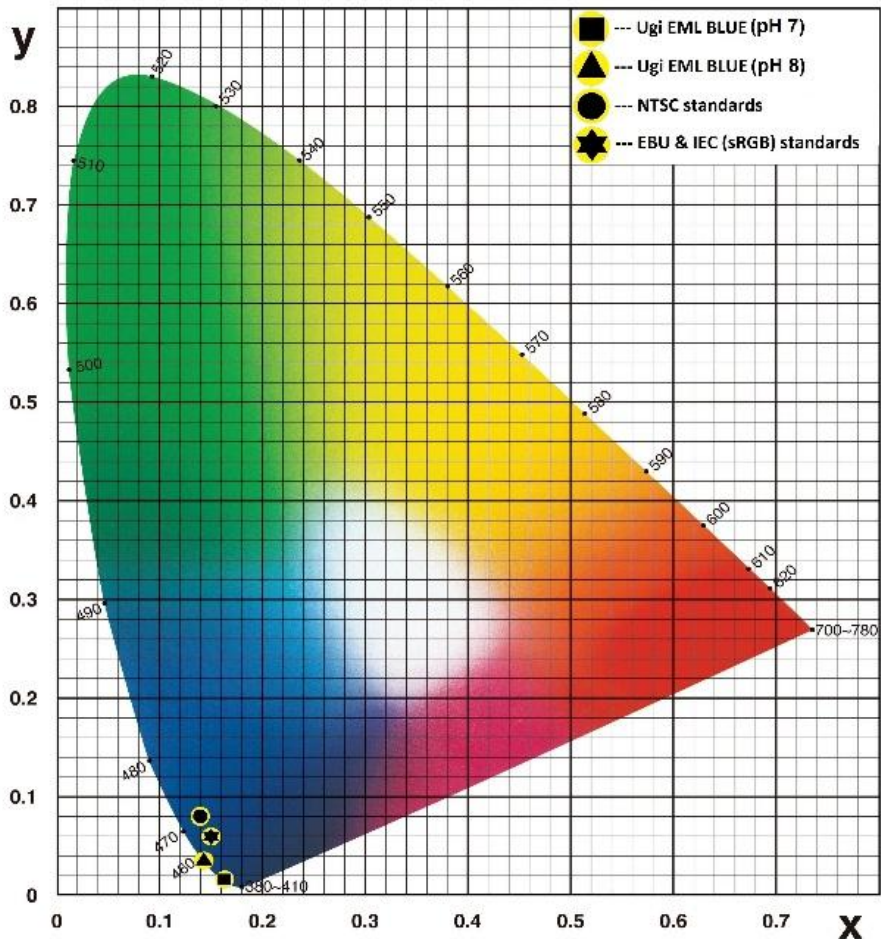


Figure 14. CIE 1931 Color System: CIE blue colors of Ugi EML BLUE (at pH 7 and pH 8), NTSC standard, EBU standard and IEC (sRGB) standard

The C.I.E. chromaticity coordinates for this intense blue color were calculated and compared with the standards. Figure 14 shows the positions of the blue color of Ugi EML BLUE (at pH 7 and pH 8), NTSC standard, EBU standard and IEC (sRGB) standard in the CIE-1931 color space. Similarly, Table 1 shows the comparison of the CIE-1931 color

space. The CIE coordinates of the Ugi EML BLUE at pH 7 (0.16, 0.01) and pH 8 (0.14, 0.03) are very near to the standard Blue CIE coordinates by the National Television System Committee (NTSC) (0.14, 0.08),^[39,40] European Broadcasting Union (EBU) (0.15, 0.06)^[41] and IEC (sRGB) (0.15, 0.06)^[42] television display criterion. As summarized in Table 2, the Ugi EML BLUE possesses excellent properties for the application as a blue emitter for a broad spectrum of applications.

2.3 Conclusions

In summary, we have demonstrated an efficient synthesis of a deep blue emitting material Ugi EML BLUE based on a multi-component coupling strategy. The integration of a bulky carboxamide moiety to the 8-position of the coumarin scaffold afforded excellent deep blue emission in the solution state with a remarkable color purity (CIE (X) 0.16 and CIE (Y) 0.01). The origin of this light emission is systematically established with the aid of experimental and computational techniques.

2.4 Structural Characterization of Ugi EML BLUE

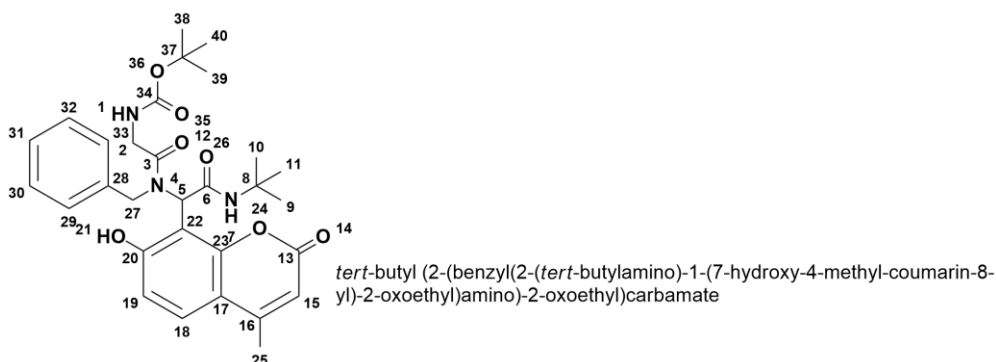


Figure 15. Structure of Ugi EML BLUE

The structure of Ugi EML BLUE is numbered as in Figure 15 and the FTIR, ^1H NMR, ^{13}C NMR, HRMS spectra are shown in supporting information. The FT-IR spectrum of the compound shows major absorptions at 3385, 3347, 1700, 1677, 1641 and 1545 cm^{-1} . The bands at 3385 and 3347 cm^{-1} are due to the stretching of the secondary NH groups. The bands at 1700, 1667 and 1641 cm^{-1} are due to the stretching of CO groups. The band at 1545 cm^{-1} is due to the aromatic C=C. The initial information obtained from FT-IR spectrum was further confirmed by ^1H NMR analysis. The two singlets at δ 1.32 and δ 1.41 are due to the nine methyl protons at positions 9, 10, 11 and nine methyl protons at 38, 39, 40. The singlet at δ 2.49 is due to the three methyl protons at C-25. The doublet observed at δ 3.75-3.80 with the J value 26Hz is due to the two methyl protons at C-2. The singlet at δ 4.83 is due to the two methyl protons at C-27. The singlet for the one proton at C-5 is observed at δ 5.87. The aromatic protons were observed as, a one proton singlet at δ 6.05, 6.31 (1H, s, Ar-OH), one proton doublet at δ 6.76-6.77 with the J value 9Hz, one proton doublet at δ 6.93-6.94 with J value 5Hz, one proton doublet at δ 7.13-7.14 with J value 7Hz, three proton multiplet at δ 7.24-7.46 and one proton doublet at δ 7.48-7.50 with J value 9Hz. The singlet at δ 6.31 is due to the hydroxyl proton at position 21. The singlets observed at δ 8.83 and δ 9.07 are due to the NH protons at the positions 1 and 7. The structure was further confirmed by ^{13}C NMR. The peaks at 18.77, 18.95, 27.72, 28.34, 28.39, 28.60, 29.48 are corresponds to the carbons at the positions 9, 10, 11, 38, 39, 40 and 25. The signals observed at 43.08 and 49.38 are due to the C-2 and C-27 carbons. The peak at 60.17 is due to the C-5 carbon. The peaks at 63.73 and 79.54 are due to

the C-8 and C-37 carbons. The signals due to the aromatic carbons are observed at 109.71, 110.38, 114.96, 116.95, 126.06, 127.15, 127.42, 127.74, 128.02, 128.49, 136.46, 151.40, 153.71. The peak at 155.45 and 155.65 are due to the C-34 and C-20 carbons. The signals observed at 160.38, 163.06 and 168.74 are due to the carbons at C-13, C-3, and C-6. Finally, the peak observed at m/z 552.27095 ($[M+H]^+$) in the mass spectrum further confirms the structure of the compound.

2.5 Experimental Section

2.5.1 Materials and Methods

All materials were obtained from commercial suppliers and used without further purification. IR spectra were recorded on a JASCO-FT/IR-4100 Fourier-transform infrared spectrometer. ^1H NMR and ^{13}C NMR spectra were obtained by Bruker amx 500 MHz spectrometer in CDCl_3 solutions. The chemical shifts (δ) values are given relative to tetramethylsilane (TMS) and the coupling constants (J) are represented in Hertz (Hz). HRMS was obtained using ESI ionization. Quantum mechanical calculations were done with Gaussian 09 software. UV-Vis absorption spectra were recorded on a Jasco V-550 UV-VIS Spectrophotometer. Fluorescence spectra were measured using Perkin Elmer LS 45 and LS 55 Spectrometers. PXRD measurements were performed on a Rigaku MiniFlex 600 X-ray Diffractometer with $\text{Cu-K}\alpha$ Monochromator of wavelength 1.541 Å. The AFM studies were done with cAFM (Asylum Research MFP3D).

2.5.2 Synthetic Procedures

2.5.2.1 Synthesis of Ugi EML BLUE

Step 1: Synthesis of 8-formyl-7-hydroxy-4-methyl-coumarin **1**: A mixture of 7-hydroxy-4-methylcoumarin (1.76 g) and hexamethylenetetramine (3.5g) in glacial acetic acid (14ml) were heated on a water bath for six hours. The hexamine adduct thus formed was hydrolyzed with 20% hydrochloric acid (26.3 ml) and the mixture was heated for another 30 minutes. After cooling, the reaction mixture was extracted with diethyl ether (15 ml x 3) and the combined ether extracts were evaporated under vacuum to obtain a pale yellow colored solution. The solution thus obtained was poured into crushed ice to obtain 8-formyl-7-hydroxy-4-methylcoumarin **1**. Pale yellow crystalline solid; Yield: 22%; M.P.: 172-174°C; IR (KBr, $\nu_{\max}/\text{cm}^{-1}$): 3448 (OH), 1745 (C=O), 1649 (C=O), 1595 (C=C); ^1H NMR δH (500 MHz, CDCl_3 , Me_4Si , δ ppm): 2.43 (3H, s, Me), 6.18 (1H, s, Ar-H), 6.88-6.90 (1H, d, $J=8.5\text{Hz}$, Ar-H), 7.71-7.72 (1H, d, $J=8.5\text{ Hz}$, Ar-H), 10.60 (1H, s, Ar-CHO), 12.19 (1H, s, Ar-OH); ^{13}C NMR δC (CDCl_3 , 125 MHz, δ ppm): 18.74, 18.91, 108.67, 111.89, 112.08, 114.24, 115.05, 132.75, 152.43, 156.18, 158.95, 165.29, 193.28; HRMS(ESI): m/z ($[\text{M}+\text{H}]^+$) calculated for $\text{C}_{11}\text{H}_8\text{O}_4$: 205.05008, found: 205.05012

Step 2: Synthesis of Ugi EML BLUE: 8-formyl-7-hydroxy-4-methylcoumarin **2** (204 mg) and benzylamine (107.16 mg) were dissolved in 8 ml methanol and stirred for 28 hours in a dry round-bottomed flask to form the imine. To this, *Boc*-protected glycine (175.18 mg) was added and stirred for another 15 minutes. Finally, *tert*-butyl isocyanide (83.13

mg) was added and stirred the whole mixture for 96 hours to complete the Ugi 4 CC. The solvent was then evaporated under vacuum and solid obtained was washed with petroleum benzene (5x3) to obtain “**Ugi EML BLUE**” (*tert*-butyl (2-(benzyl (2-(*tert*-butylamino)-1-(7-hydroxy-4-methyl-coumarin-8-yl)-2-oxoethyl) amino)-2-oxoethyl) carbamate (Scheme 2). Yellowish-brown crystalline solid; Yield: 73%; M.P.: 178°C; IR (KBr, $\nu_{\max}/\text{cm}^{-1}$): 3385 (NH), 3347 (NH), 1700 (CO), 1677 (CO), 1641 (CO), 1545 (C=C); ^1H NMR δH (500 MHz, CDCl_3 , δ ppm): 1.32 (9H, s, Me), 1.41 (9H, s, Me), 2.49 (3H, s, Me), 3.75-3.80 (2H, d, $J=26\text{Hz}$, CH_2), 4.83 (2H, s, CH_2), 5.87 (1H, s, CH), 6.05 (1H, s, Ar-H), 6.31 (1H, s, Ar-OH), 6.76-6.77 (1H, d, $J=9\text{Hz}$, Ar-H), 6.93-6.94 (1H, d, $J=5\text{Hz}$, Ar-H), 7.13-7.14 (1H, d, $J=7\text{Hz}$, Ar-H), 7.24-7.46 (3H, m, Ar-H), 7.48-7.50 (1H, d, $J=9\text{Hz}$, Ar-H), 8.83 (1H, s, NH), 9.07 (1H, s, NH); ^{13}C NMR δC (CDCl_3 , 125MHz, δ ppm): 18.77, 18.95, 27.72, 28.34, 28.39, 28.60, 29.48, 43.08, 49.38, 60.17, 63.73, 79.54, 109.71, 110.38, 114.96, 116.95, 126.06, 127.15, 127.42, 127.74, 128.02, 128.49, 136.46, 151.40, 153.71, 155.45, 155.65, 160.38, 163.06, 168.74; HRMS (ESI): m/z ($[\text{M}+\text{H}]^+$) calculated for $\text{C}_{30}\text{H}_{37}\text{N}_3\text{O}_7$: 552.27098, found: 552.27095.

2.5.2.2 Synthesis of Ugi Chloride (2)

An equimolar amount of coumarin aldehyde (8-formyl-7-hydroxy-4-methylcoumarin (204 mg)) and benzylamine (107.16 mg) were dissolved in 8 ml methanol and stirred for 30 minutes in a dry round-bottomed flask. The completion of imine formation was monitored by TLC. To this, one equivalent of Chloroacetic acid (94.5 mg) is added and stirred for another 15 minutes. Finally added one equivalent of *tert*-butyl

isocyanide (83.13 mg) and stirred the whole mixture for 96 hours. The solvent was evaporated under vacuum and the crude product obtained upon repeated washings with petroleum benzene (5 x 15mL) afforded the pure Ugi chloride (N-benzyl-N-(2-(tert-butylamino)-1-(7-hydroxy-4-methyl-coumarin-8-yl)-2-oxoethyl)-2-chloroacetamide).

2.5.2.3 Conversion of Ugi Chloride to Ugi Azide (3)

An equimolar amount of Ugi chloride (N-benzyl-N-(2-(tert-butylamino)-1-(7-hydroxy-4-methyl-coumarin-8-yl)-2-oxoethyl)-2-chloroacetamide, 470 mg) and sodium azide (65 mg) were dissolved in N,N-dimethyl formamide (5 mL). To this, potassium carbonate (414 mg) is added and stirred at room temperature for 6 hours. The mixture was diluted with cold water. The white precipitate obtained was filtered, washed repeatedly with water and dried under vacuum to afford the pure Ugi azide (2-azido-N-benzyl-N-(2-(tert-butylamino)-1-(7-hydroxy-4-methyl-2-oxo-2H-chromene-8-yl)-2-oxoethyl) acetamide).

2.5.3 Measurements of Fluorescence in various pH

Prepared a 50 ppm solution of **Ugi EML BLUE** in Ethanol and divided into equal portions. For obtaining various pH ambiances, added different volumes of 0.5M K₂CO₃ solution to each portion. Studied the fluorescence of each and selected two perfect samples (pH 7 and pH 8) for analyzing the pH sensitivity.

2.5.4 Thin film of Ugi EML BLUE for measuring the solid state UV-Vis_{abs} & PL_{ems}

The Solid state UV-Vis_{abs} & PL_{ems} Data of Ugi EML BLUE were taken by preparing a thin film of it on a glass plate.

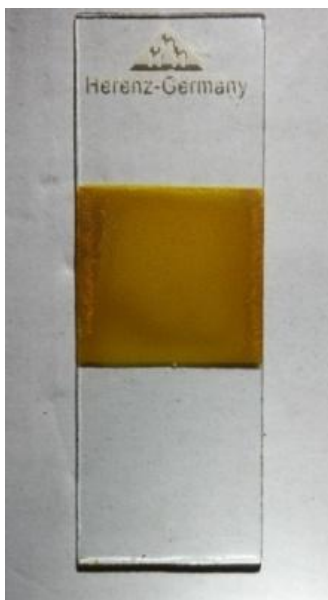


Figure 15. Ugi EML BLUE: Thin-film coated on a glass plate

2.5.5 Fluorescence Quantum Yields

The photoluminescent quantum yield of a fluorophore is determined relative to a reference compound of known quantum yield. If applied the same excitation wavelength, slit and gain bandwidths for the sample and the reference compound, then the quantum yield is calculated as

$$\text{Quantum Yield } (\phi) = \frac{QY_r \times I_s \times A_r \times \eta_s^2}{I_r \times A_s \times \eta_r^2}$$

Where,

- QY_r : *Quantum yield of the reference compound*
- I_s : *The Integrated fluorescent intensity of the sample*
- I_r : *The Integrated fluorescent intensity of the reference*
- A_s : *Absorbance at the excitation wavelength of the sample*
- A_r : *Absorbance at the excitation wavelength of reference*
- η_s : *Refractive index of the solvent used for sample*
- η_r : *Refractive index of the solvent used for reference*

(Concentration range: *In order to reduce the reabsorption effects, absorbance in the 10mm fluorescence cuvette is adjusted to the range below 0.1 at and above the excitation wavelength.*)

Results:

Solvent: *DMSO*

Reference Compound: *Anthracene*

Reference Compound Quantum Yield (ϕ) = 0.27

Ugi EML Blue, Quantum Yield (ϕ) = 0.12

Ugi EML Blue at higher P^H , Quantum Yield (ϕ) = 0.21

References

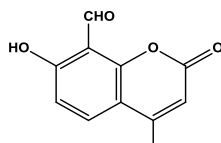
- [1] Tang, C. W.; VanSlyke, S. A. *Appl. Phys. Lett.* **1987**, *51*, 913-915.
- [2] Fleetham, T.; Li, G.; Wen, L.; Li, J. *Adv. Mater.* **2014**, *26*, 7116-7121.
- [3] Ammermann, D.; Böhler, A.; Dirr, S.; Kowalsky, W. *Int. J. Electron. Comm. (AEÜ)* **1996**, *51*, 327-332.
- [4] Hirata, S.; Sakai, Y.; Masui, K.; Tanaka, H.; Lee, S. Y.; Nomura, H.; Nakamura, N.; Yasumatsu, M.; Nakanotani, H.; Zhang, Q.; Shizu, K.; Miyazaki, H.; Adachi, C. *Nat. Mater.* **2015**, *14*, 330-336.
- [5] Sasabe, H.; Kido, J. *J. Mater. Chem. C* **2013**, *1*, 1699-1707.
- [6] Im, Y.; Byun, S. Y.; Kim, J. H.; Lee, D. R.; Oh, C. S.; Yook, K. S.; Lee, J. Y. *Adv. Funct. Mater.* **2017**, *27*, 1603007.
- [7] Graff, A.; Altmann, F.; Dzwilewski, A.; Freitag, B. *Microsc. Microanal.* **2014**, *20*, 144-145.
- [8] Feng, Y.; Zhuang, X.; Zhu, D.; Liu, Y.; Wang, Y.; Bryce, M. R. *J. Mater. Chem. C* **2016**, *4*, 10246-10252.
- [9] Hosokawa, C.; Higashi, H.; Nakamura, H.; Kusumoto, T. *Appl. Phys. Lett.* **1995**, *67*, 3853-3855.
- [10] Yang, X.; Xu, X.; Zhou, G. *J. Mater. Chem. C* **2015**, *3*, 913-944.
- [11] Zhu, M.; Yang, C. *Chem. Soc. Rev.* **2013**, *42*, 4963-4976.
- [12] Chen, J. X.; Liu, W.; Zheng, C. J.; Wang, K.; Liang, K.; Shi, Y. Z.; Ou, X. M.; Zhang, X. H. *ACS Appl. Mater. Interfaces.* **2017**, *9*, 8848-8854.
- [13] Wrona-Piotrowicz, A.; Zakrzewski, J.; M´etivier, R.; Brosseau, A.; Makal, A.; Wo´zniak, K. *RSC Adv.* **2014**, *4*, 56003-56012.
- [14] Niko, Y.; Hiroshige, Y.; Kawauchi, S.; Gen-ichi, K. *J. Org. Chem.* **2012**, *77*, 3986-3996.
- [15] Ugi, I. *Angew. Chem. Int. Ed. Engl.* **1962**, *1*, 8-21.
- [16] Dömling, A.; Ugi, I. *Angew. Chem. Int. Ed.* **2000**, *39*, 3168-3210.
- [17] Veiderma, M. *Proc. Estonian Acad. Sci. Chem.* **2007**, *56*, 98-102.

- [18] Pramitha, P.; Bahulayan, D. *Bioorg. Med. Chem. Lett.* **2012**, *22*, 2598-2603.
- [19] Alexander, L.; Klug, H. P. *J. Appl. Phys.* **1950**, *21*, 137-142.
- [20] Monshi, A.; Foroughi, M. R.; Monshi, M. R. *World J. Nano Sci. Eng.* **2012**, *2*, 154-160.
- [21] Song, W.; Lee, I.; Lee, J. Y. *Adv. Mater.* **2015**, *27*, 4358-4363.
- [22] Moorthy, J. N.; Natarajan, P.; Venkatakrisnan, P.; Huang, D. F.; Chow, T. J. *Org. Lett.* **2007**, *9*, 5215-5218.
- [23] Yang, C. H.; Guo, T. F.; Sun, I. W. *J. Lumin.* **2007**, *124*, 93-98.
- [24] Zhang, D. D.; Cai, M. H.; Zhang, Y. G.; Zhang, D. Q.; Duan, L. *Mater. Horiz.* **2016**, *3*, 145-151.
- [25] Yang, J.; Huang, J.; Li, Q.; Li, Z. *J. Mater. Chem. C* **2016**, *4*, 2663-2684.
- [26] Na, E. J.; Lee, K. H.; Han, H.; Kim, Y. K.; Yoon, S. S. *J. Nanosci. Nanotechnol.* **2013**, *13*, 554-557.
- [27] Beaujuge, P. M.; Ellinger, S.; Reynolds, J. R. *Nat. Mater.* **2008**, *7*, 795-799.
- [28] Beaujuge, P. M.; Amb, C. M.; Reynolds, J. R. *Acc. Chem. Res.* **2010**, *43*, 1396-1407.
- [29] Lakowicz, J. R. *Principles of Fluorescence Spectroscopy*, 2nd edition, Plenum Press, New York, **1999**, pp. 6-200.
- [30] Baruah, M.; Qin, W.; Flors, C.; Hofkens, J.; Vall'ee, R. A. L.; Beljonne, D.; Auweraer, M. V. D.; Borggraeve, W. M. D.; Boens, N. *J. Phys. Chem. A* **2006**, *110*, 5998-6009.
- [31] Frisch, M. J.; Trucks, G. W.; Schlegel, H. B.; Scuseria, G. E.; Robb, M. A.; Cheeseman, J. R.; Scalmani, G.; Barone, V.; Mennucci, B.; Petersson, G. A.; Nakatsuji, H.; Caricato, M.; Li, X.; Hratchian, H. P.; Izmaylov, A. F.; Bloino, J.; Zheng, G.; Sonnenberg, J. L.; Hada, M.; Ehara, M.; Toyota, K.; Fukuda, R.; Hasegawa, J.; Ishida, M.; Nakajima, T.; Honda, Y.; Kitao, O.; Nakai, H.; Vreven, T.; Montgomery, J. A., Jr.; Peralta, J. E.; Ogliaro, F.; Bearpark, M.; Heyd, J. J.; Brothers, E.; Kudin, K. N.; Staroverov, V. N.; Kobayashi, R.; Normand, J.; Raghavachari, K.; Rendell, A.; Burant, J. C.; Iyengar, S. S.; Tomasi, J.; Cossi, M.;

- Rega, N.; Millam, J. M.; Klene, M.; Knox, J. E.; Cross, J. B.; Bakken, V.; Adamo, C.; Jaramillo, J.; Gomperts, R.; Stratmann, R. E.; Yazyev, O.; Austin, A. J.; Cammi, R.; Pomelli, C.; Ochterski, J. W.; Martin, R. L.; Morokuma, K.; Zakrzewski, V. G.; Voth, G. A.; Salvador, P.; Dannenberg, J. J.; Dapprich, S.; Daniels, A. D.; Farkas, Ö.; Foresman, J. B.; Ortiz, J. V.; Cioslowski, J.; Fox, D. J., Revision A.1, Gaussian, Inc., Wallingford CT, **2009**.
- [32] Guido, C. A.; Knecht, S.; Kongsted, J.; Mennucci, B. *J. Chem. Theory Comput.* **2013**, *9*, 2209-2220.
- [33] Scott, A. P.; Radom, L. *J. Phys. Chem.* **1996**, *100*, 16502–16513.
- [34] Sortur, V.; Yenagi, J.; Tonannavar, J.; Jadhav, V. B.; Kulkarni, M. V. *Spectrochim. Acta, Part A* **2008**, *71*, 688–694.
- [35] Foresman, J. B.; Frisch, A. *Exploring Chemistry with Electronic Structure Methods*, 2nd edition, Gaussian Inc., USA, **1996**, pp. 3-161.
- [36] Laurent, A. D.; Jacquemin, D. *Int. J. Quantum Chem.* **2013**, *113*, 2019–2039.
- [37] Mennucci, B.; Cappelli, C.; Guido, C. A.; Cammi, R.; Tomasi, J. *J. Phys. Chem.* **2009**, *113*, 3009–3020.
- [38] Marenich, A. V.; Cramer, C. J.; Truhlar, D. G. *J. Phys. Chem. B* **2009**, *113*, 6378–6396.
- [39] CIE Standards, CIE-1931 Coordinates (the CIE 1931 Standard Colorimetric Observer).
- [40] NTSC Standards, National Television Standards Committee, Issued December 23, **1953**.
- [41] E. B. U. - Technical Centre - Tech. 3213-E.
- [42] IEC Standards (sRGB Standard), IEC/4WD 61966-2-1: *Colour Measurement and Management in Multimedia Systems and Equipment - Part 2-1: Default RGB Colour Space – sRGB*.

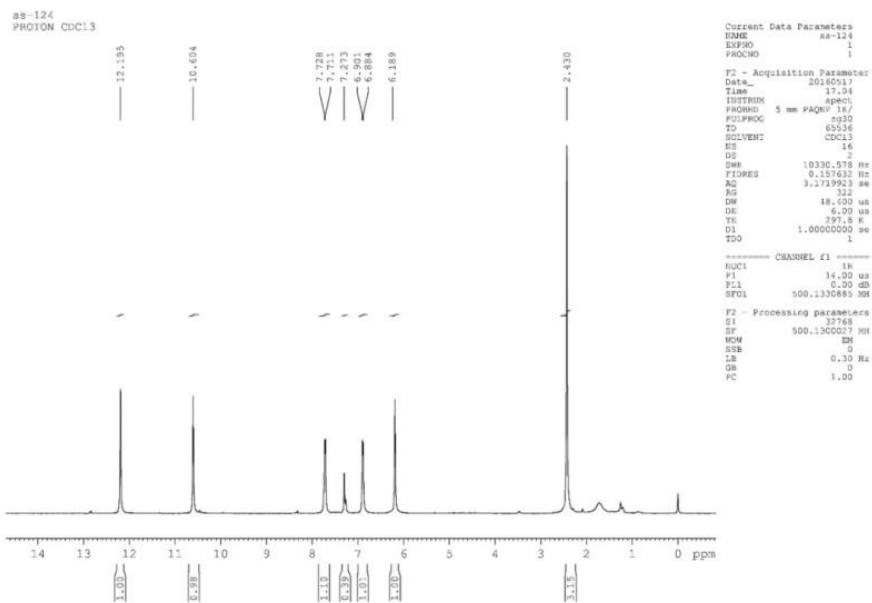
Supporting Information

Spectral details of 8-formyl-7-hydroxy-4-methylcoumarin (1)

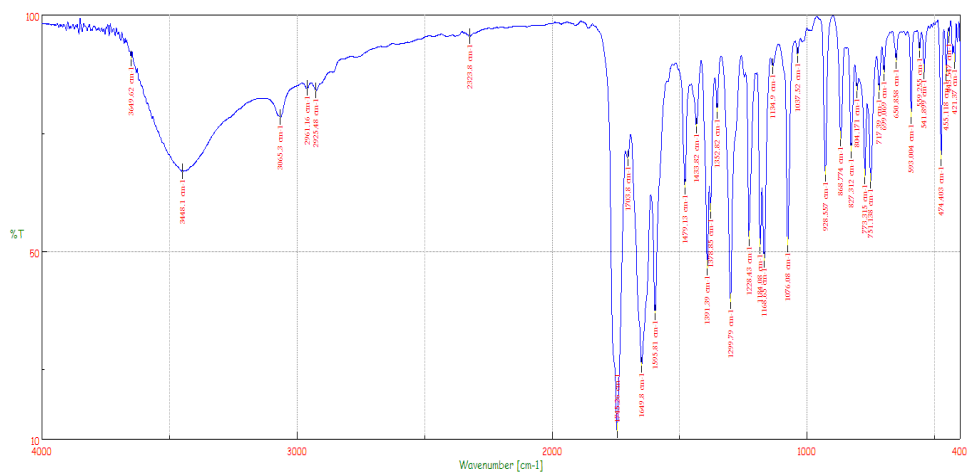


8-formyl-7-hydroxy-4-methyl-coumarin (1)

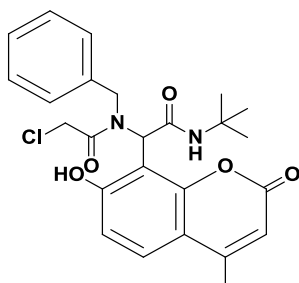
¹HNMR Spectra:



IR Spectra:

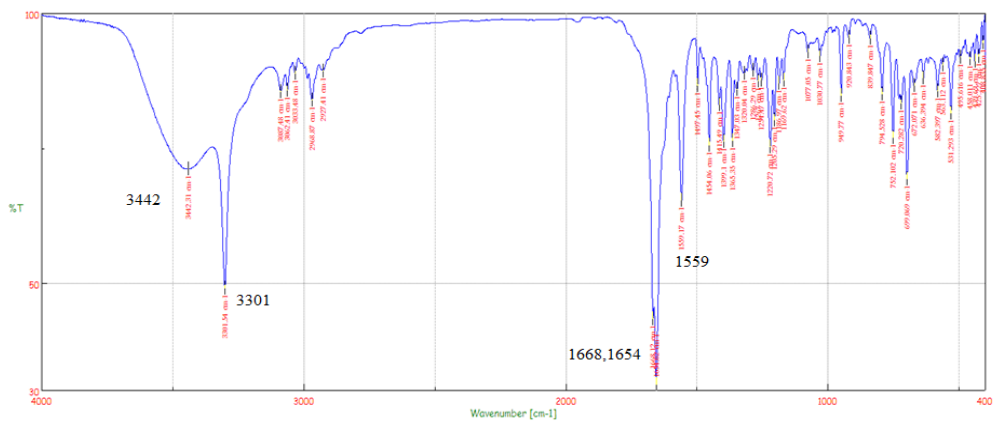


Spectral Details of Ugi Chloride (2)

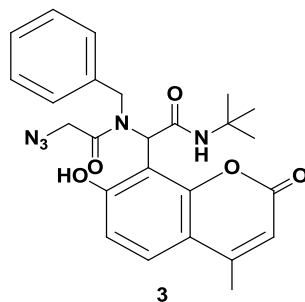


N-benzyl-*N*-(2-(*tert*-butylamino)-1-(7-hydroxy-4-methyl-coumarin-8-yl)-2-oxoethyl)-2-chloroacetamide (**2**)

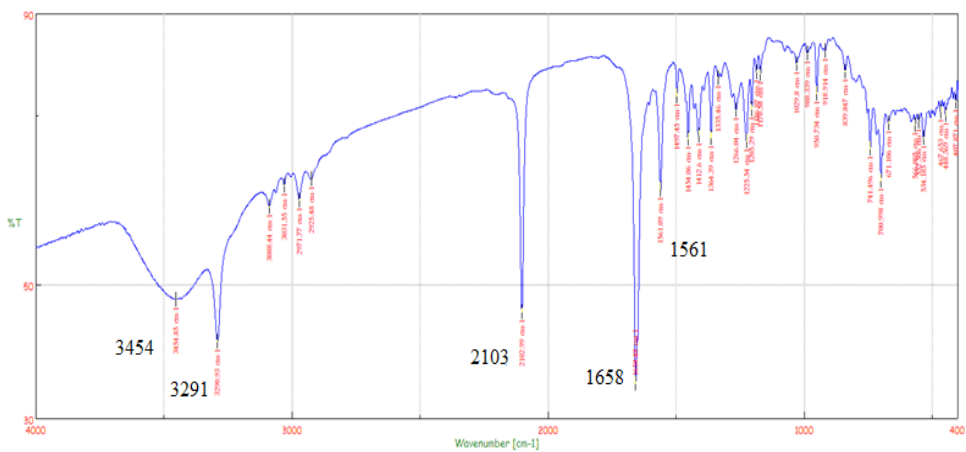
IR absorptions (KBr, $\nu_{\max}/\text{cm}^{-1}$): 3442 (OH), 3301 (NH), 1668 (CO), 1654 (CO), 1545 (C=C)



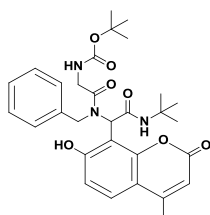
Spectral Details of Ugi Azide (3)



IR absorptions (KBr, $\nu_{\max}/\text{cm}^{-1}$): 3454 (OH), 3291 (NH), 2103 (CN₃), 1658 (CO), 1561 (C=C)

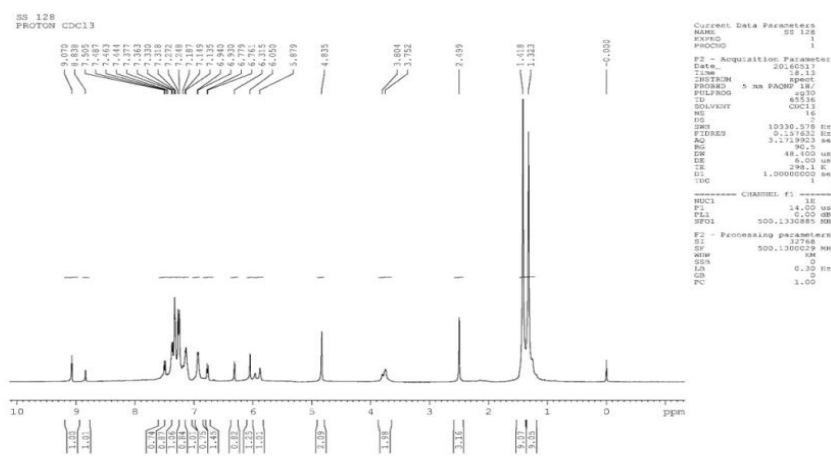


Spectral Details of Ugi EML BLUE

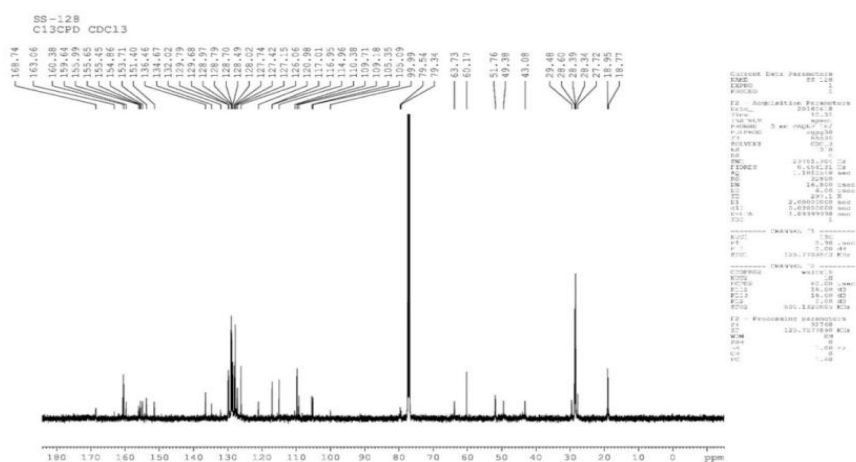


tert-butyl (2-(benzyl(2-(*tert*-butylamino)-1-(7-hydroxy-4-methyl-coumarin-8-yl)-2-oxoethyl)amino)-2-oxoethyl)carbamate

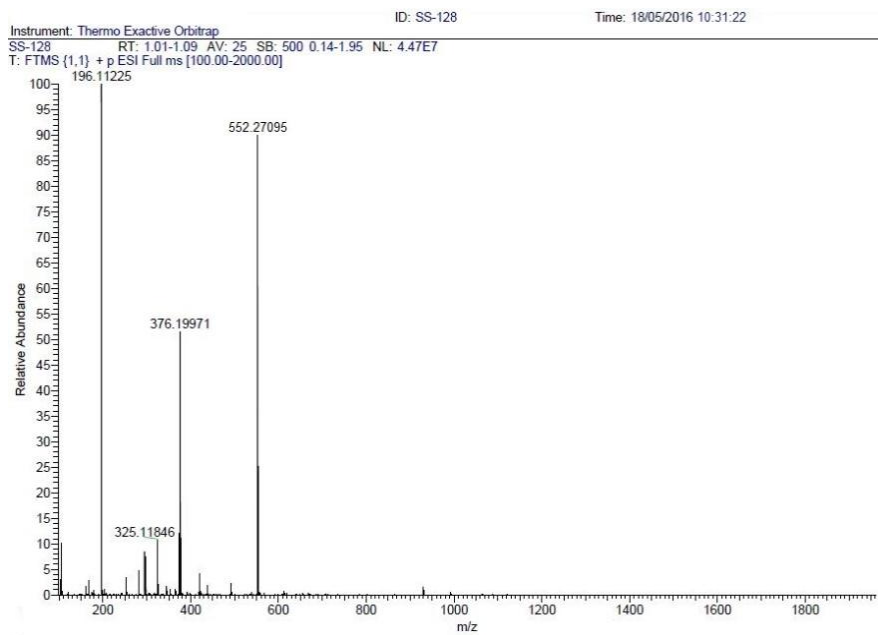
¹H NMR Spectra:



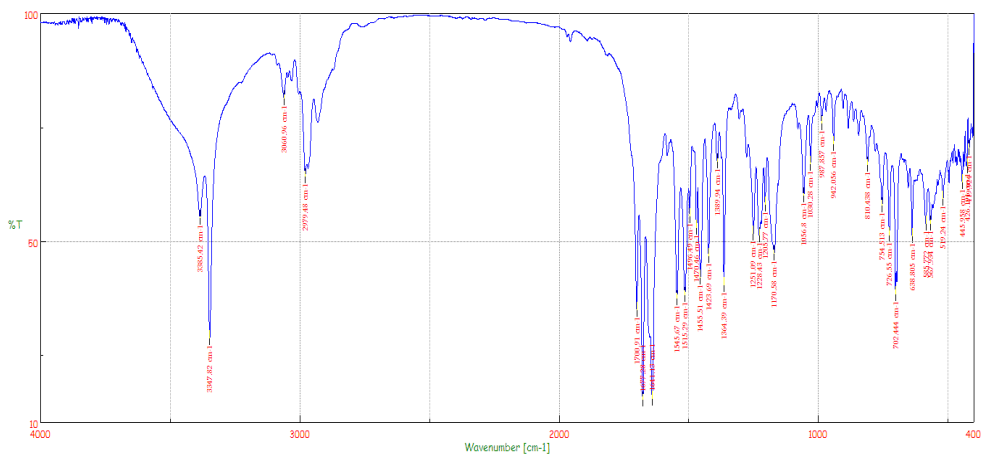
¹³C NMR Spectra:



HRMS (ESI):



IR Spectra:



STUDIES ON THE APPLICATIONS OF UGI EML BLUE FOR THE CDK2 TARGETED BIOIMAGING AND CYTOTOXIC ACTIVITIES ON HELA CELLS

3.1 Introduction

In the previous chapter we have discussed the synthesis and fluorescent properties of ‘Ugi EML BLUE’ which is having a coumarin carbamate core unit. Scaffolds functionalised with coumarin carbamate core units are known for their broad spectrum of biological activities. Hence, we decided to undertake a systematic study on the applications of this new molecule as inhibitor as well as imaging agent.

As we know, various bioimaging techniques have been developed over the past few decades for the early detection of cancer.^[1] The use of conventional imaging methods like Computed Tomography (CT), Magnetic Resonance Imaging (MRI), X-Ray, etc. are limited to the generation of information about anatomical and macroscopic tumoral details. However, today, the advanced fluorescence-based imaging techniques enable us to visualize the expression and activity of specific molecules such as proteases and protein kinases etc.^[2-6] These kind of fluorescence imaging techniques are playing a pivotal role in the selective and sensitive monitoring of the intracellular proteins whose expression or activity is drastically altered in tumor cells compared to the normal cells. For example, the Cyclin Dependent Kinase 2 (CDK2) which is essential

for the G1to S phase transition in the eukaryotic cell divisions,^[7,8] is overexpressed in many cancer cell lines.

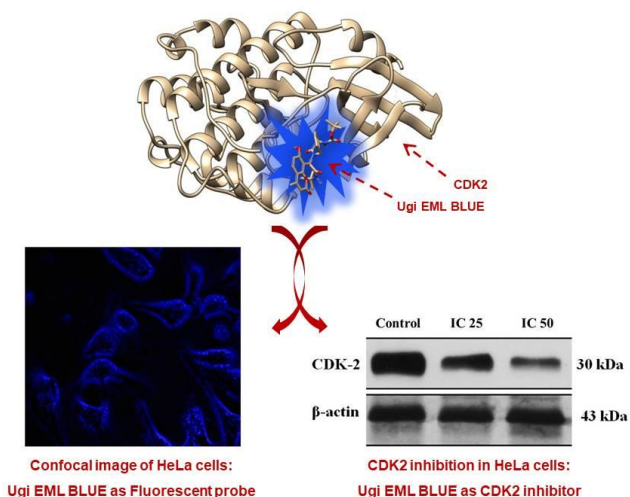


Figure 1. Dual functional applications of Ugi EML BLUE

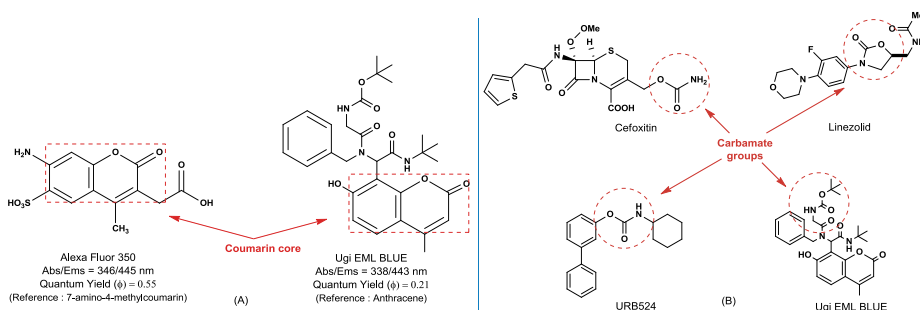


Figure 2. (A) Comparison of the structure and fluorescence properties of Alexa Fluor 350 and Ugi EML BLUE. (B) Comparison of structural features of Ugi EML BLUE and few carbamate drugs showing different metabolic stability.

For targeting this kind of specific intracellular moieties, the fluorescent probe should have decorated with appropriate functionalities to bind with specific target molecules or biomarkers. However, in many cases, the

integration of different functionalities to the fluorescent probe may lead to the loss of its cytoplasmic membrane permeability or suffer a quenching effect in its fluorescence. In recent years, FRET or ICT based small molecule fluorescent probes has emerged as a principal solution to such issues.^[9-11] Among them, ICT based probes are more potential due to their structural simplicity, high efficiency and membrane permeability.^[12-17] Alexa Fluor 350 is one of the interesting examples of such a small molecule probe that has been widely used for stable signal generation in imaging and flow cytometry.^[18] As we discussed in the earlier chapter, the Ugi EML BLUE is an ICT based blue-emitting small molecule coumarin carbamate probe¹⁹ with superior photoluminescence properties comparable with that of Alexa Fluor 350^[18] (Figure 2A). Coumarin and carbamate moieties are well known for a plethora of medicinal applications including anticancer, antibacterial, antifungal and anticoagulant activities (Figure 2B).^[20-25] Similarly, coumarin derivatives functionalized with carbamate groups are efficient for inhibiting the cell cycle arrest activity of HIV-1Vpr.^[26,27] Moreover, few recent studies show that the coumarin derivatives are capable of fluorescence chemosensory applications too.^[28-30] At the same time, coumarin molecules functionalized with a hydroxy group at the 7-position are efficient fluorophores since the presence of an electron donating group at the 7-position are known to enhance the fluorescence of such probes. ^[31-38]

Based on the efficiency of our Ugi EML BLUE as a strong fluorescent probe and also due to the presence of a medically active carbamate-amide moiety on its coumarin core, we decided to investigate

the potential of Ugi EML BLUE as a dual functional probe for imaging and subsequent inhibition of cancer cells so as to avoid the process of cell washing after imaging for therapy. We have studied the CDK2 binding properties of the Ugi EML BLUE using Auto Dock Vina ^[39] and also performed the biological studies with the HeLa cells. The Auto Dock Vina is open-source software for doing the molecular docking. By using this software we can evaluate the binding affinities of drug molecules towards any proteins or such moieties. The results obtained from computational and experimental studies showed that Ugi EML BLUE can efficiently locate and image the cellular morphology and, simultaneously act as an effective CDK2 suppressor in HeLa cells as shown in Figure 1.

3.2 Results and Discussion

3.2.1 Evaluation of the CDK2 targeted imaging potential of Ugi EML BLUE

Fundamentally, cancer/tumor developments are due to the uncontrolled cell proliferation and hence it can be controlled by preventing the abnormal cell divisions.^[40,41] Eukaryotic cell divisions are taking place through the four cellular phases such as G1, S, G2, and M and are mainly promoted by different types of specific Cyclins and Cyclin Dependent Kinases (CDK).^[8,42] Among the various cyclins, Cyclin-dependent kinase 2 (CDK2) is essential for the G1 to S phase transition during the mitotic cell divisions and its rate is high in abnormal cell divisions.^[8,42-44] The irregular cell divisions can be controlled by the arrest of G1 to S phase transition through the inhibition of CDK2. The imaging and therapy can be more facile if the fluorescent probe can work as a dual

functional material which can selectively light up and inhibit CDK2. Keeping this in mind, we started our study by evaluating the binding ability of Ugi EML BLUE with CDK2 using Auto Dock Vina 1.1.2³⁹ The docking was performed using the crystal structure of the human CDK2 (in complex with the ligand 3-hydroxychromone, PDB code 2DUV) [45] and Ugi EML BLUE for calculating its binding ability.

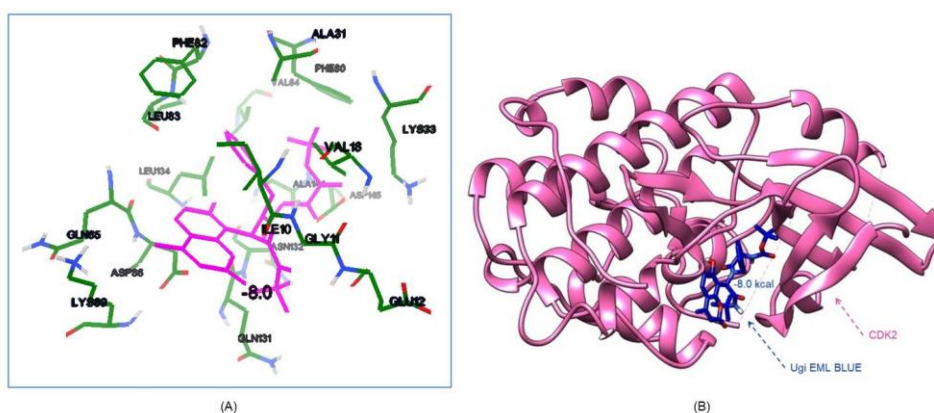


Figure 3. (A) Ugi EML BLUE in the active site of CDK2. (B) Human CDK2 (PDB ID 2DUV) in complex with Ugi EML BLUE.

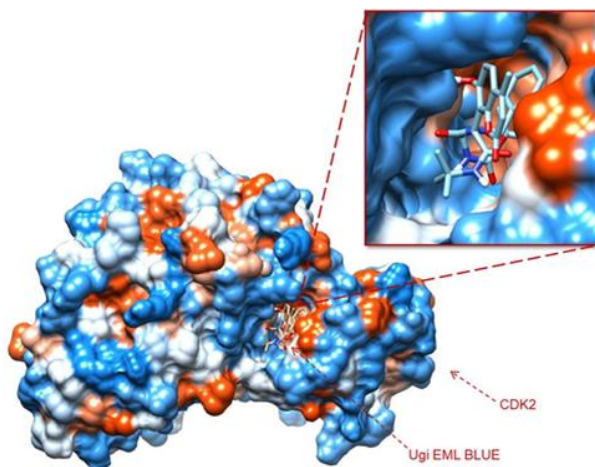


Figure 4. Encapsulation of the ligand Ugi EML BLUE into the hydrophobic pocket of CDK2

The active site of CDK2 comprises the amino acid residues such as GLY 11 (Glycine), ILE 10 (Isoleucine), VAL 16, VAL 64 (Valine), ALA 144, ALA 31 (Alanine), LEU 134, LEU 83 (Leucine), PHE 80, PHE 82 (Phenylalanine), ASP 86, ASP 145 (Aspartic acid), ASN 132 (Asparagine) and GLN 131 (Glutamine) (Figure 3A). Most of these amino acids have hydrophobic side chains favorable for the formation of a tight ‘hydrophobic pocket’ in it.^[46,47] Our docking studies showed binding energy of -8.0 kcal (Figure 3B) and which is due to the strong hydrophobic interaction between Ugi EML BLUE and the target protein. The bulky carbamate-amide functionalities present in Ugi EML BLUE also helps to encapsulate it into such hydrophobic pockets of the CDK2 as shown in Figure 4. We have also carried out the docking studies of Ugi EML BLUE with other kinases involved in cell cycles such as CDK1 (PDB ID 4Y72),^[48] CDK4 (PDB ID 1H00)^[49] and CDK6 (PDB ID 3NUP).^[50] The binding affinity values obtained from these studies are very less (-1.3 kcal, -0.8 kcal and +5.0 kcal respectively) compared to the same obtained from the docking study of Ugi EML BLUE with CDK2 (-8.0 kcal). The less binding affinity values obtained for other kinases clearly indicate the selectivity of Ugi EML Blue towards CDK2 (see supporting information for the docking mode of Ugi EML BLUE in the active site of various kinases). The impressive results obtained from the docking studies prompted us to evaluate the potential of Ugi EML BLUE as a bifunctional fluorescent probe for both imaging and inhibition of CDK2 present in cervical cancer cell line HeLa by *in vitro* bioactivity studies.

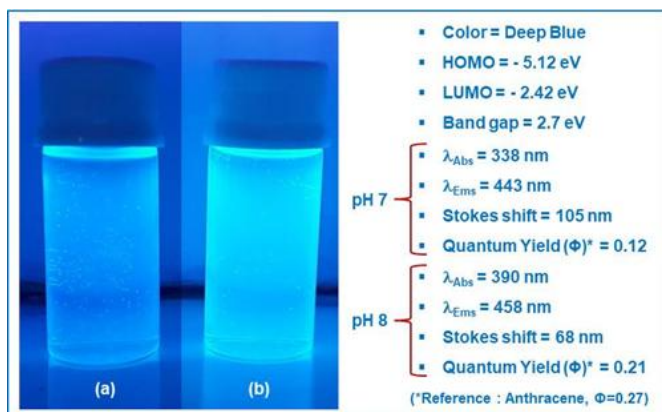


Figure 5. Summary of fluorescence and photo-physical data of Ugi EML BLUE (50 ppm solution in DMSO): a) fluorescence at pH 7, b) fluorescence at pH 8 (no significant change in intensity was observed for pH>8).

Ugi EML BLUE was obtained from the formylation of 4-methyl-7-hydroxy coumarin and subsequent ‘Ugi four-component reaction’ as discussed in Chapter 2. The photophysical properties of the Ugi EML BLUE were measured and obtained as reported earlier.^[19] The UV-Vis absorption maxima and PL emission maxima of Ugi EML BLUE at neutral pH (pH 7) are observed at 338 nm and 443 nm respectively with a large Stoke’s shift of 105 nm. The summary of fluorescence, photo-physical data and the values for its HOMO/LUMO energy levels, etc. are shown in Figure 5.

Figure 6 shows fluorescence intensity (A) and the confocal images (B) of the HeLa cells incubated with the Ugi EML BLUE at its respective IC25 and IC50 concentrations (IC25 0.25 $\mu\text{g}/\text{mL}$ and IC50 0.5 $\mu\text{g}/\text{mL}$, in PBS (pH 7.4), 1% DMSO). An intense bright fluorescent image of the cell morphology was observed (Figure 6B-c) when the cells were stained with Ugi EML BLUE at its IC50 concentration.

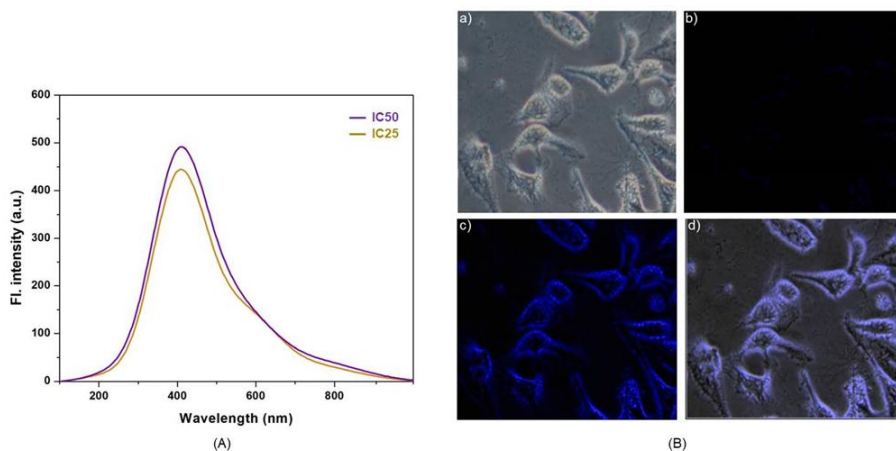


Figure 6. (A) Fluorescence intensity of the Ugi EML BLUE (in PBS (pH 7.4), 1% DMSO) when it incubated in the HeLa cells at its IC25 (0.25 µg/mL) and IC50 (0.5 µg/mL) concentrations. (B) Confocal images of HeLa cells incubated with Ugi EML BLUE (in PBS (pH 7.4), 1% DMSO): a) bright-field image, b) Fluorescence image at IC25, c) Fluorescence image at IC50, d) Overlay image of panels a to c.

This intense fluorescence obtained was due to the occurrence of intramolecular charge transfer transitions (ICT) in Ugi EML BLUE under such conditions. Moreover, as we understood from the docking studies, Ugi EML BLUE is able to bind the CDK2 on incubation due to their high binding affinity towards CDK2. From these studies, it is clear that Ugi EML BLUE can effectively target and image the CDK2 present in cancer cell lines (in this case HeLa cells).

3.2.2 Evaluation of the cytotoxicity of Ugi EML BLUE targeted against CDK2 present in human cervical cancer (HeLa) cells.

3.2.2.1 *In vitro* cytotoxic effect of the Ugi EML BLUE against the HeLa cells and primary H8 cells

We have then extended our studies to determine the effect of Ugi EML BLUE on human cervical cancer (HeLa) cells by various methods

such as MTT assay, analysis of mitochondrial membrane potential ($\Delta\psi_m$), analysis of cell cycle progress and the downregulation of CDK2 behind the apoptosis by Western blot analysis. The studies were started with the MTT assay. Figure 7 shows the *In vitro* cytotoxic effect of the Ugi EML BLUE

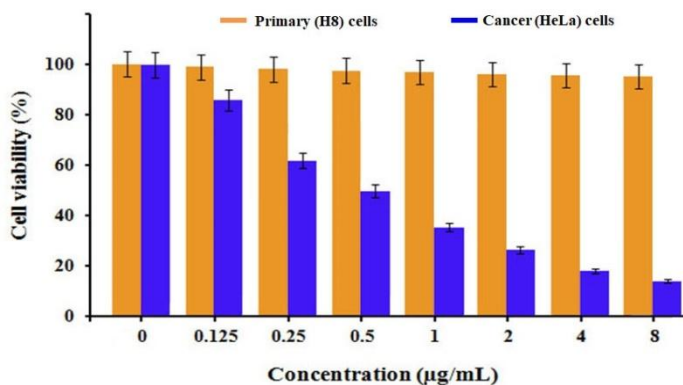


Figure 7. *In vitro* cytotoxicity activity of the Ugi EML BLUE against HeLa cells and primary H8 cells

(0, 0.125, 0.25, 0.5, 1.0, 2.0, 4.0 and 8.0 µg/mL concentrations, in PBS (pH 7.4), 1% DMSO (10µL) against the HeLa cells and primary H8 cells. The experimental results demonstrate that the Ugi EML BLUE has the ability to inhibit cell proliferation in a dose dependent manner. The IC50 value of Ugi EML BLUE against HeLa cells was calculated as 0.5 µg/mL (cell viability 49.4±1.25). At the same time, the cytotoxicity effect of Ugi EML BLUE against H8 cells did not show significant cytotoxicity at lower concentration and cytotoxicity increases very slightly with increasing concentration from 0.5 to 8.0 µg/ml in 24 hrs. From the control experiment with primary H8 cells and the cytotoxicity study with HeLa cells, it is clear that the Ugi EML BLUE is able to reduce the cell viability

of HeLa cells in a dose dependent manner and can be used effectively at low concentrations.

3.2.2.2 Morphology study

The morphology of the HeLa cells in the presence and absence of Ugi EML BLUE were also studied using inverted phase contrast microscopy. The cells of the different concentration groups are shown in Figure 8.

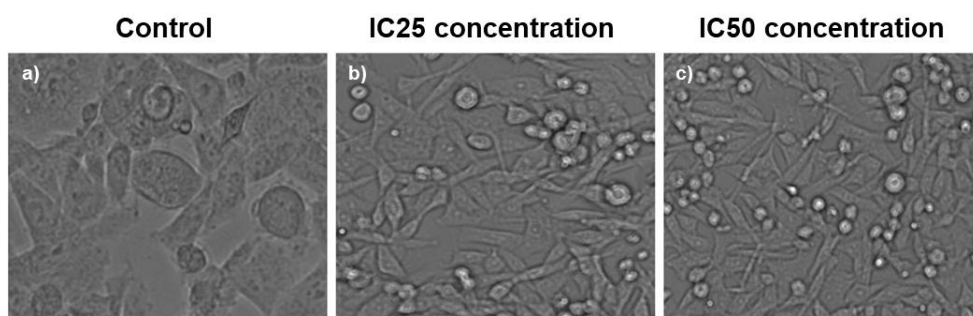


Figure 8. Inverted phase contrast microscopy images of the HeLa cells in the presence and absence of Ugi EML BLUE: a) Undamaged HeLa cells observed in the control (untreated), b) 25% cell death and its apoptotic morphology changes were observed in the HeLa cells treated with the Ugi EML BLUE at its IC25 concentration (0.25 $\mu\text{g/mL}$), c) 50% cell death and its apoptotic morphology changes were observed in the HeLa cells treated with the Ugi EML BLUE at its IC50 concentration (0.5 $\mu\text{g/mL}$).

The cells pretreated with Ugi EML BLUE were different in nature with the control (untreated). In control, the cells were closely packed and spindle shaped whereas, inhibition of cell growth was observed in the cells treated with the Ugi EML BLUE, although many of the cells were still attached to their culture plates. Many of the cells had irregular cell membranes and signs of blebbing and are serves as apparent evidence for apoptotic activation. Moreover, these apoptotic morphological change of

the Ugi EML BLUE treated HeLa cells could be visualized by using the fluorescence ability of the Ugi EML BLUE (Figure 6B) itself.

3.2.2.3 Mitochondrial membrane potential analysis

The mitochondrial membrane potential ($\Delta\psi_m$) loss of HeLa cells was analyzed with fluorescence microscopy using the dye Rh-123. As shown in Figure 9, a decrease in the mean fluorescence intensity was observed after the treatment of the cells with Ugi EML BLUE at its IC25 and IC50 concentrations respectively, where the quenching of fluorescence observed is indicating the loss of mitochondrial membrane potential.

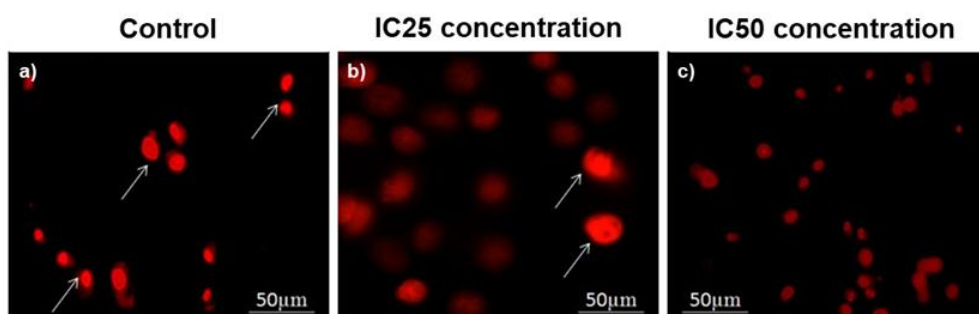


Figure 9. Fluorescence microscopy images of Rh-123 stained HeLa cells treated with Ugi EML BLUE revealing the effect of Ugi EML BLUE on the mitochondrial membrane potential ($\Delta\psi_m$): a) Intense fluorescence of Rh-123 stained HeLa cells control (untreated), b) Quenching of fluorescence observed in the Rh-123 stained HeLa cells treated with the Ugi EML BLUE at its IC25 concentration (0.25 $\mu\text{g/mL}$), c) Significant quenching of fluorescence observed in the Rh-123 stained HeLa cells treated with the Ugi EML BLUE at its IC50 concentration (0.5 $\mu\text{g/mL}$).

The loss of mitochondrial membrane potential ($\Delta\psi_m$) is due to mitochondrial membrane depolarization, which is considered as an initial and irreversible step of apoptosis.^[51] Mitochondria play an important role in an intrinsic apoptotic pathway by releasing cytochrome c, leading to

the activation of the caspase cascade.^[52] From the present study, it is clear that the Ugi EML BLUE could disrupt the functions of mitochondria at the early stages of apoptosis.

3.2.2.4 Cell cycle analysis

For understanding the cell death mechanism, the Ugi EML BLUE was investigated for its effect on cell cycle and induction of apoptosis in HeLa cells by flow cytometry. The proliferation may track from disturbing the cell cycle and to test the hypothesis, cell cycle analysis was conducted after 12 hrs exposure of the HeLa cells to the Ugi EML BLUE and the dyes under their respective IC₂₅ and IC₅₀ concentrations.

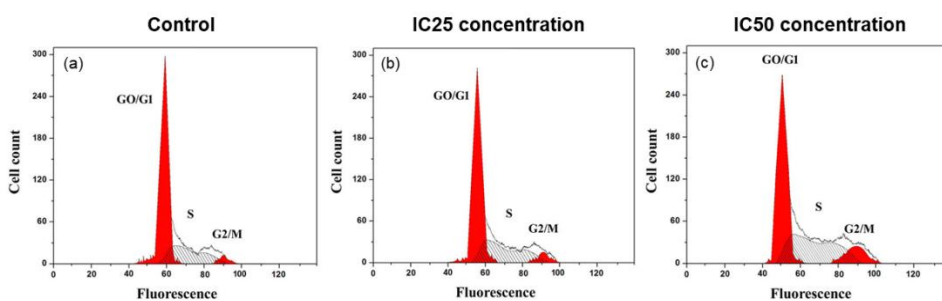


Figure 10. Cell cycle analysis of Ugi EML BLUE-treated HeLa cells by PI flow cytometry: a) Normal cell phase distribution observed in control group (untreated), b) Mild accumulation of cells in G₂/M phase was observed in HeLa cells treated with Ugi EML BLUE at its IC₂₅ (0.25 µg/mL), c) Significant accumulation of cells in G₂/M phase was observed in HeLa cells treated with Ugi EML BLUE at its IC₅₀ (0.5 µg/mL).

A normal cell phase distribution was observed in the untreated control cells (Figure 10a), whereas a dose dependent incrementing accumulation of the cells at G₂ phase of the cell cycle was observed in the HeLa cells treated with Ugi EML BLUE at its IC₂₅ and IC₅₀ concentrations (Figure 10b,c). At the same time, no such significant changes were observed in

the S phase cell distribution. The accumulation of cells at G2/M phase accompanied by the respective cell cycle arrests will serve as evidence for the CDK2 inhibition activity of Ugi EML BLUE, by means of the requirements of the CDK2 for the G1-S and G2/M phase transitions.^[53,54] This confirms that the Ugi EML BLUE could induce significant growth inhibition of HeLa cells through the induction of G2/M phase cell cycle arrest. The protein level of CDK2 was significantly elevated, whereas, the kinase activities of CDK2 were inhibited simultaneously in the Ugi EML BLUE treated cells (which was confirmed from Western blot analysis). From these results, it is clear that Ugi EML BLUE could arrest the cell cycle at G2/M checkpoint that controlled the progression of cells from G2 to M phase. The G2/M is the “DNA damage checkpoint” which evaluates the DNA content to detect the damages if any before permitting the cell to mitotic phase. Here the Ugi EML BLUE could induce damages to the DNA that leads to the G2/M cell cycle arrest in the HeLa cells to ensure its apoptosis.

3.2.2.5 Western Blot analysis and mechanisms

The western blot analysis was also performed to verify the expression of CDK2 protein in the HeLa cells treated with Ugi EML BLUE (Figure 11) using beta-actin as standard. In this study, we observed that the CDK2 expression was significantly enriched in control cells whereas the protein levels of CDK2 were significantly down-regulated in Ugi EML BLUE treated cells. All these findings serve well as evidence for the CDK2 down-regulation protocol behind the observed cell apoptosis with Ugi EML BLUE.

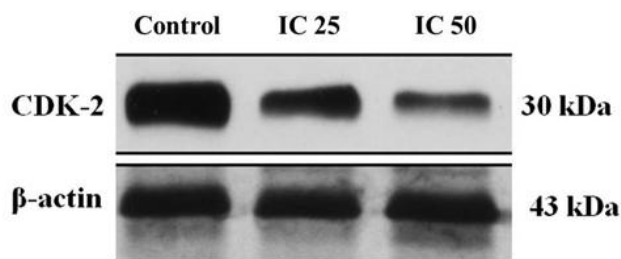


Figure 11. Western blot analysis for the CDK2 expressions in HeLa cells treated with Ugi EML BLUE at its IC50 and IC25 concentrations.

Moreover, the comparative study between the Ugi EML BLUE-CDK2 and ATP-CDK2 (PDB ID 1HCK) binding interactions were carried out to find out the location where Ugi EML BLUE is binding with CDK2. From the binding interaction studies (described before) we have obtained a strong hydrophobic interactions between the Ugi EML BLUE and the amino acid residues GLY 11 (Glycine), ILE 10 (Isoleucine), VAL 16, VAL 64 (Valine), ALA 144, ALA 31 (Alanine), LEU 134, LEU 83 (Leucine), PHE 80, PHE 82 (Phenylalanine), ASP 86, ASP 145 (Aspartic acid), ASN 132 (Asparagine) and GLN 131 (Glutamine). Among them, the ILE 10, ALA 144, ASP 145, ASP 86, ASN 132, GLN 131 are the hinge residues where ATP usually binds within CDK2 (Figure 12).^[55,56] This implies the potential of Ugi EML BLUE to interact with the ATP binding sites of the CDK2. One of the major functions of activated CDK2 is to transfer the phosphate groups from its bound ATP to the Serine and Threonine residues of the target substrates involved in DNA transcription and replication initiated in the G1 cell cycle phase.^[57]

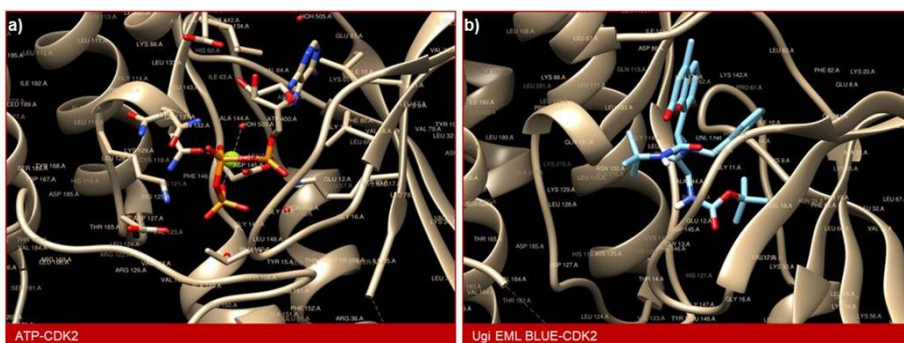


Figure 12. Comparison between the binding sites of ATP and Ugi EML BLUE in CDK2: a) ATP bound to the active site of CDK2, where the hinge residues are ILE 10, ALA 144, ASP 145, ASP 86, ASN 132 and GLN 131. b) Ugi EML BLUE bound to the active site of CDK2, where the hinge residues are GLY 11, ILE 10, VAL 16, VAL 64, ALA 144, ALA 31, LEU 134, LEU 83, PHE 80, PHE 82, ASP 86, ASP 145, ASN 132 and GLN 131.

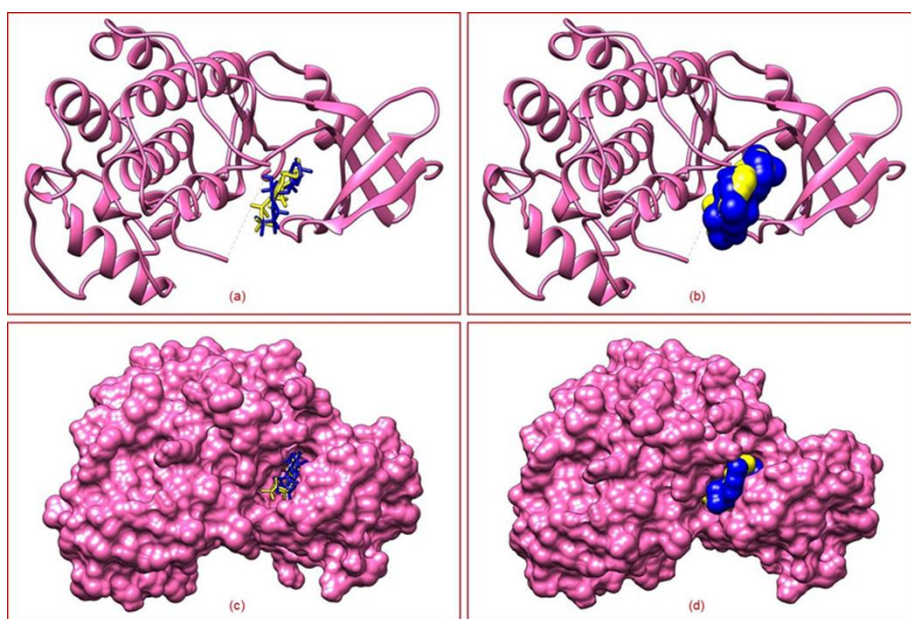


Figure 13. The hindrance effect around the ATP by the ligand Ugi EML BLUE at the ATP binding site of CDK2: (a) Superimposed structure of ATP (Yellow colored) and Ugi EML BLUE (Blue colored) in the active site. (b) Showing the dominating surface of Ugi EML BLUE over the surface of ATP in the active site. (c) ATP and Ugi EML BLUE in the hydrophobic pocket of CDK2. (d) Showing the dominating surface of Ugi EML BLUE over the ATP surface from the hydrophobic pocket.

However, the binding of Ugi EML BLUE to the active site of CDK2 creates a hindrance effect around the ATP or hide it from the vicinity of the target substrates as shown in Figure 13. This means that, due to the hindrance effect generated by Ugi EML BLUE around the ATP, the target substrates can't access the ATP even after the complete activation of CDK2 by the Cyclin E and CDK2 activating Kinase (CAK). This will lead to the breakdown of phosphate transfer from CDK2 to the target substrates involved in DNA replication and thereby leading to the unsuccessful DNA replication. Thus the prevention of replication causes the damaging of DNA which leads to the G2/M cell cycle arrest. Hence the Ugi EML BLUE can effectively interrupt the functioning of the CDK2 by preventing the phosphate transfer and down-regulates its activity in the eukaryotic cells. The results obtained from the cell cycle analysis and Western blot analysis are well in agreement with this CDK2 down regulation mechanism. The observed biological properties of the molecule are summarized in Table 1.

Compound name	Ugi EML BLUE
Solubility	DMSO, Ethanol, Ethanol-Water
Studied cell line	Human Cervical Cancer (HeLa)
Targeting protein	CDK2
IC50	0.5 µg/mL
Plausible inhibition mechanism	Perturbing the target phosphorylation from active CDK2

Table 1. Properties of Ugi EML BLUE

3.3 Conclusions

In short, we have demonstrated the use of Ugi EML BLUE for the imaging and inhibition of CDK2 present in cervical cancer cell line HeLa. The probe-cum-drug was obtained in a two-step process in which the second step is based on a multicomponent coupling strategy which is a typical example of green synthesis. The docking studies and the biological activity evaluation of Ugi EML BLUE against the human cervical cancer cell line (HeLa cell) revealed the potential of this new probe for bioimaging as well the CDK2 targeted antineoplastic applications in HeLa cells. The main advantage of this dual functionality is, it can locate the tumor cells, visualize the morphology and at the same time, it can control the cell proliferation through a CDK2 down regulation protocol accompanied by the G2 to M cell cycle arrest. This will enable the therapy without any cell washing process to remove the imaging agent. The overall properties of the probe are superior to some of the commercially available probes belongs to Alexa Fluor family. The observed drug properties can be optimized by systematic structure-activity studies to bring out its potential for imaging and inhibition of a variety of other cancer cell lines. The success of such studies will make an impact on the development of cost effective cancer therapeutics.

3.4 Experimental Section

3.4.1 Materials and Methods

The human cervical cancer cell line (HeLa) and human primary cervical cell line (H8) were procured from National Center for Cell Science (NCCS, Pune), 3-(4,5-dimethylthiazolyl-2)-2,5-

diphenyltetrazolium bromide (MTT), was purchased from Sigma-Aldrich (Bangalore, India). Analytical grade reagents were purchased from Sigma-Aldrich (Bangalore, India). All the samples were prepared in Milli-Q water.

3.4.1.1 Cell culture

Cervical cancer (HeLa) cells were procured from the National Center for Cell Sciences (NCCS), Pune, India. The cancer cells were maintained in Dulbecco's modified eagles medium (DMEM) supplemented with 2mM l-glutamine and balanced salt solution (BSS) adjusted to contain 1.5 g/L Na₂CO₃, 0.1 mM nonessential amino acids, 1 mM sodium pyruvate, 2 mM l-glutamine, 1.5 g/L glucose, 10 mM (4-(2-hydroxyethyl)-1-piperazineethane sulfonic acid) (HEPES) and 10% fetal bovine serum (GIBCO, USA). Penicillin and streptomycin (100 IU/100µg) were adjusted to 1mL/L. The cells were maintained at 37°C with 5% CO₂ in a humidified CO₂ incubator.

3.4.1.2 Evaluation of cytotoxicity against cervical cancer (HeLa) cells

The inhibitory concentration (IC₅₀) value was evaluated using an MTT [3-(4,5- dimethylthiazol-2-yl)-2,5-diphenyltetrazolium bromide] assay. Cancer cells were grown (1×10⁴cells/well) in a 96-well plate for 48 h into 75% confluence. The medium was replaced with fresh medium containing serially diluted synthesized compound (0.125µg/mL, 0.5µg/mL, 1µg/mL, 2 µg/mL, 4 µg/mL, 8 µg/mL prepared in the PBS (pH 7.4) with 1% DMSO (10µL/sample)) and the cells were further incubated for 48 h. The culture medium was removed, and 100µL of the MTT [3-(4,5-dimethylthiozol-2-yl)-3,5-diphenyl tetrazolium bromide] (Hi-Media)

solution was added to each well and incubated at 37°C for 4 h. After removal of the supernatant, 50 µL of DMSO was added to each of the wells and incubated for 10 min to solubilize the formazan crystals. The optical density was measured at 620 nm in an ELISA multi-well plate reader (Thermo Multiskan EX, USA). The OD value was used to calculate the percentage of viability using the following formula.

$$\% \text{ of cell viability} = \frac{\text{OD value of experimental sample}}{\text{OD value of experimental control}} \times 100$$

3.4.1.3 Evaluation of cytotoxicity against primary cervical (H8) cells

The effect of Ugi EML BLUE on the primary cervical (H8) cells was evaluated using an MTT [3-(4,5-dimethylthiazol-2-yl)-2,5-diphenyltetrazolium bromide] assay. The cells were grown (1×10^4 cells/well) in a 96-well plate for 48 h into 75% confluence. The medium was replaced with fresh medium containing serially diluted synthesized compound (0.125 µg/mL, 0.5 µg/mL, 1 µg/mL, 2 µg/mL, 4 µg/mL, 8 µg/mL prepared in the PBS (pH 7.4) with 1% DMSO (10 µL/sample)) and the cells were further incubated for 48 h. The culture medium was removed, and 100 µL of the MTT [3-(4,5-dimethylthiozol-2-yl)-3,5-diphenyl tetrazolium bromide] (Hi-Media) solution was added to each well and incubated at 37°C for 4 h. After removal of the supernatant, 50 µL of DMSO was added to each of the wells and incubated for 10 min to solubilize the formazan crystals. The optical density was measured at 620 nm in an ELISA multi-well plate reader (Thermo Multiskan EX, USA). The OD value was used to calculate the percentage of viability using the following formula.

$$\% \text{ of cell viability} = \frac{\text{OD value of experimental sample}}{\text{OD value of experimental control}} \times 100$$

3.4.1.4 Cell cycle analysis

HeLa cells (1×10^5) were seeded in a 6-well plate. After 24 hrs incubation at 37°C (5% CO₂), the medium was changed with fresh, supplemented or not (control) with the compound. After 24 hrs incubation, cells were harvested with trypsin, washed by PBS, fixed in 70% ethanol and stored at -20°C for 1h. The cellular nuclear DNA was stained by propidium iodide (PI) as described, briefly, followed by removing the ethanol, washed with PBS, the cells were suspended in 0.5 ml PBS containing 50 µg/ml PI and 100 µg/ml RNase and incubated at 37°C for 30 min. Flow cytometry was performed in duplicate with a BD FACS flow cytometer. From each sample, 10,000 events were collected and fluorescent signal intensity was recorded and analyzed by CellQuest and Modifit.

3.4.1.5 Rhodamine 123 Staining

Rhodamine 123 is a fluorescent dye that binds to metabolically active mitochondria. HeLa cells were treated with the Ugi EML BLUE for 24 h. The cells were washed with PBS (pH 7.4) and fixed with ice-cold 70% ethanol and incubated with 5 µg/mL Rhodamine 123 at 37°C for 30 min. The cells were then washed with PBS and examined under Nikon Eclipse fluorescence microscope (Nikon Instruments Inc., NY, USA).

3.4.1.6 Western Blot Analysis

Western blotting was performed to detect the proteins of CDK2. The HeLa cells (1×10^6) were seeded onto 100-mm culture dishes in the presence or absence of Ugi EML BLUE were treated for 48 h. Cells were then washed twice with ice-cold PBS and incubated in lysis buffer. The lysates were centrifuged at $10,000 \times g$ for 5 min at 4°C and were used as the cell protein extracts. Each of the extracts was applied to 12% SDS polyacrylamide gel electrophoresis after which the proteins were transferred onto a nitrocellulose membrane, and then blocked for 1 h using 10% skim milk in water. After washing in a PBS containing 0.1% Tween 20 for 3 times, the primary antibodies were added at a v/v ratio of 1:1000. After overnight incubation at 4°C , the primary antibodies were washed away and the secondary antibodies were added for 1 h incubation at room temperature. Finally, the enhanced chemiluminescence detection reagents were used to develop the signal of the membrane.

3.4.1.7 Bioimaging

HeLa cells were grown in 48-well culture plates at 3×10^4 cells/well or in a 35 mm confocal microscope dish with 5×10^4 cells. 0.25 $\mu\text{g}/\text{mL}$ and 0.5 $\mu\text{g}/\text{mL}$ Ugi EML BLUE solutions (PBS (pH 7.4) with 1% DMSO) were transplanted into the wells after removed culture medium and washed with PBS buffer solutions. The cells were detached by incubation with EDTA trypsin after 24 h incubation at 37°C , washed with PBS twice times, and collected by centrifugation. Then, HeLa cells were co-cultured in wells within coverslips for multiple cell passages. HeLa cells were trypsinized, suspended at appropriate intervals. Then, 4% of

paraformaldehyde was used to fix the cells for 15 min. The CLSM images of the stained cells were obtained from general imaging by an inverted Olympus BX51 fluorescence microscope and an OLYMPUS FV 1000 confocal fluorescence microscope for detailed imaging.

3.4.1.8 Docking Analysis

CDK2-Ugi EML BLUE:

The Docking studies were performed using the software AutoDock Tools (ADT) 1.5.6 and AutoDock Vina 1.1.2. The crystal structure of human CDK2 in complex with 3-hydroxychromones (PDB ID: 2DUV) was taken from the RCSB Protein Data Bank (PDB, <http://www.rcsb.org/pdb>). The 3-hydroxychromone and all water molecules were removed from the structure and added the polar hydrogen atoms. Assign the atoms as AD4 type and choose the computer gesture charges for the molecule. To assign the docking site, all maps were calculated with 1 Å spacing between grid points and the Gridbox coordinates are center $x=27.189$, $y=28.347$, $z=27.122$ and size $x=16$, $y=14$, $z=12$. The configuration file was created using these values with exhaustiveness 8 and finally saved the protein in the 'PDBQT' format. The three-dimensional structure of the compound Ugi EML BLUE was prepared by using the software GaussView and Gaussian 09. The proper torsions were assigned and saved in the PDBQT format using AutoDock Tools. Executed the docking with the command prompt using the configuration file and the results were split using the vina-split. The obtained results were analyzed using the AutoDock Tools and UCSF Chimera.

References

- [1] Weissleder, R. *Science* **2006**, *312*, 1168-1171.
- [2] Weissleder, R.; Pittet, M. J. *Nature* **2008**, *452*, 580–589.
- [3] Jaffer, F. A.; Weissleder, R. *J. Am. Med. Assoc.* **2005**, *293*, 855-862.
- [4] Fernández-Suárez, M.; Ting, A. Y. *Nat. Rev. Mol. Cell Biol.* **2008**, *9*, 929–943.
- [5] Juweid, M. E.; Cheson, B. D. *N. Engl. J. Med.* **2006**, *354*, 496-507.
- [6] Weissleder, R. *Nat. Rev. Cancer* **2002**, *2*, 11.
- [7] Morgan, D. O. *Nature* **1995**, *374*, 131–134.
- [8] Norbury, C.; Nurse, P. *Annu. Rev. Biochem.* **1992**, *61*, 441-470.
- [9] Yuan, L.; Lin, W.; Zheng, K.; Zhu, S. *Acc. Chem. Res.* **2013**, *46*, 1462-1473.
- [10] Srikun, D.; Miller, E. W.; Domaille, D. W.; Chang, C. J. *J. Am. Chem. Soc.* **2008**, *130*, 4596-4597.
- [11] Chan, J.; Dodani, S.C.; Chang, C. J. *Nat. Chem.* **2012**, *4*, 973-984.
- [12] Cheng, X.; Tang, R.; Jia, H.; Feng, J.; Qin, J.; Li, Z. *Appl. Mater. Interfaces* **2012**, *4*, 4387–4392.
- [13] Zhang, C.; Wei, L.; Wei, C.; Zhang, J.; Wang, R.; Xi, Z.; Yi, L. *Chem. Commun.* **2015**, *51*, 7505-7508.
- [14] Yuan, L.; Lin, W.; Song, J.; Yang, Y. *Chem. Commun.* **2011**, *47*, 12691-12693.
- [15] Zhang, L. J.; Wang, Z. Y.; Liua, J. T.; Miaob, J. Y.; Zhaoa, B. X. *Sens. Actuators B* **2017**, *253*, 19-26.
- [16] Georgiev, N. I.; Dimitrova, M. D.; Todorova, Y. D.; Bojinov, V. B. *Dyes Pigm.* **2016**, *131*, 9-17.
- [17] Zhang, D.; Chen, W.; Miao, Z.; Ye, Y.; Zhao, Y.; King, S. B.; Xian, M. *Chem. Commun.* **2014**, *50*, 4806-4809.

- [18] Panchuk–Voloshina, N.; Haugland, R. P.; Bishop–Stewart, J.; Bhalgat, M. K.; Millard, P. J.; Mao, F.; Leung, W. Y.; Haugland, R. P. *J. Histochem. Cytochem.* **1999**, *47*, 1179–1188.
- [19] Puthumana, S. S. E.; Damodaran, B. *ChemistrySelect* **2018**, *3*, 2951-2957.
- [20] Ghosh, A. K.; Brindisi, M. *J. Med. Chem.* **2015**, *58*, 2895–2940.
- [21] Kraljevic, T. G.; Harej, A.; Sedic, M.; Pavelic, S. K.; Stepanic, V.; Drenjancevic, D.; Talapko, J.; Raic-Malic, S. *Eur. J. Med. Chem.* **2016**, *124*, 794-808.
- [22] Emami, S.; Dadashpour, S. *Eur. J. Med. Chem.* **2015**, *102*, 611-630.
- [23] Thakur, A.; Singla, R.; Jaitak, V. *Eur. J. Med. Chem.* **2015**, *101*, 476-495.
- [24] Abdizadeh, T.; Kalani, M. R.; Abnous, K.; Tayarani-Najaran, Z.; Khashyarmanesh, B. Z.; Abdizadeh, R.; Ghodsi, R.; Hadizadeh, F. *Eur. J. Med. Chem.* **2017**, *132*, 42-62.
- [25] Basanagouda, M.; Jambagi, V. B.; Barigheid, N. N.; Laxmeshwar, S. S.; Devaru, V.; Narayanachar *Eur. J. Med. Chem.* **2014**, *74*, 225-233.
- [26] Ong, E. B. B.; Watanabe, N.; Saito, A.; Futamura, Y.; Galil, K. H. A.; Koito, A.; Najimudin, N.; Osada, H. *J. Biol. Chem.* **2011**, *286*, 14049 – 14056.
- [27] Choi, S. B.; Choong, Y. S.; Saito, A.; Wahab, H. A.; Najimudin, N.; Watanabe, N.; Osada, H.; Ong, E. B. B. *Mol. Inf.* **2014**, *33*, 742 – 748.
- [28] Hossain, S. M.; Singh, K.; Lakma, A.; Pradhan, R. N.; Singh, A. K. *Sens. Actuators, B*, **2017**, *239*, 1109-1117.
- [29] Mani, K. S.; Rajamanikandan, R.; Murugesapandian, B.; Shankar, R.; Sivaraman, G.; Ilanchelian, M.; Rajendran, S. P. *Spectrochim. Acta, Part A*, **2019**, *214*, 170-176.
- [30] Nasr, T.; Bondock, S.; Youns, M. *Eur. J. Med. Chem.* **2014**, *76*, 539–548.
- [31] Ueno, T.; Nagano, T. *Nat. Methods* **2011**, *8*, 642-645.

- [32] Rai, A.; Singh, A. K.; Tripathi, K.; Sonkar, A. K.; Chauhan, B. S.; Srikrishna, S.; James, T. D.; Mishra, L. *Sens. Actuators, B*, **2018**, *266*, 95-105.
- [33] Xia, S.; Wang, J.; Bi, J.; Wang, X.; Fang, M.; Phillips, T.; May, A.; Conner, N.; Tanasova, M.; Luo, F. T.; Liu, H. *Sens. Actuators, B*, **2018**, *265*, 699-708.
- [34] Li, S.; Zhang, D.; Xie, X.; Ma, S.; Liu, Y.; Xu, Z.; Gao, Y.; and Ye, Y. *Sens. Actuators, B*, **2016**, *224*, 661-667.
- [35] Wang, L.; Li, W.; Zhi, W.; Ye, D.; Wang, Y.; Ni, L.; Bao, X. *Dyes Pigm.* **2017**, *147*, 357-363.
- [36] Wang, L.; Li, W.; Zhi, W.; Huang, Y.; Han, J.; Wang, Y.; Ren, Y.; Ni, L. *Sens. Actuators, B*, **2018**, *260*, 243-254.
- [37] Kang, Y. F.; Qiao, H. X.; Meng, Y. L.; Cui, S. J.; Han, Y. J.; Wu, Z. Y.; Wu, J.; Jia, X. H.; Zhang, X. L.; Dai, M. Y. *RSC Adv.* **2016**, *6*, 94866-94869.
- [38] Zhang, B.; Yang, X.; Zhang, R.; Liu, Y.; Ren, X.; Xian, M.; Ye, Y.; Zhao, Y. *Anal. Chem.* **2017**, *89*, 10384-10390.
- [39] Trott, O.; Olson, A. J. *J. Comput. Chem.* **2010**, *31*, 455-461.
- [40] Evan, G.I.; Vousden, K. H. *Nature* **2001**, *411*, 342-348.
- [41] Hartwell, L. H.; Kastan, M. B. *Science* **1994**, *266*, 1821-1828.
- [42] Vermeulen, K.; Bockstaele, D. R. V.; Berneman, Z. N. *Cell Prolif.* **2003**, *36*, 131-149.
- [43] Neganova, I.; Zhang, X.; Atkinson, S.; Lako, M. *Oncogene*, **2009**, *28*, 20-30.
- [44] Lapenna, S.; Giordano, A. *Nat. Rev. Drug Discov.* **2009**, *8*, 547-566.
- [45] Lee, J.; Park, T.; Jeong, S.; Kim, K. H.; Hong, C. *Bioorg. Med. Chem. Lett.* **2007**, *17*, 1284-1287.
- [46] Young, T.; Abel, R.; Kim, B.; Berne, B. J.; Friesner, R. A. *Proc. Natl. Acad. Sci. U. S. A.* **2007**, *104*, 808-813.
- [47] Snyder, P. W.; Mecinovic, J.; Moustakas, D. T.; Thomas III, S. W.; Harder, M.; Mack, E. T.; Lockett, M. R.; Heroux, A.; Sherman, W.;

- Whitesides, G. M. *Proc. Natl. Acad. Sci. U. S. A.* **2011**, *108*, 17889-17894.
- [48] Brown, N. R.; Korolchuk, S.; Martin, M. P.; Stanley, W. A.; Moukhametzianov, R.; Noble, M. E. M.; Endicott, J. A. *Nat. Commun.* **2015**, *6*, 6769.
- [49] Beattie, J. F.; Breault, G. A.; Ellston, R. P. A.; Green, S.; Jewsbury, P. J.; Midgley, C. J.; Naven, R. T.; Minshull, C. A.; Pauptit, R. A.; Tucker, J. A.; Pease, J. E. *Bioorg. Med. Chem. Lett.* **2003**, *13*, 2955-2960.
- [50] Cho, Y. S.; Borland, M.; Brain, C.; Chen, C. H. T.; Cheng, H.; Chopra, R.; Chung, K.; Groarke, J.; He, G.; Hou, Y.; Kim, S.; Kovats, S.; Lu, Y.; Reilly, M. O.; Shen, J.; Smith, T.; Trakshel, G.; Vögtle, M.; Xu, M.; Xu, M.; Sung, M. J. *J. Med. Chem.* **2010**, *53*, 7938-7957.
- [51] Mary, T. A.; Shanthi, K.; Vimala, K.; Kannan, S. *RSC Adv.* **2016**, *6*, 22936-22949.
- [52] Thangam, R.; Senthilkumar, D.; Suresh, V.; Sathuvan, M.; Sivasubramanian, S.; Pazhanichamy, K.; Gorgun, P. K.; Kannan, S.; Gunasekaran, P.; Rengasamy, R.; Sivaraman, J. *J. Agric. Food Chem.* **2014**, *62*, 3410-3421.
- [53] Hu, B.; Mitra, J.; Heuvel, S. V. D.; Enders, G. H. *Mol. Cell. Biol.* **2001**, *21*, 2755-2766.
- [54] Furuno, N.; Elzen, N. D.; Pines, J. *J. Cell. Biol.* **1999**, *147*, 295-306.
- [55] Bondt, H. L. D.; Rosenblatt, J.; Jancarik, J.; Jones, H. D.; Morgan, D. O.; Kim, S. H. *Nature* **1993**, *363*, 595-602.
- [56] Arba, M.; Ihsan, S.; Ramadhan, L. O. A. N.; Tjahjono, D. H. *Comput. Biol. Chem.* **2017**, *67*, 9-14.
- [57] Malumbres, M.; Barbacid, M. *Nat. Rev. Cancer* **2001**, *1*, 222-231.

Supporting Information

CDK1-Ugi EML BLUE:

The docking procedure is same as given in the experimental section. The receptor is CDK1 (PDB ID: 4Y72) and the ligand is Ugi EML BLUE. The Gridbox coordinates were set up accordingly. The obtained binding affinity is -1.3 kcal.

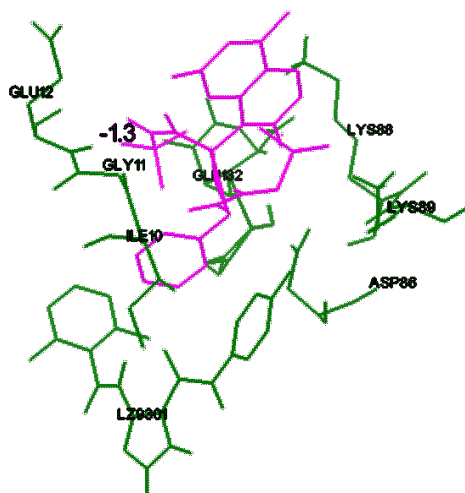


Figure 14. Ugi EML BLUE (Pink colored) in the active site of CDK1 (Green colored)

CDK4-Ugi EML BLUE:

The docking procedure is same as given in the experimental section. The receptor is CDK4 (PDB ID: 1H00) and the ligand is Ugi EML BLUE. The Gridbox coordinates were set up accordingly. The obtained binding affinity is -0.8 kcal.

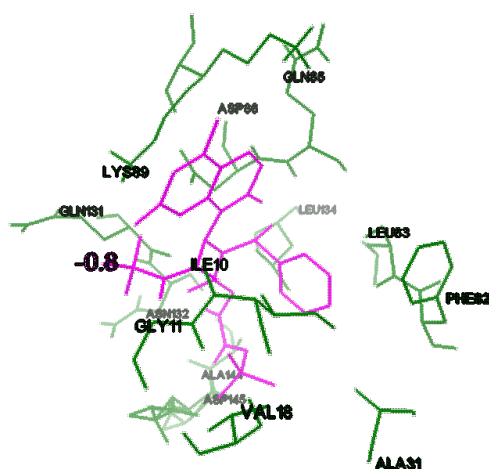


Figure 15. Ugi EML BLUE (Pink colored) in the active site of CDK4 (Green colored)

CDK6-Ugi EML BLUE:

The docking procedure is same as given in the experimental section. The receptor is CDK6 (PDB ID: 3NUP) and the ligand is Ugi EML BLUE. The Gridbox coordinates were set up accordingly. The obtained binding affinity is +5.0 kcal.

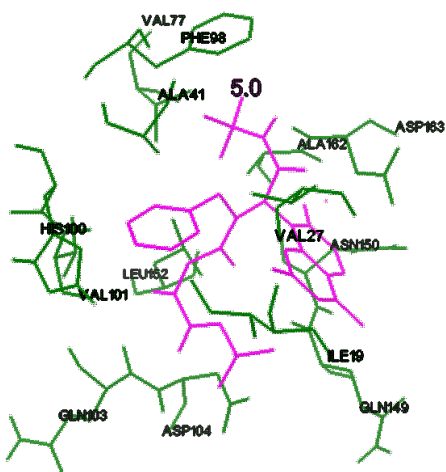


Figure 16. Ugi EML BLUE (Pink colored) in the active site of CDK6 (Green colored)

CHAPTER 4

**CHEMISTRY, CHEMICAL BIOLOGY AND
PHOTOPHYSICS OF CERTAIN NEW CHROMENE-
TRIAZOLE-COUMARIN TRIADS AS FLUORESCENT
INHIBITORS OF CDK2 AND CDK4 INDUCED CANCERS**

4.1 Introduction

In the earlier chapters, we have discussed the synthesis and medicinal chemistry applications of a coumarin based small molecule probe (Ugi EML BLUE) which shows the fluorescence imaging ability as well as the CDK2 targeted anticancer activities. As we concluded in chapter 3, the cost-effective cancer therapeutics, as well as cost-effective diagnostic or imaging agents, are highly desired in the fields of medicinal chemistry and drug discovery. Inspired by the promising results discussed in the previous chapters, we decided to continue our work on functionalizing the coumarin core with potentially privileged scaffolds such as chromene and triazole to obtain CDK inhibitors of various cancers. The Cyclin Dependent Kinases (CDKs) are the part of serine/threonine-protein kinase family with a significant role in modulating the various stages of the cell division cycle.^[1-3] It is widely accepted that the deregulation of CDKs causes its overexpression as well as chromosomal instability leading to various types of human cancers. Hence, CDKs are considered as one of the major targets in cancer therapy.^[4] Among the various CDKs, overexpressed CDK2 and its binding Cyclin partners have been observed in many tumors and some of these tumors are selectively sensitive to the inhibition of CDK2. Hence, in recent years CDK2 has emerged as a potential target in cancer therapy.^[5-8] Similarly, it is proved that CDK4 is also cooperatively involved along with CDK2 in promoting the G1 phase progression.^[9,10]

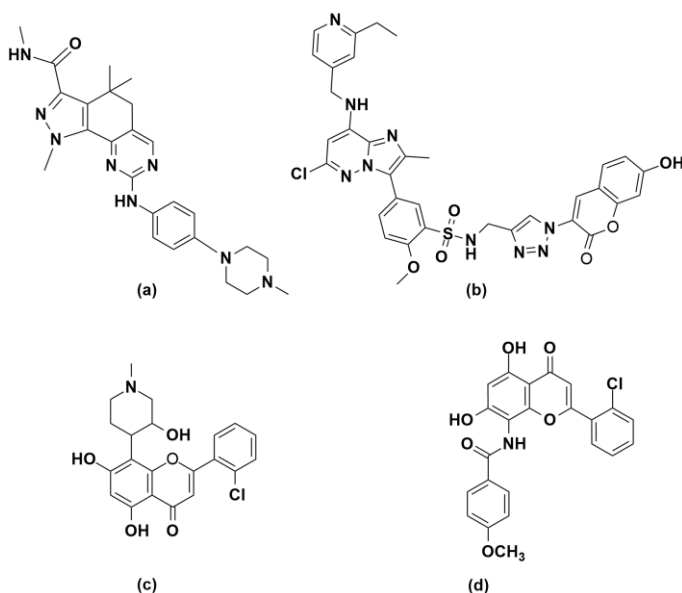


Figure 1. (a) Example for the small molecule CDK inhibitor under clinical trials (b) Example for the drug tagged with fluorescent dye (c)&(d) Example for the chromene based CDK inhibitor under clinical trials

Furthermore, overexpression of CDK4 has been observed in many tumors such as gliomas, sarcomas, lymphomas, melanomas, carcinomas of the breast and leukemias. This implies that CDK4 is also a key factor in promoting the initiation and development of tumors.^[11] Consequently, a large number of CDK inhibitors, particularly for CDK2 and CDK4 have been developed and many such small molecule inhibitors are under various phases of clinical trials and some are already in the market. Selected examples are presented in Figure 1.^[12-15]

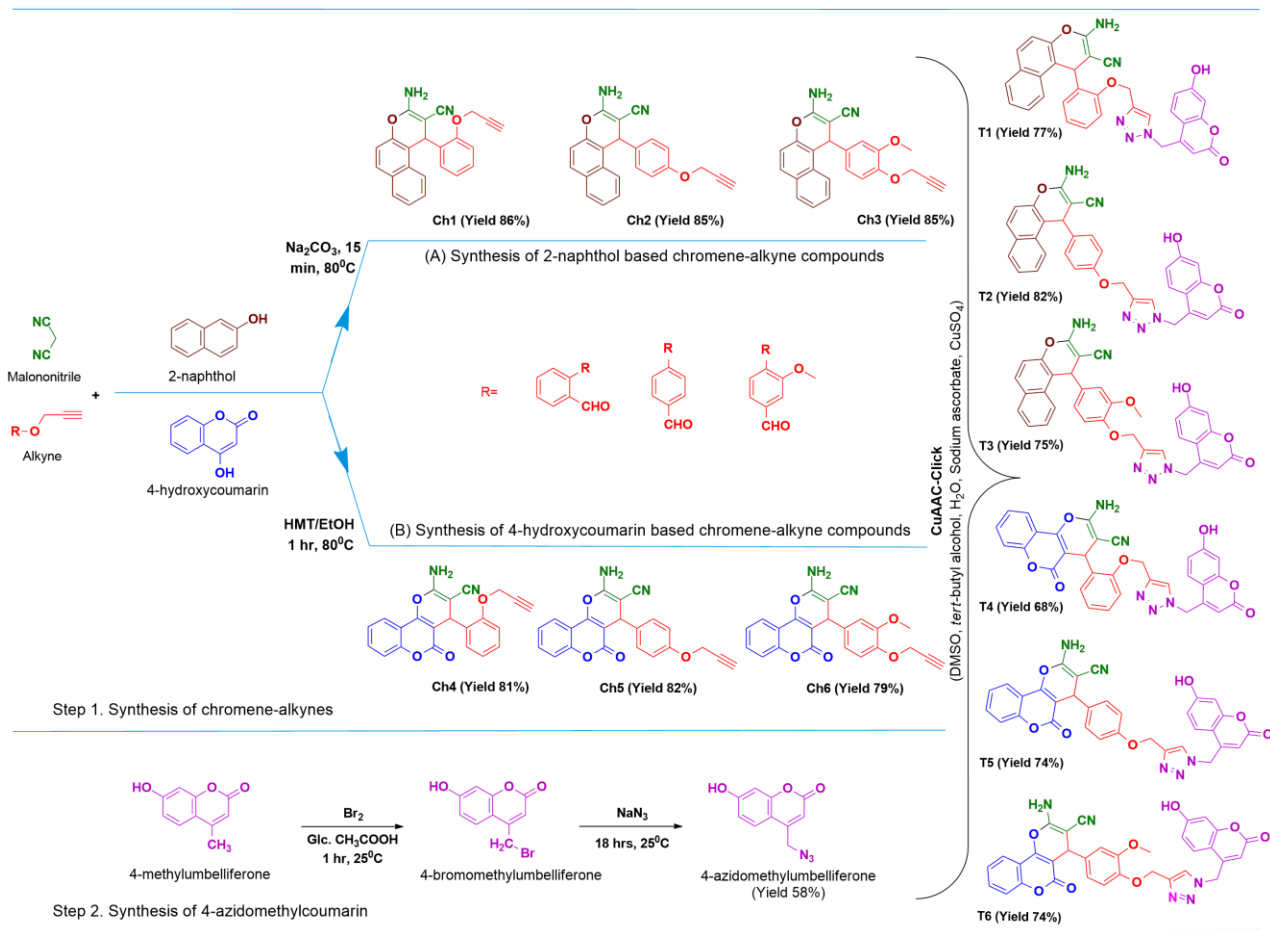
A recent trend in this field is the use of fluorescent inhibitors in which a drug tagged with a fluorescent dye has been used for monitoring the pathways involved in tumor inhibition.^[15] However, this method often retards the drug performance by affecting the selectivity, cell permeability and target binding properties due to the presence of an additional dye in the drug molecule which apparently doesn't have any significant

influence on these drug properties. An alternative strategy is the use of inherently fluorescent drug molecules for tracking and annihilation of the tumors.^[15] This method appears to be more interesting since it is based on the use of privileged scaffolds^[16-18] to construct the fluorescent drug core. However, the field is still in its infancy and a lot more to do in developing efficient and selective CDK inhibitors.

Since chromene is known for its CDK inhibition properties^[12,13] and coumarin is known for its photophysical (fluorescence) as well as biological properties,^[19-22] we decided to integrate a coumarin scaffold with various chromene moieties through a linker triazole to design fluorescent inhibitors of CDKs. We presumed that the three nitrogen atoms, as well as the two sp^2 carbon atoms on the triazole ring, could make the system electron rich and enable the electron transfer through it by acting as a bridge between the fragments to enhance the fluorescence. The synthesized molecules were then systematically investigated for their fluorescence and CDK inhibition properties on human cervical cancer cell lines (HeLa).

4.2 Results and Discussions

The overall chemistry is depicted in Scheme 1. Six alkyne derivatives of 2H-chromenes were synthesized through a solvent free multicomponent reaction (MCR) between coumarin or naphthalene with an alkyne functionalized aldehyde and malononitrile. This solvent free mechanochemical synthesis resulted in the formation of the desired chromene scaffolds in high yield and purity under simple solvent wash. The azide derivative was obtained by brominating the side chain of 4-methylumbelliferone followed by azide substitution.



Scheme 1. Synthesis of chromene-alkynes, coumarin-azide, and Chromene-Triazole-Coumarin Triads

This two-step synthesis also afforded the required material in moderate yield and high purity. The alkyne and the azide fragments were then assembled through copper catalyzed azide-alkyne (3+2) cycloaddition (CuAAC) under click chemistry conditions to obtain the Chromene-Triazole-Coumarin Triads **T1-T6**.

4.2.1 Evaluation of Fluorescence Properties

The fluorescence properties of the starting alkynes **Ch1-Ch6**, the coumarin azide, and the chromene-triazole-coumarin triads were analyzed by preparing a 50 ppm solution of each in DMSO. No characteristic fluorescence was observed for the starting alkynes and coumarin azide under UV exposure (Figure S1 in Suppo. Info.).

Sample Name	UV Abs (nm)	PL Ems (nm)	Stoke's shift (nm)	Quantum Yield (Φ)*
T1	326	442	116	0.95
T2	349	461	112	0.12
T3	370	465	95	0.08
T4	328	429	101	0.68
T5	331	410	79	0.72
T6	358	461	103	0.16

* with respect to the standard Quinine sulfate

Table 1 Fluorescence properties of Chromene-Triazole-Coumarin Triads, **T1** to **T6**

However, the triad molecules **T1**, **T4** and **T5** showed blue emissions under UV exposure as shown in Figure 2a (same under Daylight gave in Suppo. Info. Figure S2). The UV-Visible and emission spectra of the compounds **T1** to **T6** (50 ppm solution in DMSO) were measured and their quantum yields were also calculated by using quinine sulfate ($\Phi=0.54$) as standard.

Among **T1**, **T4**, and **T5**, the highest quantum yield was obtained from **T1**. Figure 3A shows the emission spectra of all the triads and Figure 3B-(a) shows the absorption and emission spectra of **T1**. (The same of **T4** and **T5** are given in Suppo. Info., Figure S3). The photophysical characterization data of all the triads are presented in Table 1.

We have then investigated the effect of pH on the fluorescence of these triads under UV exposure. For that, we prepared a 50 ppm solution of each with varying pH. The pH was regulated by adding K_2CO_3 and 1% HCl. The compounds which are non-fluorescent at neutral pH did not show any fluorescence at acidic pH as well as basic pH. We have also studied the effect of pH on the fluorescence of those compounds which are fluorescent at neutral pH. However, we have not observed any visible change in the fluorescence of these molecules with respect to changes in pH other than the observed quenching at acidic pH. A typical example of such study with triad **T1** at various pH (50 ppm solution in DMSO, under UV light) is presented in Figure 2b. In order to check whether there is any change in the absorption and emission maxima of these compounds with respect to changes in pH, we have plotted the absorption and emission spectra of **T1** at neutral pH (Figure 3B-(a), absorption maxima: 326 nm and emission maxima: 442 nm) and at pH 9.1.

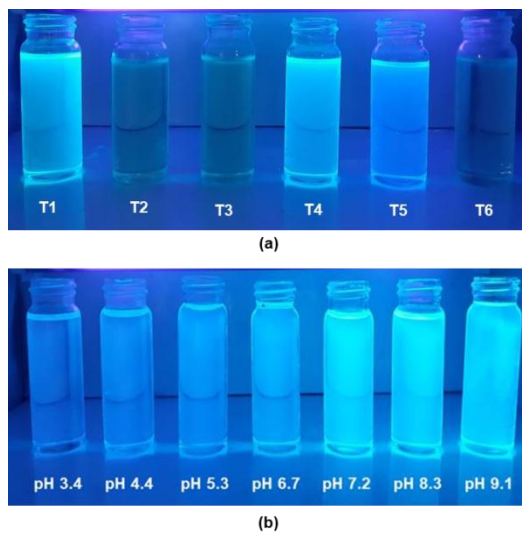


Figure 2. (a) Fluorescence of the samples **T1** to **T6** under UV-light (b) Fluorescence of compound **T1** at various pH under UV light

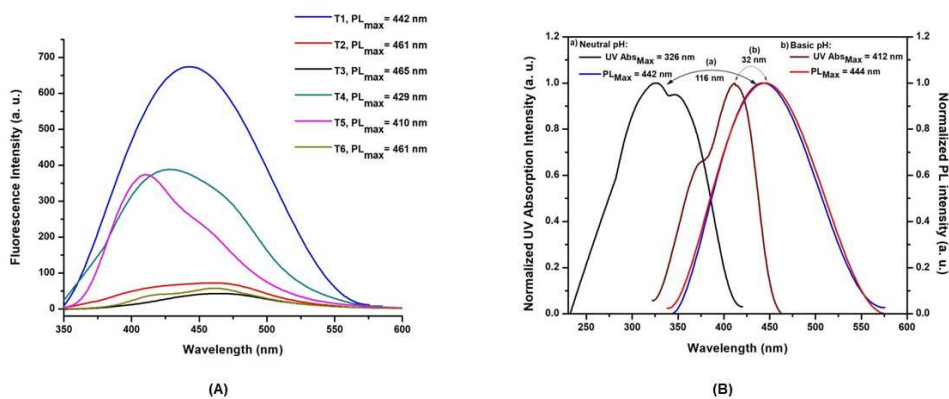


Figure 3. (A) Fluorescence spectra of **T1** to **T6** (50 p.p.m. solution in DMSO) (B) Normalized UV-PL spectra of (a) **T1** at neutral pH and (b) **T1** at pH 9.1

We have observed a significant redshift in the absorption maximum and slight red shift in the emission maximum of **T1** at alkaline pH (Figure 3B-(b); absorption maximum: 412 nm and emission maximum: 444 nm). This redshift is due to the presence of a free hydroxyl group on **T1**. At acidic pH, this hydroxyl group will get protonated and causes a decrease in the electron density in the moiety which leads to the quenching of fluorescence. However, at basic pH, the aforesaid hydroxyl group will get deprotonated and causes an increase in the electron density on the moiety which enables the easier electronic movements at lower energy leading to the redshift in the absorption spectra.^[23]

4.2.2 Fluorescence properties of the Chromene-Triazole-Coumarin triads in solid state

We have also studied the solid-state fluorescence of these compounds under UV exposure in solid state and also by plotting their solid state absorption and emission spectra. As shown in Figure 4, compound **T2**, **T3**, and **T6** showed fluorescence in the solid state which is absent in the solution state (All solid samples under UV/Day-light images are given in Suppo. Info. Figure S4). The normalized solid state UV-Vis and emission spectra of these three compounds were recorded as shown in Figure 5a.

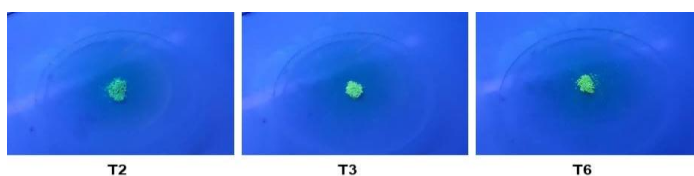


Figure 4. Solid state fluorescence of the Chromene-Triazole-Coumarin Triads **T2**, **T3**, and **T6** under UV-light

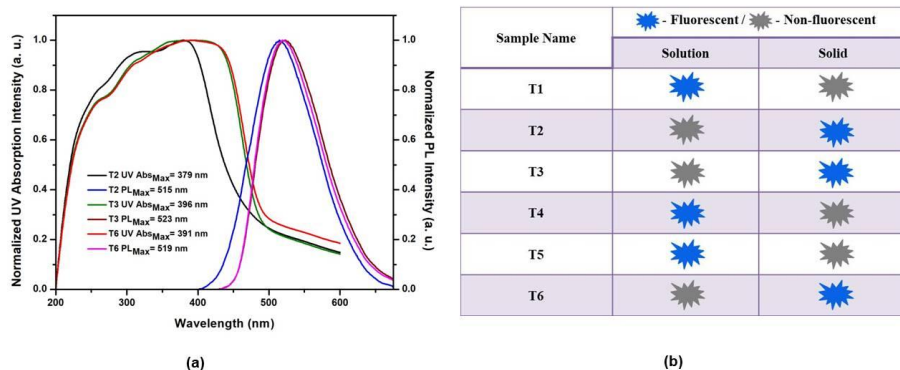


Figure 5. (a) Normalized solid state UV-PL spectra of **T2**, **T3** and **T6** (b) Summary of fluorescence observed for the Chromene-Triazole-Coumarin Triads **T1** to **T6**

We observed a considerable red shift in the absorption and emission spectra of these molecules justifying the emission color observed for these molecules under UV exposure.

From the fluorescence measurements in the solid state and solution state, the overall observation is that the compounds **T1**, **T4**, and **T5** show intense fluorescence in solution and it is quenched at the solid state. At the same time, strong solid state fluorescence is observed for the samples **T2**, **T3**, and **T6** which does not have fluorescence in solution state (Figure 5b).

For elucidating the mechanism behind the observed fluorescent properties, we decided to carry out the density functional theory (DFT) studies of these molecules.

4.2.3 DFT Studies and Fluorescence Mechanisms

We have obtained the ground state geometry (optimized structure), HOMO/LUMO orbital images and energies of **T1** to **T6** by

means of computational Density Functional Theory (DFT) using the GAUSSIAN 09 software with the basis set B3LYP/6-31G*.^[24] The DFT results obtained are then (Figure 6a-f) analyzed for drawing plausible mechanisms for the observed fluorescence properties of **T1-6**.

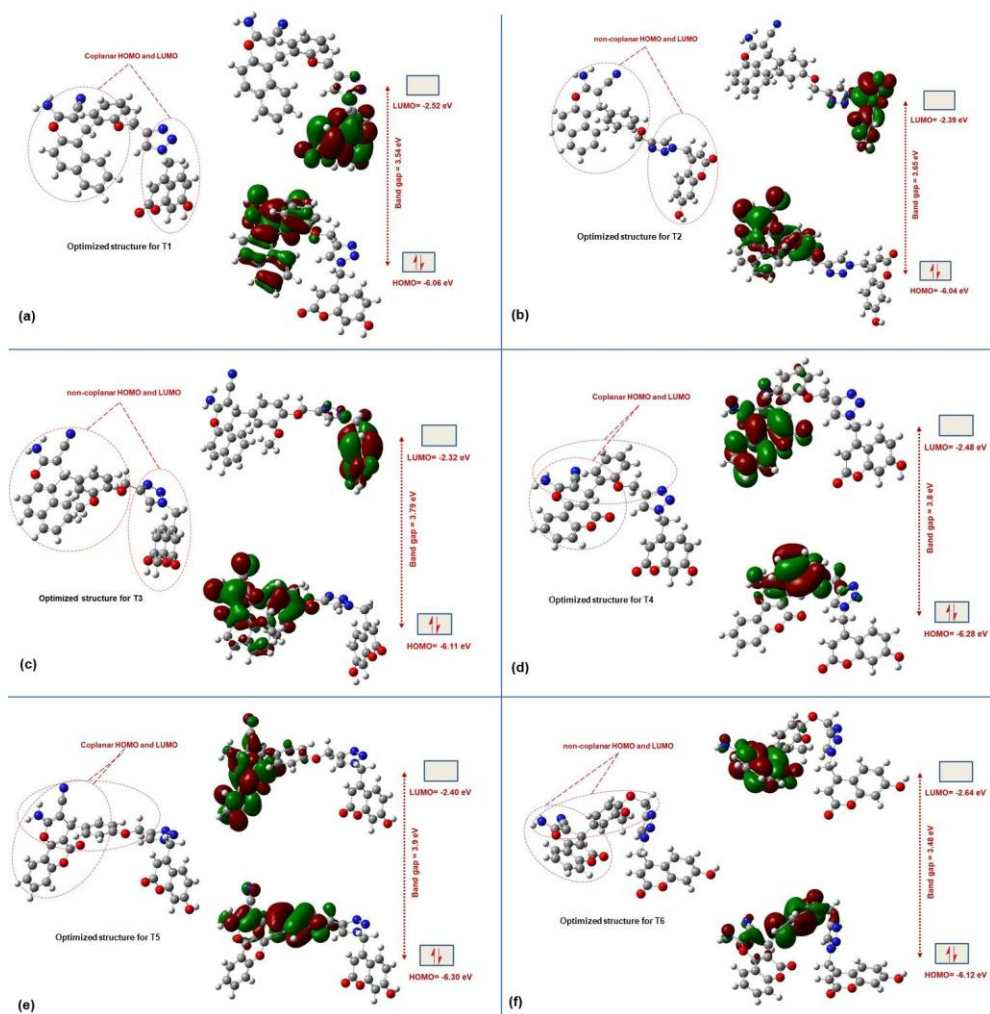


Figure 6. Optimized structure and HOMO/LUMO orbital images of Chromene-Triazole-Coumarin Triads (**T1** to **T6**) with their energies: (a) **T1** (b) **T2** (c) **T3** (d) **T4** (e) **T5** (f) **T6**

In **T1**, the HOMO orbitals comprised of the orbitals of chromene part, cyanide group, amino group, and oxy-benzene part whereas the LUMO comprised of the orbitals of coumarin and triazole rings (Figure 6a). Among these, the chromene, triazole and coumarin rings (HOMO/LUMO) are in the same plane (coplanar) to facilitate an ICT type transition to make the compound highly fluorescent.^[25]

In **T2** and **T3**, the orbitals of the chromene part, cyanide group, amino group, and oxy-benzene part combined to form the HOMO orbitals and the orbitals of coumarin and triazole combined to form the LUMO orbitals (Figure 6b and c). However, in their optimized structures, (Figure 6b and c), the chromene, triazole and coumarin rings (HOMO/LUMO) are not in coplanar state and which disables the easier electron transfer through ICT process. In compounds **T4** and **T5**, the HOMO orbitals include the orbitals of pyran moiety, cyanide group, amino group, and oxy-benzene part, whereas the LUMO orbitals include the orbitals of whole chromene part with the fused coumarin system, cyanide group and amino group (Figure 6d and e). The electronic transitions in these molecules have occurred only through one section of the molecule and the triazole-coumarin rings are not effectively participating in the same. This implies that there will only a mild ICT type transitions in these molecules. However, the optimized structure of **T4** and **T5** (Figure 6d and e) shows that their HOMO/LUMO orbitals are coplanar with each other to make easier electronic transitions. The mild ICT type transitions, as well as the coplanar orbital structures, make **T4** and **T5** fluorescent. In **T6**, the HOMO orbitals formed by the orbitals of pyran moiety, cyanide group, amino group, and oxy-benzene part and the LUMO orbitals formed by the

orbitals of whole chromene part with the fused coumarin system, cyanide group and amino group (Figure 6f). Here also the possibility of the mild ICT type transition exists.

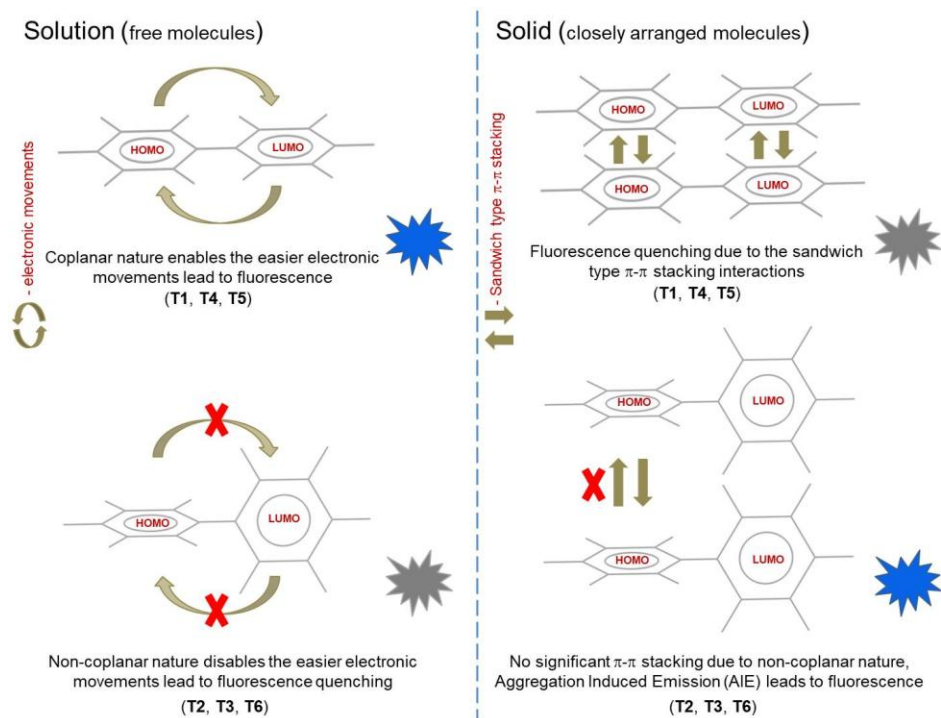


Figure 7. Plausible fluorescence mechanisms of the Chromene-Triazole-Coumarin Triads (T1 to T6)

However, due to its distorted and non-coplanar structural orientation (Figure 6f), an easier electronic transition is not feasible and which leads to fluorescence quenching in solution.

In T1, T4, and T5, the coplanar nature of the HOMO/LUMO orbitals permits very close molecular arrangements in the solid state. This leads to the quenching of fluorescence in solid state due to intermolecular

sandwich-type π - π stacking interactions.^[26] **T2**, **T3**, and **T6** have non-coplanar HOMO/LUMO orbitals and no significant π - π stacking.^[27] We assume that the solid state fluorescence observed for these samples could be due to the phenomenon of Aggregation Induced Emission (AIE).^[28-31] A plausible mechanism for the whole process is depicted in Figure 7.

4.2.4 Docking Studies of Chromene-Triazole-Coumarin Triads against CDKs

Having completed the photophysical characterization, we proceed to evaluate the anticancer properties of these molecules. Since CDKs are involved in the proliferation of various cancers, we decided to carry out a computational study on the docking properties of these molecules against major kinases such as CDK1, 2, 4 and 6 using the open-source software AutoDock Vina^[32] to estimate the binding affinities. The proteins PDB ID 4Y72 (CDK1),^[33] PDB ID 2DUV (CDK2),^[34] PDB ID 1H00 (CDK4)^[35] and PDB ID 3NUP (CDK6)^[36] were downloaded from protein data bank to carry out the docking studies with **T1-T6**. The binding affinity values obtained are presented in Table 2.

Sample Name	CDK1	CDK2	CDK4	CDK6
T1	+82.0 kcal	-6.3 kcal	-7.4 kcal	+23.9 kcal
T2	+113.1 kcal	-9.1 kcal	-9.6 kcal	+30.1 kcal
T3	+120.1 kcal	-9.4 kcal	-8.6 kcal	+37.7 kcal
T4	+106.9 kcal	-9.0 kcal	-8.3 kcal	+22.5 kcal
T5	+120.1 kcal	-10.5kcal	-9.4 kcal	+62.5 kcal
T6	+115.0 kcal	-9.0 kcal	-7.7 kcal	+35.4 kcal

Table 2. Binding affinities of Chromene-Triazole-Coumarin Triads **T1** to **T6** in the active site of CDK2 and CDK4

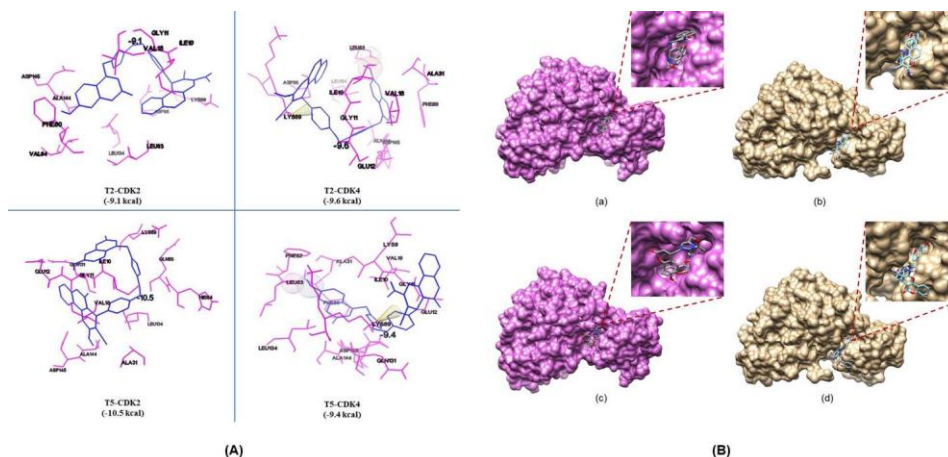


Figure 8. (A) Chromene-Triazole-Coumarin Triads **T2** and **T5** in the active site of CDK2 and CDK4 with their docking score (B) Chromene-Triazole-Coumarin Triads **T2** and **T5** encapsulated into the hydrophobic pockets of the CDK2 and CDK4: (a) **T2** with CDK2, (b) **T2** with CDK4, (c) **T5** with CDK2 and (d) **T5** with CDK4

The studies revealed that, in terms of binding affinity, the molecules are selective towards CDK2 and CDK4. Figure 8A shows the docking mode of **T2** and **T5** (these molecules showed highest binding affinity towards CDK2 and CDK4 (Table 2)) in the active site of CDK2 and CDK4 and the corresponding docking scores (same of the remaining triads are given in Suppo. Info. Figure S5). The compounds **T1** to **T6** have the binding affinities of -6.3 kcal, -9.1 kcal, -9.4 kcal, -9.0 kcal, -10.5 kcal and -9.0 kcal against CDK2, where the active site of CDK2 comprised of the amino acid residues such as GLY 11 (Glycine), ILE 10 (Isoleucine), VAL 16, VAL 64 (Valine), ALA 144, ALA 31 (Alanine), LEU 134, LEU 83 (Leucine), PHE 80, PHE 82 (Phenylalanine), ASP 86, ASP 145 (Aspartic acid), ASN 132 (Asparagine) and GLN 131 (Glutamine). Similarly, The compounds **T1** to **T6** have the binding affinities of -7.4 kcal, -9.6 kcal, -8.6 kcal, -8.3 kcal, -9.4 kcal and -7.7 kcal against CDK4, where the

active site of CDK4 comprised of the amino acid residues such as ILE 10 (Isoleucine), VAL 18 (Valine), GLY 11 (Glycine), LEU 83 (Leucine), GLU 12 (Glutamic acid), LYS 89 (Lysine), ALA 31 (Alanine), ASP 86 (Aspartic acid), PHE 80, PHE 82 (Phenylalanine). Most of these amino acids have hydrophobic side chains favorable for the formation of a tight ‘hydrophobic pocket’ in the kinase.^[37,38] The observed high binding energies for the triads were due to the strong hydrophobic interaction between the compounds and the target proteins. The bulky coumarin, triazole, chromene moieties present in triads also helps to encapsulate them into such hydrophobic pockets of the CDK2 and CDK4 (Figure 8B). Moreover, In the cases of CDK4, apart from hydrophobic interactions, there is a possibility of hydrogen bonding and π -cation interactions between the inhibitor molecule and the kinase to enhance the binding affinities (Figure 8a and Figure S5). The absence of significant binding affinity of the molecules towards CDK1 and CDK6 implies that the molecules are more selective towards CDK2 and CDK4. Since the molecules **T2** and **T5** showed highest binding affinity towards CDK2 and CDK4, these two molecules have been selected for *in vitro* screening against human cervical cancer cell line (HeLa).

4.2.5 Evaluation of *in vitro* cytotoxic activities of T2 and T5 against Human Cervical Cancer Cell line (HeLa)

The cytotoxic effects of the Chromene-Triazole-Coumarin Triads **T2** and **T5** were evaluated with the MTT Assay analysis. The cell cycle analysis and Western Blot analysis were performed to study their plausible apoptotic mechanisms. Figure 9 shows the *in vitro* cytotoxic activity of the compound **T2** (1.5, 3, 4.5, 6, 7.5, 9, 10.5 and 12 $\mu\text{g/mL}$

concentrations, in PBS (pH 7.4), 1% DMSO (10 μ L) and compound **T5** (1, 2, 3, 4, 5, 6, 7 and 8 μ g/mL concentrations, in PBS (pH 7.4), 1% DMSO (10 μ L) against the HeLa cells. As shown in Figure 9, molecules **T2** and **T5** exhibited dose-dependent cytotoxicity on HeLa cells. The IC₅₀ values of **T2** and **T5** against HeLa cells were calculated as 7.5 μ g/mL and 4 μ g/mL (in 48 hrs) respectively.

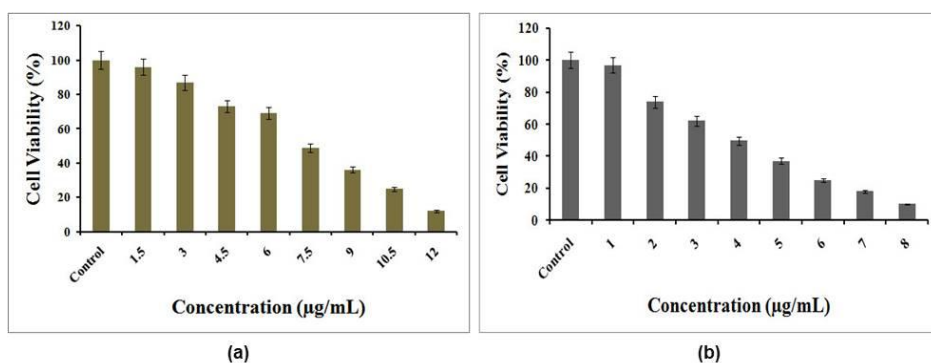


Figure 9. (a) *In vitro* cytotoxicity activity of the compound **T2** against HeLa cells (b) *In vitro* cytotoxicity activity of the compound **T5** against HeLa cells

4.2.6 Morphology Study

The morphology of the HeLa cells in the presence and absence of the **T2** and **T5** were also studied using inverted phase contrast microscopy. The cells of the different concentration groups are shown in Figure 10A and B. The cells pretreated with the **T2** and **T5** were different in nature with the control (untreated). In control, the cells were closely packed and spindle shaped whereas, inhibition of cell growth was observed in the cells treated with the **T2** and **T5**, although many of the cells were still attached to their culture plates. Many cells had irregular cell membranes and signs of blebbing and are serves as apparent evidence

for apoptotic activation. Further, we extended our studies to the Western Blot analysis and the Cell cycle analysis to understand the plausible mechanisms behind the apoptosis with **T2** and **T5**.

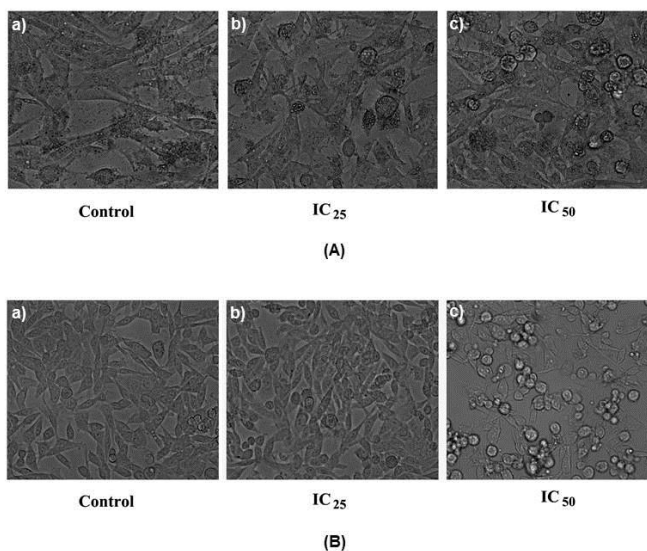


Figure 10. (A) Inverted phase contrast microscopy images of the HeLa cells in the presence and absence of **T2**: a) Undamaged HeLa cells observed in the control (untreated), b) 25% cell death and its apoptotic morphology changes were observed in the HeLa cells treated with the **T2** at its IC₂₅ concentration (4.5 $\mu\text{g}/\text{mL}$), c) 50% cell death and its apoptotic morphology changes were observed in the HeLa cells treated with the **T2** at its IC₅₀ concentration (7.5 $\mu\text{g}/\text{mL}$). (B) Inverted phase contrast microscopy images of the HeLa cells in the presence and absence of **T5**: a) Undamaged HeLa cells observed in the control (untreated), b) 25% cell death and its apoptotic morphology changes were observed in the HeLa cells treated with the **T5** at its IC₂₅ concentration (2 $\mu\text{g}/\text{mL}$), c) 50% cell death and its apoptotic morphology changes were observed in the HeLa cells treated with the **T5** at its IC₅₀ concentration (4 $\mu\text{g}/\text{mL}$).

4.2.7 Western Blot Analysis

The cervical cancer HeLa cells were treated with IC₂₅ and IC₅₀ concentrations of the samples **T2** and **T5** separately for 24 hrs and then performed the western blotting using beta-actin as an internal standard. We identified that CDK2 and CDK4 expression were significantly enriched in cervical cancers and was functionally required for the tumor

proliferation *in vitro*. The Western Blot analysis shows that the protein levels of

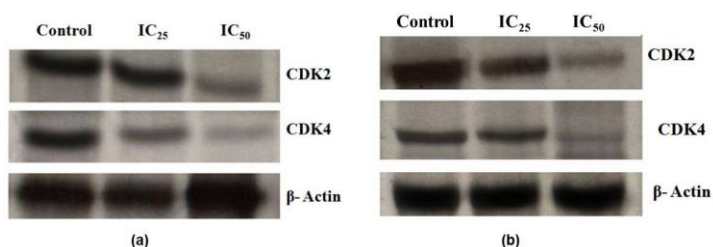


Figure 11. (a) Western blot analysis for the CDK2 and CDK4 expressions in HeLa cells treated with compound **T2** at its IC₂₅ and IC₅₀ concentrations (b) Western blot analysis for the CDK2 and CDK4 expressions in HeLa cells treated with compound **T5** at its IC₂₅ and IC₅₀ concentrations

CDK2 and CDK4 (components of the Cyclin-CDK complexes that are active in G1 and S phase) were altered after **T2** and **T5** treatments (Figure 11). Our findings reveal that the protein levels of CDKs were significantly down-regulated in **T2** and **T5** treated cells when compared to the control. The result from the Western Blot analysis justifies the data obtained from the docking studies as well as the CDK2/CDK4 inhibition protocol behind the observed apoptosis.

4.2.8 Cell cycle analysis

Figure 12 shows the Cell-cycle analysis of **T2** and **T5** treated HeLa cells by PI flow cytometry. In the case of **T2** treated HeLa cells, a significant increase in the S phase cell distribution was observed when compared to the control cells. The S phase fraction increased from 18.39 to 30.51 and 34.58 in HeLa cells after treatment with the IC₂₅, IC₅₀ of the sample **T2** respectively (Figure 12A). No such significant increments were observed for the G₀/G₁ or G₂/M phase distributions. This implies

the accumulation of cells at the S phase and the S phase cell cycle arrest which leads to the apoptosis. Similarly, in the case of **T5** treated HeLa cells, a significant increase in the G1 phase cell distribution was observed when compared to

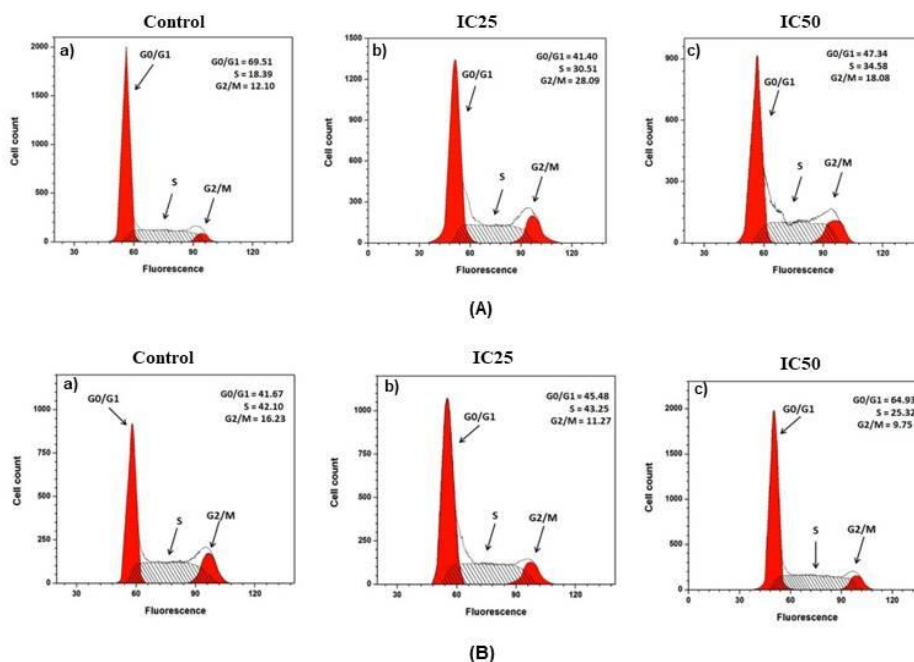


Figure 12. (A) Cell cycle analysis of compound **T2**-treated HeLa cells by PI flow cytometry: a) Normal cell phase distribution observed in control group (untreated), b) Mild accumulation of cells in S phase was observed in HeLa cells treated with **T2** at its IC25 (4.5 $\mu\text{g/mL}$), c) Significant accumulation of cells in S phase was observed in HeLa cells treated with **T2** at its IC50 (7.5 $\mu\text{g/mL}$). (B) Cell cycle analysis of compound **T5**-treated HeLa cells by PI flow cytometry: a) Normal cell phase distribution observed in control group (untreated), b) Mild accumulation of cells in G1 phase was observed in HeLa cells treated with **T5** at its IC25 (2 $\mu\text{g/mL}$), c) Significant accumulation of cells in G1 phase was observed in HeLa cells treated with **T5** at its IC50 (4 $\mu\text{g/mL}$).

the control. The G1 phase fraction increased from 41.67 to 45.48 and 64.93 in HeLa cells respectively after the treatment with the IC25, IC50 concentrations of the sample **T5** (Figure 12B). No such significant

increments were observed for the S or G2/M phase distributions. This implies the accumulation of cells at the G1 phase and the G1 phase cell cycle arrest which leads to the apoptosis. From the Western Blot results, we already observed that the selective down regulation of the kinases CDK2/CDK4 which are crucial for the G1 as well as S phase progressions. These results obtained from the Western Blot and the Cell cycle analysis together would give account for the CDK2/CDK4 inhibition protocol behind the observed apoptosis with the Chromene-Triazole-Coumarin Triads **T2** and **T5**.

4.3 Comparison between Chromene-Triazole-Coumarin Triads T1, T2, T5, and Ugi EML BLUE

The Chromene-Triazole-Coumarin Triads and Ugi EML BLUE were prepared by integrating different organic moieties to the various positions of the 7-hydroxy-4-methylcoumarin (Figure 13). The preparation of Ugi EML BLUE was through the formylation of 7-hydroxy-4-methylcoumarin (at 8th position of coumarin) followed by the Ugi four-component reaction (Ugi-4CR) which is discussed in the chapter-2. At the same time, the preparation of Triads were through the azidification of the 7-hydroxy-4-methyl coumarin (on the methyl group at 4th position) followed by a Copper catalysed Alkyne-Azide Cycloaddition (CuAAC) Click reaction, where the alkynes were synthesized through an 'active methylene-intermediated' multicomponent reaction (MCR) (discussed early in this chapter).

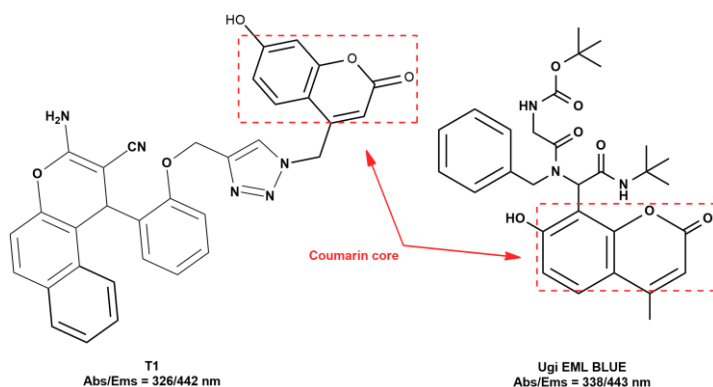


Figure 13. Comparison between Chromene-Triazole-Coumarin Triad-1 (**T1**) and Ugi EML BLUE

Parameters	Name of sample	
	Chromene-Triazole-Coumarin Triad 1 (T1)	Ugi EML BLUE
UV Abs _{Max} (nm) (solution)	326	338
PL _{Max} (nm) (solution)	442	443
Stoke's Shift (nm)	116	105
Quantum Yield (Φ)	0.95 (Ref: Quininesulfate, $\Phi=0.54$)	0.12 (Ref: Anthracene, $\Phi=0.27$)
Number of synthetic steps	Three	Two
Synthetic protocol	MCR-Click	MCR

Table 3. Fluorescence properties of **T1** and Ugi EML BLUE

Thus the synthesis of Ugi EML BLUE is a multicomponent reaction (MCR) based two-step process, where the synthesis of Triads is an MCR-Click based three-step process. The appropriate integration protocols and the selection of scaffolds or functionalities made the molecules **T1** and Ugi EML BLUE highly fluorescent. The Ugi EML BLUE shows strong fluorescence in the solution state as well as solid state, but the **T1** shows the fluorescence only in solution. The solid state fluorescence of the **T1** quenched due to the intermolecular π - π stacking interactions, which is discussed early in this chapter. Hence, the solution state fluorescence

properties of Ugi EML BLUE and the **T1** are summarized in table 3. The presence of Chromene moiety (another benzopyran based well-known fluorophore) coupled to the coumarin core, through the electron rich triazole bridge causes the large intramolecular charge transfer transitions (ICT) within the molecule. Moreover, the integration of more electron rich groups to the core enhances the number of electrons involving the electronic transitions lead to high fluorescence. All these factors are contributing towards the high quantum yield (Φ) and fluorescence intensity observed for the **T1** when compared to the Ugi EML BLUE.

Similarly, the **T2**, **T5** and Ugi EML BLUE were shown cytotoxic activities against human cervical cancer (HeLa) cells (Figure 14). All the samples were shown the appreciable binding affinities to their targeting kinases and all are evaluated against the HeLa cells for their cytotoxic activities. The IC₅₀ values obtained for the **T2**, **T5** and Ugi EML BLUE are 7.5 $\mu\text{g/mL}$, 4 $\mu\text{g/mL}$ and 0.5 $\mu\text{g/mL}$ respectively. The overall biological properties of these samples are summarized in table 4. Even though the **T2** and **T5** show the high binding affinities and having the more biologically active species with them, the Ugi EML BLUE shows the better IC₅₀ value. This may be due to the effect of the large size of the Chromene-Triazole- Coumarin Triads on comparison with the Ugi EML BLUE. The large size may negatively affect the permeability of the compound to the cell membranes.

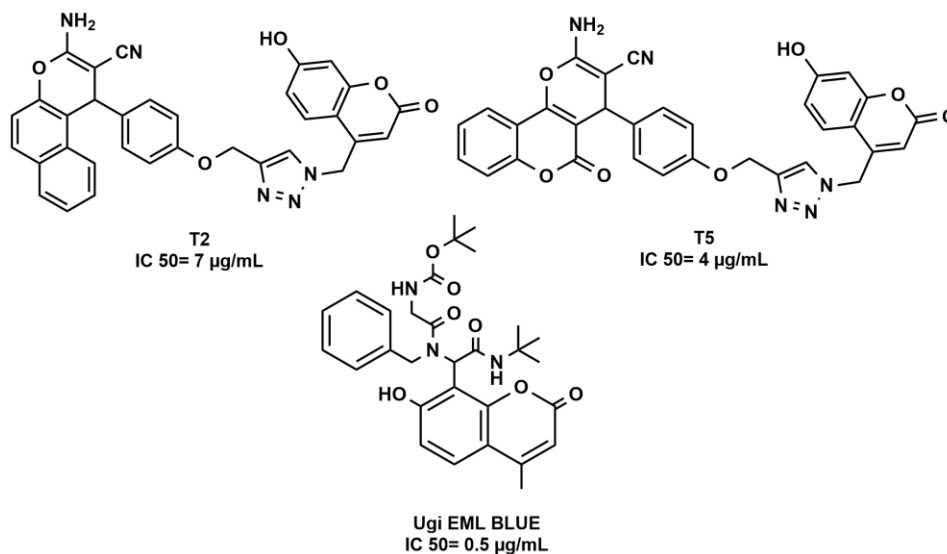


Figure 14. Comparison between Chromene-Triazole-Coumarin Triads (**T2** and **T5**) and Ugi EML BLUE

Parameters	Name of the sample		
	Chromene-Triazole Coumarin Triad-2 (T2)	Chromene-Triazole-Coumarin Triad-5 (T5)	Ugi EML BLUE
Targeting kinase	CDK2/CDK4	CDK2/CDK4	CDK2
Binding Affinity (kcal)	-9.1/-9.6	-10.5/-9.4	-8.0
IC50 (µg/mL)	7.5	4	0.5
Apoptotic Path	S phase arrest	G1 phase arrest	G2 phase arrest

Table 4. Cytotoxic properties of **T2**, **T5**, and Ugi EML BLUE

4.4 Conclusions

We have successfully synthesized six Chromene-Triazole-Coumarin Triad molecules **T1** to **T6**. The synthesis includes the azide substitution on 7-hydroxy-4-methylcoumarin followed by a copper catalyzed azide-alkyne cycloaddition (CuAAC), where the alkynes were prepared through a solvent free mechanochemical multicomponent

reaction (MCR). Among the six compounds, **T1**, **T4**, and **T5** showed strong fluorescence in solution in which **T1** afforded the highest quantum yield. **T2**, **T3**, and **T6** showed strong fluorescence in the solid state. The mechanism related to the origin of the fluorescence was derived from computational studies and the data obtained are perfectly in agreement with the experimental results. The photophysical studies revealed that the fluorescence properties of these new molecules are comparable with some of the commercial fluorophores based on functionalized coumarin heterocycles. Binding affinity calculation revealed that the molecules are selective towards CDK2 and CDK4 kinases. Among the six molecules, **T2** and **T5** showed highest docking scores and hence these molecules were systematically investigated for their tumor suppression activities on human cervical cancer cells (HeLa). The results obtained from MTT, Western Blot and Cell cycle analysis are promising to undertake further investigations on selectivity, toxicity, etc. to promote these molecules as affordable fluorescent inhibitors of CDK2/CDK4 induced cancers.

4.5 Structural Characterizations

4.5.1. Structural characterization of 2-amino-5-oxo-4-(2-(prop-2-yn-1-yloxy)phenyl)-4,5-dihydropyrano[3,2-c]chromene-3-carbonitrile (*Ch4*)

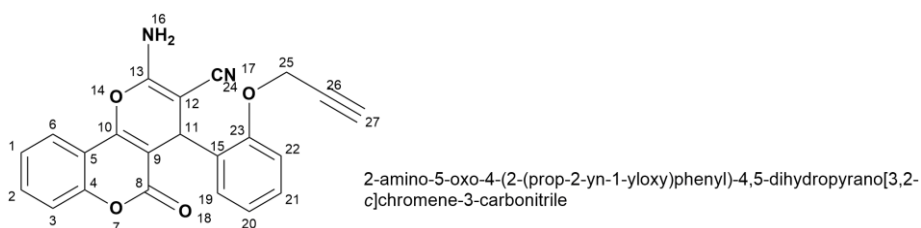
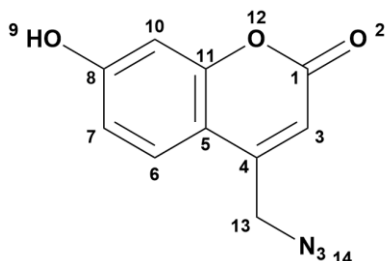


Figure 15. Structure of sample **Ch4**

The alkyne functionalized chromene **Ch4** is taken as a representative example for a general discussion on structure elucidation. The atoms in the sample **Ch4** are numbered as shown in Figure 15 and the FTIR, ^1H NMR, ^{13}C NMR, HRMS are shown in supporting information. The FT-IR spectrum of the compound shows major absorptions at 3576, 3354, 3278, 3147, 2925, 2892, 2191, 2130, 1675, 1606 and 1576 cm^{-1} . The bands at 3576 and 3354 cm^{-1} are due to the presence of the NH_2 group. Similarly, the bands at 3278 and 2130 cm^{-1} are due to the stretching of alkyne CH and alkyne C-C bond respectively. The bands at 3147, 2925 and 2892 cm^{-1} correspond to the stretching of aromatic alkene and alkane CH. The band at 2191 cm^{-1} is due to the CN stretching. The band for the group C=O found at 1675 cm^{-1} . The bands at 1606 and 1576 are due to the aromatic alkenes. The initial information obtained from FT-IR spectrum was further confirmed by ^1H NMR analysis. The singlet at δ 3.86 is due to the alkyne CH proton at the position C-27. The singlet at δ 4.66 is due to the methyl proton at the position C-11. The singlet at δ 4.77 is due to the two methyl protons at the position C-25. The aromatic protons were observed as, a one proton singlet at δ 6.03, two proton multiplet at δ 6.91-6.92, two proton multiplet at 7.07-7.14, two proton singlet at 7.25, one proton doublet at δ 7.39-7.41 with J value 8Hz, one proton multiplet at δ 7.60-7.63. The singlet at δ 7.85 is due to the two protons at position 16 (NH_2). Finally, the peak observed at m/z 371.1021 ($[\text{M}+\text{H}]^+$) in the mass spectrum further confirms the structure of the compound.

4.5.2. Structural Characterization of 4-(azidomethyl)-7-hydroxy-2H-chromene-2-one (Coumarin-azide)



4-(azidomethyl)-7-hydroxy-2H-chromen-2-one

Figure 16. Structure of coumarin-azide

The **coumarin-azide** is numbered as in Figure 16 and the FTIR, ^1H NMR, ^{13}C NMR, HRMS are shown in supporting information. The FT-IR spectrum of the compound shows major absorptions at 3502, 3068, 2918, 2120, 1682, 1610, 1566 cm^{-1} . The band at 3502 cm^{-1} is due to the stretching of OH. The bands at 3068 and 2918 cm^{-1} are due to the stretching of aromatic alkene C-H and alkane C-H respectively. The band at 2120 cm^{-1} is the characteristic band due to the azide linked to the carbon. The band at 1682 cm^{-1} is due to the stretching of C=O. The bands at 1610 and 1566 cm^{-1} are due to the stretching of alkene C=C. The initial information obtained from FT-IR spectrum was further confirmed by ^1H NMR analysis. The singlet at δ 2.14 is corresponding to the two methyl protons at position C-13. The aromatic protons were observed as, a one proton singlet at δ 6.66, one proton doublet at δ 6.73-6.76 with the J value 12Hz, one proton doublet at δ 6.82-6.84 with the J value 8Hz, one proton doublet at δ 7.36-7.38 with the J value 9Hz, one proton doublet at δ 7.66-7.69 with the J value 9Hz. The singlet at δ 8.22 is due to the one proton at position 9 (OH). The structure was further confirmed by ^{13}C NMR. The

peaks observed at 167.01 and 163.01 are due to the carbons C-1 and C-8. The signals due to the other aromatic carbons C-3 to C-7, C-10, C-11 were observed at 156.67, 154.65, 129.31, 127.95, 125.01, 113.65, 112.75, 112.31, 102.13. The peak observed at 56.303 is due to the carbon at C-13. Finally, the peak observed at m/z 217.0118 (M^+) in the mass spectrum further confirms the structure of the compound.

4.5.3. Structural Characterization of 2-amino-4-(2-((1-((7-hydroxy-2-oxo-2H-chromene-4-yl)methyl)-1H-1,2,3-triazol-4-yl)methoxy)phenyl)-5-oxo-4,5-dihydropyrano[3,2-c]chromene-3-carbonitrile (T4):

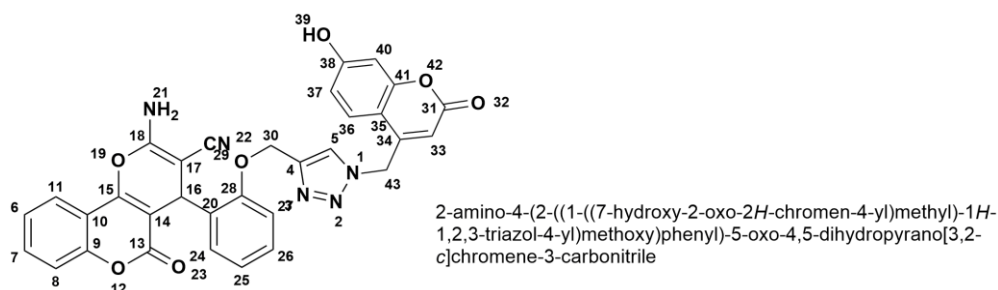


Figure 17. Structure of **T4**

The Chromene-Triazole-Coumarin Triad 4 (**T4**) is taken as a representative example for a general discussion on structure elucidation. The structural constituents of the sample **T4** are numbered as in Figure 17 and the FTIR, ^1H NMR, ^{13}C NMR, HRMS are shown in supporting information. The FT-IR spectrum of the compound shows major absorptions at 3505, 3441, 3386, 2922, 2952, 2189, 1706, 1674, 1606, 1572 cm^{-1} . The band at 3505 cm^{-1} is due to the stretching of OH group. The bands at 3441 and 3386 cm^{-1} correspond to the stretching of primary amine. The band at 2952 cm^{-1} is due to the stretching of CH at C-16. The

band at 2189 cm^{-1} is due to the stretching of CN group in the moiety. The bands for the C=O groups were observed at 1706 and 1674 cm^{-1} . The bands at 1606 and 1572 cm^{-1} correspond to the stretching of aromatic C=C groups. The initial information obtained from FT-IR spectrum was further confirmed by ^1H NMR analysis. The singlet at δ 4.60 is due to the two protons at the position C-43. The singlet at δ 4.92 is due to the one proton at the position C-16. The one proton singlet for the OH proton at the position O-39 was observed at δ 5.15. The signal for the two protons at the position C-30 was observed as a doublet at 5.36-5.42 with the J value 20Hz. The aromatic protons were observed as, one proton singlet at δ 6.24, three proton multiplet at δ 6.77-7.06, three proton multiplet at δ 7.20-7.31, one proton triplet at δ 7.52-7.50, five proton multiplet at δ 7.86-7.92. The singlet at δ 8.24 is due to the two protons of the primary amine group at the position N-21. The structure was further confirmed by ^{13}C NMR. The signals observed at 33.39, 55.97, 56.59, 67.91, 77.61 and 78.71 are due to the carbons at the positions C-16, C-17, C-43, and C-30. The signals observed at 152.04, 155.38, 158.52, 159.64 are due to the carbons at the positions C-13, C-15, C-28, C-31, C-38. The signals due to the other aromatic carbons were observed at 103.01, 113.03, 113.15, 116.38, 121.26, 122.53, 124.55, 128.46, 129.78, 130.72, 131.03 and 132.69. Finally, the peak observed at m/z 588.1510 ($[\text{M}+\text{H}]^+$) in the mass spectrum further confirms the structure of the compound.

4.6 Experimental Section

4.6.1 Materials and Methods

All reagents and solvents were obtained from commercial suppliers and used without further purification. IR spectra were recorded

on a JASCO-FT/IR-4100 Fourier-transform infrared spectrometer. ^1H NMR and ^{13}C NMR spectra were obtained by Bruker amx 400/500 MHz spectrometer in DMSO/ CDCl_3 solutions. The chemical shifts (δ) values are given relative to tetramethylsilane (TMS) and the coupling constants (J) are represented in Hertz (Hz). HRMS was obtained using ESI ionization. Quantum mechanical calculations were done with Gaussian 09 software. UV-Vis absorption spectra were recorded on a Jasco V-550 UV-VIS Spectrophotometer. Fluorescence spectra were measured using Perkin Elmer LS 45 and LS 55 and Horiba Fluoromax-4 Spectrometers.

The human cervical cancer cell line (HeLa) was procured from National Center for Cell Science (NCCS, Pune), 3-(4,5-dimethylthiazolyl-2)-2,5-diphenyltetrazolium bromide (MTT), was purchased from Sigma-Aldrich (Bangalore). Analytical grade reagents were purchased from Sigma-Aldrich (Bangalore). All the samples were prepared in Milli-Q water.

4.6.2. Synthetic Procedures

(1) *3-amino-1-(2-(prop-2-yn-1-yloxy)phenyl)-1H-benzo[f]chromene-2 carbonitrile (Ch1)*: A mixture of propargylated salicylaldehyde (160 mg, 1mmol), 2-naphthol (144mg, 1 mmol), malononitrile (66mg, 1mmol) and sodium carbonate (0.106 mg, 0.01mmol) were mixed together by using a mortar and pestle. The mixture was heated in an oven at 80°C for 5 minutes and mixed again. The process was repeated thrice. After cooling, the mixture was washed with hot water and the solid separated was filtered and dried. The product was then recrystallized from hot ethanol to obtain pure **Ch1**: 320mg (Yield 86%) White solid M.P.: 112°C . IR

absorptions (KBr, $\nu_{\max}/\text{cm}^{-1}$): 3475, 3317, 3299, 3188, 3066, 2916, 2862, 2172, 2127, 1909, 1646, 1583, 1515, 1490, 1451, 1415, 1376, 1293, 1255, 1232, 1183. $^1\text{H-NMR}$ δH (500 MHz, DMSO, δ ppm): 3.31 (1H, s, CH), 3.69 (2H, s, $-\text{OCH}_2$), 5.0 (1H, s, Ar-H), 7.08-7.40 (8H, m, Ar-H), 7.67-8.00 (3H, m, Ar-H), 8.46 (2H, s, Ar-NH₂). $^{13}\text{C NMR}$ δC (DMSO, 125MHz, δ ppm): 22.30, 56.24, 59.15, 78.17, 79.15, 112.98, 117.05, 117.98, 121.72, 122.72, 126.82, 128.45, 128.48, 129.83, 130.43, 132.66, 133.88, 138.75, 156.42, 171.97, 200.79. EIMS: m/z ($[\text{M}+\text{H}]^+$) calculated for C₂₃H₁₆N₂O₂: 353.12, found: 353.37

(2) 3-amino-1-(4-(prop-2-yn-1-yloxy)phenyl)-1H-benzo[f] chromene-2-carbonitrile (Ch2): A mixture of propargylated 4-hydroxy benzaldehyde (160 mg, 1mmol), 2-naphthol (144mg, 1 mmol), malononitrile (66mg, 1mmol) and sodium carbonate (0.106 mg, 0.01mmol) were mixed together by using a mortar and pestle. The mixture was heated in an oven at 80°C for 5 minutes and mixed again. The process was repeated thrice. After cooling, the mixture was washed with hot water and the solid separated was filtered and dried. The product was then recrystallized from hot ethanol to obtain pure **Ch2**: 315mg (Yield 85%) White solid M.P.: 113°C. IR absorptions (KBr, $\nu_{\max}/\text{cm}^{-1}$): 3462, 3379, 3272, 3084, 3031, 2930, 2972, 2222, 2129, 1652, 1584, 1554, 1507, 1455, 1429, 1373, 1316, 1257, 1235, 1191. $^1\text{H NMR}$ δH (400 MHz, DMSO, δ ppm): 3.31 (1H, s, CH), 3.68 (2H, s, Ar-O-CH₂), 4.97 (1H, s, Ar-H), 7.07-7.23 (2H, m, Ar-H), 7.25 (2H, s, Ar-H), 7.37-7.40 (1H, t, Ar-H), 7.67-7.68 (1H, d, 8Hz, Ar-H), 7.74-7.77 (1H, t, Ar-H), 7.99-8.00 (2H, d, J=8Hz, Ar-H), 8.42 (2H, s, Ar-NH₂). $^{13}\text{C NMR}$ δC (DMSO, 100MHz, δ ppm): 22.38, 56.24, 59.15, 78.17, 79.15, 112.98, 117.05, 117.98, 121.72, 122.72, 126.82,

128.45, 128.48, 129.83, 130.43, 132.66, 133.88, 138.75, 156.42, 171.97, 200.79. EIMS: m/z ($[M+H]^+$) calculated for $C_{23}H_{16}N_2O_2$: 353.12, found: 353.35

(3) **3-amino-1-(3-methoxy-4-(prop-2-yn-1-yloxy) phenyl)-1Hbenzo[*f*]chromene-2-carbonitrile (Ch3)**: A mixture of propargylated 4-hydroxy-3-methoxybenzaldehyde (190 mg, 1mmol), 2-naphthol (144mg, 1 mmol), malononitrile (66mg, 1mmol) and sodium carbonate (0.106 mg, 0.01mmol) were mixed together by using a mortar and pestle. The mixture was heated in an oven at 80°C for 5 minutes and mixed again. The process was repeated thrice. After cooling, the mixture was washed with hot water and the solid separated was filtered and dried. The product was then recrystallized from hot ethanol to obtain pure **Ch3**: 340mg (Yield 85%) as Yellow solid M.P.: 115°C. IR absorptions (KBr, ν_{max}/cm^{-1}): 3502, 3369, 3277, 3068, 3031, 2969, 2928, 2220, 2128, 1673, 1583, 1563, 1510, 1451, 1417, 1377, 1342, 1305, 1288, 1204, 1182, 1143. 1H NMR δ_H (400 MHz, DMSO, δ ppm): 3.33 (1H, s, CH), 3.67 (2H, s, Ar-O-CH₂), 3.82 (3H, s, Ar-O-CH₃), 4.98 (1H, s, Ar-H), 7.08-7.31 (7H, m, Ar-H), 7.37-7.40 (1H, t, Ar-H), 7.67-8.00 (3H, m, Ar-H), 8.46 (2H, s, Ar-NH₂). ^{13}C NMR δ_C (DMSO, 100MHz, δ ppm): 27.82, 54.24, 56.15, 59.28, 78.17, 79.15, 112.98, 117.05, 117.98, 121.72, 122.72, 128.70, 128.76, 128.93, 129.77, 130.43, 132.66, 134.96, 139.76, 157.30, 172.82. EIMS: m/z ($[M+H]^+$) calculated for $C_{24}H_{18}N_2O_3$: 382.13, found: 382.32

(4) **2-amino-5-oxo-4-(2-(prop-2-yn-1-yloxy)phenyl)-4,5 dihydropyrano**

[3,2-*c*]chromene-3-carbonitrile (Ch4): A mixture of propargylated salicylaldehyde (160 mg, 1mmol), 4-hydroxy coumarin (162mg, 1 mmol),

malononitrile (66mg, 1mmol) and hexamethylenetetramine (0.140 mg, 0.01mmol) were dissolved in minimum amount of ethanol. The reaction mixture is refluxed in a round bottom flask for one hour. The reaction mixture was then poured into cooled water and the precipitated solid was washed with water, filtered and dried. The product was recrystallized from hot ethanol to obtain pure **Ch4**: 313 mg (Yield 81%) as White solid, M.P.:122°C. IR absorptions (KBr, $\nu_{\max}/\text{cm}^{-1}$): 3576, 3354, 3278, 3147, 2925, 2892, 2191, 2130, 1675, 1606, 1576, 1489, 1449, 1411, 1377, 1337, 1310, 1272, 1247, 1229, 1212, 1174, 1111, 1064. ^1H NMR δH (500 MHz, CDCl_3 , δ ppm): 3.86 (1H, s, CH), 4.66 (1H, s, Ar-H), 4.77 (2H, s, Ar-O-CH₂), 6.03 (1H, s, Ar-H), 6.91-6.92 (2H, m, Ar-H), 7.07-7.14 (2H, m, Ar-H), 7.25 (2H, s, Ar-H), 7.39-7.41 (1H, d, 8Hz, Ar-H), 7.60-7.63 (1H, m, Ar-H), 7.85 (2H, s, Ar-NH₂). HRMS: m/z ($[\text{M}+\text{H}]^+$) calculated for $\text{C}_{22}\text{H}_{14}\text{N}_2\text{O}_4$: 371.0953, found: 371.1021

(5) 2-amino-5-oxo-4-(4-(prop-2-yn-1-yloxy)phenyl)-4,5 dihydropyrano

[3,2-c]chromene-3-carbonitrile (Ch5): A mixture of propargylated 4-hydroxy benzaldehyde (160 mg, 1mmol), 4-hydroxy coumarin (162mg, 1 mmol), malononitrile (66mg, 1mmol) and hexamethylenetetramine (0.140 mg, 0.01mmol) were dissolved in minimum amount of ethanol. The reaction mixture is refluxed in a round bottom flask for one hour. The reaction mixture was then poured into cooled water and the precipitated solid was washed with water, filtered and dried. The product was recrystallized from hot ethanol to obtain pure **Ch5**: 318 mg (Yield 82%) as White solid, M.P.:125°C. IR absorptions (KBr, $\nu_{\max}/\text{cm}^{-1}$): 3388, 3291, 3200, 3073, 2224, 2198, 2122, 1708, 1669, 1602, 1558, 1507, 1454, 1402,

1374, 1352, 1305, 1263, 1232, 1214, 1178, 1092. ¹H NMR δH(500 MHz, CDCl₃, δ ppm): 3.83 (1H, s, CH), 4.66 (1H, s, Ar-H), 4.77 (2H, s, Ar-O-CH₂), 6.03 (1H, s, Ar-H), 6.91-6.92 (2H, m, Ar-H), 7.07-7.14 (2H, m, Ar-H), 7.25 (2H, s, Ar-H), 7.38-7.41 (1H, d, 12Hz, Ar-H), 7.60-7.66 (2H, m, Ar-H), 7.85 (2H, s, Ar-NH₂). HRMS: m/z (M⁺) calculated for C₂₂H₁₄N₂O₄: 371.0953, found: 371.0965

(6) 2-amino-4-(3-methoxy-4-(prop-2-yn-1-yloxy)phenyl)-5-oxo-4,5-dihydropyrano[3,2-c]chromene-3-carbonitrile (Ch6): A mixture of propargylated 4-hydroxy-3-methoxybenzaldehyde (190 mg, 1mmol), 4-hydroxy coumarin (162mg, 1 mmol), malononitrile (66mg, 1mmol) and hexamethylenetetramine (0.140 mg, 0.01mmol) were dissolved in minimum amount of ethanol. The reaction mixture is refluxed in a round bottom flask for one hour. The reaction mixture was then poured into cooled water and the precipitated solid was washed with water, filtered and dried. The product was recrystallized from hot ethanol to obtain pure **Ch6**: 330 mg (Yield 79%) as Yellow solid, M.P.:123°C. IR absorptions (KBr, ν_{max}/cm⁻¹): 3406, 3324, 3278, 3032, 2960, 2931, 2217, 2196, 2118, 1693, 1671, 1601, 1588, 1565, 1509, 1454, 1418, 1380, 1344, 1310, 1266, 1213, 1179, 1141, 1112, 1062, 1011. ¹H NMR δH(400 MHz, DMSO, δ ppm): 3.44 (2H, s, -O-CH₂), 3.73 (3H, s, Ar-OCH₃), 3.81 (1H, s, CH), 4.42 (1H, s, Ar-H), 6.72-6.97 (3H, m, Ar-H), 7.23-7.25 (1H, d, 10Hz, Ar-H), 7.42-7.49 (1H, m, Ar-H), 7.58-7.93 (1H, m, Ar-H), 8.31 (2H, s, Ar-NH₂). HRMS: m/z ([M+H]⁺) calculated for C₂₃H₁₆N₂O₅: 401.1059, found: 401.1118

(7) **4-(azidomethyl)-7-hydroxy-2H-chromen-2-one (Coumarin-azide)**: 4-bromomethyl-7-hydroxycoumarin (255 mg, 1mmol) and sodium azide (65 mg, 1mmol) were dissolved in minimum quantity of N, N-Dimethylformamide (DMF) in a round bottomed flask. The reaction mixture was stirred for 18 hrs at 60°C. The mixture was then poured into excess of ice cold water. The solid product obtained was washed with water, filtered and dried. The product was recrystallized from hot ethanol to obtain pure **coumarin-azide**: 186 mg (Yield 58%) as Brown solid, M.P.:186°C. IR absorptions (KBr, $\nu_{\max}/\text{cm}^{-1}$): 3502, 3068, 2918, 2827, 2744, 2196, 2120, 1682, 1610, 1566, 1515, 1471, 1334, 1362, 1342, 1312, 1253, 1205, 1152, 1098. ^1H NMR δH (400 MHz, DMSO, δ ppm): 2.14 (2H, s, CH_2), 6.66 (1H, s, Ar-H), 6.73-6.76 (1H, d, $J=12\text{Hz}$, Ar-H), 6.82-6.84 (1H, d, $J=8\text{Hz}$, Ar-H), 7.36-7.38 (1H, d, $J=9\text{Hz}$, Ar-H), 7.66-7.69 (1H, d, $J=9\text{Hz}$, Ar-H), 8.22 (1H, s, Ar-OH). ^{13}C NMR δC (DMSO, 100MHz, δ ppm): 167.01, 163.01, 156.67, 154.65, 129.31, 127.95, 125.01, 113.65, 112.75, 112.31, 102.13, 56.30. HRMS: m/z (M^+) calculated for $\text{C}_{10}\text{H}_7\text{N}_3\text{O}_3$: 217.0487, found: 217.0118

(8) **3-amino-1-(2-((1-((7-hydroxy-2-oxo-2H-chromen-4-yl)methyl)-1H-1,2,3-triazol-4-yl)methoxy)phenyl)-1H-benzo[f]chromene-2-carbonitrile (T1)**: **Ch1** (88 mg, 0.25 mmol) and **coumarin-azide** (54.3 mg, 0.25 mmol) were dissolved in 2 mL of DMSO. To this mixture, 8 mL of *t*-BuOH, 4 mL of water, $\text{CuSO}_4 \cdot 5\text{H}_2\text{O}$ (40 mg), and sodium ascorbate (80 mg) were added and stirred at room temperature for 48 hrs. The reaction mixture was then poured in to cold water. The precipitated solid was collected, washed with water and dried. The dried product was washed with diethyl ether (5 mL) to afford **T1**: 110 mg (Yield 77%) as White

solid, M.P.: 192°C. IR absorptions (KBr, $\nu_{\max}/\text{cm}^{-1}$): 3467, 3443, 3359, 3181, 3067, 2921, 2190, 1763, 1727, 1696, 1647, 1598, 1513, 1486, 1455, 1406, 1321, 1292, 1213, 1174, 1136, 1083, 1016. ^1H NMR δH (400 MHz, DMSO, δ ppm): 5.02 (1H, s, Ar-OH), 5.30 (1H, s, Ar-H), 5.50 (2H, s, ArN-CH₂), 5.58 (2H, s, Ar-O-CH₂), 6.50 (1H, s, Ar-H), 6.87 (2H, s, Ar-H), 7.24 (1H, s, Ar-H), 7.41-7.46 (3H, d, J=20Hz, Ar-H), 7.69-7.98 (4H, m, Ar-H), 8.25 (2H, s, Ar-NH₂), 8.48-8.52 (3H, d, J=16.8Hz, Ar-H). ^{13}C NMR δC (DMSO, 100MHz, δ ppm): 18.95, 55.52, 56.55, 64.03, 78.32, 108.71, 112.09, 114.29, 126.58, 126.88, 127.46, 127.76, 128.89, 128.97, 132.89, 146.03, 152.64, 157.79, 165.29. HRMS (ESI): m/z (M⁺) calculated for C₃₃H₂₃N₅O₅: 569.1699, found: 569.1683

(9) 3-amino-1-(4-((1-((7-hydroxy-2-oxo-2H-chromen-4-yl)methyl)-1H-1,2,3-triazol-4-yl)methoxy)phenyl)-1H-benzo[f]chromene-2-carbonitrile (T2): **Ch2** (88 mg, 0.25 mmol) and **coumarin-azide** (54.3 mg, 0.25 mmol) were dissolved in 2 mL of DMSO. To this mixture, 8 mL of *t*-BuOH, 4 mL of water, CuSO₄ 5H₂O (40 mg), and sodium ascorbate (80 mg) were added and stirred at room temperature for 48 hrs. The reaction mixture was then poured in to cold water. The precipitated solid was collected, washed with water and dried. The dried product was washed with diethyl ether (5 mL) to afford **T2**: 116 mg (Yield 82%) as White solid, M.P.:196°C. IR absorptions (KBr, $\nu_{\max}/\text{cm}^{-1}$): 3441, 3405, 3346, 3083, 3030, 2925, 2223, 1729, 1598, 1585, 1509, 1475, 1430, 1375, 1317, 1260, 1236, 1184, 1089, 1048, 1010. ^1H NMR δH (400 MHz, DMSO, δ ppm): 4.61-4.69 (3H, m, Ar-H, ArN-CH₂), 5.15-5.22 (3H, m, Ar-OH, Ar-O-CH₂), 6.93 (1H, s, Ar-H), 7.04 (2H, s, Ar-H), 7.15-7.22 (6H, t, Ar-H), 7.38-7.48 (3H, m, Ar-H), 7.65-7.75 (3H, m, Ar-H), 7.91-7.93 (1H, d, J=9Hz, Ar-H),

8.27 (2H, s, Ar-NH₂). ¹³C NMR δC (DMSO, 100MHz, δ ppm): 18.98, 53.88, 61.98, 74.02, 108.70, 112.08, 114.31, 127.85, 128.08, 129.35, 132.91, 138.21, 152.69, 156.17, 159.25, 165.29. HRMS (ESI): m/z (M⁺) calculated for C₃₃H₂₃N₅O₅: 569.1699, found: 569.1685

(10) 3-amino-1-(4-((1-((7-hydroxy-2-oxo-2H-chromen-4-yl)methyl)-1H-1,2,3-triazol-4-yl)methoxy)-3-methoxyphenyl)-1H-benzof[f]chromene-2-carbonitrile (T3): **Ch3** (95.6 mg, 0.25 mmol) and **coumarin-azide** (54.3 mg, 0.25 mmol) were dissolved in 2 mL of DMSO. To this mixture, 8 mL of *t*-BuOH, 4 mL of water, CuSO₄ 5H₂O (40 mg), and sodium ascorbate (80 mg) were added and stirred at room temperature for 48 hrs. The reaction mixture was then poured in to cold water. The precipitated solid was collected, washed with water and dried. The dried product was washed with diethyl ether (5 mL) to afford **T3**: 112 mg (Yield 75%) as Yellow solid, M.P.:198°C. IR absorptions (KBr, ν_{max}/cm⁻¹): 3561, 3472, 3368, 3086, 3028, 2928, 2220, 1729, 1694, 1570, 1509, 1456, 1418, 1376, 1338, 1270, 1201, 1146, 1010. ¹H NMR δH(400 MHz, DMSO, δ ppm): 3.28 (3H, s, -O-CH₃), 4.62-4.69 (3H, m, Ar-H, ArN-CH₂), 5.15-5.22 (3H, m, Ar-OH, Ar-O-CH₂), 6.93 (1H, s, Ar-H), 7.04 (2H, s, Ar-H), 7.15-7.22 (4H, t, Ar-H), 7.38-7.48 (3H, m, Ar-H), 7.65-7.75 (3H,m, Ar-H), 7.91-7.93 (1H, d, J=7Hz, Ar-H), 8.26 (2H, s, Ar-NH₂). ¹³C NMR δC(DMSO, 100MHz, δ ppm): 21.08, 55.54, 56.20, 64.08, 77.58, 112.46, 113.40, 113.87, 114.64, 124.79, 126.38, 148.95, 151.86, 160.36, 162.21. HRMS (ESI): m/z (M⁺) calculated for C₃₄H₂₅N₅O₆: 599.1804, found: 599.1839

(11) **2-amino-4-(2-((1-((7-hydroxy-2-oxo-2H-chromen-4-yl)methyl)-1H-1,2,3-triazol-4-yl)methoxy)phenyl)-5-oxo-4,5-dihydropyran[3,2-c]chromene-3-carbonitrile (T4):** **Ch4** (92.6 mg, 0.25 mmol) and **coumarin-azide** (54.3 mg, 0.25 mmol) were dissolved in 2 mL of DMSO. To this mixture, 8 mL of *t*-BuOH, 4 mL of water, CuSO₄ 5H₂O (40 mg), and sodium ascorbate (80 mg) were added and stirred at room temperature for 48 hrs. The reaction mixture was then poured in to cold water. The precipitated solid was collected, washed with water and dried. The dried product was washed with diethyl ether (5 mL) to afford **T4**: 100 mg (Yield 68%) as White solid, M.P.:198°C. IR absorptions (KBr, $\nu_{\max}/\text{cm}^{-1}$): 3505, 3441, 3386, 2922, 2952, 2611, 2189, 1706, 1674, 1606, 1572, 1491, 1454, 1377, 1329, 1234, 1174. ¹H NMR δ H(400 MHz, DMSO, δ ppm): 4.60 (2H, s, ArN-CH₂), 4.92 (1H, s, Ar-H), 5.15 (1H, s, Ar-OH), 5.36-5.42 (2H, d, J=20.4Hz, Ar-O-CH₂), 6.241 (1H, s, Ar-H), 6.77-7.06 (3H, m, Ar-H), 7.20-7.31 (3H, m, Ar-H), 7.52-7.50 (1H, t, Ar-H), 7.86-7.92 (5H, m, Ar-H), 8.24 (2H, s, Ar-NH₂). ¹³C NMR δ C (DMSO, 100MHz, δ ppm): 33.39, 55.97, 56.59, 67.91, 77.61, 78.71, 103.01, 113.03, 113.15, 116.38, 121.26, 122.53, 124.55, 128.46, 129.78, 130.72, 131.03, 132.69, 152.04, 155.38, 158.52, 159.64. HRMS (ESI): m/z ([M+H]⁺) calculated for C₃₂H₂₁N₅O₇: 588.1441, found: 588.1510

(12) **2-amino-4-(4-((1-((7-hydroxy-2-oxo-2H-chromen-4-yl)methyl)-1H-1,2,3-triazol-4-yl)methoxy)phenyl)-5-oxo-4,5-dihydropyran[3,2-c]chromene-3-carbonitrile (T5):** **Ch5** (92.6 mg, 0.25 mmol) and **coumarin-azide** (54.3 mg, 0.25 mmol) were dissolved in 2 mL of DMSO. To this mixture, 8 mL of *t*-BuOH, 4 mL of water, CuSO₄ 5H₂O (40 mg), and sodium ascorbate (80 mg) were added and stirred at room

temperature for 48 hrs. The reaction mixture was then poured in to cold water. The precipitated solid was collected, washed with water and dried. The dried product was washed with diethyl ether (5 mL) to afford **T5**: 108 mg (Yield 74%) as White solid, M.P.:190°C. IR absorptions (KBr, $\nu_{\text{max}}/\text{cm}^{-1}$): 3494, 3477, 3388, 3072, 2916, 2227, 1660, 1603, 1504, 1384, 1311, 1250, 1173, 1116, 1021. ^1H NMR δH (400 MHz, DMSO, δ ppm): 4.68 (2H, s, ArN-CH₂), 4.94 (1H, s, Ar-H), 5.15 (1H, s, Ar-OH), 5.38-5.40 (2H, d, J=10Hz, Ar-O-CH₂), 6.20 (1H, s, Ar-H), 6.77-7.01 (4H, m, Ar-H), 7.25-7.34 (3H, m, Ar-H), 7.51-7.59 (1H, t, Ar-H), 7.81-7.98 (5H, m, Ar-H), 8.256 (2H, s, Ar-NH₂). ^{13}C NMR δC (DMSO, 100MHz, δ ppm): 30.94, 55.55, 56.20, 73.96, 77.59, 102.15, 112.47, 113.41, 114.64, 115.85, 123.48, 123.62, 124.80, 126.38, 131.45, 135.85, 148.96, 151.86, 152.02, 160.59, 163.41. HRMS (ESI): m/z ([M+Na]⁺) calculated for C₃₂H₂₁ N₅O₇: 610.1441, found: 610.1327

(13) 2-amino-4-(4-((1-((7-hydroxy-2-oxo-2H-chromen-4-yl)methyl)-1H-1,2,3-triazol-4-yl)methoxy)-3-methoxyphenyl)-5-oxo-4,5-dihydropyrano[3,2-c]chromene-3-carbonitrile (T6): **Ch6** (100.1 mg, 0.25 mmol) and **coumarin-azide** (54.3 mg, 0.25 mmol) were dissolved in 2 mL of DMSO. To this mixture, 8 mL of *t*-BuOH, 4 mL of water, CuSO₄ 5H₂O (40 mg), and sodium ascorbate (80 mg) were added and stirred at room temperature for 48 hrs. The reaction mixture was then poured in to cold water. The precipitated solid was collected, washed with water and dried. The dried product was washed with diethyl ether (5 mL) to afford **T6**: 115 mg (Yield 74%) as Yellow solid, M.P.: 202°C. IR absorptions (KBr, $\nu_{\text{max}}/\text{cm}^{-1}$): 3558, 3440, 3362, 3085, 3028, 2929, 2612, 2220, 1728, 1695, 1563, 1509, 1455, 1420, 1376, 1338, 1269. ^1H NMR δH (400 MHz,

DMSO, δ ppm): 3.80 (3H, s, -OCH₃), 4.39 (1H, s, Ar-OH), 4.64 (2H, s, ArN-CH₂), 4.95 (2H, s, Ar-O-CH₂), 5.44 (1H, s, Ar-OH), 6.13 (1H, s, Ar-OH), 7.23-7.30 (3H, t, Ar-H), 7.55-7.64 (4H, m, Ar-H), 7.88-7.90 (2H, d, J=6Hz, Ar-H), 8.25 (2H, s, Ar-NH₂), 8.32 (2H, s, Ar-H). ¹³C NMR δ C (DMSO, 100MHz, δ ppm): 35.20, 53.55, 55.20, 57.90, 63.56, 73.56, 77.59, 103.61, 106.72, 114.11, 115.49, 119.46, 123.04, 124.02, 127.56, 131.08, 152.35, 154.69, 164.66, 167.30. HRMS (ESI): m/z (M⁺) calculated for C₃₃H₂₃N₅O₈: 617.1546, found: 617.1519

4.6.3 Biochemical Procedures

4.6.3.1 Cell culture

Cervical cancer (HeLa) cells and were procured from the National Center for Cell Sciences (NCCS), Pune, India. The cancer cells were maintained in Dulbecco's modified eagles medium (DMEM) supplemented with 2mM l-glutamine and balanced salt solution (BSS) adjusted to contain 1.5 g/L Na₂CO₃, 0.1 mM nonessential amino acids, 1 mM sodium pyruvate, 2 mM l-glutamine, 1.5 g/L glucose, 10 mM (4-(2-hydroxyethyl)-1-piperazineethane sulfonic acid) (HEPES) and 10% fetal bovine serum (GIBCO, USA). Penicillin and streptomycin (100 IU/100 μ g) were adjusted to 1mL/L. The cells were maintained at 37°C with 5% CO₂ in a humidified CO₂ incubator.

4.6.3.2 Evaluation of cytotoxicity [MTT Assay]

The inhibitory concentration (IC₅₀) value was evaluated using an MTT [3-(4,5- dimethylthiazol-2-yl)-2,5-diphenyltetrazolium bromide] assay. Cancer cells and were grown (1 \times 10⁴ cells/well) in a 96-well plate

for 48 h into 75% confluence. The medium was replaced with fresh medium containing serially diluted synthesized compounds, and the cells were further incubated for 48 h. The culture medium was removed, and 100 μ L of the MTT [3-(4,5-dimethylthiazol-2-yl)-3,5-diphenyl tetrazolium bromide] (Hi-Media) solution was added to each well and incubated at 37°C for 4 h. After removal of the supernatant, 50 μ L of DMSO was added to each of the wells and incubated for 10 minutes to solubilize the formazan crystals. The optical density was measured at 620 nm in an ELISA multi-well plate reader (Thermo Multiskan EX, USA). The OD value was used to calculate the percentage of viability using the following formula.

$$\% \text{ of viability} = \frac{\text{OD value of experimental sample}}{\text{OD value of experimental control}} \times 100$$

4.6.3.3 Morphological study

The HeLa cells that were grown on coverslips (1×10^5 cells/coverslip) were incubated with disintegrin at the IC50 concentration, and they were then fixed in ethanol: acetic acid solution (3:1, v/v). The coverslips were gently mounted on glass slides for the morphometric analysis. Three monolayers per experimental group were photomicrographed. The morphological changes of the HeLa cells were analyzed using Nikon (Japan) bright-field inverted light microscopy at 40 \times magnification.

4.6.3.4 Cell cycle analysis

HeLa cells (1×10^5) were seeded in a 6-well plate. After 24 hrs incubation at 37°C (5% CO₂), the medium was changed with fresh,

supplemented or not (control) with the compound (1, 2 and 4 μ M). After 24 hrs incubation, cells were harvested with trypsin, washed by PBS, fixed in 70% ethanol and stored at -20°C for 1h. The cellular nuclear DNA was stained by propidium iodide (PI) as described, briefly, followed by removing the ethanol, washed with PBS, the cells were suspended in 0.5 ml PBS containing 50 μ g/ml PI and 100 μ g/ml RNase and incubated at 37°C for 30 min. Flow cytometry was performed in duplicate with a BD FACS flow cytometer. From each sample, 10,000 events were collected and fluorescent signal intensity was recorded and analyzed by CellQuest and Modifit.

4.6.3.5 Western Blot Analysis

Western blotting was performed to detect the proteins of CDK2 and CDK4. The HeLa cells (1×10^6) were seeded into 100mm culture dishes in the presence or absence of compound **T2** and compound **T5** were treated for 48 h. Cells were then washed twice with ice cold PBS and incubated in lysis buffer. The lysates were centrifuged at $10,000 \times g$ for 5 min at 4°C and were used as the cell protein extracts. Each of the extracts was applied to 12% SDS polyacrylamide gel electrophoresis after which the proteins were transferred onto a nitrocellulose membrane, and then blocked for 1 h using 10% skim milk in water. After washing in a PBS containing 0.1% Tween 20 for 3 times, the primary antibodies were added at a v/v ratio of 1:1000. After overnight incubation at 4°C, the primary antibodies were washed away and the secondary antibodies were added for 1 h incubation at room temperature. Finally, the enhanced chemiluminescence detection reagents were used to develop the signal of the membrane.

References

- [1] Evan, G.I.; Vousden, K. H. *Nature* **2001**, *411*, 342-348.
- [2] Hartwell, L. H.; Kastan, M. B. *Science* **1994**, *266*, 1821-1828.
- [3] Vermeulen, K.; Bockstaele, D. R. V.; Berneman, Z. N. *Cell Prolif.* **2003**, *36*, 131-149.
- [4] Malumbres, M.; Barbacid, M. *Nat. Rev. Cancer* **2001**, *1*, 222-231.
- [5] Shapiro G. I. *J. Clin. Oncol.* **2006**, *24*, 1770-1783.
- [6] Zheng, J.; Li, Q.; Wang, W.; Wang, Y.; Fu, X.; Wang, W.; Fan, L.; Yan, W. *Oncol. Rep.* **2016**, *35*, 809-816.
- [7] Shi X. N.; Li, H.; Yao, H.; Liu, X.; Li, L.; Leung, K. S.; Kung, H. F.; Lu, D.; Wong, M. H.; Lin, M. C. *PLoS One* **2015**, *10*, e0132072. DOI:10.1371/journal.pone.013207
- [8] Lim, T. G.; Lee, S. Y.; Huang, Z.; Lim, D. Y.; Chen, H.; Jung, S. K.; Bode, A. M.; Lee, K. W.; Dong, Z. *Cancer Prev. Res.* **2014**, *7*, 466-474.
- [9] Hu, B.; Mitra, J.; Heuvel, S. V. D.; Enders, G. H. *Mol. Cell. Biol.* **2001**, *21*, 2755-2766.
- [10] Furuno, N.; Elzen, N. D.; Pines, J. *J. Cell. Biol.* **1999**, *147*, 295-306.
- [11] Ortega, S.; Malumbres, M.; Barbacid, M. *Biochim. Biophys. Acta.* **2002**, *1602*, 73-87.
- [12] Ahn, Y. M.; Vogeti, L.; Liu, C. J.; Santhapuram, H. K. R.; White, J. M.; Vasandani, V.; Mitscher, L. A.; Lushington, G. H.; Hanson, P. R.; Powell, D. R.; Himes, R. H.; Roby, K. F.; Ye, Q.; Georg, G. I. *Bioorg. Med. Chem.*, 2007, **15**, 702-713.
- [13] Hong, C. Y.; Park, T. S.; Kim, Y. K.; Lee, J. H.; Kim, J. H.; Kim, D. M.; Son, H. S.; Kim, S. W.; Kim, E. E. K. *CDK Inhibitors Having Flavone Structures*. US Patent US 6,500,846 B1, Dec. 31, **2002**.
- [14] Tadesse, S.; Caldon, E. C.; Tilley, W.; Wang, S. *J. Med. Chem.*, 2019, **62**, 4233-4251.
- [15] Humpolickova, J.; Mejdrová, I.; Matousova, M.; Nencka, R.; Boura, E. *J. Med. Chem.* 2017, **60**, 119-127.

- [16] Horton, D. A.; Bourne, G. T.; Smythe, M. L. *Chem. Rev.* **2003**, *103*, 893-930.
- [17] Nicolaou, K. C.; Pfefferkorn, J. A.; Roecker, A. J.; Cao, G.-Q.; Barluenga, S.; Mitchell, H. J. *J. Am. Chem. Soc.* **2000**, *122*, 9939.
- [18] Evans, B. E.; et al. *J. Med. Chem.* **1988**, *31*, 2235-2246.
- [19] Xia, S.; Wang, J.; Bi, J.; Wang, X.; Fang, M.; Phillips, T.; May, A.; Conner, N.; Tanasova, M.; Luo, F. T.; Liu, H. *Sens. Actuators, B*, **2018**, *265*, 699-708.
- [20] Xiaohong, C.; Runli, T.; Huizhen, J.; Jun, F.; Jingui, Q.; Zhen, Li. *Appl. Mater. Interfaces* **2012**, *4*, 4387-4392.
- [21] Emami, S.; Dadashpour, S. *Eur. J. Med. Chem.* **2015**, *102*, 611-630.
- [22] Thakur, A.; Singla, R.; Jaitak, V. *Eur. J. Med. Chem.* **2015**, *101*, 476-495.
- [23] Lakowicz, J. R. *Principles of Fluorescence Spectroscopy*, 2nd edition, Plenum Press, New York, **1999**.
- [24] Frisch, M. J.; Trucks, G. W.; Schlegel, H. B.; Scuseria, G. E.; Robb, M. A.; Cheeseman, J. R.; Scalmani, G.; Barone, V.; Mennucci, B.; Petersson, G. A.; Nakatsuji, H.; Caricato, M.; Li, X.; Hratchian, H. P.; Izmaylov, A. F.; Bloino, J.; Zheng, G.; Sonnenberg, J. L.; Hada, M.; Ehara, M.; Toyota, K.; Fukuda, R.; Hasegawa, J.; Ishida, M.; Nakajima, T.; Honda, Y.; Kitao, O.; Nakai, H.; Vreven, T.; Montgomery, J. A., Jr.; Peralta, J. E.; Ogliaro, F.; Bearpark, M.; Heyd, J. J.; Brothers, E.; Kudin, K. N.; Staroverov, V. N.; Kobayashi, R.; Normand, J.; Raghavachari, K.; Rendell, A.; Burant, J. C.; Iyengar, S. S.; Tomasi, J.; Cossi, M.; Rega, N.; Millam, J. M.; Klene, M.; Knox, J. E.; Cross, J. B.; Bakken, V.; Adamo, C.; Jaramillo, J.; Gomperts, R.; Stratmann, R. E.; Yazyev, O.; Austin, A. J.; Cammi, R.; Pomelli, C.; Ochterski, J. W.; Martin, R. L.; Morokuma, K.; Zakrzewski, V. G.; Voth, G. A.; Salvador, P.; Dannenberg, J. J.; Dapprich, S.; Daniels, A. D.; Farkas, Ö.; Foresman, J. B.; Ortiz, J. V.; Cioslowski, J.; Fox, D. J., Revision A.1, Gaussian, Inc., Wallingford CT, **2009**.
- [25] Osorio-Martínez, C. A.; Urías-Benavides, A.; Gómez-Durán, C. F. A.; Bañuelos, J.; Esnal, I.; Arbeloa, I. L.; Peña-Cabrera, E. *J. Org. Chem.* **2012**, *77*, 5434-5438.
- [26] Zhao, Y. J.; Miao, K.; Zhu, Z.; Fan, L. J. *ACS Sens.* **2017**, *2*, 842-847.

- [27] Moorthy, J. N.; Natarajan, P.; Venkatakrishnan, P.; Huang, D. F.; Chow, T. *J. Org. Lett.* **2007**, *9*, 5215-5218.
- [28] Yuan, W. Z.; Lu, P.; Chen, S.; Lam, J. W. Y.; Wang, Z.; Liu, Y.; Kwok, H. S.; Ma, Y.; Tang, B. Z. *Adv. Mater.* **2010**, *22*, 2159-2163.
- [29] Hong, Y.; Lam, J. W. Y.; Tang, B. Z. *Chem. Soc. Rev.* **2011**, *40*, 5361-5388.
- [30] Chan, C. Y. K.; Zhao, Z.; Lam, J. W. Y.; Liu, J.; Chen, S.; Lu, P.; Mahtab, F.; Chen, X.; Sung, H. H. Y.; Kwok, H. S.; Ma, Y.; Williams, I. D.; Wong, K. S.; Tang, B. Z. *Adv. Funct. Mater.* **2012**, *22*, 378-389.
- [31] Tong, H.; Dong, Y.; Hong, Y.; Halussler, M.; Lam, J. W. Y.; Sung, H. H. Y.; Yu, X.; Sun, J.; Williams, I. D.; Kwok, H. S.; Tang, B. Z. *J. Phys. Chem. C* **2007**, *111*, 2287-2294.
- [32] Trott, O.; Olson, A. J. *J. Comput. Chem.* **2010**, *31*, 455-461.
- [33] Brown, N. R.; Korolchuk, S.; Martin, M. P.; Stanley, W. A.; Moukhametzianov, R.; Noble, M. E. M.; Endicott, J. A. *Nat. Commun.* **2015**, *6*, 6769.
- [34] Lee, J.; Park, T.; Jeong, S.; Kim, K. H.; Hong, C. *Bioorg. Med. Chem. Lett.* **2007**, *17*, 1284-1287.
- [35] Beattie, J. F.; Breault, G. A.; Ellston, R. P. A.; Green, S.; Jewsbury, P. J.; Midgley, C. J.; Naven, R. T.; Minshull, C. A.; Pauptit, R. A.; Tucker, J. A.; Pease, J. E. *Bioorg. Med. Chem. Lett.* **2003**, *13*, 2955-2960.
- [36] Cho, Y. S.; Borland, M.; Brain, C.; Chen, C. H. T.; Cheng, H.; Chopra, R.; Chung, K.; Groarke, J.; He, G.; Hou, Y.; Kim, S.; Kovats, S.; Lu, Y.; Reilly, M. O.; Shen, J.; Smith, T.; Trakshel, G.; Vögtle, M.; Xu, M.; Xu, M.; Sung, M. J. *J. Med. Chem.* **2010**, *53*, 7938-7957.
- [37] Young, T.; Abel, R.; Kim, B.; Berne, B. J.; Friesner, R. A. *Proc. Natl. Acad. Sci. U. S. A.* **2007**, *104*, 808-813.
- [38] Snyder, P. W.; Mecinovic, J.; Moustakas, D. T.; Thomas III, S. W.; Harder, M.; Mack, E. T.; Lockett, M. R.; Heroux, A.; Sherman, W.; Whitesides, G. M. *Proc. Natl. Acad. Sci. U. S. A.* **2011**, *108*, 17889-17894.

Supporting Information

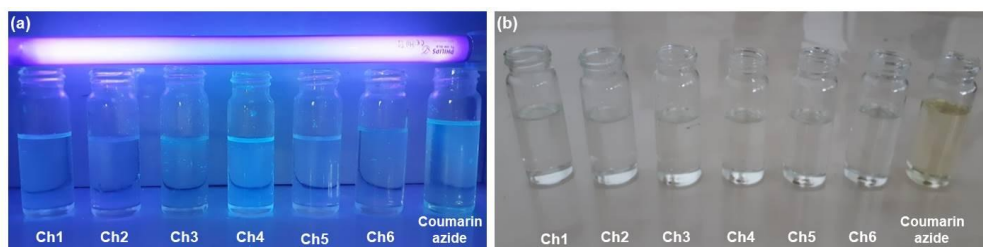


Figure S1. Starting alkynes Ch1 to Ch6 and Coumarin-azide under UV exposure: (a) samples under UV light (b) samples under Day-light

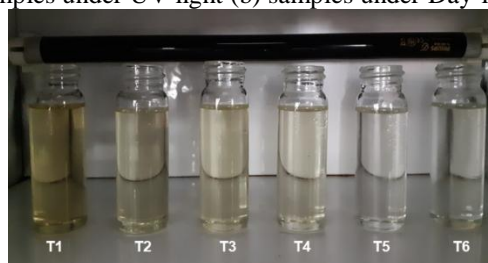


Figure S2. Compounds **T1** to **T6** (50 ppm solution in DMSO) under Day-light

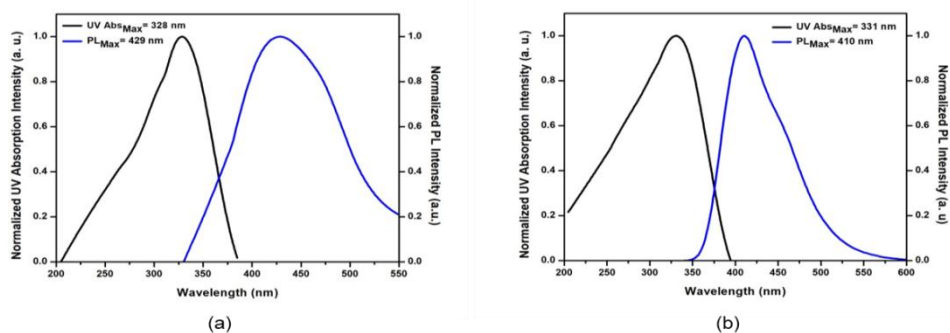


Figure S3. Absorption and emission spectra of (a) **T4** and (b) **T5**

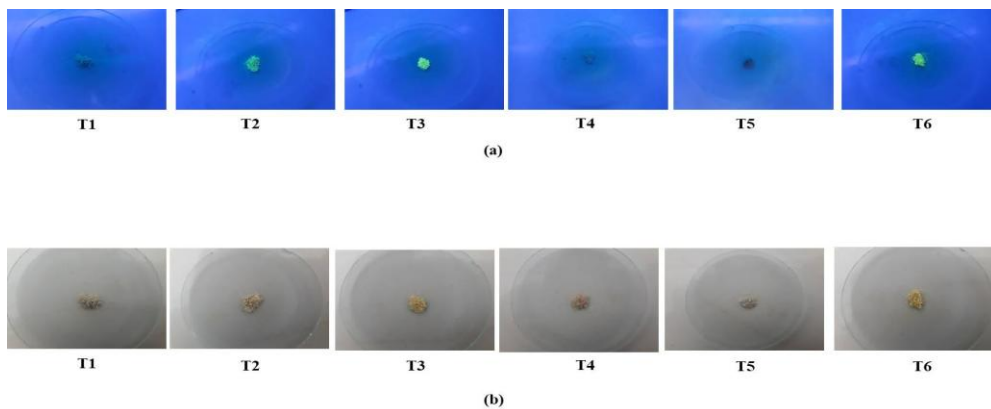


Figure S4. Triads **T1** to **T6**, solid samples under (a) UV-light (b) Daylight

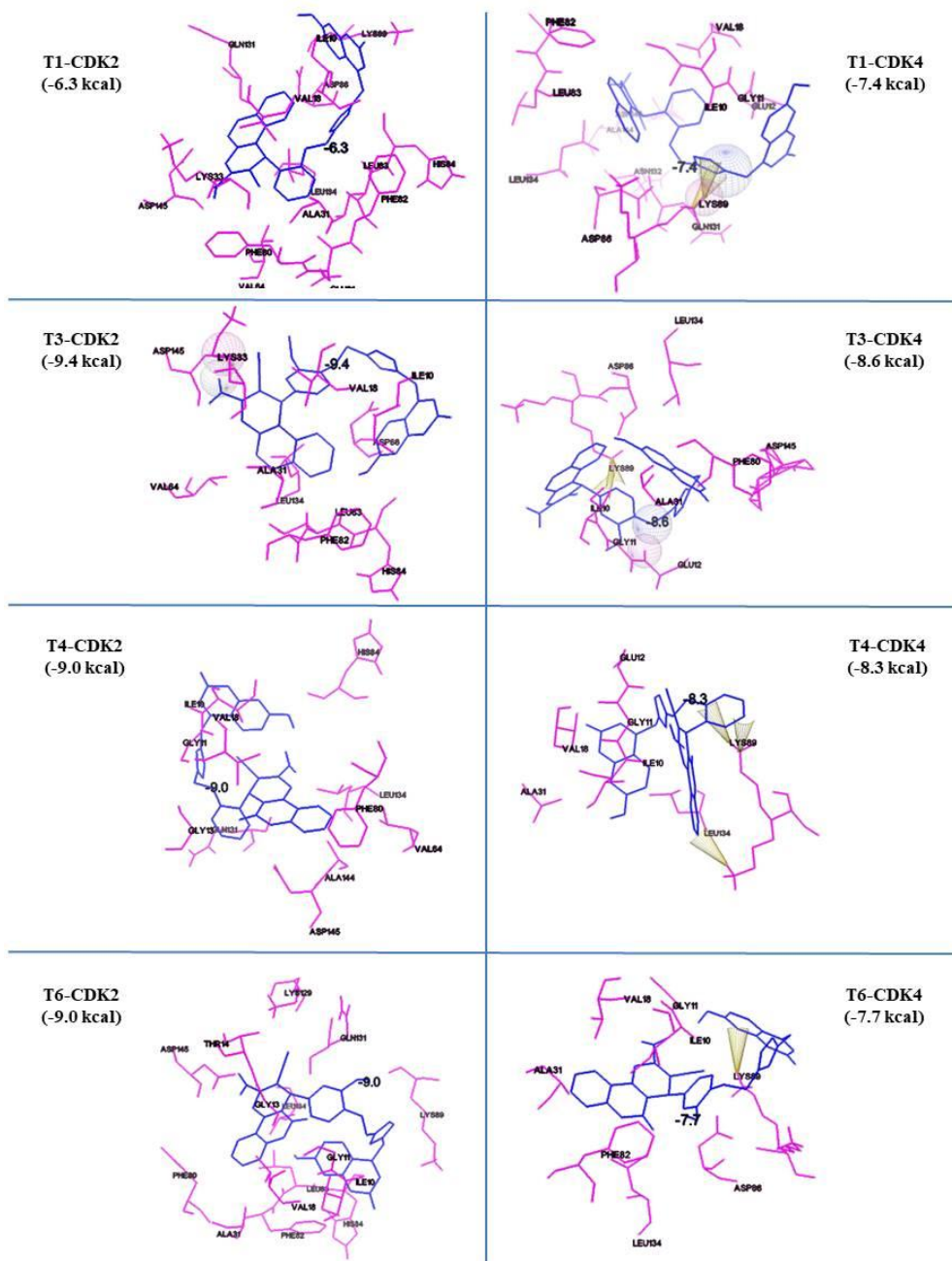
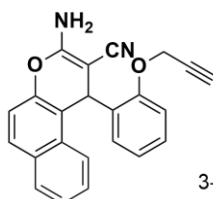


Figure S5. Docking mode of Chromene-Triazole-Coumarin Triads **T1**, **T3**, **T4** and **T6** in the active site of CDK2 and CDK4 with their corresponding docking score

Spectral Details

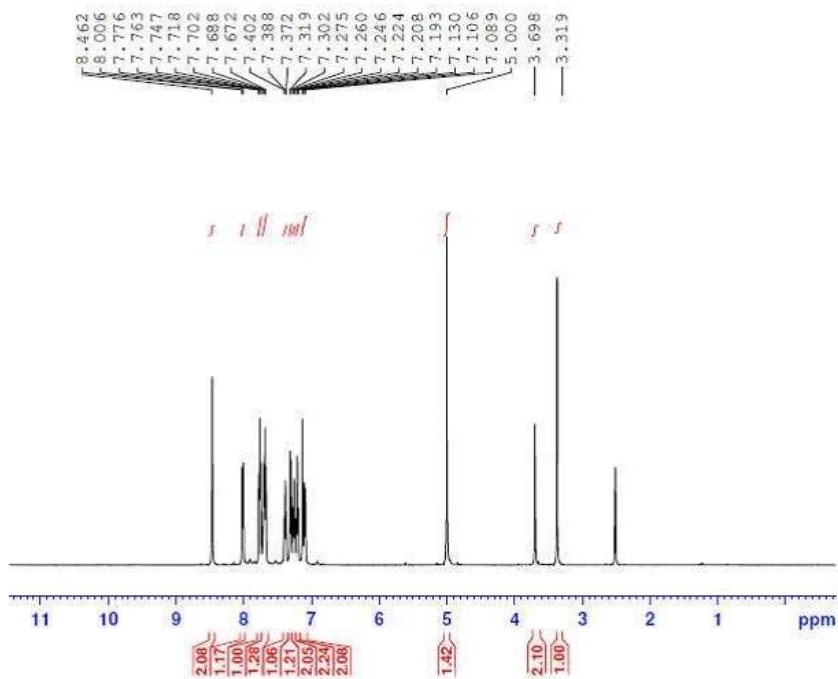
Spectral Details of Chromene-Alkyne 1 (**Ch1**)



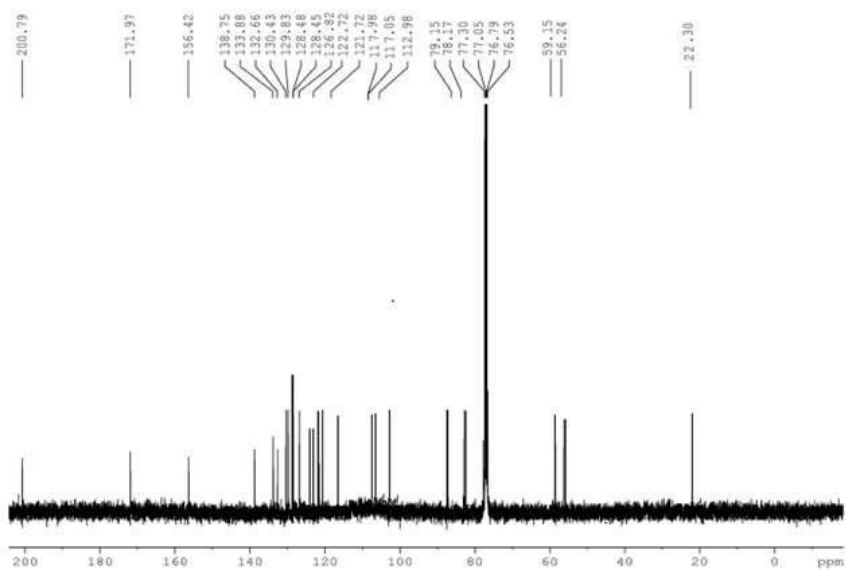
3-amino-1-(2-(prop-2-yn-1-yloxy)phenyl)-1*H*-benzo[*f*]chromene-2-carbonitrile

¹H-NMR spectra:

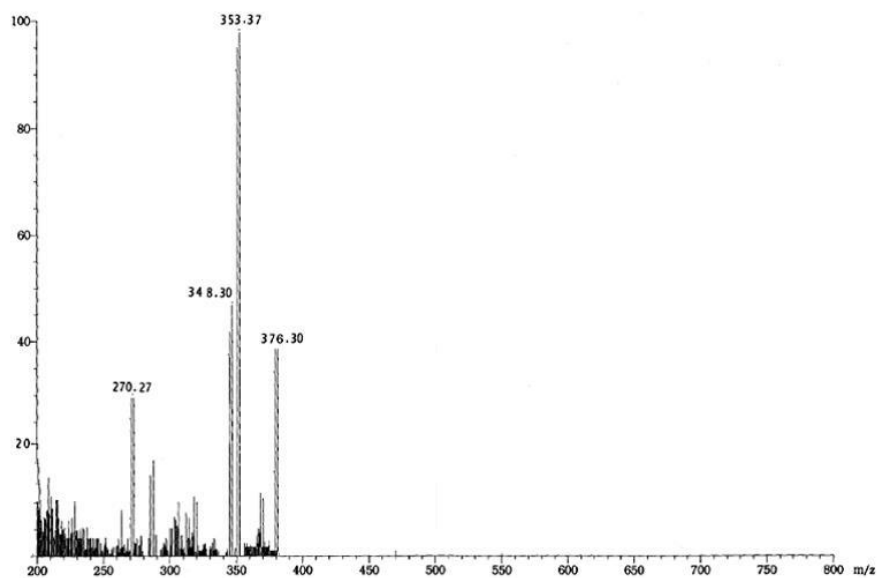
PROTON DMSO C:\Bruker\TOPSPIN nmr



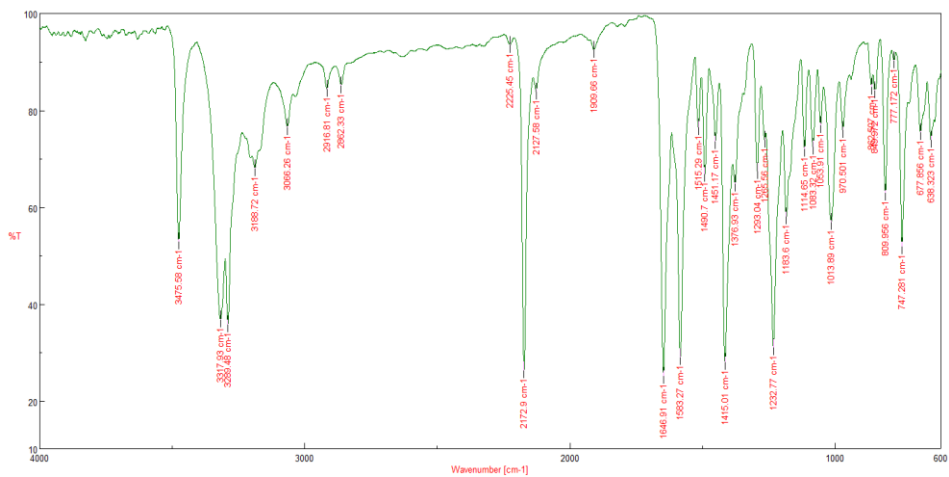
¹³C-NMR Spectra:



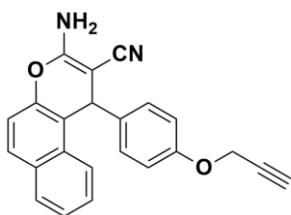
EIMS:



IR Spectra:

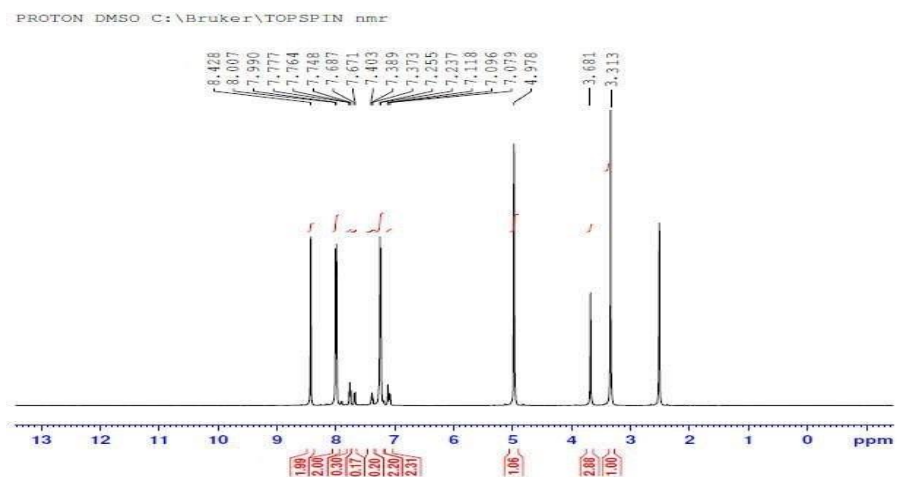


Spectral Details of Chromene-Alkyne 2 (Ch2)

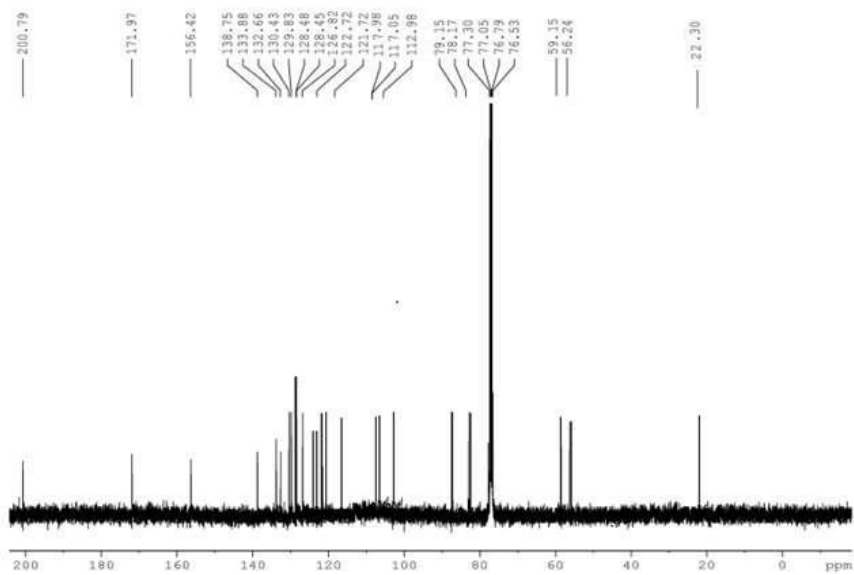


3-amino-1-(4-(prop-2-yn-1-yloxy)phenyl)-1H-benzo[f]chromene-2-carbonitrile

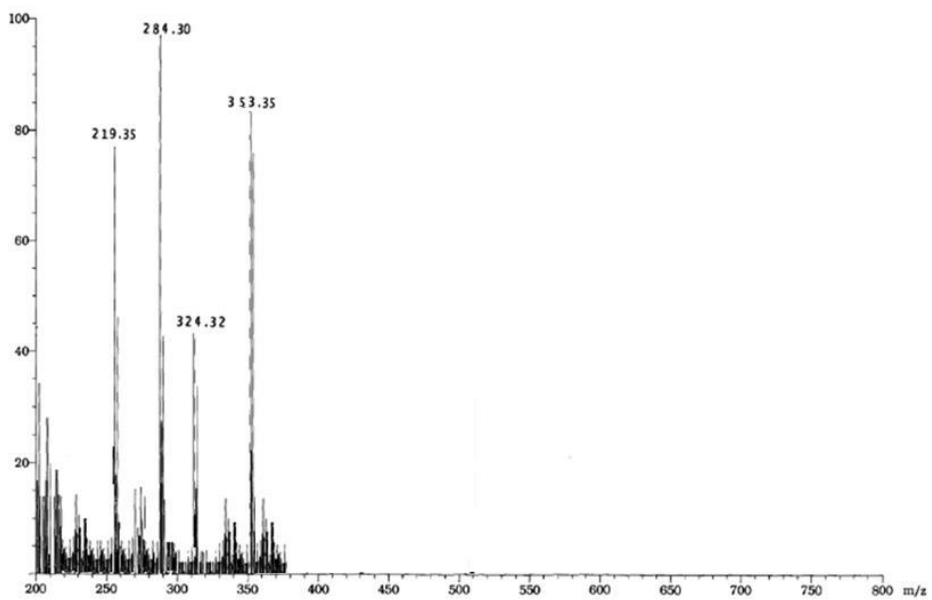
¹H-NMR spectra:



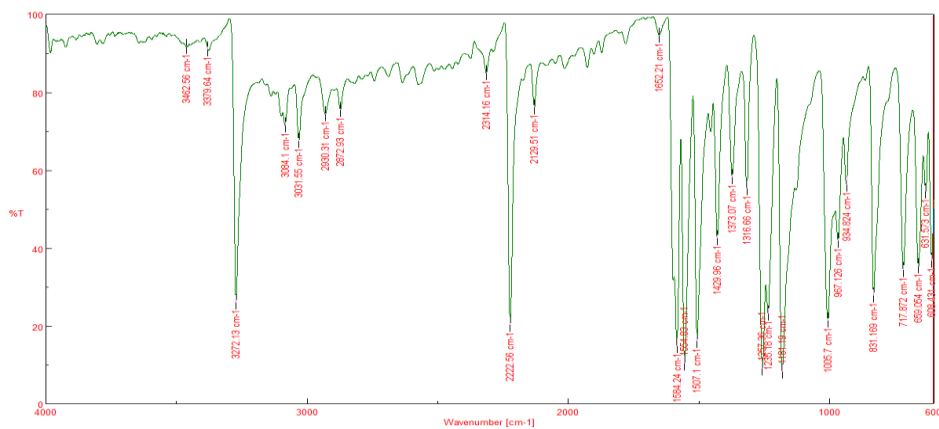
¹³C-NMR Spectra:



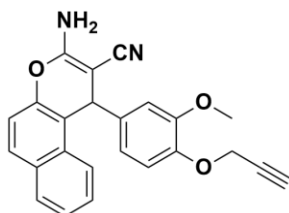
EIMS:



IR Spectra:

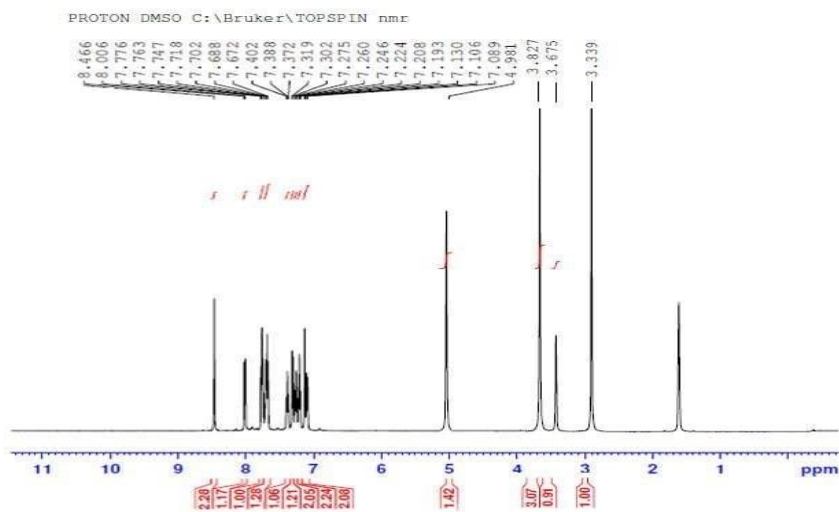


Spectral Details of Chromene-Alkyne 3 (Ch3)

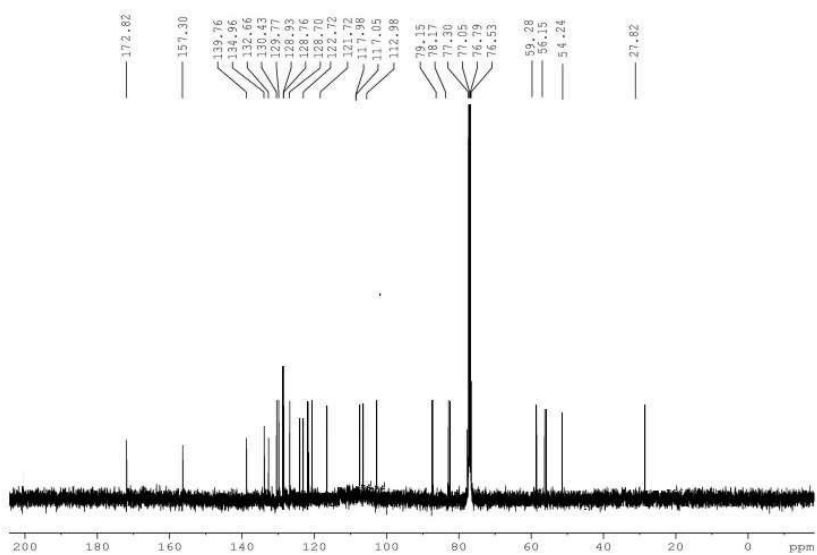


3-amino-1-(3-methoxy-4-(prop-2-yn-1-yloxy)phenyl)-1H-benzo[f]chromene-2-carbonitrile

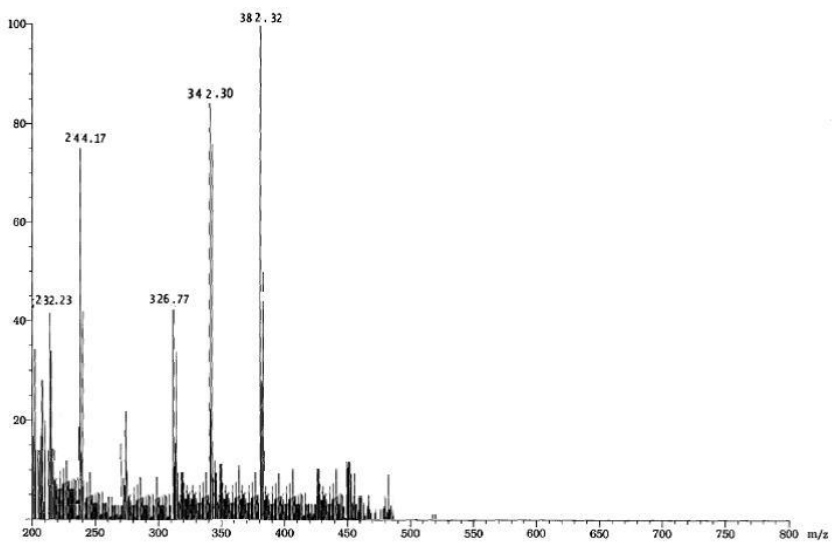
¹H-NMR spectra:



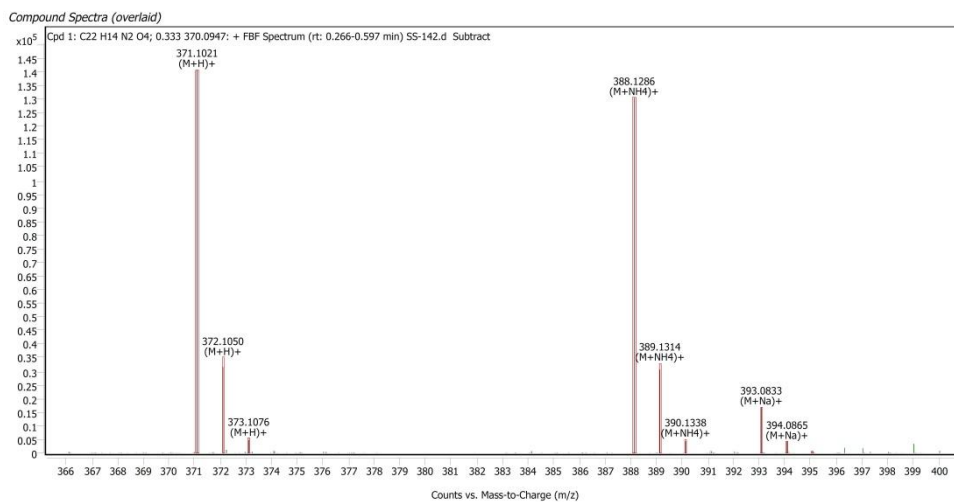
¹³C-NMR Spectra:



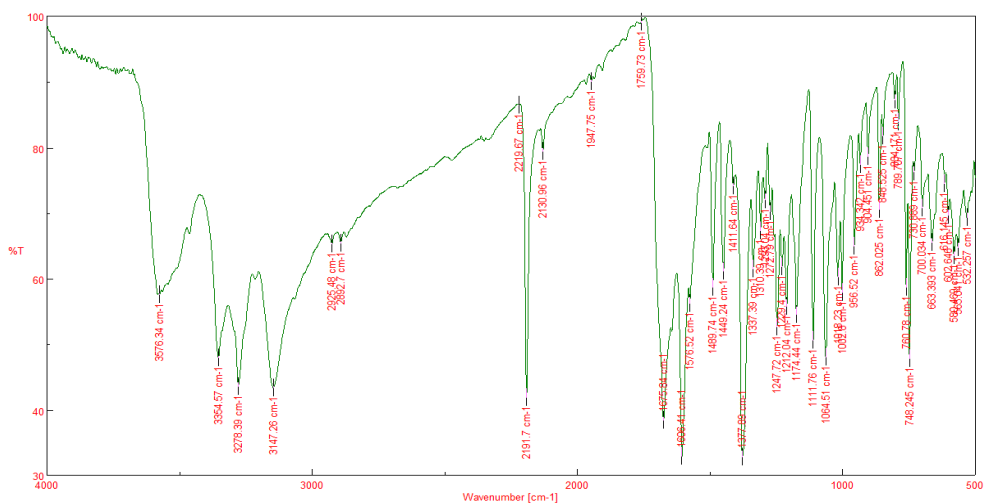
EIMS:



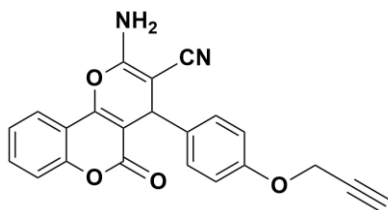
HRMS:



IR Spectra:

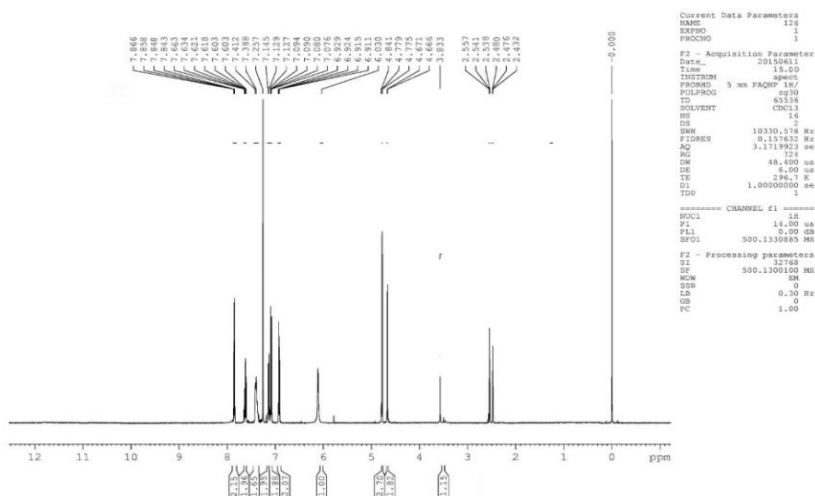


Spectral Details of Chromene-Alkyne 5 (Ch5)

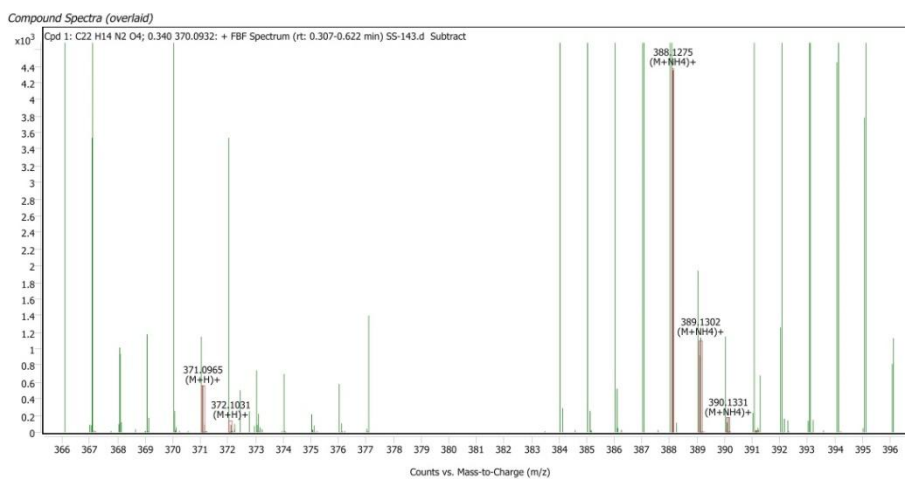


2-amino-5-oxo-4-(4-(prop-2-yn-1-yloxy)phenyl)-4,5-dihydroprano[3,2-c]chromene-3-carbonitrile

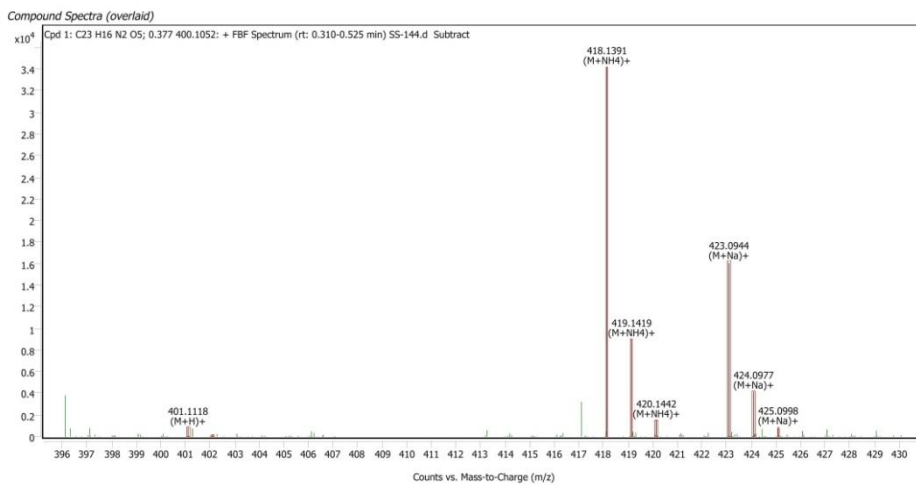
¹H-NMR spectra:



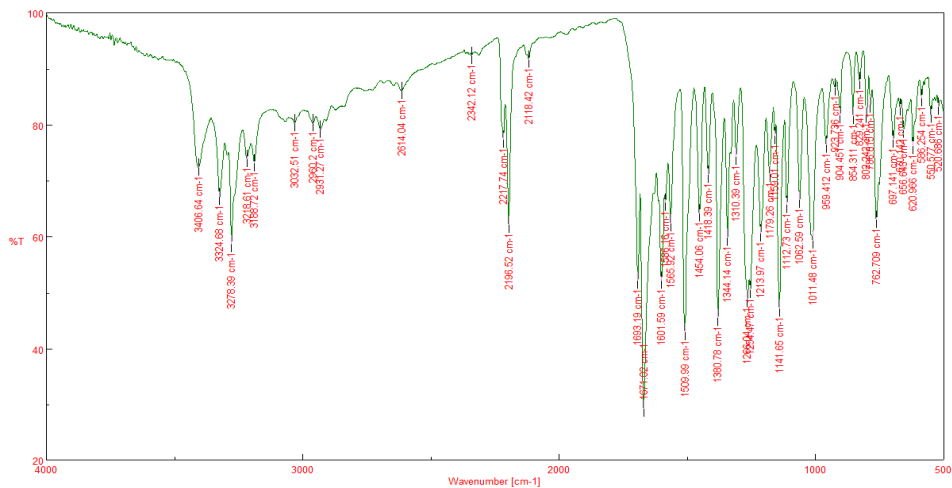
HRMS:



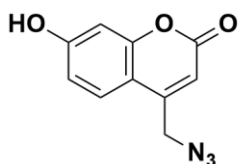
HRMS:



IR Spectra:

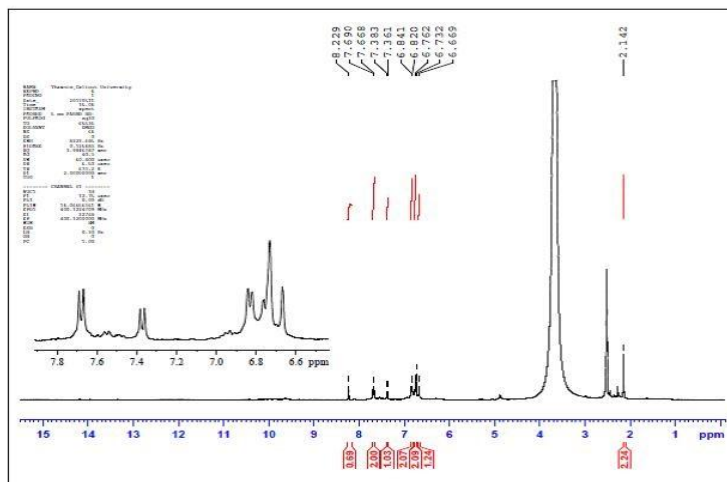


Spectral Details of 4-azidomethylumbelliferone (Coumarin-azide)

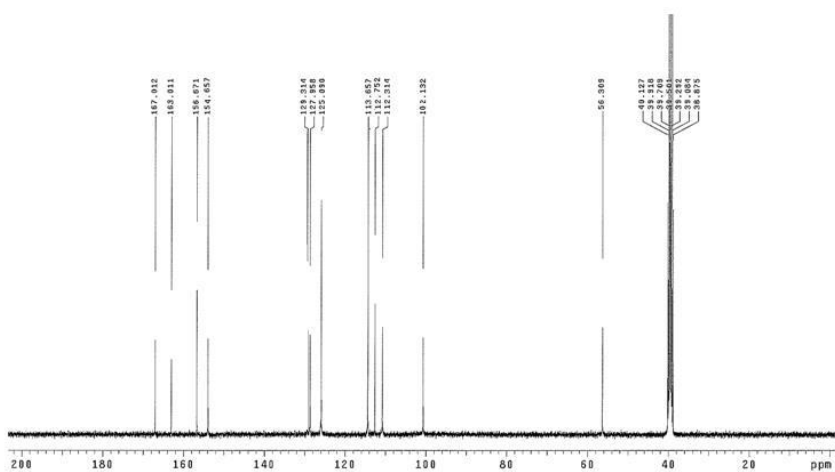


4-(azidomethyl)-7-hydroxy-2*H*-chromen-2-one

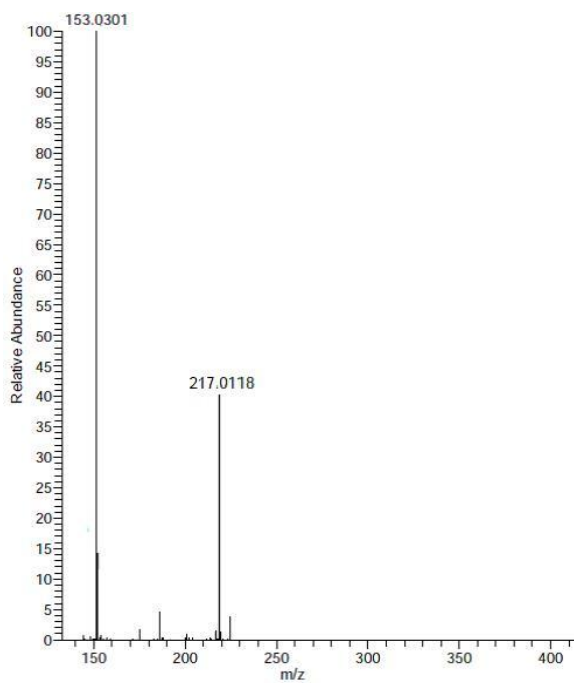
¹H-NMR spectra:



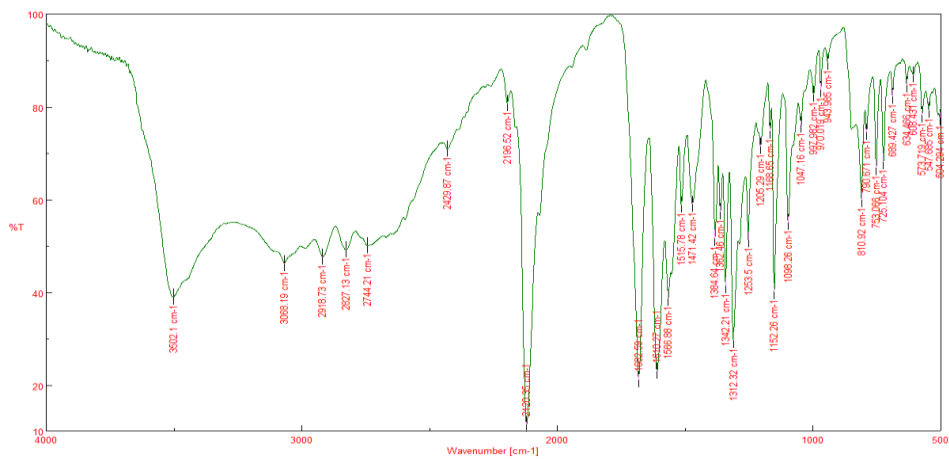
¹³C-NMR Spectra:



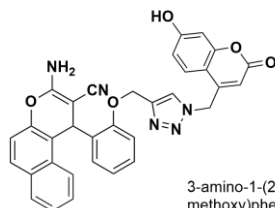
HRMS:



IR Spectra:

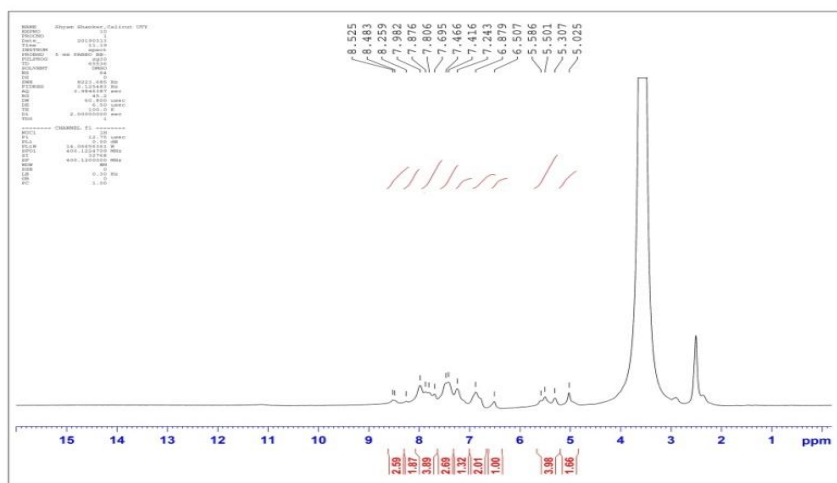


Spectral Details of T1:

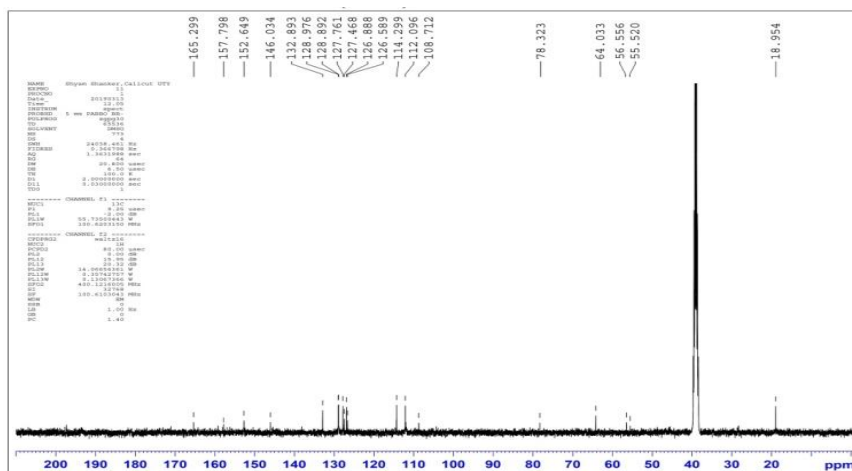


3-amino-1-(2-((1-((7-hydroxy-2-oxo-2H-chromen-4-yl)methyl)-1H-1,2,3-triazol-4-yl)methoxy)phenyl)-1H-benzo[f]chromene-2-carbonitrile

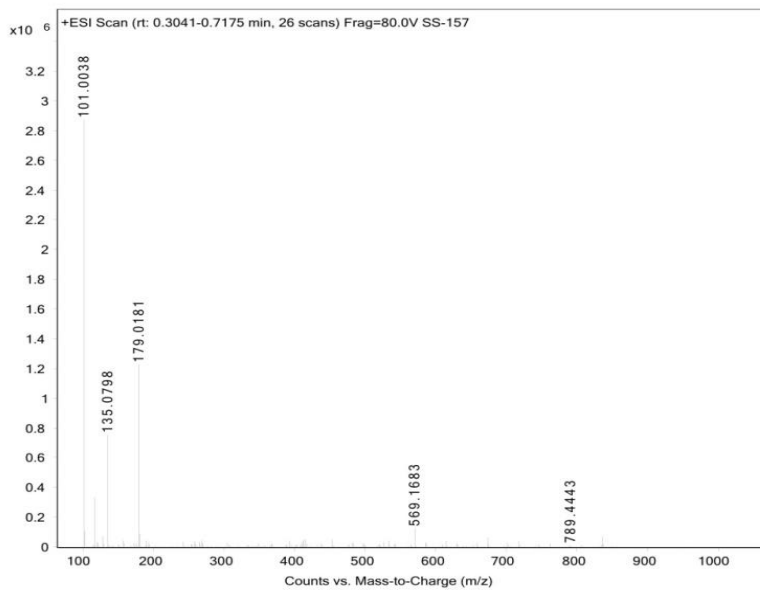
¹H-NMR spectra:



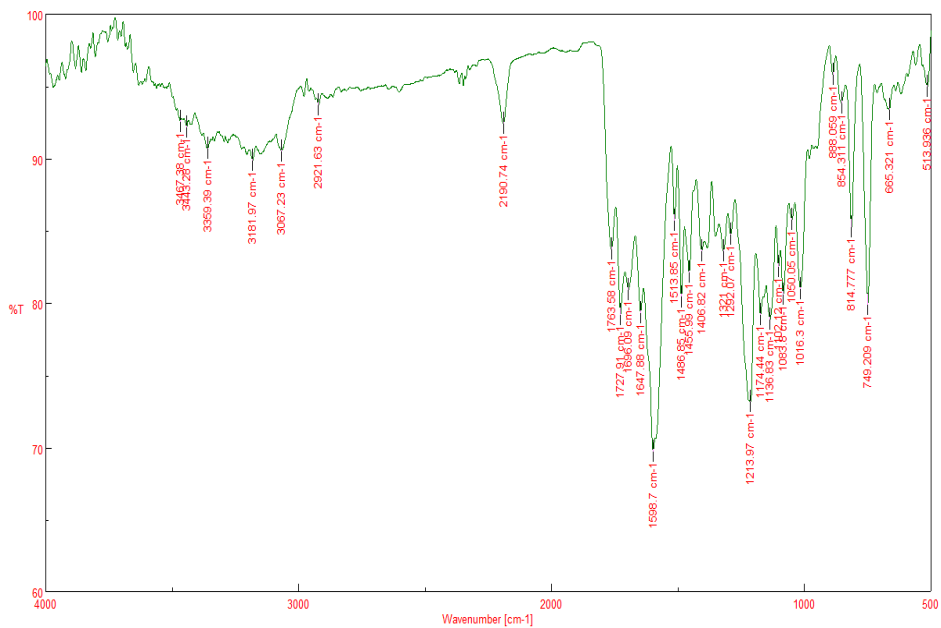
¹³C-NMR Spectra:



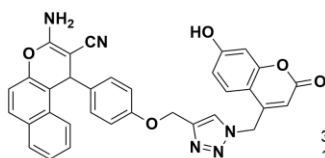
HRMS:



IR Spectra:

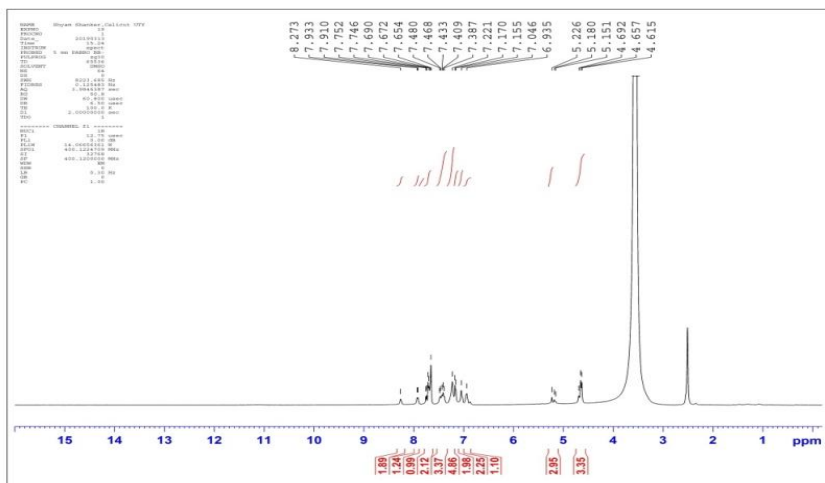


Spectral Details of T2:

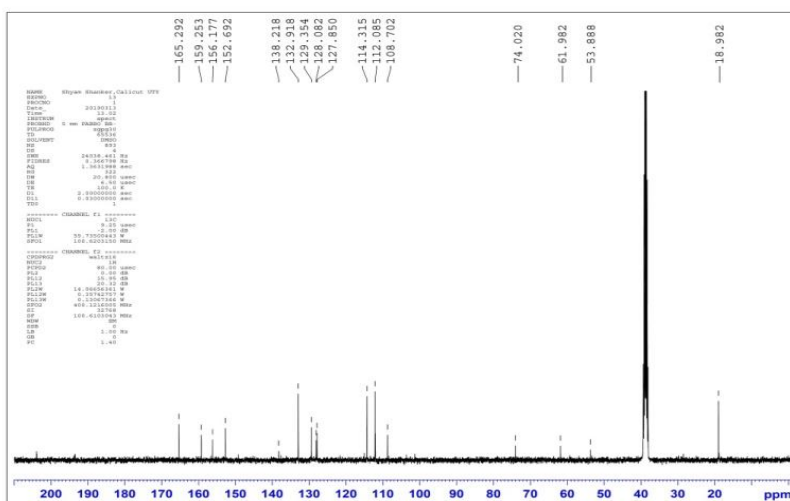


3-amino-1-(4-((1-((7-hydroxy-2-oxo-2H-chromen-4-yl)methyl)-1H-1,2,3-triazol-4-yl)methoxy)phenyl)-1H-benzof[chromene-2-carbonitrile

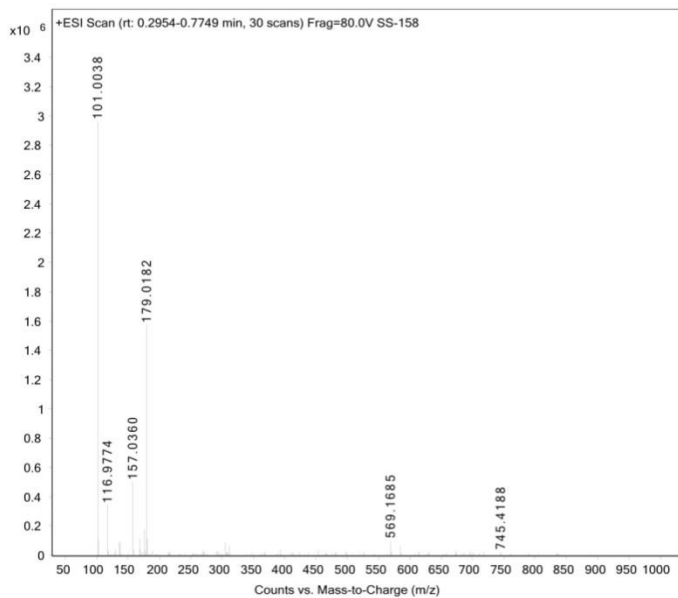
¹H-NMR:



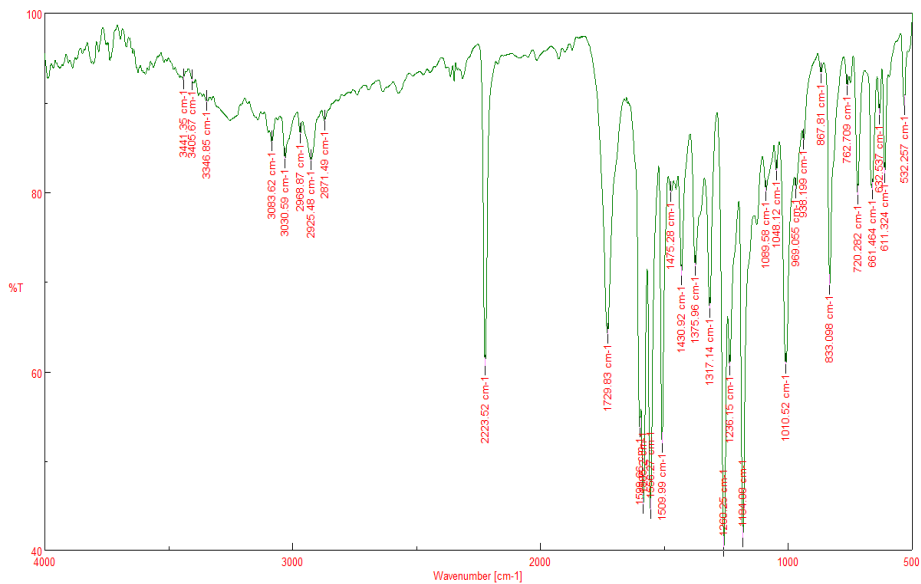
¹³C-NMR Spectra:



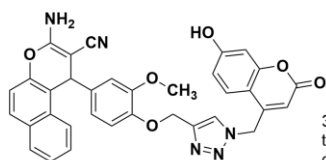
HRMS:



IR Spectra:

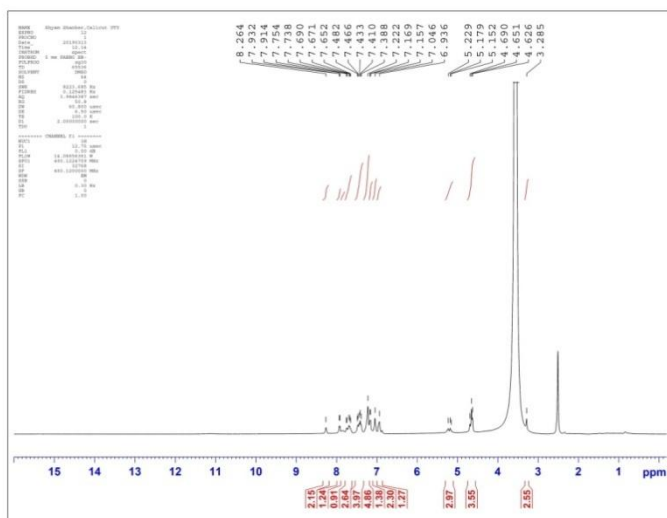


Spectral Details of T3:

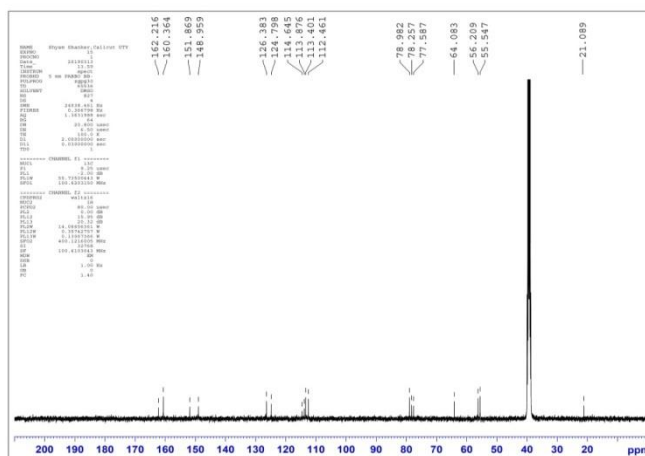


3-amino-1-4-((1-((7-hydroxy-2-oxo-2H-chromen-4-yl)methyl)-1H-1,2,3-triazol-4-yl)methoxy)-3-methoxyphenyl)-1H-benzo[f]chromene-2-carbonitrile

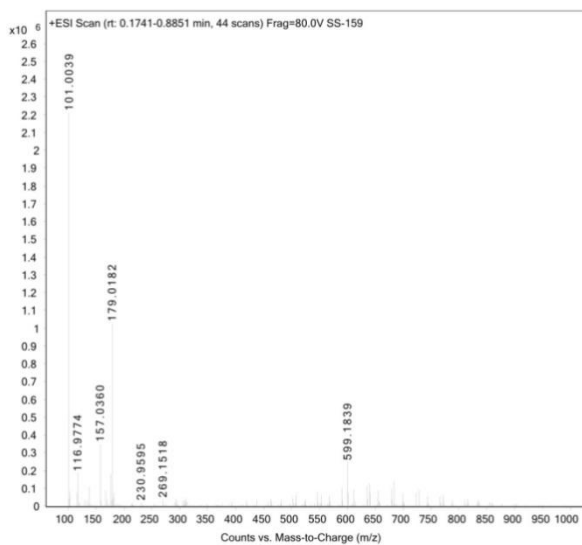
¹H-NMR Spectra:



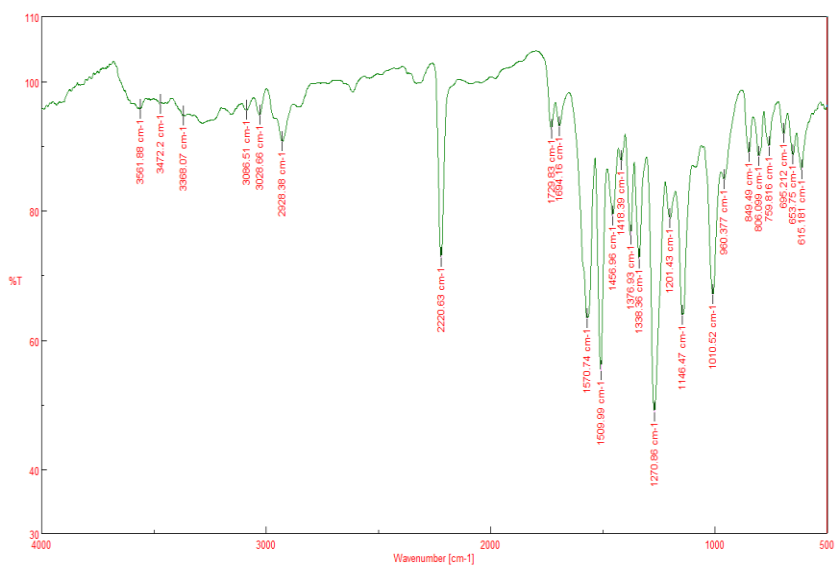
¹³C-NMR Spectra:



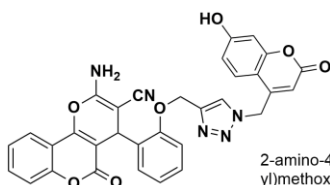
HRMS:



IR Spectra:

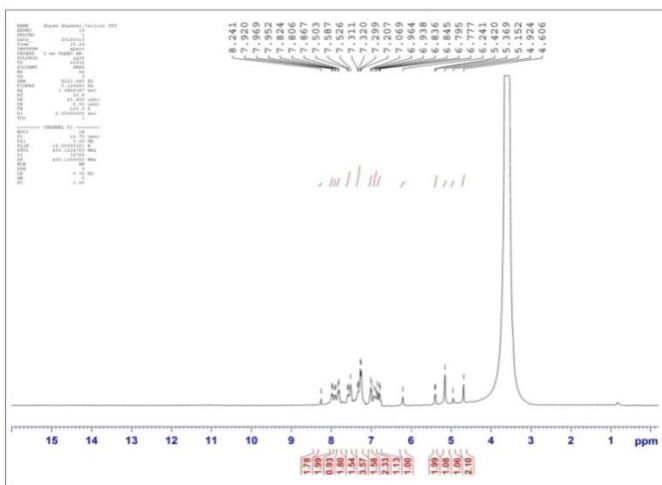


Spectral Details of **T4**:

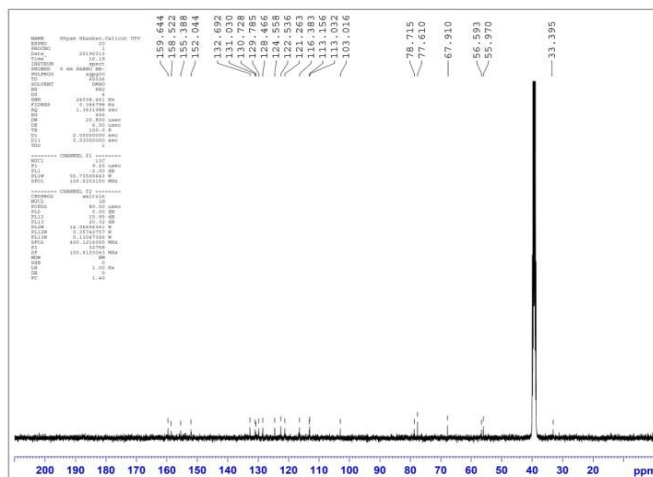


2-amino-4-(2-((1-(7-hydroxy-2-oxo-2H-chromen-4-yl)methyl)-1H-1,2,3-triazol-4-yl)methoxy)phenyl)-5-oxo-4,5-dihydroprano[3,2-c]chromene-3-carbonitrile

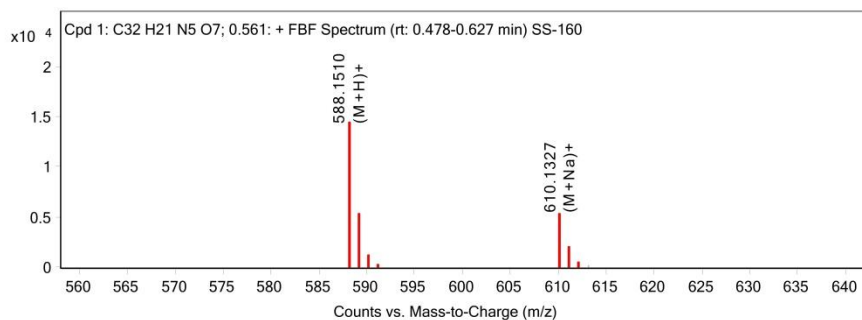
¹H-NMR Spectra:



¹³C-NMR Spectra:



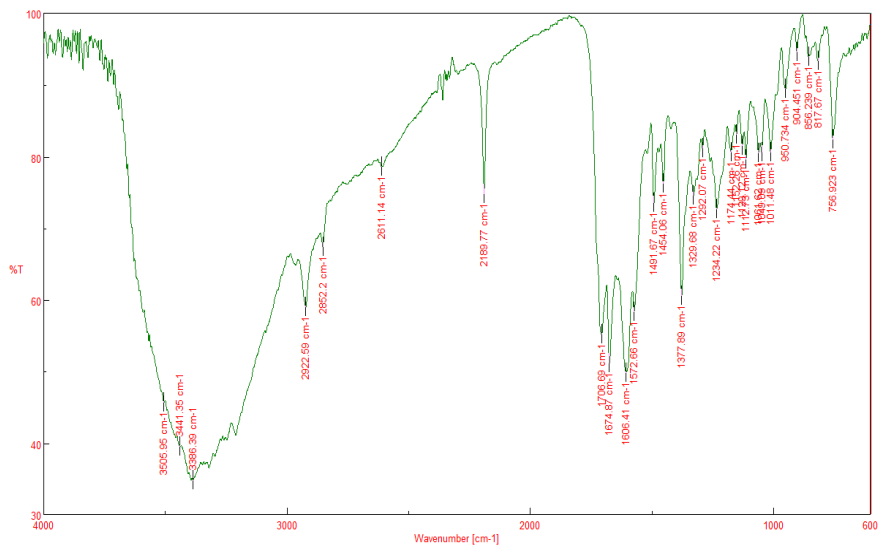
HRMS:



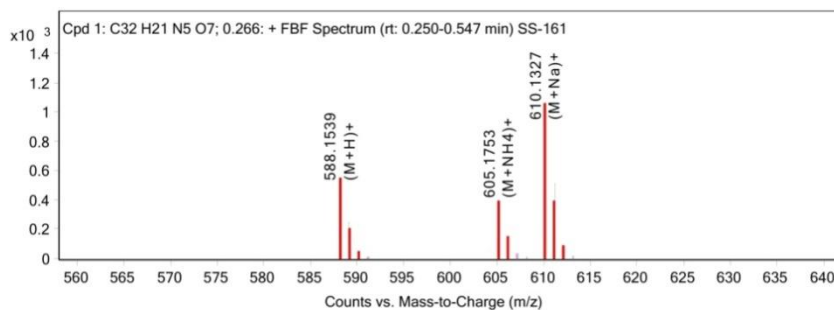
MS Spectrum Peak List

m/z	z	Abund	Ion
588.151	1	14450.09	(M+H)+
589.1336	1	5028.03	(M+H)+
590.1593	1	1088.4	(M+H)+
591.1611	1	148.06	(M+H)+
610.1327	1	5104.92	(M+Na)+
611.136	1	2031.72	(M+Na)+
612.1366	1	536.34	(M+Na)+

IR Spectra:



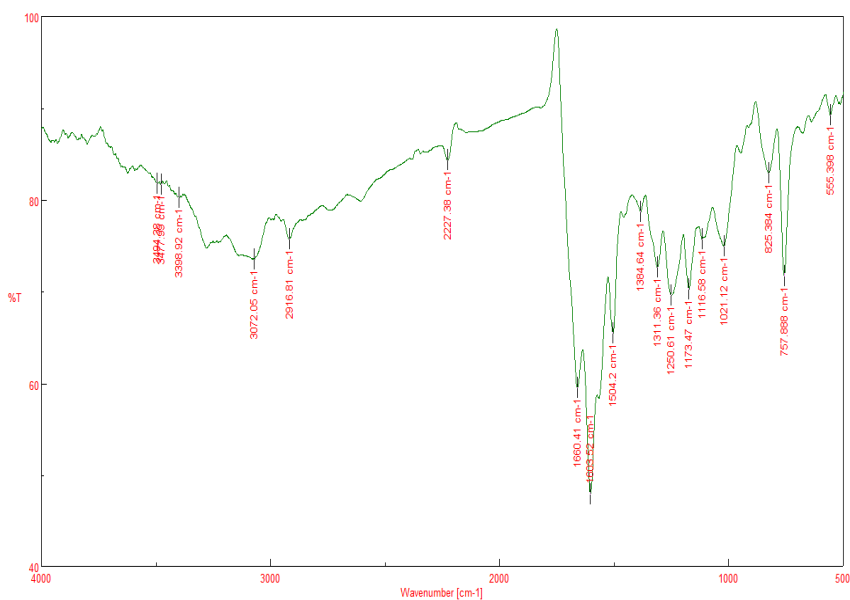
HRMS:



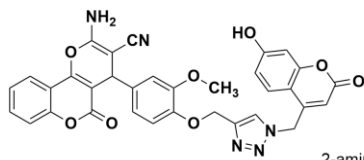
MS Spectrum Peak List

m/z	z	Abund	Ion
588.1539	1	516.73	(M+H) ⁺
589.1548	1	253.31	(M+H) ⁺
590.1597	1	23.38	(M+H) ⁺
605.1753	1	393.75	(M+NH4) ⁺
606.1803	1	114.54	(M+NH4) ⁺
610.1327	1	962.47	(M+Na) ⁺
611.1348	1	517.38	(M+Na) ⁺
612.1348	1	46.68	(M+Na) ⁺

IR Spectra:

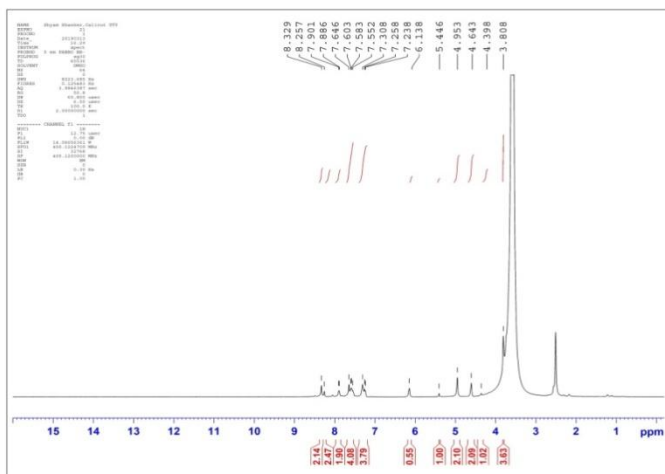


Spectral Details of T6:

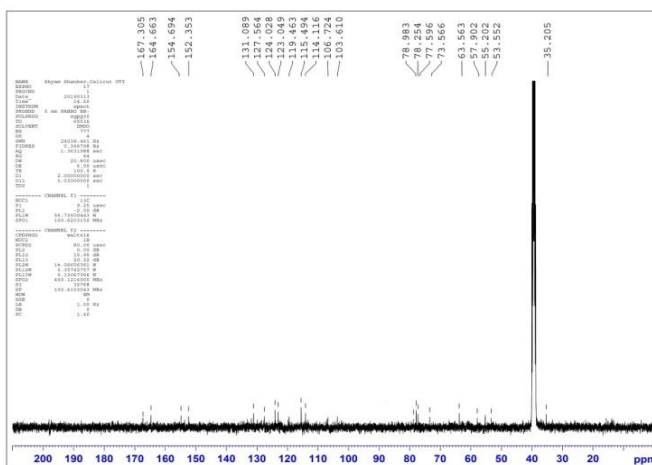


2-amino-4-((1-((7-hydroxy-2-oxo-2H-chromen-4-yl)methyl)-1H-1,2,3-triazol-4-yl)methoxy)-3-methoxyphenyl)-5-oxo-4,5-dihydroprano[3,2-c]chromene-3-carbonitrile

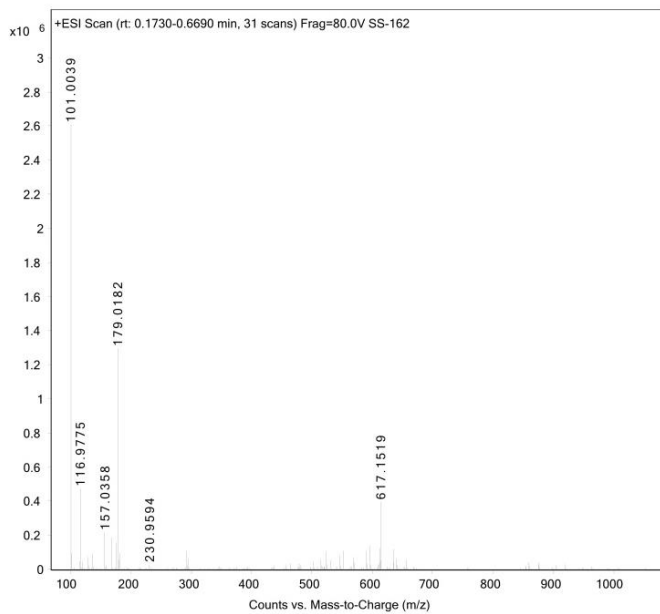
¹H-NMR Spectra:



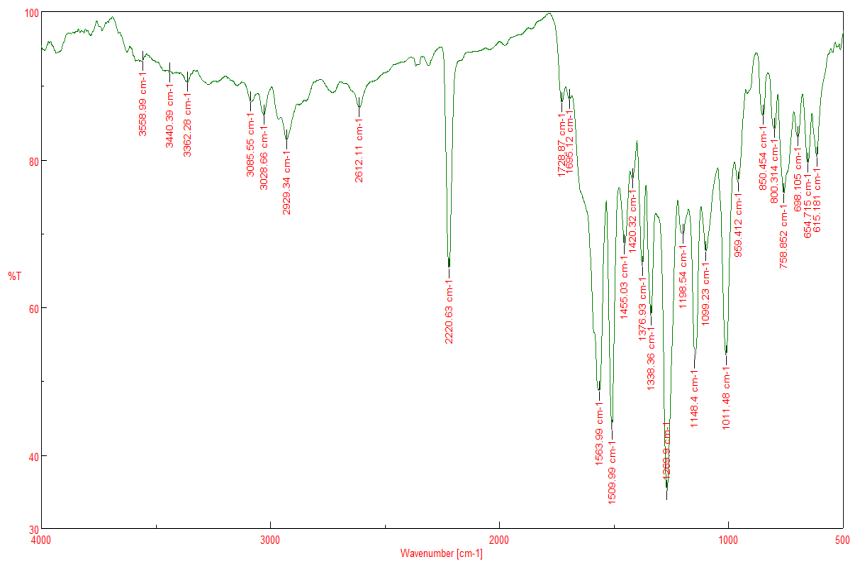
¹³C-NMR Spectra:



HRMS:



IR Spectra:



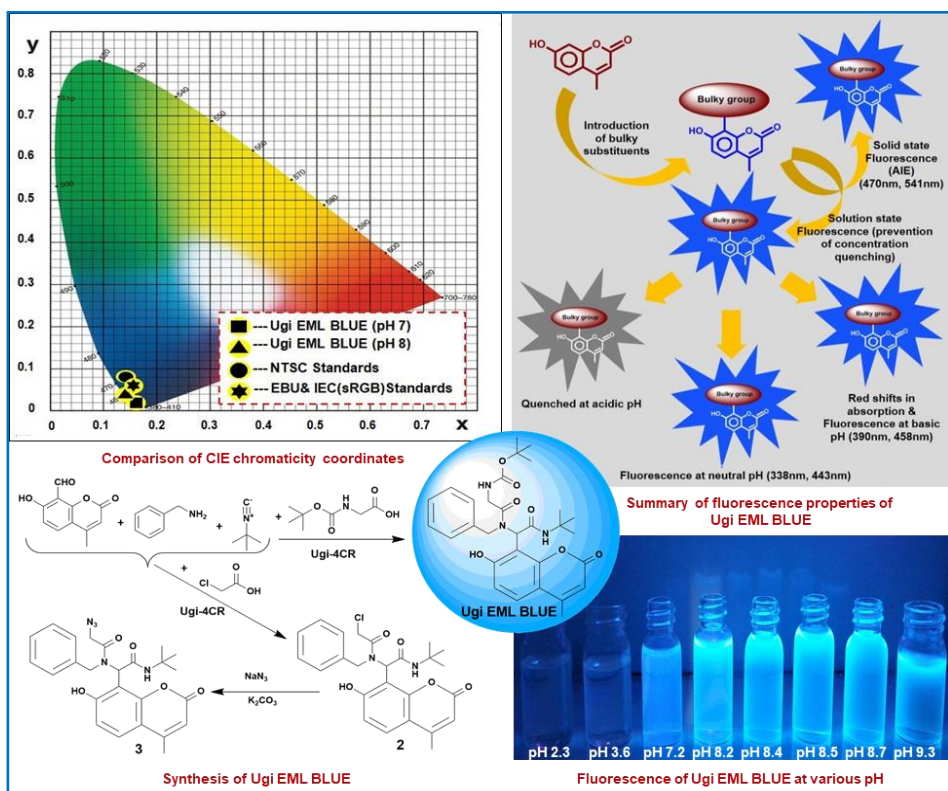
CONCLUSIONS AND FUTURE PERSPECTIVES

As discussed in chapters 2 to 4, this study has demonstrated the development of facile synthetic routes to the efficient fluorescent probes/inhibitors decorated with the appropriate functionalities and their applications in various fields such as material, bioimaging and anticancer agents.

The thesis is divided into five chapters. The first chapter presents an overview of the importance of simple and properly functionalized coumarin/chromene derivatives in the fields of material applications, cellular level bioimaging and medicinal applications. Moreover, few potential synthetic strategies which can be used for the proper functionalization of the aforesaid molecules also discussed in this chapter.

In chapter 2, presented a multicomponent reaction (MCR) assisted step economic protocol for the synthesis of coumarin based deep blue emitting fluorescent molecule named as “Ugi EML BLUE” suitable for the applications related to light emission. The solution state and solid state fluorescence, pH sensitivity and significant physical properties were evaluated. The integration of a bulky carboxamide moiety to the 8-position of a coumarin scaffold through MCR afforded an excellent deep blue emission in the solution state with remarkable color purity (λ_{ems} 443nm; C.I.E. X=0.162, Y=0.012; HOMO/LUMO=-5.94eV/-1.60eV) suitable for a broad spectrum of applications. A plausible mechanism for

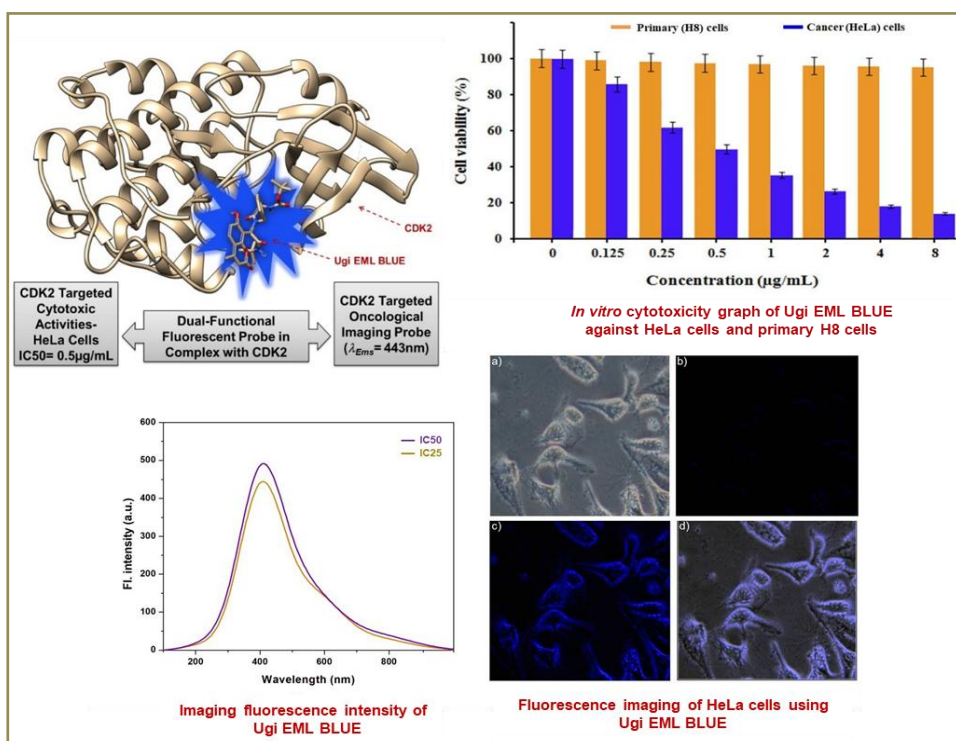
the observed fluorescence is also provided based on experimental and computational data analysis. A graphical representation of the work presented in chapter 2 is given in Scheme 1.



Scheme 1. Graphical representation of the work presented in chapter 2

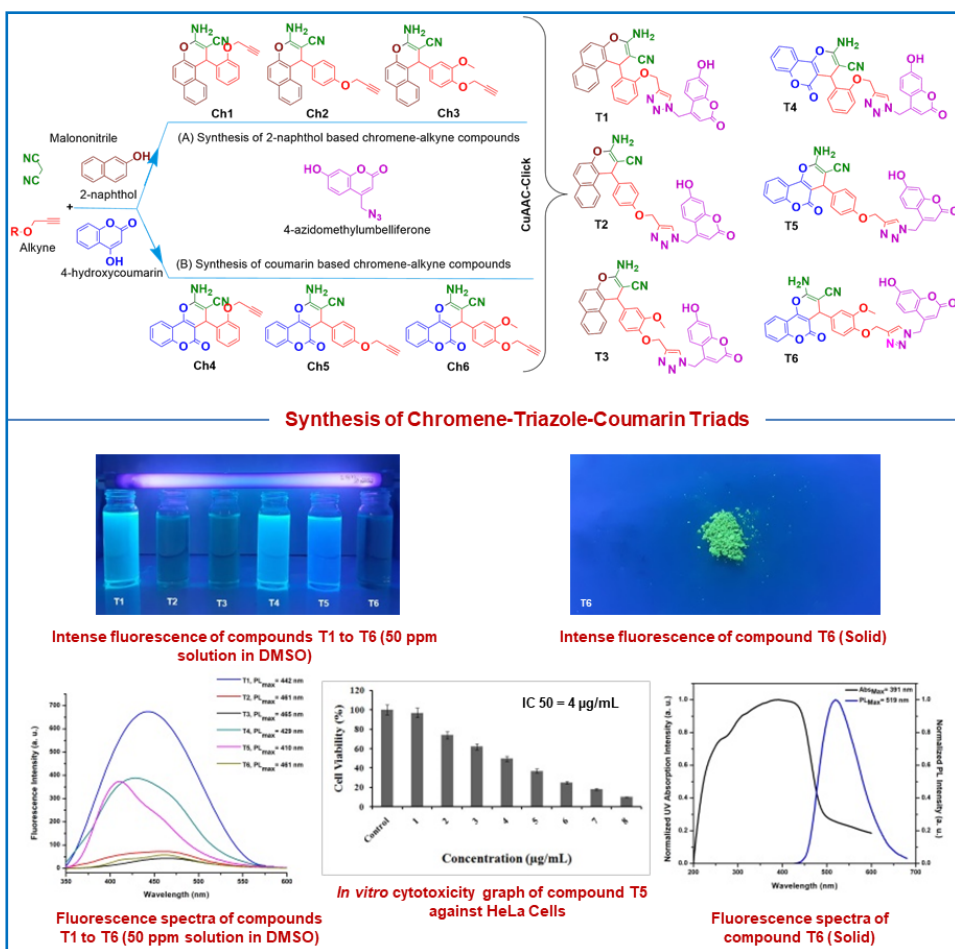
Chapter 3 is the continuation of chapter 2 and presented the biological applications of the Intramolecular Charge Transfer (ICT) based blue-emitting fluorescent probe Ugi EML BLUE. The binding properties of the Ugi EML BLUE against human CDK2 protein were studied via docking methods. The docking studies showed that Ugi EML BLUE can effectively interact with the ATP binding sites of CDK2. The positive results obtained from the docking studies were extended to the bioimaging as well as antineoplastic applications on HeLa cells. The *in*

in vitro biological activity studies revealed the remarkable potential of Ugi EML BLUE as a dual functional molecule that can be used not only as a CDK2 targeted fluorescent probe for bioimaging (λ_{abs} 338 nm, λ_{ems} 443nm) but also as a CDK2 targeted inhibitor for HeLa cells (IC 50: 0.5 $\mu\text{g}/\text{mL}$). At the subcellular level, Ugi EML BLUE can selectively interact with the ATP binding sites of the activated CDK2 to arrest the transfer of phosphate groups from its bound ATP to the serine and threonine residues of the target substrates involved in DNA transcription and replication initiated at the G1 cell cycle phase and which will lead to the inhibition of tumor growth. Graphical abstract of the work presented in chapter 3 is presented in Scheme 2.



Scheme 2. Graphical representation of the work presented in chapter 3

In chapter 4, presented a new series of Chromene-Triazole-Coumarin Triads (**T1** to **T6**) synthesized through the employment of a solvent free mechanochemical multicomponent reaction followed by copper catalyzed (3+2) azide-alkyne cycloaddition (click chemistry). The molecules were investigated for their fluorescence and CDKs induced anticancer properties.



Scheme 3. Graphical representation of the work presented in chapter 4

Half numbers of the molecules such as **T1**, **T4** and **T5** showed fluorescence in the solution state through ICT based electronic transitions whereas, the other half such as **T2**, **T3** and **T6** showed solid state fluorescence through aggregation induction. Computational studies on binding affinity revealed that all the molecules are in general selective towards CDK2 and CDK4. The studies on *in vitro* biological activities showed that the molecules **T2** and **T5** are promising for undertaking further studies to develop them as fluorescent inhibitors of CDK2/CDK4 induced tumors. **T2** and **T5** showed an IC₅₀ of 7.5 μg/mL and 4 μg/mL respectively against human cervical cancer cell line (HeLa). A graphical representation of the work presented in chapter 3 is given in Scheme 3.

In conclusion, during this whole work, we have decorated the Coumarin and Chromene moieties with suitable functionalities using the MCR-Click protocols and obtained the simple or triazole linked peptidomimetic fluorophores. The overall photophysical, as well as biological properties observed for such probes, are comparable with many of the commercially available probes. However, the observed properties can be optimized by in-depth photophysical, structure-activity studies and biochemical analysis to bring out their potential for various material applications as well as the imaging and inhibition of a variety of the cancer cells. The success of such studies will make an impact on the development of cost-effective cancer therapeutics and efficient fluorescent probes for the broad spectrum of applications. The photophysical and biological properties of the selected molecules in this work are summarized in Table 1 to Table 4.

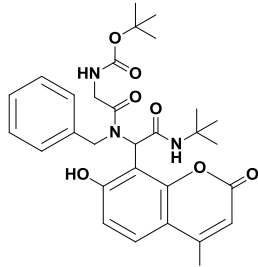
 <p><i>tert</i>-butyl (2-(benzyl(2-(<i>tert</i>-butylamino)-1-(7-hydroxy-4-methyl-coumarin-8-yl)-2-oxoethyl)amino)-2-oxoethyl)carbamate</p>	
Compound name	Ugi EML BLUE
Appearance	Yellowish-brown solid
Melting Point(°C)	178
UVabs Max (nm) (solution)	338 (pH 7), 390 (pH 8)
PLens Max (nm) (solution)	443 (pH 7), 458 (pH 8)
Quantum Yield (Φ)	0.12 (pH 7), 0.21 (pH 8)
Color	Deep Blue
C.I.E. (x, y) (pH7)	0.16, 0.01
C.I.E. (x, y) (pH8)	0.14, 0.03
UVabs Max (nm) (solid)	470
PLens Max (nm) (solid)	541
HOMO (eV)	-5.12
LUMO (eV)	-2.42
Number of Synthetic Steps	2
Synthetic strategy	MCR
Solubility	DMSO, Ethanol, Ethanol-Water
Studied cell line	Human Cervical Cancer (HeLa)
Targeting protein	CDK2
IC50	0.5 µg/mL
Plausible inhibition mechanism	Perturbing the target phosphorylation from active CDK2

Table 1. Photophysical and Biological properties of Ugi EML BLUE

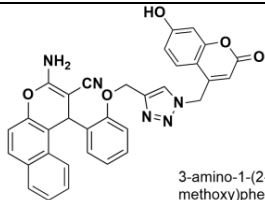
 3-amino-1-(2-((1-((7-hydroxy-2-oxo-2H-chromen-4-yl)methyl)-1H-1,2,3-triazol-4-yl)methoxy)phenyl)-1H-benzof[chromene-2-carbonitrile	
Compound name	Chromene-Triazole-Coumarin Triad 1 (T1)
Appearance	White solid
Solubility	DMSO
Melting Point(°C)	192
UV Abs_{Max} (nm) (solution)	326
PL_{Max} (nm) (solution)	442
HOMO (eV)	-6.06
LUMO (eV)	-2.52
Stoke's Shift (nm)	116
Quantum Yield (Φ)	0.95 (Ref: Quininesulphate, Φ=0.54)
Number of synthetic steps	Three
Synthetic protocol	MCR-Click

Table 2. Photophysical properties of Chromene-Triazole-Coumarin Triad 1

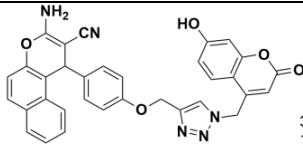
 3-amino-1-(4-((1-((7-hydroxy-2-oxo-2H-chromen-4-yl)methyl)-1H-1,2,3-triazol-4-yl)methoxy)phenyl)-1H-benzof[chromene-2-carbonitrile	
Compound name	Chromene-Triazole-Coumarin Triad 2 (T2)
Appearance	White solid
Melting Point(°C)	196
Solubility	DMSO
UVabs Max (nm) (solid)	379
PLens Max (nm) (solid)	515
HOMO (eV)	-6.04
LUMO (eV)	-2.39
Targeting kinase	CDK2/CDK4
Binding Affinity (kcal)	-9.1/-9.6
Studied cell line	Human Cervical Cancer (HeLa)
IC 50 (µg/mL)	7.5
Apoptotic Path	S phase arrest

Table 3. Photophysical and Biological properties of Chromene-Triazole-Coumarin Triad 2

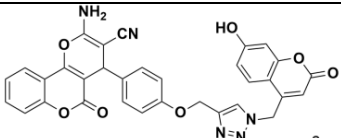
 2-amino-4-(4-((1-((7-hydroxy-2-oxo-2H-chromen-4-yl)methyl)-1H-1,2,3-triazol-4-yl)methoxy)phenyl)-5-oxo-4,5-dihydroprano[3,2-c]chromene-3-carbonitrile	
Compound name	Chromene-Triazole-Coumarin Triad 5 (T5)
Appearance	White solid
Melting Point(°C)	190
Solubility	DMSO
UVabs Max (nm) (solution)	331
PLems Max (nm) (solution)	410
Stoke's Shift (nm)	79
HOMO (eV)	-6.30
LUMO (eV)	-2.40
Quantum Yield (Φ)	0.72 (Ref: Quininesulphate, Φ=0.54)
Targeting kinase	CDK2/CDK4
Binding Affinity (kcal)	-10.5/-9.4
Studied cell line	Human Cervical Cancer (HeLa)
IC 50 (µg/mL)	4
Apoptotic Path	G1 phase arrest

Table 4. Photophysical and Biological properties of Chromene-Triazole-Coumarin Triad 5

Research papers published

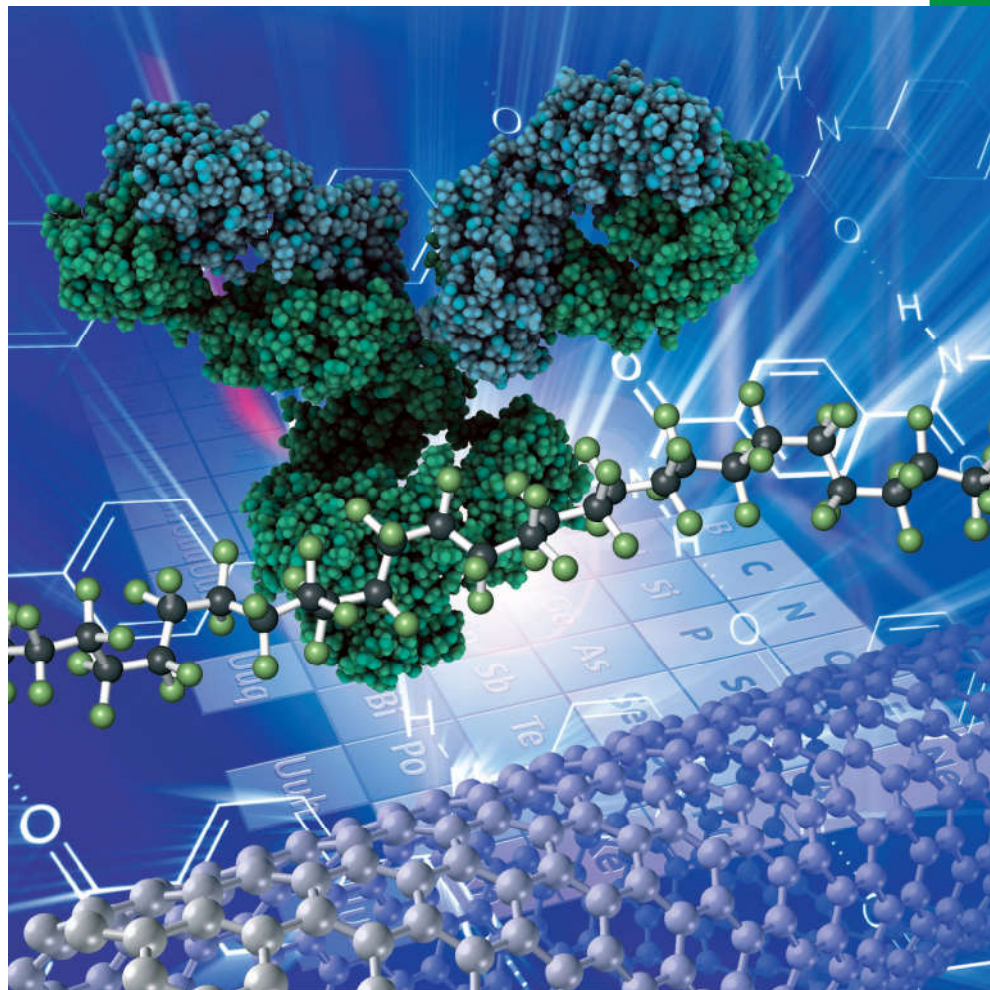
1. Puthumana, S. S. E.; Bahulayan, D. Multicomponent-Reaction-(MCR-) Assisted Synthesis of a Coumarin-Based Deep Blue Emitter for OLEDs and Related Applications, *ChemistrySelect* **2018**, *3*, 2951-2957.
2. Puthumana, S. S. E.; Bahulayan, D. ICT-Based Blue-Emitting Dual-Functional Probe (Ugi EML BLUE) for Bio-Imaging and Cytotoxic Activities on HeLa Cells, *ChemistrySelect* **2019**, *4*, 5366–5374.
3. Shyam Shankar, E. P.; Bahulayan, D. Chemistry, Chemical Biology and Photophysics of Certain New Chromene-Triazole-Coumarin Triads as Fluorescent Inhibitors of CDK2 and CDK4 Induced Cancers, *New J. Chem.* **2019**, *43*, 13863-13872.

Research Publications

Chemistry **SELECT** ✓

www.chemistryselect.org

A journal of



REPRINT

WILEY-VCH

Energy Technology & Environmental Science

Multicomponent-Reaction- (MCR-) Assisted Synthesis of a Coumarin-Based Deep Blue Emitter for OLEDs and Related Applications

Shyam Shankar Eramangalam Puthumana and Bahulayan Damodaran^{*[a]}

The lighting and display solutions of the future are Organic Light Emitting Diodes (OLEDs). For the electron transportation, hole transportation and light emission, sequential layers of specially designed organic molecules and materials are used in OLEDs. The perfect blue-emitters showing CIE (Commission Internationale de l'Eclairage) coordinates with a y-component

smaller than 0.1 are highly desired for OLED technology. Herein we report an efficient step economic protocol for the synthesis of a deep blue emitting fluorescent molecule named as "Ugi EML BLUE" ($\lambda_{\text{em}} = 443 \text{ nm}$; C.I.E. X=0.162, Y=0.012; HOMO/LUMO = -5.94 eV/-1.60 eV) suitable for the emissive layers (EML) of OLEDs and related applications.

Introduction

Organic Light Emitting Diodes (OLEDs) have potential applications in the area of ultra-thin full color displays as well as solid state lighting.^[1,2] In general, an OLED consists of three organic layers sandwiched between the electrodes. The organic layers adjacent to cathode and anode are the Electron Transport Layer (ETL) and Hole Transport Layer (HTL) respectively. The electrons and holes are injected from the opposite poles to these organic layers and are collected at the Emissive Layer (EML). The electron-hole recombination at the emissive layer leads to the formation of singlet excitons that decay radiatively.^[3,4] Emissive layer usually consists of light emitting dyes or such small organic molecules which plays a crucial role in the external quantum efficiency (EQE) of the LED or OLED. Full color display is generally achieved by mixing equal intensity and equal stability red, yellow, green and deep blue emitters together. In this combination, the blue emitter helps to reduce the power consumption of the device as well to generate other colors. Highly conjugated fluorescent or phosphorescent molecular systems are currently used as deep blue emitters in OLEDs.^[5-10] However, an inherent problem with these blue emitters is their wide band gap causing poor charge injection, exciton instability and consequent poor device performance. Molecules based on pyrene, anthracene, fluorene, di(styryl)arylene etc. are the most studied systems in this category showing excellent fluorescent quantum yield in solution state. However, these molecules suffer a fluorescence quenching in the solid state due to aggregation.

One of the methods to overcome fluorescence quenching at solid state is the introduction of bulky substituents to the emission core to attain non-coplanar structures of the emitters with restricted rotation.^[11,12] Such rational strategies have been employed to attain non-coplanar structures of anthracene, pyrene and coumarin derivatives by integrating bulky substituents such as tetraphenylsilane, triphenylbenzene, spirobifluorene or various carboxamide derivatives to them.^[13,14] However, the synthesis of such molecules involves multi-step protocols leading to the escalation of manufacturing cost. As an attempt to address this material problem, we decided to integrate various bulky carboxamide groups to the 8-position of 4-methyl-7-hydroxy coumarin core as shown in Figure 1.



Figure 1. Structure of coumarin derivatives and their Photoluminescence under UV light

[a] S. S. E. Puthumana, Prof. B. Damodaran
Department of Chemistry
University of Calicut
Malappuram 673635, Kerala, India
E-mail: bahulayan@yahoo.com

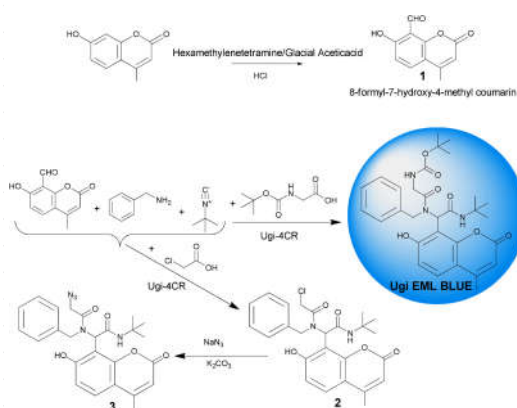
Supporting information for this article is available on the WWW under <https://doi.org/10.1002/slct.201702989>

Three new compounds such as **2**, **3** and Ugi EML BLUE were synthesized of which Ugi EML BLUE showed strong fluorescence in solution as well as in the solid state. The synthetic methodology was based on an Ugi four-component condensation (Ugi-4CC) which is a unique multicomponent reaction (MCR) for the diversity oriented synthesis of *N*-acylamino-carboxamides.^[15–18] Weak emission was observed for **2** and **3** with carboxamide groups at the 8 position of the coumarin. However, a significant enhancement in the blue emission was observed with Ugi EML BLUE which is obtained by substituting chlorine or the azide in **2** and **3** with a *tert*-butyl carbamate group.

Results and Discussion

The studies were started with the introduction of a carboxamide moiety at the 8 position of the coumarin core. For this we decided to use Ugi 4CR as our synthetic tool. Since Ugi reaction needs an aldehyde component along with an amine, a carboxylic acid and an isocyanide to produce carboxamide derivatives, we decided to introduce an aldehyde group to the 8 position of the coumarin.

This reaction was carried out as shown in Scheme 1 and the coumarin aldehyde **1** was obtained in high purity. The



Scheme 1. Synthesis of **1**, **2**, **3** and Ugi EML BLUE

coumarin aldehyde **1** was then reacted with chloroacetic acid, benzylamine (electron rich), *tert*-butyl isocyanide (contains an electron pushing *tert*-butyl group and ‘–NC’ bond which makes the molecule electron dense) to form the carboxamide chloride **2** as shown in Scheme 1. **2** showed a weak fluorescence under UV light (Figure 2E) and no fluorescence in the solid state under UV irradiation. Subsequently, chlorine in **2** was substituted with an azide moiety to obtain **3** by reacting **2** with sodium azide as shown in Scheme 1. This compound also showed a very weak fluorescence in the solution state (Figure 2F) and no fluorescence in the solid state. The weak fluorescence observed for the starting 7-hydroxy-4-methyl coumarin, its aldehyde

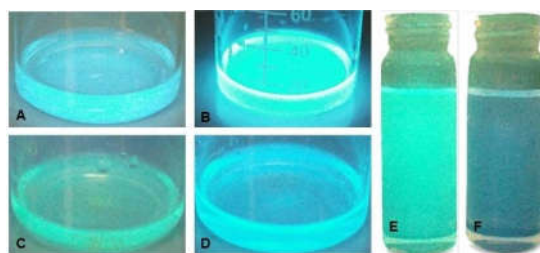


Figure 2. Fluorescence of 7-hydroxy-4-methyl coumarin at pH 7 (A) and pH 8 (B), Fluorescence of **1** at pH 7 (C) and pH 8 (D), Fluorescence of **2** (E) and **3** (F).

derivative **1** in neutral and alkaline pH are shown in Figures 2A–D. Since all the three compounds showed only weak fluorescence, we decided to introduce a more bulky group to the 8 position of the coumarin. For this, we used Boc-glycine as our carboxylic acid component in the Ugi 4CR, as shown in Scheme 1. The Ugi EML BLUE thus obtained showed significant enhancement in fluorescence in the solution state as shown in Figure 3. A thin film of this material was prepared by drop casting an ethanol solution of this material on top of a glass substrate. This thin film also showed strong fluorescence as shown in Figure 4. The film was then kept at ambient and photographed its fluorescence at various time intervals. The film did not show any significant decrease in fluorescence even after one day. However, the same film when subjected to heat

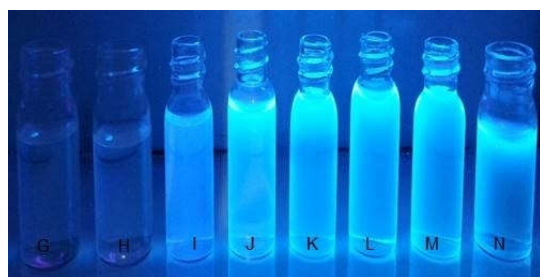


Figure 3. Fluorescence of Ugi EML BLUE at G) pH 2.3, H) pH 3.6, I) pH 7.2, J) pH 8.2, K) pH 8.4, L) pH 8.5, M) pH 8.7, N) pH 9.3



Figure 4. Solid state Fluorescence of Ugi EML BLUE: O) an air dried film made by drop casting an ethanol solution of Ugi EML BLUE on a glass substrate. P) Yellowish-green fluorescence showed by film O when subjected to thermal annealing at 70°C for 15 minutes. Q) Reinstating the bluish fluorescence by ethanol vapour etching.

treatment at 70°C for 15 minutes showed a yellowish green fluorescence as shown in Figure 4P.

The structural and photo-physical characterization of Ugi EML BLUE was carried out using XRD, NMR, AFM, thermo gravimetric, UV-Vis and fluorescence measurements. Figure 5 shows the X-Ray diffraction pattern of the Ugi EML BLUE and from the graph it is clear that the material is crystalline in nature. The Full Width at Half Maxima (FWHM) of the prominent peak observed at 2θ 18.92° is 0.600°, the inter planar distance (d) is 4.686 Å and the approximate particle size is 14.0 nm.^[19,20] The ultrafine size of the material allows the preparation of ultrafine thin layers while constructing the OLED devices.^[21–26,1–10] In addition to this, the molecule possess a sharp melting point (178°C) and which is in good agreement with the same obtained from the thermogravimetric analysis (Figure 6). The sharp melting at relatively high temperature also ensures good physicochemical properties towards its lighting applications.

Figure 7 shows the AFM histogram of the particle size distribution and Figure 8 shows the AFM images of Ugi EML BLUE. The AFM study of Ugi EML BLUE showed uniformly dispersed particles with an average size of 14–15 nm, which is

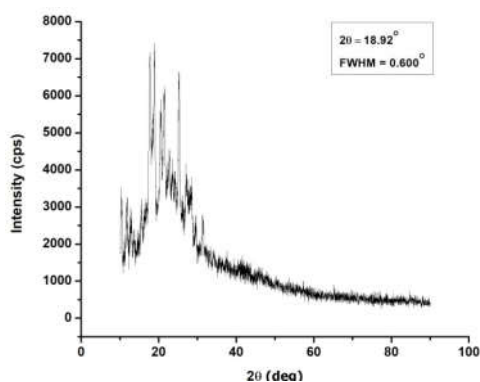


Figure 5. X-Ray diffraction pattern of Ugi EML BLUE

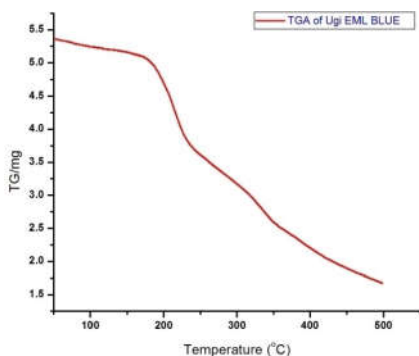


Figure 6. Thermogravimetric data of Ugi EML BLUE

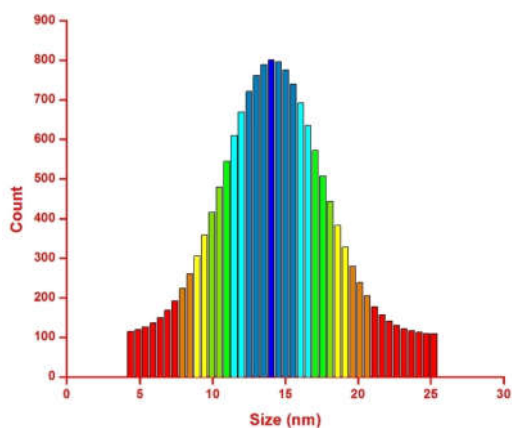


Figure 7. AFM Histogram: Size distribution of Ugi EML BLUE particles

in good agreement with the approximate particle size measured using X-Ray diffraction analysis.

The UV-Vis and PL spectra of the Ugi EML BLUE (50 ppm solution in DMSO) are shown in Figure 9 (pH 7). The solution state UV-Vis absorption maxima and PL emission maxima are observed at 338 nm and 443 nm respectively with a large Stokes shift of 105 nm. Ugi EML BLUE showed strong fluorescence in the solid state as well. The solid state UV-Vis absorption maxima and PL emission maxima of Ugi EML BLUE were observed at 470 nm and 541 nm respectively (Figure 10). The solid state fluorescence observed for the molecule is due to the unconventional phenomenon of Aggregation Induced Emission (AIE). The observed red shifts in the solid state absorption and emission are due to the restriction of intramolecular rotation (RIR) due to aggregation which in turn helps to create a pool of electrons conjugated within the system leading to red shifts in the absorption and emission. The solid state and solution state PL emission peaks at longer wavelengths (541 nm and 443 nm) reveal the presence of a transition like donor (coumarin core) to acceptor (introduced bulky groups) intramolecular charge transfer (ICT) transition in the system.^[27,28]

Interestingly, the solution state fluorescence of Ugi EML BLUE is sensitive to the changes in pH. The UV-Vis absorption and PL spectra of the Ugi EML BLUE (50 ppm solution in DMSO) at neutral pH (pH 7) and alkaline pH (pH 8) are shown in Figure 9. At pH 8 the UV-Vis absorption maxima and emission maxima are red-shifted to 390 nm and 458 nm respectively, whereas at acidic pH the fluorescence was found to be quenched.

In Ugi EML BLUE, the intramolecular charge transfer (ICT) type electronic transitions in between the coumarin core and the introduced bulky substituents are responsible for the characteristic absorption and emission properties observed at various pH. At neutral pH, the electronic transitions occur normally on excitation and showed the absorption and emission peaks at 338 nm and 443 nm respectively. However in

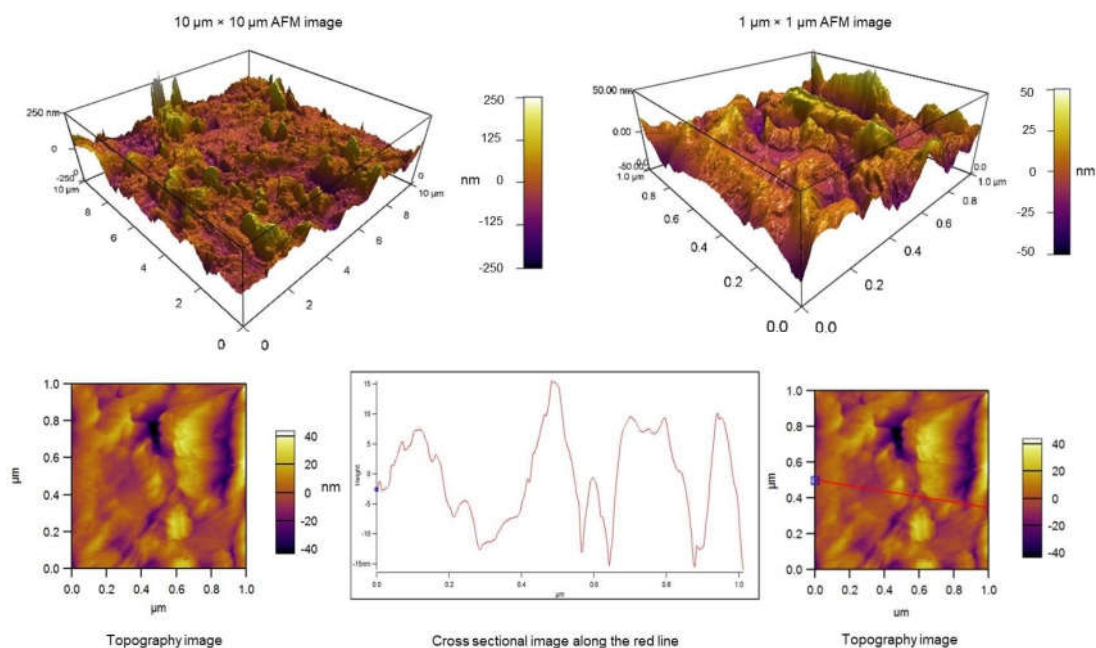


Figure 8. AFM images of Ugi EML BLUE

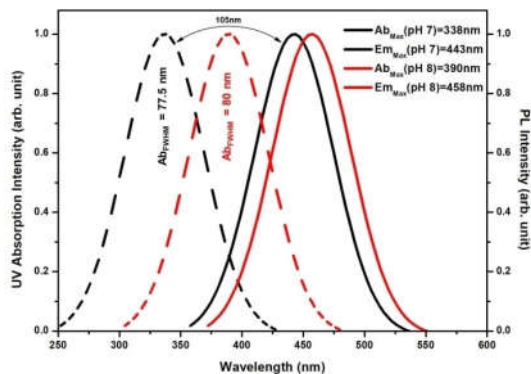


Figure 9. UV-Vis absorption (dashed lines) and PL spectra (solid lines) of Ugi EML BLUE at pH 7 and pH 8

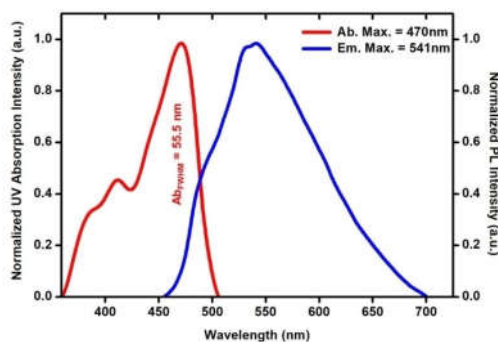


Figure 10. Solid state absorption and emission spectra of Ugi EMLBLUE

the basic condition, the hydroxyl proton of coumarin core are in the deprotonate state and can cause resonance transformations. Due to this resonance, the overall electron density in the coumarin core increases and which in turn reduces the energy requirement for the ICT type electronic transitions within the system. This causes the red shift of the absorption and emission peaks to 390 nm and 458 nm respectively. Similarly, at acidic pH the abstraction of transitive electrons by the hydrons will hinder the electronic transitions from the coumarin core

leading to the quenching of the fluorescence.^[29,30] These observations are summarized in the Figure 11.

The fluorescence quantum yields of the material Ugi EML BLUE at pH 7 and 8 were measured in DMSO using anthracene as the standard ($\phi = 0.27$) and were found to be 0.12 and 0.21 respectively.

The ground state geometry, HOMO/LUMO energies and the theoretical absorption wavelength of the Ugi EML BLUE in gas phase were obtained by means of density functional theory (DFT) and TD-DFT using the GAUSSIAN 09 software with the basis set B3LYP/6-31G*.^[31] The B3LYP/6-31G* basis set chosen

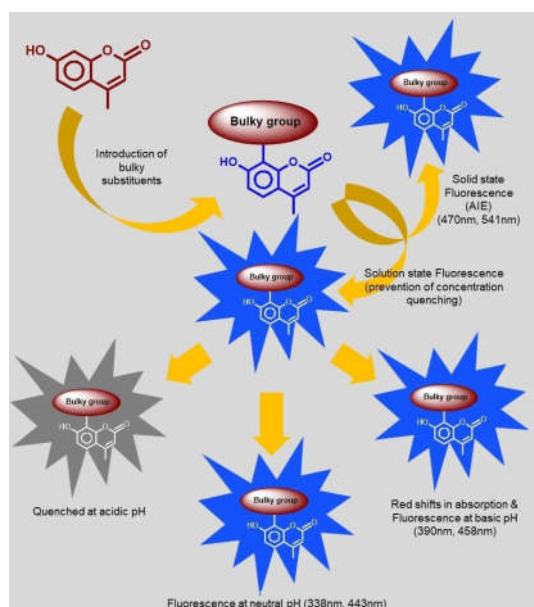


Figure 11. Summarized fluorescence properties of Ugi EML BLUE

for the DFT calculations was on the basis of the structural features of the molecule as well as on the basis of previous reports on its use in small organic molecules.^[32–36] In the present study with B3LYP/6-31G* basis set showed stable 'ground state absorption energy' and is very close to the experimental values. Figure 12 shows the optimized ground state geometry of Ugi EML BLUE and Figure 13 shows the images of HOMO and LUMO obtained by DFT method from which we can understand

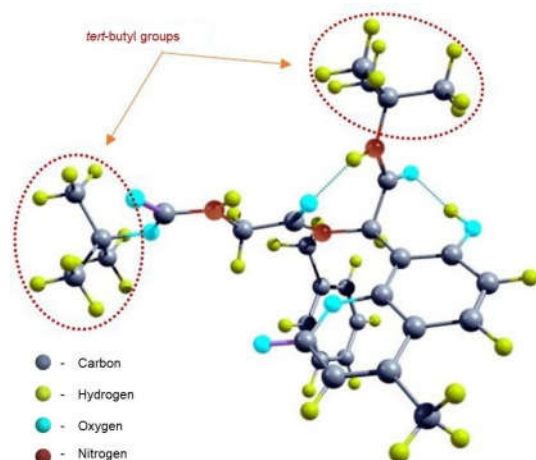


Figure 12. The optimized ground state geometry of Ugi EML BLUE

the extending of electron delocalisation through the bulkier substituents introduced on the coumarin core.

The Figure 13(A_H-A_L) reveals that the molecular conformation with two upper terminal *tert*-butyl group ensures the prevention of concentration quenching and enhances the fluorescence.^[21–26] The amide groups adjacent to the *tert*-butyl groups at each terminal pull the electrons while the *tert*-butyl groups push the electrons and the electron rich phenyl group shuttles the electron through the bonds inside and outside the ring. This push-pull mechanism enhances easier electronic movements. The optimized ground state geometry obtained for Ugi EML BLUE also supports the above mechanism perfectly. The DFT study also account for the ICT type transition within the Ugi EML BLUE molecule which we already understood from its observed longer emission peaks. The HOMO consist of the electron dense orbitals of coumarin core alone while the LUMO consists of the orbitals of coumarin core and the bulky groups (Figure 13 (B_H-B_L)), which implies the transfer of electrons from the coumarin core (donor) to the bulky groups (acceptor) on excitation. This extended electronic delocalisation observed in between the coumarin core and bulky groups help to facilitate the ICT type transitions in the molecule. From the TD-DFT calculations, the values of the absorption wavelength and the band gap at gas phase (theoretical) obtained are 482 nm and 2.6 eV respectively. The HOMO/LUMO energy levels of the Ugi EML BLUE are -5.12 eV/-2.42 eV respectively with a band gap of 2.7 eV which is responsible for the intense blue radiative decay of the excitons.^[1–4]

The TD-DFT computations were also carried out in a solvent (DMSO) environment using the solvent model IEFPCM.^[35,37,38] The solvent phase TD-DFT showed an absorption maxima at 346 nm and a band gap of 2.8 eV for the material. The solvent phase calculations are also in good agreement with the experimental data obtained.

The C.I.E. chromaticity coordinates for the intense blue color was calculated and compared with the standards. Figure 14 shows the positions of blue color of Ugi EML BLUE (at pH 7 and pH 8), NTSC standard, EBU standard and IEC (sRGB) standard in the CIE-1931 color space. Similarly, Table 1 shows

CIE coordinates	Ugi EML BLUE pH 7	Ugi EML BLUE pH 8	NTSC standard	EBU Standard	IEC Standard (sRGB)
CIE (x)	0.16	0.14	0.14	0.15	0.15
CIE (y)	0.01	0.03	0.08	0.06	0.06

the comparison of the C.I.E. chromaticity coordinates of Ugi EML BLUE with various color standards. The CIE coordinates of the Ugi EML BLUE at pH 7 (0.16, 0.01) and pH 8 (0.14, 0.03) are very near to the standard Blue CIE coordinates by the National Television System Committee (NTSC) (0.14, 0.08),^[39,40] European Broadcasting Union (EBU) (0.15, 0.06)^[41] and IEC (sRGB) (0.15, 0.06)^[42] television display criterion. As summarized in Table 2,

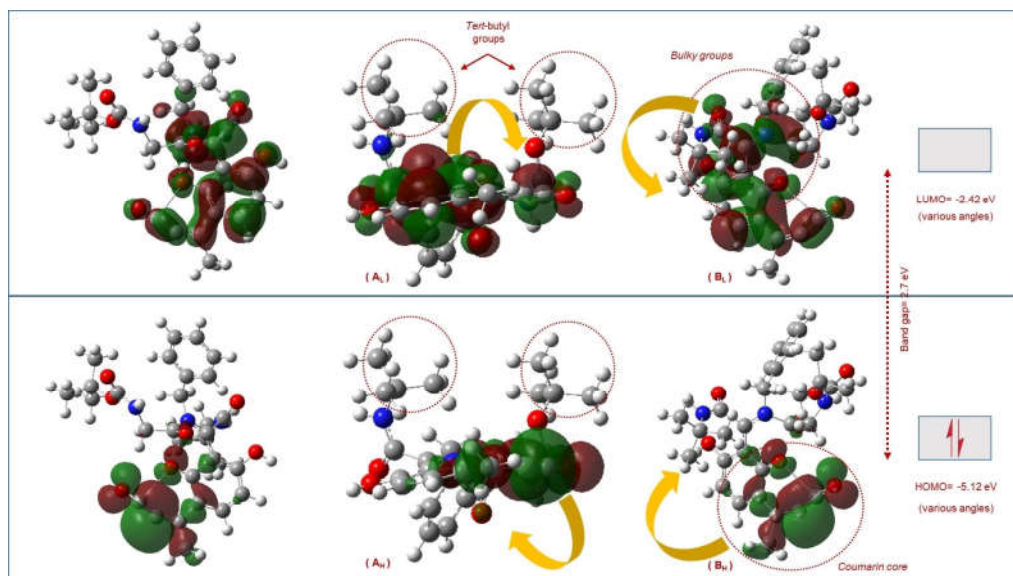


Figure 13. The images of HOMO and LUMO computed by DFT/B3LYP/6-31G* method.

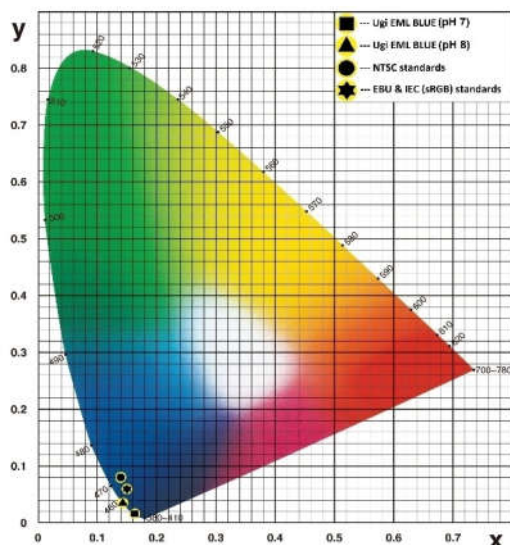


Figure 14. CIE 1931 Color System: CIE blue colors of Ugi EML BLUE (at pH 7 and pH 8), NTSC standard, EBU standard and IEC (sRGB) standard

the Ugi EML BLUE possess excellent color properties as blue emitter for a broad spectrum of applications.

Conclusions

In summary, we demonstrated an efficient synthesis of a deep blue emitting material Ugi EML BLUE based on a multi-component coupling strategy. The integration of a bulky carboxamide moiety to the 8-position of the coumarin scaffold afforded excellent deep blue emission in the solution state with a remarkable color purity (CIE (X) 0.16 and CIE (Y) 0.01). The air-dried thin film of the material showed yellowish green emission which can switch back to deep blue emission by simple solvent vapour etching.

Supporting Information Summary

Synthetic procedure, copies of FT-IR, ¹HNMR, ¹³CNMR, HRMS, XRD, AFM images, TD-DFT data, solid state and solution state UVabs/PLEms spectra of Ugi EML BLUE are available in the Supporting Information.

Table 2. Properties of Ugi EML BLUE.

Appearance	Melting Point(°C)	UVabs Max (nm)	PLEms Max (nm)	Color	C.I.E. (x, y) at pH 7	C.I.E. (x, y) at pH 8	HOMO (eV)	LUMO (eV)	Number of Synthetic Steps
Yellowish-brown solid	178	338 (at pH 7), 390 (at pH 8)	443 (at pH 7), 458 (at pH 8)	Deep Blue	0.16, 0.01	0.14, 0.03	-5.12	-2.42	2

Acknowledgements

Shyam Shankar Eramangalam Puthumana thanks University of Calicut, Kerala, India for the research fellowship.

Conflict of Interest

The authors declare no conflict of interest.

Keywords: Blue Emitter · EML Blue · MCR · OLED · Ugi EML BLUE

- [1] C. W. Tang, S. A. VanSlyke, *Appl. Phys. Lett.* **1987**, *51*, 913–915.
- [2] T. Fleetham, G. Li, L. Wen, J. Li, *Adv. Mater.* **2014**, *26*, 7116–7121.
- [3] D. Ammermann, A. Böhler, S. Dirr, W. Kowalsky, *Int. J. Electron. Comm. (AEÜ)* **1996**, *51*, 327–332.
- [4] S. Hirata, Y. Sakai, K. Masui, H. Tanaka, S. Y. Lee, H. Nomura, N. Nakamura, M. Yasumatsu, H. Nakanotani, Q. Zhang, K. Shizu, H. Miyazaki, C. Adachi, *Nat. Mater.* **2015**, *14*, 330–336.
- [5] H. Sasabe, J. Kido, *J. Mater. Chem. C* **2013**, *1*, 1699–1707.
- [6] Y. Im, S. Y. Byun, J. H. Kim, D. R. Lee, C. S. Oh, K. S. Yook, J. Y. Lee, *Adv. Funct. Mater.* **2017**, *27*, 1603007.
- [7] A. Graff, F. Altmann, A. Dzwilewski, B. Freitag, *Microsc. Microanal.* **2014**, *20*, 144–145.
- [8] Y. Feng, X. Zhuang, D. Zhu, Y. Liu, Y. Wang, M. R. Bryce, *J. Mater. Chem. C* **2016**, *4*, 10246–10252.
- [9] C. Hosokawa, H. Higashi, H. Nakamura, T. Kusumoto, *Appl. Phys. Lett.* **1995**, *67*, 3853–3855.
- [10] X. Yang, X. Xu, G. Zhou, *J. Mater. Chem. C* **2015**, *3*, 913–944.
- [11] M. Zhu, C. Yang, *Chem. Soc. Rev.* **2013**, *42*, 4963–4976.
- [12] X. Chen, W. Liu, C. J. Zheng, K. Wang, K. Liang, Y. Z. Shi, X. M. Ou, X. H. Zhang, *ACS Appl. Mater. Interfaces.* **2017**, *9*, 8848–8854.
- [13] A. Wrona-Piotrowicz, J. Zakrzewski, R. M'etivier, A. Brosseau, A. Makal, K. Woźniak, *RSC Adv.* **2014**, *4*, 56003–56012.
- [14] Y. Niko, Y. Hiroshige, S. Kawauchi, K. Gen-ichi, *J. Org. Chem.* **2012**, *77*, 3986–3996.
- [15] I. Ugi, *Angew. Chem. Int. Ed. Engl.* **1962**, *1*, 8–21.
- [16] A. Dömling, I. Ugi, *Angew. Chem. Int. Ed.* **2000**, *39*, 3168–3210.
- [17] M. Veiderma, *Proc. Estonian Acad. Sci. Chem.* **2007**, *56*, 98–102.
- [18] P. Pramitha, D. Bahulayan, *Bioorg. Med. Chem. Lett.* **2012**, *22*, 2598–2603.
- [19] L. Alexander, H. P. Klug, *J. Appl. Phys.* **1950**, *21*, 137–142.
- [20] A. Monshi, M. R. Foroughi, M. R. Monshi, *World J. Nano Sci. Eng.* **2012**, *2*, 154–160.
- [21] W. Song, I. Lee, J. Y. Lee, *Adv. Mater.* **2015**, *27*, 4358–4363.
- [22] J. N. Moorthy, P. Natarajan, P. Venkatakrishnan, D. F. Huang, T. J. Chow, *Org. Lett.* **2007**, *9*, 5215–5218.
- [23] C. H. Yang, T. F. Guo, I. W. Sun, *J. Lumin.* **2007**, *124*, 93–98.
- [24] D. D. Zhang, M. H. Cai, Y. G. Zhang, D. Q. Zhang, L. Duan, *Mater. Horiz.* **2016**, *3*, 145–151.
- [25] J. Yang, J. Huang, Q. Li, Z. Li, *J. Mater. Chem. C* **2016**, *4*, 2663–2684.
- [26] E. J. Na, K. H. Lee, H. Han, Y. K. Kim, S. S. Yoon, *J. Nanosci. Nanotechnol.* **2013**, *13*, 554–557.
- [27] P. M. Beaujuge, S. Ellinger, J. R. Reynolds, *Nat. Mater.* **2008**, *7*, 795–799.
- [28] P. M. Beaujuge, C. M. Amb, J. R. Reynolds, *Acc. Chem. Res.* **2010**, *43*, 1396–1407.
- [29] J. R. Lakowicz, *Principles of Fluorescence Spectroscopy*, 2nd edition, Plenum Press, New York, **1999**, pp. 6–200.
- [30] M. Baruah, W. Qin, C. Flors, J. Hofkens, R. A. L. Vall'ee, D. Beljonne, M. V. D. Auweraer, W. M. D. Borggraeve, N. Boens, *J. Phys. Chem. A* **2006**, *110*, 5998–6009.
- [31] M. J. Frisch, G. W. Trucks, H. B. Schlegel, G. E. Scuseria, M. A. Robb, J. R. Cheeseman, G. Scalmani, V. Barone, B. Mennucci, G. A. Petersson, H. Nakatsuji, M. Caricato, X. Li, H. P. Hratchian, A. F. Izmaylov, J. Bloino, G. Zheng, J. L. Sonnenberg, M. Hada, M. Ehara, K. Toyota, R. Fukuda, J. Hasegawa, M. Ishida, T. Nakajima, Y. Honda, O. Kitao, H. Nakai, T. Vreven, J. A. Montgomery, Jr., J. E. Peralta, F. Ogliaro, M. Bearpark, J. J. Heyd, E. Brothers, K. N. Kudin, V. N. Staroverov, R. Kobayashi, J. Normand, K. Raghavachari, A. Rendell, J. C. Burant, S. S. Iyengar, J. Tomasi, M. Cossi, N. Rega, J. M. Millam, M. Klene, J. E. Knox, J. B. Cross, V. Bakken, C. Adamo, J. Jaramillo, R. Gomperts, R. E. Stratmann, O. Yazyev, A. J. Austin, R. Cammi, C. Pomelli, J. W. Ochterski, R. L. Martin, K. Morokuma, V. G. Zakrzewski, G. A. Voth, P. Salvador, J. J. Dannenberg, S. Dapprich, A. D. Daniels, O. Farkas, J. B. Foresman, J. V. Ortiz, J. Cioslowski, D. J. Fox, Gaussian 09, Revision A.1, Gaussian, Inc., Wallingford CT, **2009**.
- [32] C. A. Guido, S. Knecht, J. Kongsted, B. Mennucci, *J. Chem. Theory Comput.* **2013**, *9*, 2209–2220.
- [33] A. P. Scott, L. Radom, *J. Phys. Chem.* **1996**, *100*, 16502–16513.
- [34] V. Sortur, J. Yenagi, J. Tonannavar, V. B. Jadhav, M. V. Kulkarni, *Spectrochim. Acta, Part A* **2008**, *71*, 688–694.
- [35] J. B. Foresman, A. Frisch, *Exploring Chemistry with Electronic Structure Methods*, 2nd edition, Gaussian Inc., USA, **1996**, pp. 3–161.
- [36] A. D. Laurent, D. Jacquemin, *Int. J. Quantum Chem.* **2013**, *113*, 2019–2039.
- [37] B. Mennucci, C. Cappelli, C. A. Guido, R. Cammi, J. Tomasi, *J. Phys. Chem. A* **2009**, *113*, 3009–3020.
- [38] A. V. Marenich, C. J. Cramer, D. G. Truhlar, *J. Phys. Chem. B* **2009**, *113*, 6378–6396.
- [39] CIE Standards, CIE-1931 Coordinates (the CIE 1931 Standard Colorimetric Observer).
- [40] NTSC Standards, National Television Standards Committee, Issued December 23, **1953**.
- [41] E. B. U. - Technical Centre - Tech. 3213-E.
- [42] IEC Standards (sRGB Standard), IEC/4WD 61966–2–1: *Colour Measurement and Management in Multimedia Systems and Equipment - Part 2–1: Default RGB Colour Space – sRGB*.

Submitted: December 9, 2017

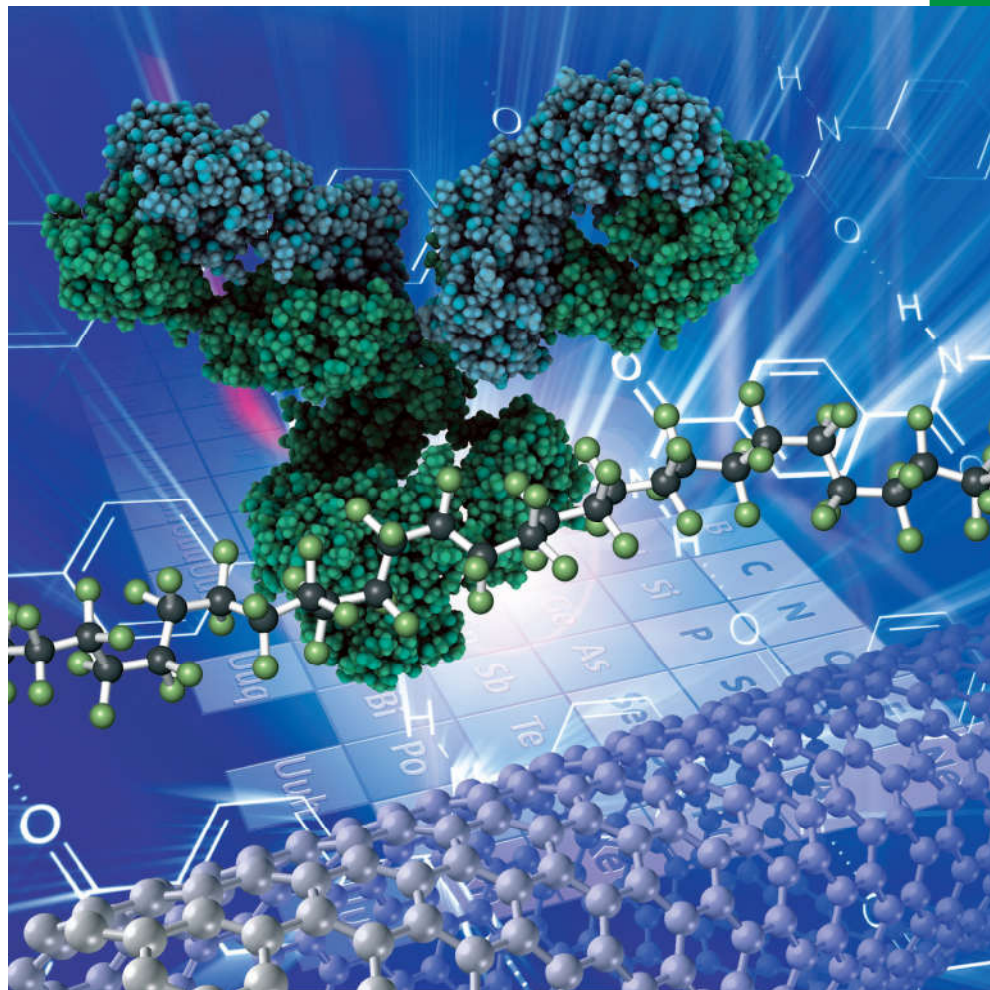
Revised: March 5, 2018

Accepted: March 6, 2018

Chemistry **SELECT** ✓

www.chemistryselect.org

A journal of



REPRINT

WILEY-VCH

Medicinal Chemistry & Drug Discovery

ICT-Based Blue-Emitting Dual-Functional Probe (Ugi EML BLUE) for Bio-Imaging and Cytotoxic Activities on HeLa Cells

Shyam Shankar Eramangalam Puthumana and Bahulayan Damodaran^{*,[a]}

An Intramolecular Charge Transfer (ICT) based blue emitting fluorescent probe (Ugi EML BLUE) has been developed and its binding properties against human CDK2 protein have been studied via docking methods. The docking studies showed that, Ugi EML BLUE can effectively interact with the ATP binding sites of CDK2. The positive results obtained from the docking studies have been extended to the bio-imaging as well as antineoplastic applications in HeLa cells. The *in vitro* biological activity studies revealed the remarkable potential of Ugi EML BLUE as a dual-functional molecule that can be used not

only as a CDK2-targeted fluorescent probe for bio-imaging (λ_{obs} 338 nm, λ_{ems} 443 nm) but also as a CDK2 targeted inhibitor for HeLa cells (IC 50: 0.5 $\mu\text{g}/\text{mL}$). At the sub cellular level, Ugi EML BLUE can selectively interact with the ATP binding sites of the activated CDK 2 to arrest the transfer of phosphate groups from its bound ATP to the serine and threonine residues of the target substrates involved in DNA transcription and replication initiated at the G1 cell cycle phase and which will lead to the inhibition of tumor growth.

Introduction

Various bio-imaging techniques have been developed over the past few decades for the early detection of cancer.^[1] The use of conventional imaging methods like Computed Tomography (CT), Magnetic Resonance Imaging (MRI), X-Ray etc. are limited to the generation of information about anatomical and macroscopic tumoral details. However, today, the advanced fluorescence-based imaging techniques enable us to visualize the expression and activity of specific molecules such as proteases and protein kinases etc.^[2–6] These kind of fluorescence-imaging techniques are playing a pivotal role in the selective and sensitive monitoring of the intracellular proteins whose expression or activity is drastically altered in tumor cells compared to the normal cells. For example the Cyclin Dependent Kinase 2 (CDK2) which is essential for the G1-to S phase-transition in the eukaryotic cell divisions,^[7,8] is over-expressed in many cancer cell lines. For targeting this kind of specific intracellular moieties, the fluorescent probe should have decorated with appropriate functionalities to bind with specific target molecules or biomarkers. However, in many cases, the integration of different functionalities to the fluorescent probe may lead to the loss of its cytoplasmic membrane permeability or suffer a quenching effect in its fluorescence. In recent years, FRET or ICT based, small molecule fluorescent probes have been emerged as a principal solution

to such issues.^[9–11] Among them, ICT based probes are more potential due to their structural simplicity, high efficiency and membrane permeability.^[12–17] Alexa Fluor 350 is one of the interesting examples of such a small molecule probe that has been widely used for stable signal generation in imaging and flow cytometry.^[18] We have recently developed an ICT based blue emitting coumarin carbamate named as Ugi EML BLUE^[19] with photoluminescence properties comparable to that of Alexa Fluor 350^[18] (Figure 2A). Coumarin and carbamate moieties are well known for a plethora of medicinal applications including anti-bacterial, anti-fungal and anti-coagulant activities (Figure 2B).^[20–25] Similarly, coumarin derivatives functionalized with carbamate groups are efficient for inhibiting the cell cycle arrest activity of HIV-1Vpr.^[26,27] Moreover, few recent studies show that the coumarin derivatives are capable of fluorescence chemosensory applications too.^[28–30] At the same time, coumarin molecules functionalized with a hydroxy group at the 7-position are efficient fluorophores since the presence of an electron donating group at the 7-position are known to enhance the fluorescence of such probes.^[31–38]

Based on the efficiency of our Ugi EML BLUE as a strong fluorescent probe and also due to the presence of a medically active carbamate-amide moiety on its coumarin core, we decided to investigate the potential of Ugi EML BLUE as a dual functional probe for imaging and subsequent inhibition of cancer cells so as to avoid the process of cell washing after imaging for therapy. We have studied the CDK2 binding properties of the Ugi EML BLUE using Auto Dock Vina^[39] and also performed the biological studies with the HeLa cells. The Auto Dock Vina is an open-source software for doing the molecular docking with which we can evaluate the binding affinities of our molecule with any proteins or such moieties. The results obtained from computational and experimental

[a] S. S. E. Puthumana, Prof. B. Damodaran
Department of Chemistry, University of Calicut, Malappuram 673635,
Kerala, India
E-mail: bahulayan@yahoo.com
cue2994@uoc.ac.in

Supporting information for this article is available on the WWW under
<https://doi.org/10.1002/slct.201900474>

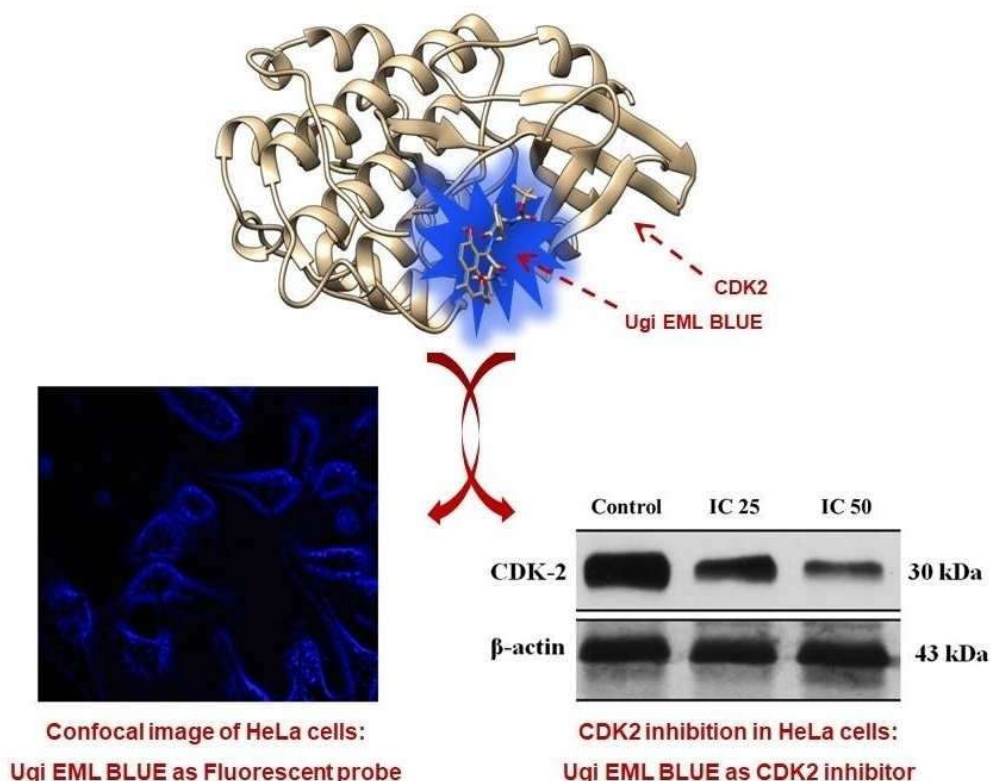


Figure 1. Dual functional applications of Ugi EML BLUE

studies showed that, Ugi EML BLUE can efficiently locate and image the cellular morphology and, simultaneously act as an effective CDK2 suppressor in HeLa cells as shown in Figure 1.

Results and Discussion

Evaluation of the CDK2 targeted imaging potential of Ugi EML BLUE

Fundamentally, cancer/tumor developments are due to the uncontrolled cell proliferation and hence it can be controlled by preventing the abnormal cell divisions.^[40,41] Eukaryotic cell divisions are taking place through the four cellular-phases such as G1, S, G2 and M and are mainly promoted by different types of specific Cyclins and Cycline Dependent Kinases (CDK).^[18,42]

Among the various cyclins, Cyclin dependent kinase 2 (CDK2) is essential for the G1/S phase-transitions during the mitotic cell divisions and its rate is high in abnormal cell divisions.^[18,42–44] The irregular cell divisions can be controlled by the arrest of G1/S phase transition through the inhibition of CDK2. The imaging and therapy can be more facile if the fluorescent probe can work as a dual functional material which

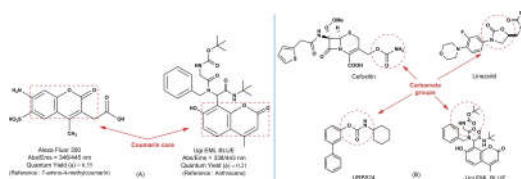


Figure 2. (A) Comparison of the structure and fluorescence properties of Alexa Fluor 350 and Ugi EML BLUE. (B) Comparison of structural features of Ugi EML BLUE and few carbamate drugs showing different metabolic stability.

can selectively light-up and inhibit CDK2. Keeping this in mind, we started our study by evaluating the binding ability of Ugi EML BLUE with CDK2 using Auto Dock Vina 1.1.2.^[39] The docking was performed using the crystal structure of the human CDK2 (in complex with the ligand 3-hydroxychromone, PDB code 2DUV)^[45] and Ugi EML BLUE for calculating its binding ability. The active site of CDK2 comprises the amino acid residues such as GLY 11 (Glycine), ILE 10 (Isoleucine), VAL 16, VAL 64 (Valine), ALA 144, ALA 31 (Alanine), LEU 134, LEU 83 (Leucine), PHE 80, PHE 82 (Phenylalanine), ASP 86, ASP 145

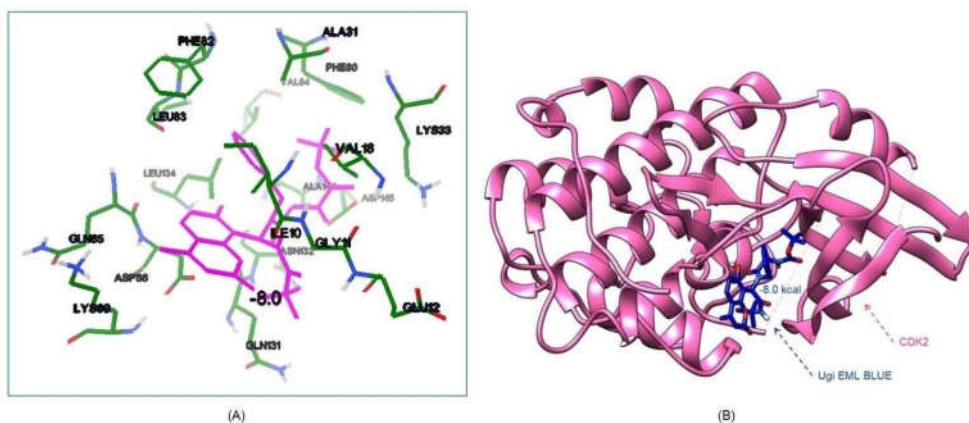


Figure 3. (A) Ugi EML BLUE in the active site of CDK2. (B) Human CDK2 (PDB ID 2DUV) in complex with Ugi EML BLUE.

(Aspartic acid), ASN 132 (Asparagine) and GLN 131 (Glutamine) (Figure 3A). Most of these amino acids have hydrophobic side chains favorable for the formation of a tight 'hydrophobic pocket' in it.^[46,47] Our docking studies showed a binding energy of -8.0 kcal (Figure 3B) and which is due to the strong hydrophobic interaction between Ugi EML BLUE and the target protein. The bulky carbamate-amide functionalities present in Ugi EML BLUE also helps to encapsulate it in to such hydrophobic pockets of the CDK2 as shown in Figure 4. We have also

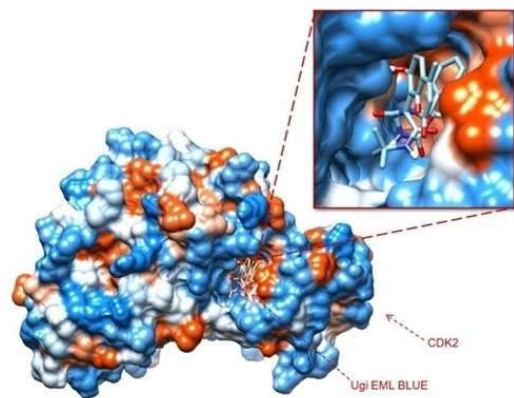
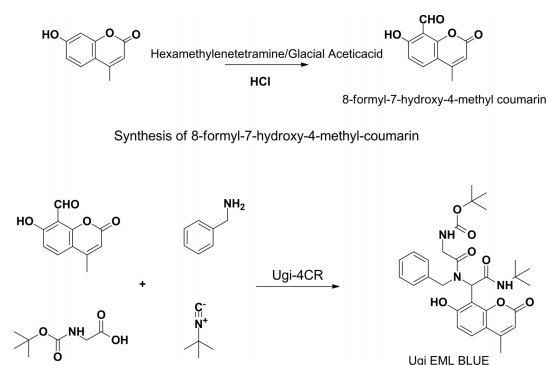


Figure 4. Encapsulation of the ligand Ugi EML BLUE into the hydrophobic pocket of CDK2

carried out the docking studies of Ugi EML BLUE with other kinases involved in cell cycles such as CDK1 (PDB ID 4Y72),^[48] CDK4 (PDB ID 1H00)^[49] and CDK6 (PDB ID 3NUP).^[50] The binding affinity values obtained from these studies are very less (-1.3 kcal, -0.8 kcal and $+5.0$ kcal respectively) compared to

the same obtained from the docking study of Ugi EML BLUE with CDK2 (-8.0 kcal). The less binding affinity values obtained for other kinases clearly indicate the selectivity of Ugi EML Blue towards CDK2 (see supporting information for the docking mode of Ugi EML BLUE in the active site of various kinases). The impressive results obtained from the docking studies prompted us to evaluate the potential of Ugi EML BLUE as a bi-functional fluorescent probe for both imaging and inhibition of CDK2 present in cervical cancer cell line HeLa by *in vitro* bio-activity studies.

Ugi EML BLUE was obtained from the formylation of 4-methyl-7-hydroxy coumarin and subsequent 'Ugi-four component reaction' as shown in Scheme 1. The photo-physical



Scheme 1. Synthesis of Ugi EML BLUE

properties of the Ugi EML BLUE were measured and were obtained as reported earlier.^[19] The UV-Vis absorption maxima and PL emission maxima of Ugi EML BLUE at neutral pH (pH 7) are observed at 338 nm and 443 nm respectively with a large

Stokes shift of 105 nm. The fluorescence of the molecule, its photo-physical data and the values for its HOMO/LUMO energy levels etc. are shown in Figure 5.

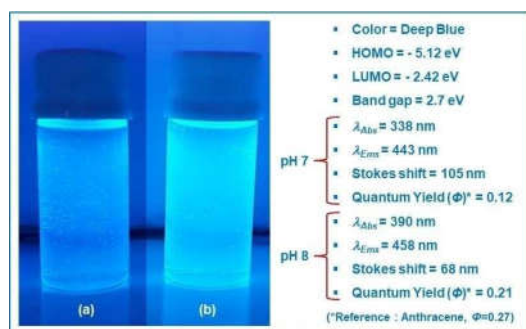


Figure 5. Fluorescence and photo-physical data of Ugi EML BLUE (50 ppm solution in DMSO): a) fluorescence at pH 7, b) fluorescence at pH 8 (no significant change in intensity was observed for pH > 8).

Figure 6 shows fluorescence intensity (A) and the confocal images (B) of the HeLa cells incubated with the Ugi EML BLUE at its respective IC₂₅ and IC₅₀ concentrations (IC₂₅ 0.25 µg/mL and IC₅₀ 0.5 µg/mL, in PBS (pH 7.4), 1% DMSO). An intense bright fluorescent image of the cell morphology was observed (Figure 6B-c) when the cells were stained with Ugi EML BLUE at its IC₅₀ concentration. This intense fluorescence obtained was due to the occurrence of intramolecular charge transfer transitions (ICT) in Ugi EML BLUE under such conditions.

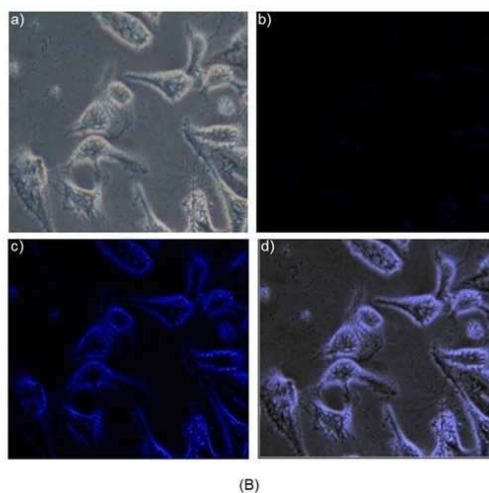
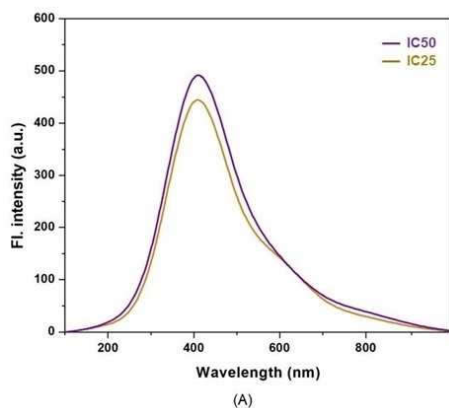


Figure 6. (A) Fluorescence intensity of the Ugi EML BLUE (in PBS (pH 7.4), 1% DMSO) when it incubated in the HeLa cells at its IC₂₅ (0.25 µg/mL) and IC₅₀ (0.5 µg/mL) concentrations. (B) Confocal images of HeLa cells incubated with Ugi EML BLUE (in PBS (pH 7.4), 1% DMSO): a) bright-field image, b) Fluorescence image at IC₂₅, c) Fluorescence image at IC₅₀, d) Overlay image of panels a to c.

Moreover, as we understood from the docking studies, Ugi EML BLUE is able to bind the CDK2 on incubation due to their high binding affinity towards CDK2. From these studies, it is clear that, Ugi EML BLUE can effectively target and image the CDK2 present in cancer cell lines (in this case HeLa cells).

Evaluation of the cytotoxicity of Ugi EML BLUE targeted against CDK2 present in human cervical cancer (HeLa) cells.

We have then extended our studies to determine the effect of Ugi EML BLUE on human cervical cancer (HeLa) cells by various methods such as MTT assay, analysis of mitochondrial membrane potential ($\Delta\psi_m$), analysis of cell cycle progress and the down regulation of CDK2 behind the apoptosis by Western blot analysis. The studies were started with the MTT assay. Figure 7 shows the *In vitro* cytotoxic effect of the Ugi EML BLUE (0, 0.125, 0.25, 0.5, 1.0, 2.0, 4.0 and 8.0 µg/mL concentrations, in PBS (pH 7.4), 1% DMSO (10 µL) against the HeLa cells and primary H8 cells. The experimental results demonstrate that the Ugi EML BLUE has the ability to inhibit the cell proliferation in a dose-dependent manner. The IC₅₀ value of Ugi EML BLUE against HeLa cells was calculated as 0.5 µg/mL (cell viability 49.4 ± 1.25). At the same time, the cytotoxicity effect of Ugi EML BLUE against H8 cells did not show significant cytotoxicity at lower concentration and cytotoxicity increases very slightly with increasing concentration from 0.5 to 8.0 µg/mL in 24 hrs. From the control experiment with primary H8 cells and the cytotoxicity study with HeLa cells, it is clear that the Ugi EML BLUE is able to reduce the cell viability of HeLa cells in a dose dependent manner and can be used effectively at low concentrations.

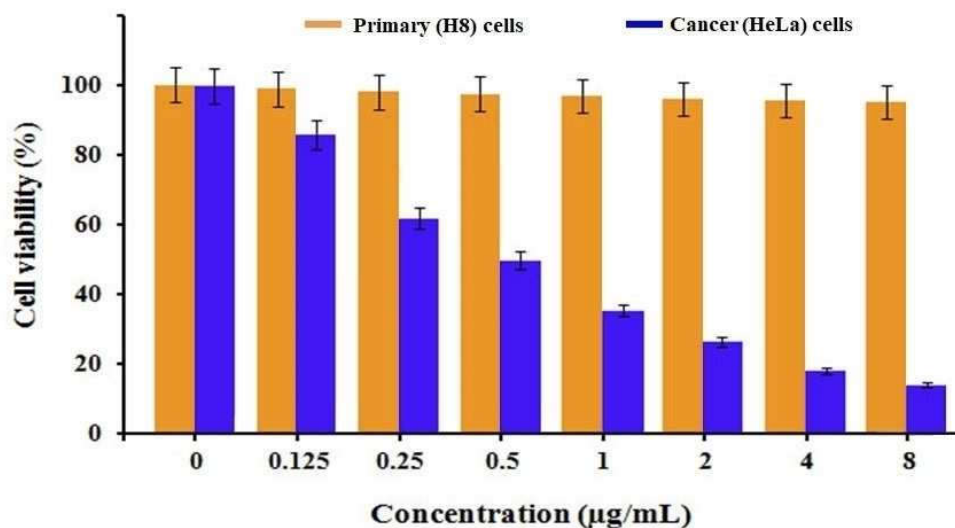


Figure 7. *In vitro* cytotoxic activity of the Ugi EML BLUE against HeLa cells and primary H8 cells

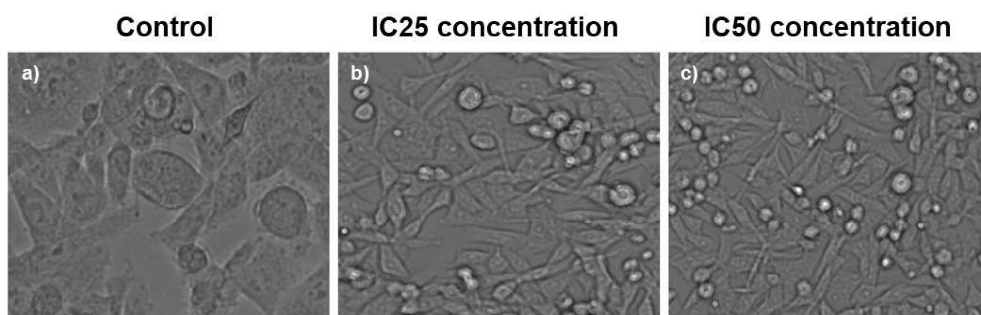


Figure 8. Inverted phase contrast microscopy images of the HeLa cells in the presence and absence of Ugi EML BLUE : a) Undamaged HeLa cells observed in the control (untreated), b) 25% cell death and its apoptotic morphology changes were observed in the HeLa cells treated with the Ugi EML BLUE at its IC25 concentration (0.25 µg/mL), c) 50% cell death and its apoptotic morphology changes were observed in the HeLa cells treated with the Ugi EML BLUE at its IC50 concentration (0.5 µg/mL).

The morphology of the HeLa cells in the presence and absence of Ugi EML BLUE were also studied using inverted phase contrast microscopy. The cells of the different concentration groups are shown in Figure 8. The cells pre-treated with Ugi EML BLUE were different in nature with the control (untreated). In control, the cells were closely packed and spindle shaped whereas, an inhibition of cell growth was observed in the cells treated with the Ugi EML BLUE, although many of them were attached to their culture plates. Irregular cell membranes and signs of blebbing were also observed and are serves as apparent evidence for apoptotic activation. Moreover, these apoptotic morphological change of the Ugi EML BLUE-treated HeLa cells could be visualized by using the fluorescence ability of the Ugi EML BLUE (Figure 6B) itself.

The mitochondrial membrane potential ($\Delta\psi_m$) loss of HeLa cells was analyzed with fluorescence microscopy using the dye Rh-123. As shown in Figure 9, a decrease in the mean fluorescence intensity was observed after the treatment of the cells with Ugi EML BLUE at its IC25 and IC50 concentrations respectively, where the quenching of fluorescence observed is indicating the loss of mitochondrial membrane potential. The loss of mitochondrial membrane potential ($\Delta\psi_m$) is due to mitochondrial membrane depolarization, which is considered as an initial and irreversible step of apoptosis.^[51] Mitochondria play an important role in an intrinsic apoptotic pathway by releasing cytochrome c, leading to the activation of the caspase cascade.^[52] From the present study, it is clear that, the Ugi EML

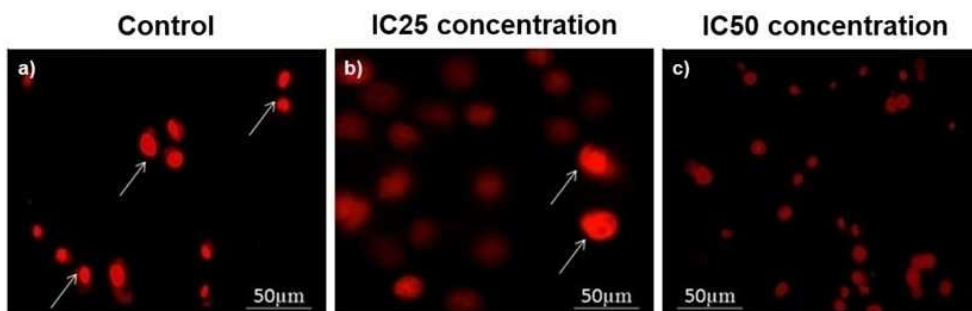


Figure 9. Fluorescence microscopy images of Rh-123 stained HeLa cells treated with Ugi EML BLUE revealing the effect of Ugi EML BLUE on the mitochondrial membrane potential ($\Delta\psi_m$): a) Intense fluorescence of Rh-123 stained HeLa cells control (untreated), b) Quenching of fluorescence observed in the Rh-123 stained HeLa cells treated with the Ugi EML BLUE at its IC₂₅ concentration (0.25 $\mu\text{g/mL}$), c) Significant quenching of fluorescence observed in the Rh-123 stained HeLa cells treated with the Ugi EML BLUE at its IC₅₀ concentration (0.5 $\mu\text{g/mL}$).

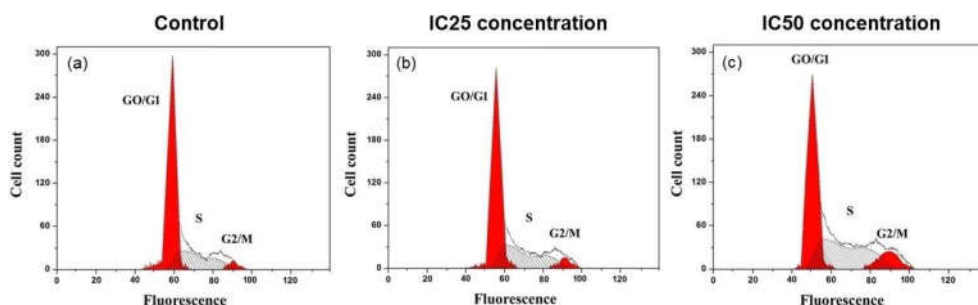


Figure 10. Cell cycle analysis of Ugi EML BLUE-treated HeLa cells by PI flow cytometry: a) Normal cell-phase distribution observed in control group (untreated), b) Mild accumulation of cells in G₂/M phase was observed in HeLa cells treated with Ugi EML BLUE at its IC₂₅ (0.25 $\mu\text{g/mL}$), c) Significant accumulation of cells in G₂/M phase was observed in HeLa cells treated with Ugi EML BLUE at its IC₅₀ (0.5 $\mu\text{g/mL}$).

BLUE could disrupt the functions of mitochondria at the early stages of apoptosis.

For understanding the cell death mechanism, the Ugi EML BLUE was investigated for its effect on cell cycle and induction of apoptosis in HeLa cells by flow cytometry. The proliferation may track from disturbing the cell cycle and to test the hypothesis, cell cycle analysis were conducted after 12 h exposure of the HeLa cells to the Ugi EML BLUE and the dyes under their respective IC₂₅ and IC₅₀ concentrations. A normal cell-phase distribution was observed in the untreated control cells (Figure 10a), whereas a dose-dependent incrementing-accumulation of the cells at G₂ phase of cell cycle was observed in the HeLa cells treated with Ugi EML BLUE at its IC₂₅ and IC₅₀ concentrations (Figure 10b,c). At the same time, no such significant changes were observed in the S phase cell distribution. The accumulation of cells at G₂/M phase accompanied by the respective cell cycle arrest will serve as the evidence for the CDK2-inhibiting activity of Ugi EML BLUE, by means of the requirements of the CDK2 for the G₁/S as well as G₂/M phase transitions.^[53,54] This confirms that, the Ugi EML BLUE could induce significant growth inhibition of HeLa cells

through the induction of G₂/M phase cell cycle arrest. The protein level of CDK2 was significantly elevated, whereas, the kinase activities of CDK2 was inhibited simultaneously in the Ugi EML BLUE-treated cells (which was confirmed from Western blot analysis). From these results, it is clear that, Ugi EML BLUE could arrest the cell cycle at G₂/M checkpoint that controlled the progression of cells from G₂ to M phase. The G₂/M is the "DNA damage checkpoint" which evaluates the DNA content to detect the damages if any before permitting the cell to mitotic phase. Here the Ugi EML BLUE could induce damages to the DNA that leads to the G₂/M cell cycle arrest in the HeLa cells to ensure its apoptosis.

The western blot analysis was also performed to verify the expression of CDK2 protein in the HeLa cells treated with Ugi EML BLUE (Figure 11) using beta-actin as standard. In this case, the CDK2 expression was significantly enriched in control cells whereas the protein levels of CDK2 were significantly down-regulated in Ugi EML BLUE treated cells. All these findings serve as evidence for the CDK2 down regulation protocol behind the observed cell apoptosis with Ugi EML BLUE. Moreover, comparison between the Ugi EML BLUE-CDK2 and ATP-CDK2

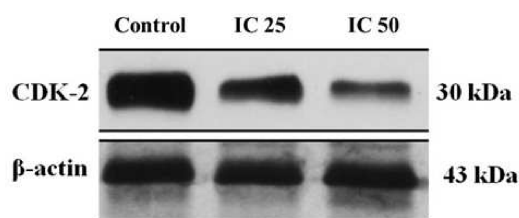


Figure 11. Western blot analysis for the CDK2 expressions in HeLa cells treated with Ugi EML BLUE at its IC₅₀ and IC₂₅ concentrations.

(PDB ID 1HKC) binding interactions were carried out to understand the location where Ugi EML BLUE is binding with CDK2. From the binding interaction studies (described before) we have obtained a strong hydrophobic interactions between the Ugi EML BLUE and the amino acid residues GLY 11 (Glycine), ILE 10 (Isoleucine), VAL 16, VAL 64 (Valine), ALA 144, ALA 31 (Alanine), LEU 134, LEU 83 (Leucine), PHE 80, PHE 82 (Phenylalanine), ASP 86, ASP 145 (Aspartic acid), ASN 132 (Asparagine) and GLN 131 (Glutamine). Among them, the ILE 10, ALA 144, ASP 145, ASP 86, ASN 132, GLN 131 are the hinge residues where ATP usually binds with in CDK2 (Figure 12).^[55,56] This implies the potential of Ugi EML BLUE to interact with the ATP binding sites of the CDK2. One of the major functions of activated CDK2 is to transfer the phosphate groups from its bound ATP to the Serine and Threonine residues of the target substrates involved in DNA transcription and replication initiated in the G₁ cell cycle phase.^[57] However, the binding of Ugi EML BLUE to the active site of CDK2 creates a hindrance effect around the ATP or hide it from the vicinity of the target substrates as shown in Figure 13. Which means that, due to the hindrance effect generated by Ugi EML BLUE around the ATP, the target substrates can't access the ATP even after the complete activation of CDK2 by the Cyclin E and CDK2

activating Kinase (CAK). This will lead to the breakdown of phosphate transfer from CDK2 to the target substrates involved in DNA replication and thereby leading to the unsuccessful DNA replication. Thus the prevention of replication causes the damaging of DNA which leads to the G₂/M cell cycle arrest. Hence, the Ugi EML BLUE can effectively interrupt the functioning of the CDK2 by preventing the phosphate transfer and down regulates its activity in the eukaryotic cells. The results obtained from the cell cycle analysis and Western blot analysis are well in agreement with this CDK2 down regulation mechanism. All the observed biological properties of the molecule are summarized in Table 1.

Table 1. Properties of Ugi EML BLUE	
Compound name	Ugi EML BLUE
Solubility	DMSO, Ethanol, Ethanol-Water
Studied cell line	Human Cervical Cancer (HeLa)
Targeting protein	CDK 2
IC ₅₀	0.5 µg/mL
Plausible inhibition mechanism	Perturbing the target phosphorylation from active CDK 2

Conclusions

In short, we have demonstrated the development of a dual functional fluorescent probe for the imaging and inhibition of CDK2 present in cervical cancer cell line HeLa. The probe-cum-drug was obtained in a two-step process in which the second step is based on a multicomponent coupling strategy, which is a typical example of green synthesis. The docking studies and the biological activity evaluation of Ugi EML BLUE against the human cervical cancer cell line (HeLa cell) revealed the potential of this new probe for bio imaging as well as the CDK2 targeted antineoplastic applications in HeLa cells. The main

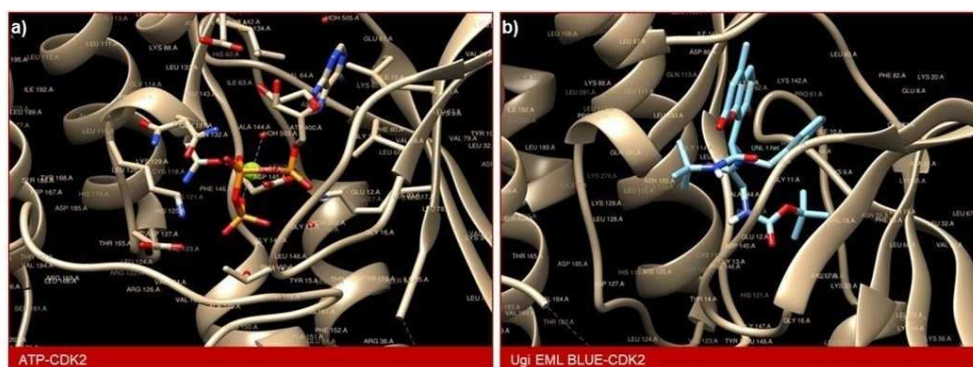


Figure 12. Comparison between the binding sites of ATP and Ugi EML BLUE in CDK2: a) ATP bound to the active site of CDK2, where the hinge residues are ILE 10, ALA 144, ASP 145, ASP 86, ASN 132 and GLN 131. b) Ugi EML BLUE bound to the active site of CDK2, where the hinge residues are GLY 11, ILE 10, VAL 16, VAL 64, ALA 144, ALA 31, LEU 134, LEU 83, PHE 80, PHE 82, ASP 86, ASP 145, ASN 132 and GLN 131.

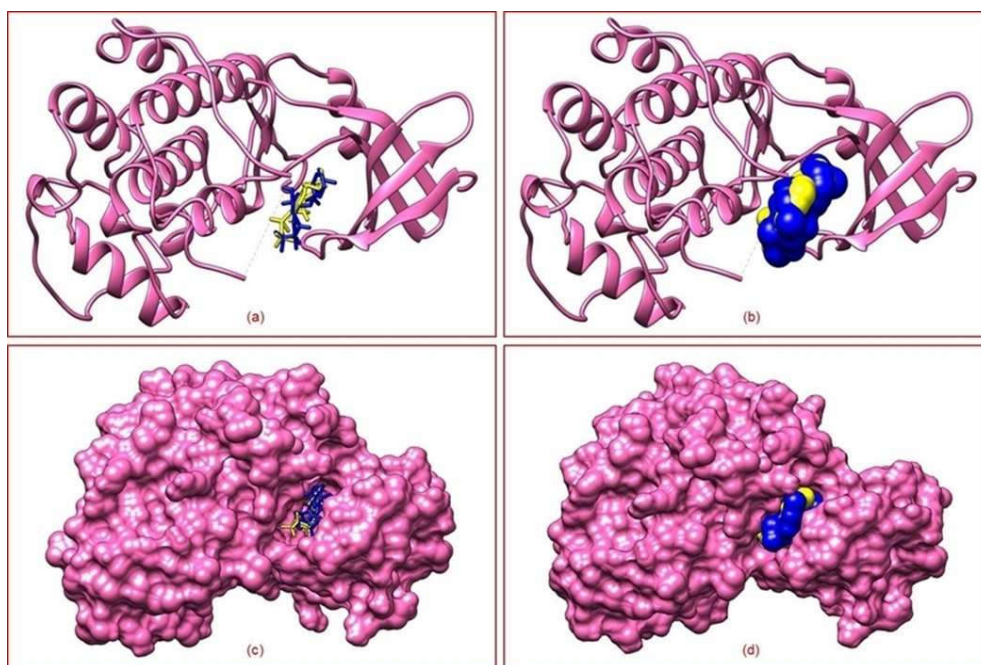


Figure 13. The hindrance effect around the ATP by the ligand Ugi EML BLUE at the ATP binding site of CDK2: (a) Super imposed structure of ATP (Yellow colored) and Ugi EML BLUE (Blue colored) in the active site. (b) Showing the dominating surface of Ugi EML BLUE over the surface of ATP in the active site. (c) ATP and Ugi EML BLUE in the hydrophobic pocket of CDK2. (d) Showing the dominating surface of Ugi EML BLUE over the ATP surface from the hydrophobic pocket.

advantage of this dual functionality is, it can locate the tumour cells, visualize the morphology and at the same time, it can control the cell proliferation through a CDK2 down regulation protocol accompanied by the G2 to M cell cycle arrest. This will enable the therapy without any cell washing process to remove the imaging agent. The photophysical as well as the biological properties of the probe is superior to some of the commercially available probes belongs to Alexa Fluor family. The observed drug properties can be optimized by systematic structure activity studies to bring out its potential for imaging and inhibition of a variety of other cancer cell lines. Success of such studies will make an impact on the development of cost effective cancer therapeutics.

Supporting Information Summary

Details of materials used for this study, Synthetic procedure of Ugi EML BLUE and the spectral details; Procedures of Cell culture, Cytotoxicity Evaluation, Cell Cycle Analysis, Rhodamine 123 Staining, Western Blot Analysis, Bio-imaging and Docking study are available in the supporting information.

Acknowledgements

Shyam Shankar Eramangalam Puthumana thanks University of Calicut, Kerala, India for the research fellowship.

Conflict of Interest

The authors declare no conflict of interest.

Keywords: Bio-Imaging · CDK2 · Coumarin Carbamate · Fluorescent Probe · Ugi EML BLUE

- [1] R. Weissleder, *Science* **2006**, *312*, 1168–1171.
- [2] R. Weissleder, M. J. Pittet, *Nature* **2008**, *452*, 580–589.
- [3] F. A. Jaffer, R. Weissleder, *J. Am. Med. Assoc.* **2005**, *293*, 855–862.
- [4] M. Fernández-Suárez, A. Y. Ting, *Nat. Rev. Mol. Cell Biol.* **2008**, *9*, 929–943.
- [5] M. E. Juweid, B. D. Cheson, *N. Engl. J. Med.* **2006**, *354*, 496–507.
- [6] R. Weissleder, *Nat. Rev. Cancer* **2002**, *2*, 11.
- [7] D. O. Morgan, *Nature* **1995**, *374*, 131–134.
- [8] C. Norbury, P. Nurse, *Annu. Rev. Biochem.* **1992**, *61*, 441–470.
- [9] L. Yuan, W. Lin, K. Zheng, S. Zhu, *Acc. Chem. Res.* **2013**, *46*, 1462–1473.
- [10] D. Srikun, E. W. Miller, D. W. Domaille, C. J. Chang, *J. Am. Chem. Soc.* **2008**, *130*, 4596–4597.
- [11] J. Chan, S. C. Dodani, C. J. Chang, *Nat. Chem.* **2012**, *4*, 973–984.
- [12] X. Cheng, R. Tang, H. Jia, J. Feng, J. Qin, Z. Li, *Appl. Mater. Interfaces* **2012**, *4*, 4387–4392.
- [13] C. Zhang, L. Wei, C. Wei, J. Zhang, R. Wang, Z. Xi, L. Yi, *Chem. Commun.* **2015**, *51*, 7505–7508.

- [14] L. Yuan, W. Lin, J. Song, Y. Yang, *Chem. Commun.* **2011**, *47*, 12691–12693.
- [15] L. J. Zhang, Z. Y. Wang, J. T. Liua, J. Y. Miaob, B. X. Zhaoa, *Sens. Actuators B* **2017**, *253*, 19–26.
- [16] N. I. Georgiev, M. D. Dimitrova, Y. D. Todorova, V. B. Bojinov, *Dyes Pigm.* **2016**, *131*, 9–17.
- [17] D. Zhang, W. Chen, Z. Miao, Y. Ye, Y. Zhao, S. B. King, M. Xian, *Chem. Commun.* **2014**, *50*, 4806–4809.
- [18] N. Panchuk–Voloshina, R. P. Haugland, J. Bishop–Stewart, M. K. Bhalgat, P. J. Millard, F. Mao, W. Y. Leung, R. P. Haugland, *J. Histochem. Cytochem.* **1999**, *47*, 1179–1188.
- [19] S. S. E. Puthumana, B. Damodaran, *ChemistrySelect* **2018**, *3*, 2951–2957.
- [20] A. K. Ghosh, M. Brindisi, *J. Med. Chem.* **2015**, *58*, 2895–2940.
- [21] T. G. Kraljevic, A. Harej, M. Sedic, S. K. Pavelic, V. Stepanic, D. Drenjanecvic, J. Talapko, S. Raic–Malic, *Eur. J. Med. Chem.* **2016**, *124*, 794–808.
- [22] S. Emami, S. Dadashpour, *Eur. J. Med. Chem.* **2015**, *102*, 611–630.
- [23] A. Thakur, R. Singla, V. Jaitak, *Eur. J. Med. Chem.* **2015**, *101*, 476–495.
- [24] T. Abdizadeh, M. R. Kalani, K. Abnous, Z. Tayarani–Najaran, B. Z. Khashyarmansh, R. Abdizadeh, R. Ghodsi, F. Hadizadeh, *Eur. J. Med. Chem.* **2017**, *132*, 42–62.
- [25] M. Basanagouda, V. B. Jambagi, N. N. Barigidad, S. S. Laxmeshwar, V. Devaru, Narayanachar, *Eur. J. Med. Chem.* **2014**, *74*, 225–233.
- [26] E. B. Ong, N. Watanabe, A. Saito, Y. Futamura, K. H. A. Galil, A. Koito, N. Najimudin, H. Osada, *J. Biol. Chem.* **2011**, *286*, 14049–14056.
- [27] S. B. Choi, Y. S. Choong, A. Saito, H. A. Wahab, N. Najimudin, N. Watanabe, H. Osada, E. B. B. Ong, *Mol. Inf.* **2014**, *33*, 742–748.
- [28] S. M. Hossain, K. Singh, A. Lakma, R. N. Pradhan, A. K. Singh, *Sens. Actuators, B* **2017**, *239*, 1109–1117.
- [29] K. S. Mani, R. Rajamanikandan, B. Murugesapandian, R. Shankar, G. Sivaraman, M. Ilanchelian, S. P. Rajendran, *Spectrochim. Acta, Part A* **2019**, *214*, 170–176.
- [30] T. Nasr, S. Bondock, M. Youns, *Eur. J. Med. Chem.* **2014**, *76*, 539–548.
- [31] T. Ueno, T. Nagano, *Nat. Methods* **2011**, *8*, 642–645.
- [32] A. Rai, A. K. Singh, K. Tripathi, A. K. Sonkar, B. S. Chauhan, S. Srikrishna, T. D. James, L. Mishra, *Sens. Actuators B* **2018**, *266*, 95–105.
- [33] S. Xia, J. Wang, J. Bi, X. Wang, M. Fang, T. Phillips, A. May, N. Conner, M. Tanasova, F. T. Luo, H. Liu, *Sens. Actuators B* **2018**, *265*, 699–708.
- [34] S. Li, D. Zhang, X. Xie, S. Ma, Y. Liu, Z. Xu, Y. Gao, Y. Ye, *Sens. Actuators B* **2016**, *224*, 661–667.
- [35] L. Wang, W. Li, W. Zhi, D. Ye, Y. Wang, L. Ni, X. Bao, *Dyes Pigm.* **2017**, *147*, 357–363.
- [36] L. Wang, W. Li, W. Zhi, Y. Huang, J. Han, Y. Wang, Y. Ren, L. Ni, *Sens. Actuators B* **2018**, *260*, 243–254.
- [37] Y. F. Kang, H. X. Qiao, Y. L. Meng, S. J. Cui, Y. J. Han, Z. Y. Wu, J. Wu, X. H. Jia, X. L. Zhang, M. Y. Dai, *RSC Adv.* **2016**, *6*, 94866–94869.
- [38] B. Zhang, X. Yang, R. Zhang, Y. Liu, X. Ren, M. Xian, Y. Ye, Y. Zhao, *Anal. Chem.* **2017**, *89*, 10384–10390.
- [39] O. Trott, A. J. Olson, *J. Comput. Chem.* **2010**, *31*, 455–461.
- [40] G. I. Evan, K. H. Vousden, *Nature* **2001**, *411*, 342–348.
- [41] L. H. Hartwell, M. B. Kastan, *Science* **1994**, *266*, 1821–1828.
- [42] K. Vermeulen, D. R. V. Bockstaele, Z. N. Berneman, *Cell Prolif.* **2003**, *36*, 131–149.
- [43] I. Neganova, X. Zhang, S. Atkinson, M. Lako, *Oncogene* **2009**, *28*, 20–30.
- [44] S. Lapenna, A. Giordano, *Nat. Rev. Drug Discov.* **2009**, *8*, 547–566.
- [45] J. Lee, T. Park, S. Jeong, K. H. Kim, C. Hong, *Bioorg. Med. Chem. Lett.* **2007**, *17*, 1284–1287.
- [46] T. Young, R. Abel, B. Kim, B. J. Berne, R. A. Friesner, *Proc. Natl. Acad. Sci. U. S. A.* **2007**, *104*, 808–813.
- [47] P. W. Snyder, J. Mecinovic, D. T. Moustakas, S. W. Thomas III, M. Harder, E. T. Mack, M. R. Lockett, A. Heroux, W. Sherman, G. M. Whitesides, *Proc. Natl. Acad. Sci. U. S. A.* **2011**, *108*, 17889–17894.
- [48] N. R. Brown, S. Korolchuk, M. P. Martin, W. A. Stanley, R. Moukhametzianov, M. E. M. Noble, J. A. Endicott, *Nat. Commun.* **2015**, *6*, 6769.
- [49] J. F. Beattie, G. A. Breault, R. P. A. Ellston, S. Green, P. J. Jewsbury, C. J. Midgley, R. T. Naven, C. A. Minshull, R. A. Pauptit, J. A. Tucker, J. E. Pease, *Bioorg. Med. Chem. Lett.* **2003**, *13*, 2955–2960.
- [50] Y. S. Cho, M. Borland, C. Brain, C. H. T. Chen, H. Cheng, R. Chopra, K. Chung, J. Groarke, G. He, Y. Hou, S. Kim, S. Kovats, Y. Lu, M. O. Reilly, J. Shen, T. Smith, G. Trakshel, M. Vögtle, M. Xu, M. J. Sung, *J. Med. Chem.* **2010**, *53*, 7938–7957.
- [51] T. A. Mary, K. Shanthi, K. Vimala, S. Kannan, *RSC Adv.* **2016**, *6*, 22936–22949.
- [52] R. Thangam, D. Senthilkumar, V. Suresh, M. Sathuvan, S. Sivasubramanian, K. Pazhanichamy, P. K. Gorlagunta, S. Kannan, P. Gunasekaran, R. Rengasamy, J. Sivaraman, *J. Agric. Food Chem.* **2014**, *62*, 3410–3421.
- [53] B. Hu, J. Mitra, S. V. D. Heuvel, G. H. Enders, *Mol. Cell. Biol.* **2001**, *21*, 2755–2766.
- [54] N. Furuno, N. D. Elzen, J. Pines, *J. Cell. Biol.* **1999**, *147*, 295–306.
- [55] H. L. D. Bondt, J. Rosenblatt, J. Jancarik, H. D. Jones, D. O. Morgan, S. H. Kim, *Nature* **1993**, *363*, 595–602.
- [56] M. Arba, S. Ihsan, L. O. A. N. Ramadhan, D. H. Tjahjono, *Comput. Biol. Chem.* **2017**, *67*, 9–14.
- [57] M. Malumbres, M. Barbacid, *Nat. Rev. Cancer* **2001**, *1*, 222–231.

Submitted: February 6, 2019

Accepted: April 29, 2019



Cite this: *New J. Chem.*, 2019, 43, 13863

Chemistry, chemical biology and photophysics of certain new chromene–triazole–coumarin triads as fluorescent inhibitors of CDK2 and CDK4 induced cancers†

E. P. Shyam Shankar  and Damodaran Bahulayan *

A new series of chromene–triazole–coumarin triads (**T1** to **T6**) have been synthesized through the employment of a solvent-free mechanochemical multicomponent reaction, followed by a copper catalyzed (3+2) azide–alkyne cycloaddition (click chemistry). The molecules were investigated for their fluorescence and CDK induced anticancer properties. Half of the molecules (**T1**, **T4**, and **T5**) showed fluorescence in the solution state through ICT based electronic transitions, whereas the other half (**T2**, **T3**, and **T6**) showed solid-state fluorescence through aggregation induction. Computational studies on binding affinity revealed that all the molecules are generally selective towards CDK2 and CDK4. The *in vitro* biological activity studies showed that the molecules **T2** and **T5** exhibit potential as fluorescent inhibitors of CDK2/CDK4 induced tumors. **T2** and **T5** showed an IC₅₀ of 7.5 μg mL⁻¹ and 4 μg mL⁻¹ respectively against the human cervical cancer cell line (HeLa).

Received 5th June 2019,
Accepted 5th August 2019

DOI: 10.1039/c9nj02924a

rsc.li/njc

Introduction

Cyclin dependent kinases (CDKs) are a part of the serine/threonine-protein kinase family with a significant role in modulating the various stages of the cell division cycle.^{1–3} It is widely accepted that the deregulation of CDKs causes their overexpression as well as chromosomal instability, leading to various types of human cancers. Hence, CDKs are considered as one of the major targets in cancer therapy.⁴ Among the various CDKs, overexpressed CDK2 and its binding cyclin partners have been observed in many tumors and some of these tumors are selectively sensitive to the inhibition of CDK2. Hence, in recent years CDK2 has emerged as a potential target in cancer therapy.^{5–8} Similarly, it is proved that CDK4 is also cooperatively involved along with CDK2 in promoting the G1 phase progression.^{9,10} Furthermore, overexpression of CDK4 has been observed in many tumors such as gliomas, sarcomas, lymphomas, melanomas, breast carcinomas, and leukemias. This implies that CDK4 is also a key factor in promoting the initiation and development of tumors.¹¹ Consequently, a large number of CDK inhibitors, particularly CDK2 and CDK4 inhibitors, have been developed and many such small molecule inhibitors are under various phases of clinical trials, with some already on the market. Selected examples are presented in Fig. 1.^{12–15}

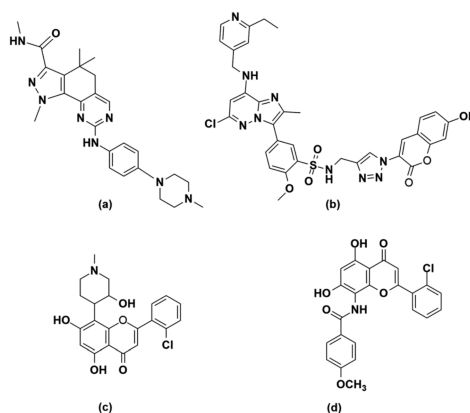


Fig. 1 Examples of (a) a small molecule CDK inhibitor under clinical trials and (b) a drug molecule tagged with a fluorescent dye. (c and d) The chromene based CDK inhibitors.

Fluorescence based bioimaging, as well as biosensor applications, is very efficient and common.^{16–18} A recent trend in this field is the use of fluorescent inhibitors in which a drug tagged with a fluorescent dye has been used for monitoring the pathways involved in tumor inhibition.¹⁵ However, this method often retards the drug performance by affecting the selectivity, cell permeability and target binding properties due to the presence of an additional dye in the drug molecule, which doesn't have any

Department of Chemistry, University of Calicut, Malappuram 673635, Kerala, India. E-mail: bahulayan@yahoo.com, cue2994@uoc.ac.in

† Electronic supplementary information (ESI) available. See DOI: 10.1039/c9nj02924a

significant influence on the properties of the drug. An alternative strategy is the use of inherently fluorescent drug molecules for tracking and annihilation of tumors.¹⁵ This method appears to be more interesting since it is based on the use of privileged scaffolds to construct the fluorescent drug core. However, the field is still in its infancy and significant further research is required to develop efficient and selective CDK inhibitors.

We have been working on the development of privileged scaffold based drug molecules for some time and we were able to publish some interesting findings.^{19–21} Since chromene is known for its CDK inhibition properties^{12,13} and coumarin is known for its photophysical (fluorescence) as well as biological properties,^{22–25} we decided to integrate a coumarin scaffold with various chromene moieties through a linker triazole to design fluorescent inhibitors of CDKs. We presumed that the three nitrogen atoms, as well as the two sp^2 carbon atoms on the triazole ring, could make the system electron rich and enable electron transfer through the fragments to enhance the fluorescence. The synthesized molecules were then systematically investigated for their fluorescence and CDK inhibition properties on human cervical cancer cell lines (HeLa).

Results and discussion

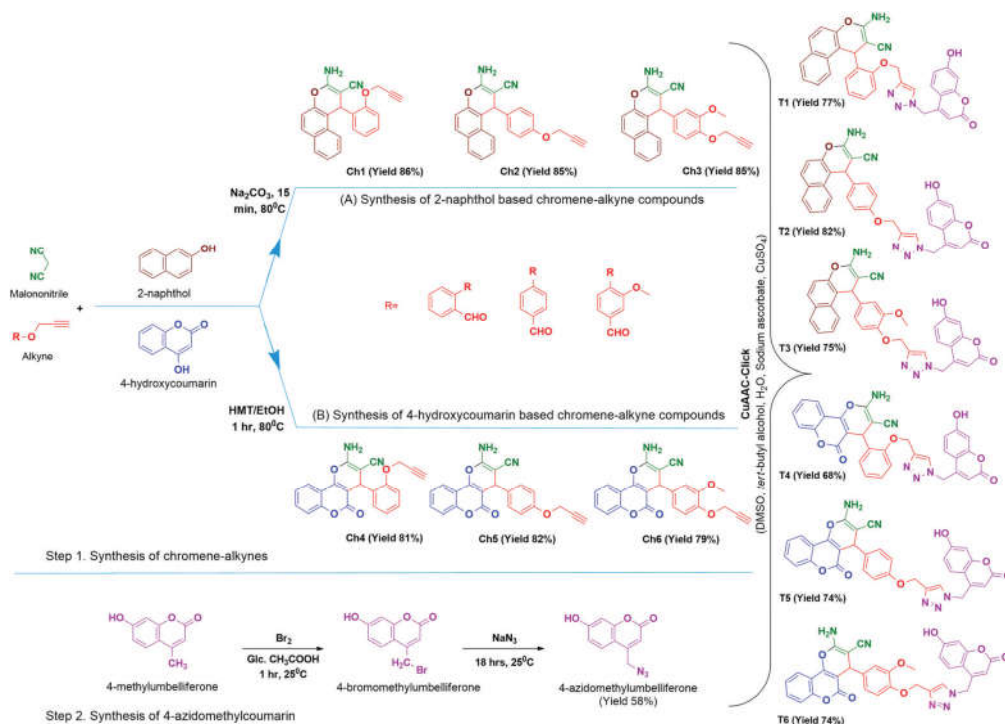
The overall chemistry is depicted in Scheme 1. Six alkyne-derivatives of 2*H*-chromenes were synthesized through a solvent-free multi-component reaction (MCR) of coumarin or naphthalene with an

alkyne-functionalized aldehyde and malononitrile. This solvent-free mechanochemical synthesis resulted in the formation of the desired chromene scaffolds in high yield and purity after simple solvent wash. The azide derivative was obtained by brominating the side chain of 4-methylumbelliferone, followed by azide substitution. This two-step synthesis also afforded the required material in moderate yield and high purity. The alkyne and the azide fragments were then assembled through copper catalyzed azide–alkyne (3+2) cycloaddition (CuAAC), under click chemistry conditions, to obtain chromene–triazole–coumarin triads **T1–T6**.

Evaluation of fluorescence properties

The fluorescence properties of the starting alkynes **Ch1–Ch6**, coumarin-azide, and chromene–triazole–coumarin triads were analyzed by preparing a 50 ppm solution of each in DMSO. No characteristic fluorescence was observed for the starting alkynes and coumarin-azide under UV exposure (Fig. S1 in ESI[†]). However, the triad molecules **T1**, **T4** and **T5** showed blue emission under UV exposure as shown in Fig. 2a (the same under visible light is given in ESI,[†] Fig. S2). The UV-visible and emission spectra of compounds **T1** to **T6** (50 ppm solution in DMSO) were measured and their quantum yields were also calculated by using quinine sulfate ($\Phi = 0.54$) as standard.

Among **T1**, **T4**, and **T5**, the highest quantum yield was obtained from **T1**. Fig. 3A shows the emission spectra of all the triads and Fig. 3B(a) shows the absorption and emission



Scheme 1 Synthesis of chromene-alkynes, coumarin-azide, and chromene–triazole–coumarin triads.

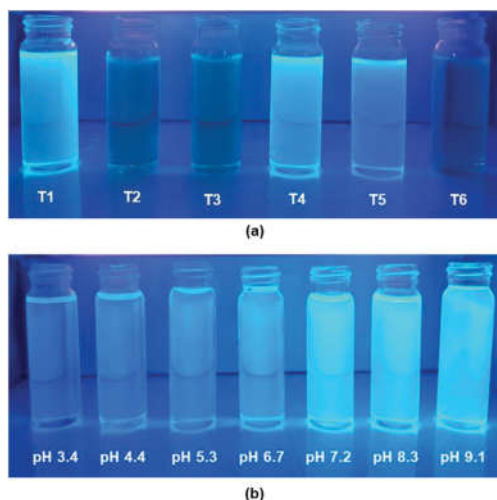


Fig. 2 (a) Fluorescence of the samples **T1** to **T6** under UV-light. (b) Fluorescence of compound **T1** at various pH under UV-light.

spectra of **T1** (those of **T4** and **T5** are given in ESI,† Fig. S3). The photophysical characterization data of all the triads are presented in Table 1.

We then investigated the effect of pH on the fluorescence of these triads under UV exposure. We prepared a 50 ppm solution of each with varying pH. The pH was regulated by adding K_2CO_3 and 1% HCl. The compounds which are non-fluorescent at neutral pH did not show any fluorescence at acidic pH either. We also studied the effect of pH on the fluorescence of those compounds which are fluorescent at neutral pH. However, we did not observe any visible change in the fluorescence of these molecules with respect to changes in pH other than the quenching observed at acidic pH. A typical example of such a study with triad **T1** at various pH (50 ppm solution in DMSO, under UV-light) is presented in Fig. 2b.

We plotted the absorption and emission spectra of **T1** at neutral pH (Fig. 3B(a), absorption maxima: 326 nm and emission

Table 1 Fluorescence properties of chromene–triazole–coumarin triads, **T1** to **T6**

Sample name	UV _{Abs} (nm)	PL _{Ems} (nm)	Stokes shift (nm)	Quantum yield (Φ) ^a
T1	326	442	116	0.95
T2	349	461	112	0.12
T3	370	465	95	0.08
T4	328	429	101	0.68
T5	331	410	79	0.72
T6	358	461	103	0.16

^a With respect to the standard quinine sulfate.

maxima: 442 nm) and at pH 9.1, in order to check whether there is any change with respect to changes in pH.

We observed a significant redshift in the absorption maximum and a slight red shift in the emission maximum of **T1** at alkaline pH (Fig. 3B(b); absorption maximum: 412 nm and emission maximum: 444 nm). This redshift is due to the presence of a free hydroxyl group on **T1**. At acidic pH, this hydroxyl group will get protonated, which causes a decrease in the electron density on the moiety, leading to the quenching of fluorescence. But at basic pH, this hydroxyl group will get deprotonated, causing an increase in the electron density on the moiety, which enables more efficient electron transfer at lower energy leading to the redshift in the absorption spectra.²⁶

Fluorescence properties of the chromene–triazole–coumarin triads in solid-state

We also studied the solid-state fluorescence of these compounds under UV exposure in solid-state, and also by plotting their solid-state absorption and emission spectra. As shown in Fig. 4, compounds **T2**, **T3**, and **T6** showed fluorescence in the solid-state which is absent in the solution state (images of all solid samples under UV and visible light are given in ESI,† Fig. S4). The normalized solid-state UV-vis and emission spectra of these three compounds were recorded as shown in Fig. 5a. We observed a considerable red shift in the absorption and emission spectra of these molecules, which corroborates the emission color observed for these molecules under UV exposure.

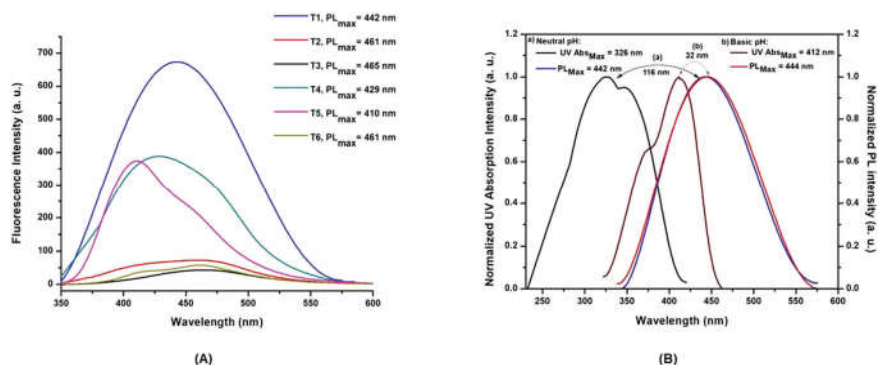


Fig. 3 (A) Fluorescence spectra of **T1** to **T6** (50 p.p.m. solution in DMSO). (B) Normalized UV-PL spectra of (a) **T1** at neutral pH and (b) **T1** at pH 9.1.

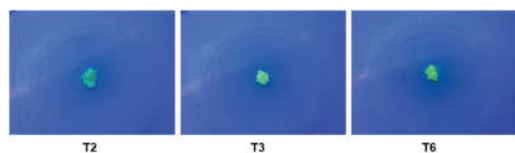


Fig. 4 Solid-state fluorescence of the chromene–triazole–coumarin triads **T2**, **T3**, and **T6** under UV-light.

From the fluorescence measurements in the solid-state and solution state, the overall observation is that compounds **T1**, **T4**, and **T5** show intense fluorescence in solution, which is quenched in the solid-state. At the same time, strong solid-state fluorescence is observed for samples **T2**, **T3**, and **T6**, which do not have fluorescence in solution state (Fig. 5b).

To understand the mechanisms behind the observed fluorescence properties, we decided to carry out density functional theory (DFT) calculations for these molecules.

DFT studies and fluorescence mechanisms

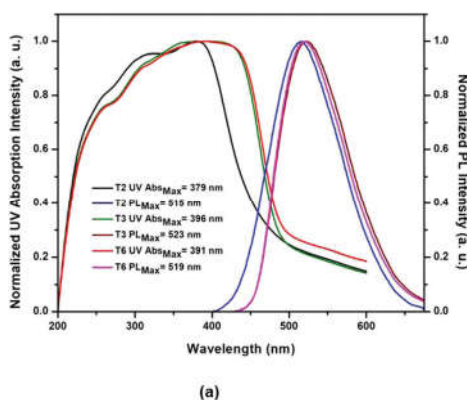
We obtained the ground state geometry (optimized structure), HOMO/LUMO orbital images and energies of **T1** to **T6** by means of computational density functional theory (DFT) using the GAUSSIAN 09 software with the basis set B3LYP/6-31G*.²⁷ The DFT results obtained were then analyzed by drawing plausible mechanisms for the observed fluorescence properties of **T1–6** (Fig. 6a–f).

In **T1**, the HOMO orbitals are comprised of the orbitals of chromene, the cyanide group, the amino group, and the oxy-benzene group, whereas the LUMO is comprised of the orbitals of coumarin and triazole rings (Fig. 6a). Among these, the chromene, triazole and coumarin rings (HOMO/LUMO) are in the same plane (coplanar), which facilitates an ICT-type transition, making the compound highly fluorescent.²⁸

In **T2** and **T3**, the orbitals of the chromene, cyanide, amino and oxy-benzene groups combined to form the HOMO orbitals

and the orbitals of coumarin and triazole combined to form the LUMO orbitals (Fig. 6b and c). However, in their optimized structures (Fig. 6b and c), the chromene, triazole and coumarin rings (HOMO/LUMO) are not in the co-planar state, which disables the efficient electron transfer through an ICT process. In compounds **T4** and **T5**, the HOMO orbitals include the orbitals of the pyran moiety, cyanide group, amino group, and oxy-benzene part, whereas the LUMO orbitals include the orbitals of chromene with the fused coumarin system, cyanide group and amino group (Fig. 6d and e). The electronic transitions in these molecules occur only through one section of the molecule and the triazole-coumarin rings are not effectively participating in the process. This implies that there will only be mild ICT-type transitions in these molecules. However, the optimized structure of **T4** and **T5** (Fig. 6d and e) shows that their HOMO/LUMO orbitals are coplanar with each other, facilitating more efficient electronic transitions. The mild ICT-type transitions, as well as the coplanar orbital structures, enable the fluorescence of **T4** and **T5**. In **T6**, the HOMO orbitals are formed by the orbitals of the pyran moiety, cyanide group, amino group and oxy-benzene part, and the LUMO orbitals are formed by the orbitals of the whole chromene part with the fused coumarin system, cyanide group and amino group (Fig. 6f). Here also the possibility of the mild ICT-type transition exists. However, due to its distorted and non-coplanar structural orientation (Fig. 6f), the more efficient electronic transition is not feasible, which leads to fluorescence quenching in solution.

In **T1**, **T4**, and **T5**, the coplanar nature of the HOMO/LUMO orbitals permits very close molecular arrangements in the solid-state. This leads to the quenching of fluorescence in solid-state due to intermolecular sandwich-type π - π stacking interactions.²⁹ **T2**, **T3** and **T6** have non-coplanar HOMO/LUMO orbitals and no significant π - π stacking.³⁰ We assume that the solid-state fluorescence observed for these samples could be due to the phenomenon of aggregation induced emission (AIE).^{31–34} A plausible mechanism for the whole process is depicted in Fig. 7.



Sample Name	☀ - Fluorescent / ☹ - Non-fluorescent	
	Solution	Solid
T1	☀	☹
T2	☹	☀
T3	☹	☀
T4	☀	☹
T5	☀	☹
T6	☹	☀

Fig. 5 (a) Normalized solid-state UV and emission spectra of **T2**, **T3** and **T6**. (b) Summary of fluorescence observed for the chromene–triazole–coumarin triads **T1** to **T6**.

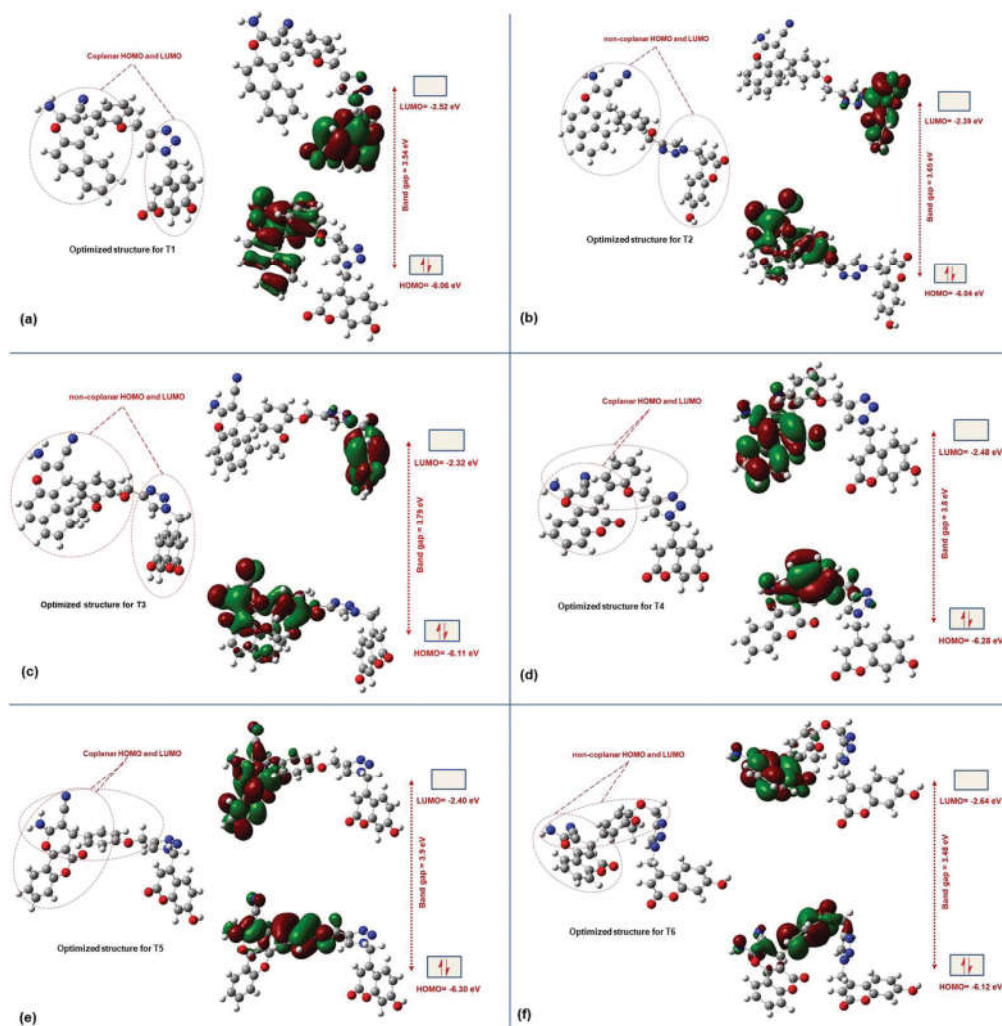


Fig. 6 Optimized structure and HOMO/LUMO orbital images of chromene-triazole-coumarin triads (**T1** to **T6**) with their energies: (a) **T1**, (b) **T2**, (c) **T3**, (d) **T4**, (e) **T5**, (f) **T6**.

Docking studies of chromene-triazole-coumarin triads against CDKs

Having completed the photophysical characterization, we proceeded to evaluate the anticancer properties of these molecules. Since CDKs are involved in the proliferation of various cancers, we decided to carry out a computational study on the docking properties of these molecules against major kinases such as CDK1, 2, 4 and 6. We used the open-source software AutoDock Vina³⁵ to estimate the binding affinities. The proteins PDB ID 4Y72 (CDK1),³⁶ PDB ID 2DUV (CDK2),³⁷ PDB ID 1H00 (CDK4)³⁸ and PDB ID 3NUP (CDK6)³⁹ were downloaded from the Protein Data Bank to carry out the docking studies with **T1**–**T6**. The binding affinity values obtained are presented in Table 2.

The studies revealed that, in terms of binding affinity, the molecules are selective towards CDK2 and CDK4. Fig. 8A shows the docking mode of **T2** and **T5** (these molecules showed the highest binding affinity towards CDK2 and CDK4 (Table 2)) in the active site of CDK2 and CDK4 and the corresponding docking scores (the same for the remaining triads are given in ESI,† Fig. S5). Compounds **T1** to **T6** have binding affinities of -6.3 kcal, -9.1 kcal, -9.4 kcal, -9.0 kcal, -10.5 kcal and -9.0 kcal against CDK2, where the active site of CDK2 is comprised of amino acid residues such as GLY 11 (glycine), ILE 10 (isoleucine), VAL 16, VAL 64 (valine), ALA 144, ALA 31 (alanine), LEU 134, LEU 83 (leucine), PHE 80, PHE 82 (phenylalanine), ASP 86, ASP 145 (aspartic acid), ASN 132 (asparagine) and GLN 131 (glutamine).

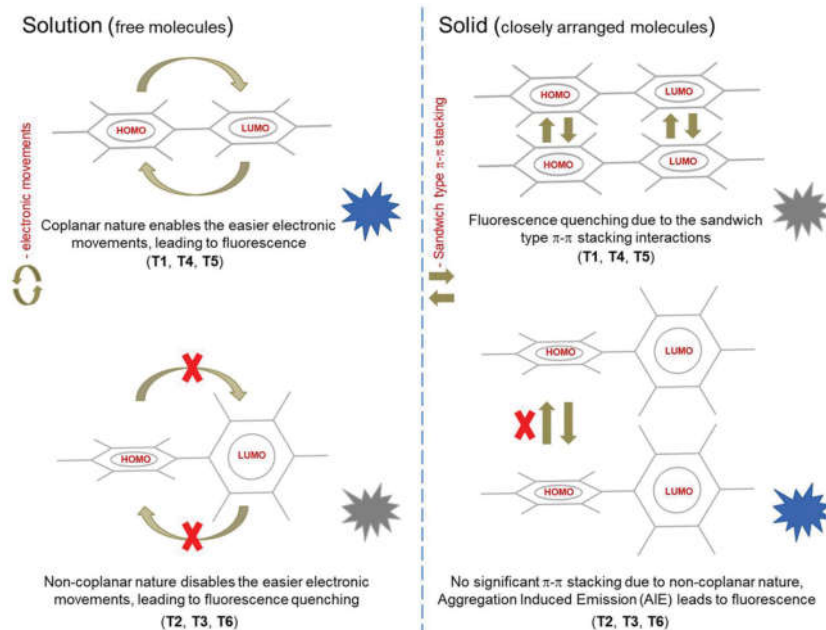


Fig. 7 Plausible fluorescence mechanisms of the chromene–triazole–coumarin triads (**T1** to **T6**).

Table 2 Binding affinities of chromene–triazole–coumarin triads **T1** to **T6** in the active site of CDK2 and CDK4

Sample name	CDK1	CDK2	CDK4	CDK6
T1	+82.0 kcal	−6.3 kcal	−7.4 kcal	+23.9 kcal
T2	+113.1 kcal	−9.1 kcal	−9.6 kcal	+30.1 kcal
T3	+120.1 kcal	−9.4 kcal	−8.6 kcal	+37.7 kcal
T4	+106.9 kcal	−9.0 kcal	−8.3 kcal	+22.5 kcal
T5	+120.1 kcal	−10.5 kcal	−9.4 kcal	+62.5 kcal
T6	+115.0 kcal	−9.0 kcal	−7.7 kcal	+35.4 kcal

Similarly, compounds **T1** to **T6** have binding affinities of −7.4 kcal, −9.6 kcal, −8.6 kcal, −8.3 kcal, −9.4 kcal and −7.7 kcal against CDK4, where the active site of CDK4 is comprised of amino acid residues such as ILE 10 (isoleucine), VAL 18 (valine), GLY 11 (glycine), LEU 83 (leucine), GLU 12 (glutamic acid), LYS 89 (lysine), ALA 31 (alanine), ASP 86 (aspartic acid), and PHE 80, PHE 82 (phenylalanine). Most of these amino acids have hydrophobic side chains favorable for the formation of a tight ‘hydrophobic pocket’ in the kinase.^{40,41} The observed high binding energies for the triads were due to the strong hydrophobic interaction between the compounds and the target proteins. The bulky coumarin-triazole-chromene moieties present in the triads also help to encapsulate them into such hydrophobic pockets of CDK2 and CDK4 (Fig. 8B). Moreover, in the case of CDK4, apart from hydrophobic interactions, there is a possibility of hydrogen bonding and π -cation interactions between the inhibitor molecule and the kinase to enhance the binding affinities (Fig. 8A and Fig. S5, ESI[†]). The absence of significant binding affinity of the molecules towards CDK1 and CDK6 implies that the molecules are

more selective towards CDK2 and CDK4. Since molecules **T2** and **T5** showed the highest binding affinity towards CDK2 and CDK4, these two molecules have been selected for *in vitro* screening against the human cervical cancer cell line (HeLa).

Evaluation of *in vitro* cytotoxic activities of **T2** and **T5** against the human cervical cancer cell line (HeLa)

The cytotoxic effects of chromene–triazole–coumarin triads **T2** and **T5** were evaluated by carrying out the MTT-Assay. The cell cycle analysis and Western blot analysis were performed to study their plausible apoptotic mechanisms. Fig. 9 shows the *in vitro* cytotoxic activity of compound **T2** (1.5, 3, 4.5, 6, 7.5, 9, 10.5 and 12 $\mu\text{g mL}^{-1}$ concentrations, in PBS (pH 7.4), 1% DMSO (10 μL)) and compound **T5** (1, 2, 3, 4, 5, 6, 7 and 8 $\mu\text{g mL}^{-1}$ concentrations, in PBS (pH 7.4), 1% DMSO (10 μL)) against HeLa cells. As shown in the figure, **T2** and **T5** exhibited dose-dependent cytotoxicity in HeLa cells. The IC₅₀ values of **T2** and **T5** against HeLa cells were calculated as 7.5 $\mu\text{g mL}^{-1}$ and 4 $\mu\text{g mL}^{-1}$ (in 48 h) respectively.

The morphology of HeLa cells in the presence and absence of **T2** and **T5** was also studied by using inverted phase-contrast microscopy. The cells of the different concentration groups are shown in Fig. 10A and B. The cells pretreated with **T2** and **T5** are different in nature to the control (untreated). In the control, the cells were closely packed and spindle shaped, whereas inhibition of cell growth was observed in the cells treated with **T2** and **T5**, although many of the cells were still attached to their culture plates. Many cells showed irregular cell membranes and signs of blebbing, which serve as apparent evidence for apoptotic activation.

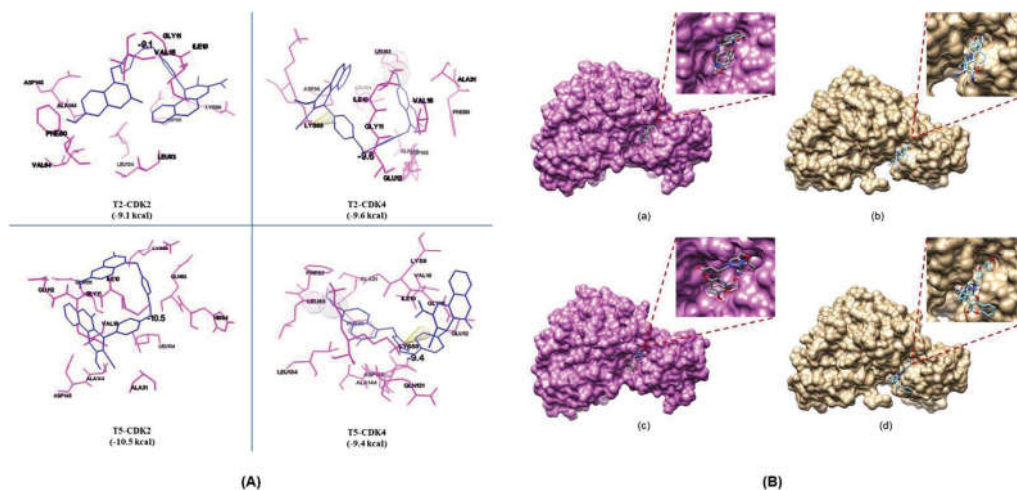


Fig. 8 (A) Chromene–triazole–coumarin triads **T2** and **T5** in the active site of CDK2 and CDK4 with their docking score, (B) Chromene–triazole–coumarin triads **T2** and **T5** encapsulated into the hydrophobic pockets of CDK2 and CDK4: (a) **T2** with CDK2, (b) **T2** with CDK4, (c) **T5** with CDK2, (d) **T5** with CDK4.

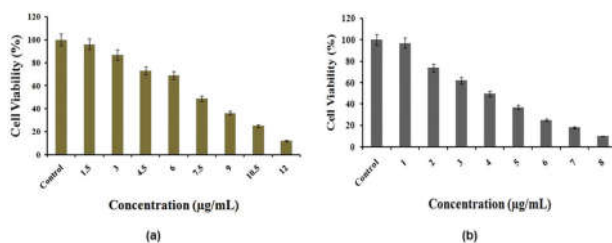


Fig. 9 (a) *In vitro* cytotoxicity activity of compound **T2** against HeLa cells. (b) *In vitro* cytotoxicity activity of compound **T5** against HeLa cells.

We extended our studies to Western blot analysis and cell cycle analysis to understand the plausible mechanisms behind the apoptosis with **T2** and **T5**. The cervical cancer HeLa cells were treated with IC₂₅ and IC₅₀ concentrations of samples **T2** and **T5** separately for 24 h and then Western blotting was performed using beta-actin as an internal standard. We identified that CDK2 and CDK4 expression was significantly enriched in cervical cancers and was functionally required for tumor proliferation *in vitro*. The Western blot analysis shows that the protein levels of CDK2 and CDK4 (components of the cyclin-CDK complexes that are active in G1 and S phase) were altered after **T2** and **T5** treatments (Fig. 11). Our findings reveal that the protein levels of CDKs were significantly down-regulated in **T2** and **T5** treated cells when compared to the control. The result from the Western blot analysis justifies the data obtained from the docking studies as well as the CDK2/CDK4 inhibition protocol behind the observed apoptosis.

Fig. 12 shows the cell-cycle analysis of **T2** and **T5** treated HeLa cells by PI flow cytometry. In the case of **T2** treated HeLa cells, a significant increase in the S phase cell distribution was observed when compared to the control cells. The S phase

fraction increased from 18.39 to 30.51 and 34.58 in HeLa cells after treatment with IC₂₅ and IC₅₀ concentrations of sample **T2** respectively (Fig. 12A). No such significant increments were observed for the G₀/G₁ or G₂/M phase distributions. This implies the accumulation of cells at the S phase and the S phase cell-cycle arrest, which leads to apoptosis. Similarly, in the case of **T5** treated HeLa cells, a significant increase in the G₁ phase cell distribution was observed when compared to the control.

The G₁ phase fraction increased from 41.67 to 45.48 and 64.93 in HeLa cells respectively after the treatment with IC₂₅ and IC₅₀ concentrations of sample **T5** (Fig. 12B). No such significant increments were observed for the S or G₂/M phase distributions. This implies the accumulation of cells at the G₁ phase and the G₁ phase cell-cycle arrest, which leads to apoptosis. From the Western blot results, we observed the selective down-regulation of the kinases CDK2/CDK4 which are crucial for G₁ as well as S phase progression. These results obtained from the Western blot and the cell-cycle analysis together would account for the CDK2/CDK4 inhibition protocol behind the observed apoptosis with chromene–triazole–coumarin triads **T2** and **T5**.

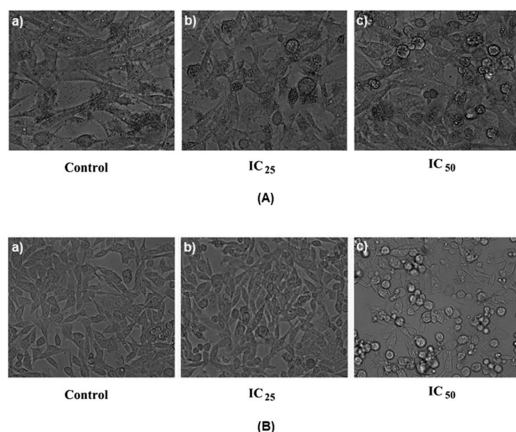


Fig. 10 (A) Inverted phase contrast microscopy images of HeLa cells in the presence and absence of **T2**: (a) undamaged HeLa cells observed in the control (untreated), (b) 25% cell death and its apoptotic morphology changes were observed in HeLa cells treated with **T2** at its IC₂₅ concentration ($4.5 \mu\text{g mL}^{-1}$), (c) 50% cell death and its apoptotic morphology changes were observed in HeLa cells treated with **T2** at its IC₅₀ concentration ($7.5 \mu\text{g mL}^{-1}$). (B) Inverted phase contrast microscopy images of HeLa cells in the presence and absence of **T5**: (a) undamaged HeLa cells observed in the control (untreated), (b) 25% cell death and its apoptotic morphology changes were observed in HeLa cells treated with **T5** at its IC₂₅ concentration ($2 \mu\text{g mL}^{-1}$), (c) 50% cell death and its apoptotic morphology changes were observed in HeLa cells treated with **T5** at its IC₅₀ concentration ($4 \mu\text{g mL}^{-1}$).

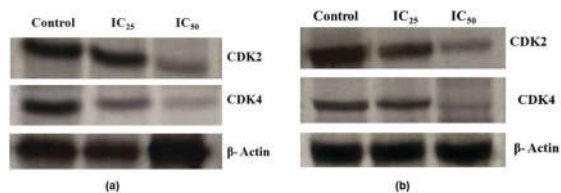


Fig. 11 (a) Western blot analysis for the CDK2 and CDK4 expressions in HeLa cells treated with compound **T2** at its IC₂₅ and IC₅₀ concentrations. (b) Western blot analysis for the CDK2 and CDK4 expressions in HeLa cells treated with compound **T5** at its IC₂₅ and IC₅₀ concentrations.

Conclusions

We have successfully synthesized six chromene–triazole–coumarin triad molecules **T1** to **T6**. The synthesis includes the azide substitution on 7-hydroxy-4-methylcoumarin, followed by a copper catalyzed azide–alkyne cycloaddition (CuAAC), where the alkynes were prepared through a solvent-free mechanochemical multicomponent reaction (MCR). Among the six compounds, **T1**, **T4**, and **T5** showed strong fluorescence in solution, of which **T1** afforded the highest quantum yield. **T2**, **T3**, and **T6** showed strong fluorescence in solid-state. The mechanism related to the origin of fluorescence was derived from computational studies and the data obtained are in perfect agreement with the experimental results. The photophysical studies revealed that the fluorescence properties of these new

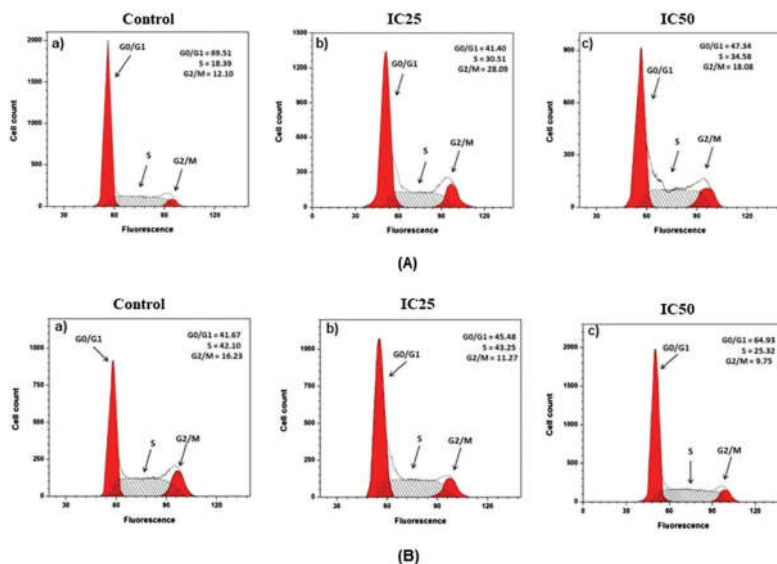


Fig. 12 (A) Cell cycle analysis of compound **T2**-treated HeLa cells by PI flow cytometry: (a) normal cell-phase distribution observed in the control group (untreated), (b) mild accumulation of cells in S phase was observed in HeLa cells treated with **T2** at its IC₂₅ ($4.5 \mu\text{g mL}^{-1}$), (c) significant accumulation of cells in S phase was observed in HeLa cells treated with **T2** at its IC₅₀ concentration ($7.5 \mu\text{g mL}^{-1}$). (B) Cell cycle analysis of compound **T5**-treated HeLa cells by PI flow cytometry: (a) normal cell-phase distribution observed in the control group (untreated), (b) mild accumulation of cells in G1 phase was observed in HeLa cells treated with **T5** at its IC₂₅ ($2 \mu\text{g mL}^{-1}$), (c) significant accumulation of cells in G1 phase was observed in HeLa cells treated with **T5** at its IC₅₀ concentration ($4 \mu\text{g mL}^{-1}$).

molecules are comparable with some of the commercial fluorophores based on functionalized coumarin heterocycles. Binding affinity calculations revealed that the molecules are selective towards CDK2 and CDK4 kinases. Among the six molecules, T2 and T5 showed the highest docking scores and hence these molecules were systematically investigated for their tumor suppression activities on human cervical cancer cells (HeLa). The promising results obtained from MTT, Western blot, and cell cycle analysis should encourage further investigations on selectivity, toxicity, etc. to promote these molecules as affordable fluorescent inhibitors of CDK2/CDK4 induced cancers.

Conflicts of interest

There are no conflicts to declare.

Acknowledgements

Shyam Shankar Eramangalam Puthumana thanks the University of Calicut, Kerala, India for the research fellowship. The authors wish to thank the Central Instrumentation Facility (CIF), University of Calicut, Kerala, India for providing the computational lab facilities.

References

- 1 G. I. Evan and K. H. Vousden, *Nature*, 2001, **411**, 342–348.
- 2 L. H. Hartwell and M. B. Kastan, *Science*, 1994, **266**, 1821–1828.
- 3 K. Vermeulen, D. R. V. Bockstaele and Z. N. Berneman, *Cell Proliferation*, 2003, **36**, 131–149.
- 4 M. Malumbres and M. Barbacid, *Nat. Rev. Cancer*, 2001, **1**, 222–231.
- 5 G. I. Shapiro, *J. Clin. Oncol.*, 2006, **24**, 1770–1783.
- 6 J. Zheng, Q. Li, W. Wang, Y. Wang, X. Fu, W. Wang, L. Fan and W. Yan, *Oncol. Rep.*, 2016, **35**, 809–816.
- 7 X. N. Shi, H. Li, H. Yao, X. Liu, L. Li, K. S. Leung, H. F. Kung, D. Lu, M. H. Wong and M. C. Lin, *PLoS One*, 2015, **10**, e0132072, DOI: 10.1371/journal.pone.0132072.
- 8 T. G. Lim, S. Y. Lee, Z. Huang, D. Y. Lim, H. Chen, S. K. Jung, A. M. Bode, K. W. Lee and Z. Dong, *Cancer Prev. Res.*, 2014, **7**, 466–474.
- 9 B. Hu, J. Mitra, S. V. D. Heuvel and G. H. Enders, *Mol. Cell Biol.*, 2001, **21**, 2755–2766.
- 10 N. Furuno, N. D. Elzen and J. Pines, *J. Cell Biol.*, 1999, **147**, 295–306.
- 11 S. Ortega, M. Malumbres and M. Barbacid, *Biochim. Biophys. Acta*, 2002, **1602**, 73–87.
- 12 Y. M. Ahn, L. Vogeti, C. J. Liu, H. K. R. Santhapuram, J. M. White, V. Vasandani, L. A. Mitscher, G. H. Lushington, P. R. Hanson, D. R. Powell, R. H. Himes, K. F. Roby, Q. Ye and G. I. Georg, *Bioorg. Med. Chem.*, 2007, **15**, 702–713.
- 13 C. Y. Hong, T. S. Park, Y. K. Kim, J. H. Lee, J. H. Kim, D. M. Kim, H. S. Son, S. W. Kim and E. E. K. Kim, *CDK Inhibitors Having Flavone Structures*, *US Pat.*, US 6,500,846 B1, 2002.
- 14 S. Tadesse, E. C. Caldon, W. Tilley and S. Wang, *J. Med. Chem.*, 2019, **62**, 4233–4251.
- 15 J. Humpolickova, I. Mejdrová, M. Matousova, R. Nencka and E. Boura, *J. Med. Chem.*, 2017, **60**, 119–127.
- 16 M. Fernández-Suárez and A. Y. Ting, *Nat. Rev. Mol. Cell Biol.*, 2008, **9**, 929–943.
- 17 S. O. Raja, G. Sivaraman, A. Mukherjee, C. Duraisamy and A. Gulyani, *ChemistrySelect*, 2017, **2**, 4609–4616.
- 18 A. Gulyani, E. Vitriol, R. Allen, J. Wu, D. Gremyachinskiy, S. Lewis, B. Dewar, L. M. Graves, B. K. Kay, B. Kuhlman, T. Elston and K. M. Hahn, *Nat. Chem. Biol.*, 2011, **7**, 437–444.
- 19 R. Pathoor and D. Bahulayan, *New J. Chem.*, 2018, **42**, 6810–6816.
- 20 P. Thasnim and D. Bahulayan, *New J. Chem.*, 2017, **41**, 13483–13489.
- 21 S. S. E. Puthumana and B. Damodaran, *ChemistrySelect*, 2019, **4**, 5366–5374.
- 22 S. Xia, J. Wang, J. Bi, X. Wang, M. Fang, T. Phillips, A. May, N. Conner, M. Tanasova, F. T. Luo and H. Liu, *Sens. Actuators, B*, 2018, **265**, 699–708.
- 23 C. Xiaohong, T. Runli, J. Huizhen, F. Jun, Q. Jingui and L. Zhen, *ACS Appl. Mater. Interfaces*, 2012, **4**, 4387–4392.
- 24 S. Emami and S. Dadashpour, *Eur. J. Med. Chem.*, 2015, **102**, 611–630.
- 25 A. Thakur, R. Singla and V. Jaitak, *Eur. J. Med. Chem.*, 2015, **101**, 476–495.
- 26 J. R. Lakowicz, *Principles of Fluorescence Spectroscopy*, 2nd edn, Plenum Press, New York, 1999.
- 27 M. J. Frisch, G. W. Trucks, H. B. Schlegel, G. E. Scuseria, M. A. Robb, J. R. Cheeseman, G. Scalmani, V. Barone, B. Mennucci, G. A. Petersson, H. Nakatsuji, M. Caricato, X. Li, H. P. Hratchian, A. F. Izmaylov, J. Bloino, G. Zheng, J. L. Sonnenberg, M. Hada, M. Ehara, K. Toyota, R. Fukuda, J. Hasegawa, M. Ishida, T. Nakajima, Y. Honda, O. Kitao, H. Nakai, T. Vreven, J. A. Montgomery, Jr., J. E. Peralta, F. Ogliaro, M. Bearpark, J. J. Heyd, E. Brothers, K. N. Kudin, V. N. Staroverov, R. Kobayashi, J. Normand, K. Raghavachari, A. Rendell, J. C. Burant, S. S. Iyengar, J. Tomasi, M. Cossi, N. Rega, J. M. Millam, M. Klene, J. E. Knox, J. B. Cross, V. Bakken, C. Adamo, J. Jaramillo, R. Gomperts, R. E. Stratmann, O. Yazyev, A. J. Austin, R. Cammi, C. Pomelli, J. W. Ochterski, R. L. Martin, K. Morokuma, V. G. Zakrzewski, G. A. Voth, P. Salvador, J. J. Dannenberg, S. Dapprich, A. D. Daniels, O. Farkas, J. B. Foresman, J. V. Ortiz, J. Cioslowski and D. J. Fox, *Gaussian 09, Revision A.1*, Gaussian, Inc., Wallingford CT, 2009.
- 28 C. A. Osorio-Martínez, A. Urías-Benavides, C. F. A. Gómez-Durán, J. Bañuelos, I. Esnal, I. L. Arbeloa and E. Peña-Cabrera, *J. Org. Chem.*, 2012, **77**, 5434–5438.
- 29 Y. J. Zhao, K. Miao, Z. Zhu and L. J. Fan, *ACS Sens.*, 2017, **2**, 842–847.
- 30 J. N. Moorthy, P. Natarajan, P. Venkatakrisnan, D. F. Huang and T. J. Chow, *Org. Lett.*, 2007, **9**, 5215–5218.
- 31 W. Z. Yuan, P. Lu, S. Chen, J. W. Y. Lam, Z. Wang, Y. Liu, H. S. Kwok, Y. Ma and B. Z. Tang, *Adv. Mater.*, 2010, **22**, 2159–2163.

- 32 Y. Hong, J. W. Y. Lam and B. Z. Tang, *Chem. Soc. Rev.*, 2011, **40**, 5361–5388.
- 33 C. Y. K. Chan, Z. Zhao, J. W. Y. Lam, J. Liu, S. Chen, P. Lu, F. Mahtab, X. Chen, H. H. Y. Sung, H. S. Kwok, Y. Ma, I. D. Williams, K. S. Wong and B. Z. Tang, *Adv. Funct. Mater.*, 2012, **22**, 378–389.
- 34 H. Tong, Y. Dong, Y. Hong, M. Häußler, J. W. Y. Lam, H. H. Y. Sung, X. Yu, J. Sun, I. D. Williams, H. S. Kwok and B. Z. Tang, *J. Phys. Chem. C*, 2007, **111**, 2287–2294.
- 35 O. Trott and A. J. Olson, *J. Comput. Chem.*, 2010, **31**, 455–461.
- 36 N. R. Brown, S. Korolchuk, M. P. Martin, W. A. Stanley, R. Moukhametzianov, M. E. M. Noble and J. A. Endicott, *Nat. Commun.*, 2015, **6**, 6769.
- 37 J. Lee, T. Park, S. Jeong, K. H. Kim and C. Hong, *Bioorg. Med. Chem. Lett.*, 2007, **17**, 1284–1287.
- 38 J. F. Beattie, G. A. Breault, R. P. A. Ellston, S. Green, P. J. Jewsbury, C. J. Midgley, R. T. Naven, C. A. Minshull, R. A. Pauptit, J. A. Tucker and J. E. Pease, *Bioorg. Med. Chem. Lett.*, 2003, **13**, 2955–2960.
- 39 Y. S. Cho, M. Borland, C. Brain, C. H. T. Chen, H. Cheng, R. Chopra, K. Chung, J. Groarke, G. He, Y. Hou, S. Kim, S. Kovats, Y. Lu, M. O. Reilly, J. Shen, T. Smith, G. Trakshel, M. Vögtle, M. Xu, M. Xu and M. J. Sung, *J. Med. Chem.*, 2010, **53**, 7938–7957.
- 40 T. Young, R. Abel, B. Kim, B. J. Berne and R. A. Friesner, *Proc. Natl. Acad. Sci. U. S. A.*, 2007, **104**, 808–813.
- 41 P. W. Snyder, J. Mecinovic, D. T. Moustakas, S. W. Thomas III, M. Harder, E. T. Mack, M. R. Lockett, A. Heroux, W. Sherman and G. M. Whitesides, *Proc. Natl. Acad. Sci. U. S. A.*, 2011, **108**, 17889–17894.